THÈSE

En vue de l'obtention du

DOCTORAT DE L'UNIVERSITÉ DE TOULOUSE

Délivré par : *l'Institut Supérieur de l'Aéronautique et de l'Espace (ISAE)*
Cotutelle internationale *Northwestern Polytechnical University (NPU)*

Présentée et soutenue le *16/07/2015* **par :**

Cheng CHENG

GNSS Multipath and Interference Mitigation Using Bayesian Methods

JURY

Jianguo HUANG	Professeur d'Université	Président
André FERRARI	Professeur d'Université	Rapporteur
Min WU	Professeur d'Université	Rapporteur
Jean-Yves TOURNERET	Professeur d'Université	Directeur de thèse
Vincent CALMETTES	Ingénieur Chercheur	Co-directeur de thèse
Quan PAN	Professeur d'Université	Co-directeur de thèse
Yong HE	Professeur d'Université	Examinateur

École doctorale et spécialité :
MITT : Signal, Image, Acoustique et Optimisation
Unité de Recherche :
Institut Supérieur de l'Aéronautique et de l'Espace, Équipe DEOS-SCANR
Northwestern Polytechnical University, School of Automation
Directeur(s) de Thèse :
Jean-Yves TOURNERET, *Vincent CALMETTES* et *Quan PAN*
Rapporteurs :
André FERRARI et *Min WU*

As heaven maintains vigor through movement,
a gentle man should constantly strive for self-perfection.
As earth's condition is receptive devotion,
a gentle man should hold the outer world with a broad mind.

~"*I Ching, the Book of Changes*"

Abstract

Global Navigation Satellite Systems (GNSS) receivers calculate the user position, velocity and time by using the signals received from a set of navigation satellites. In constricted environments, such as urban canyons or other intensive obstruction scenarios, the signal transmitted by the satellite is subject to reflection or diffraction and can follow different paths, commonly known as multipath (MP) interferences, before arriving at the antenna of the GNSS receiver. The MP interferences affect the signal processing results at different stages in the receiver. For instance, MP signals modify the correlation and discriminator functions and can introduce errors in pseudo-range (PR) and carrier phase measurements, resulting finally in GNSS-based positioning errors. Therefore the MP interference can be considered as a dominant error source in these complex situations. This thesis investigates MP mitigation techniques based on signal processing methods at different stages of the GNSS receiver. By analyzing and comparing the state-of-the-art MP mitigation approaches, innovative MP mitigation techniques are proposed in order to reduce the impact of MP interferences on the GNSS receiver, and to improve the positioning accuracy based on GNSS. The main issues that have been addressed in this thesis are summarized as follows:

1. The MP mitigation techniques inside the GNSS receiver can be formulated as a problem of signal parameter estimation. Considering that the presence and absence of MP signals depend on several factors related to the vehicle environment and motion, it is difficult to use a specific propagation model to capture the dynamics of the MP signal parameters when the vehicle is moving. We propose to use two kinds of models for describing the line-of-sight (LOS) and MP signal parameters. Moreover, a multi-correlator based receiver is exploited with the advantage to fully characterize the impact of MP signals on the correlation function by providing samples of the whole correlation function. A maximum likelihood-based unscented Kalman filter (UKF) is then investigated to estimate the LOS and MP signal parameters iteratively. The posterior Cramér-Rao bound of the LOS signal parameter estimation in the absence of MP interferences is derived and used as the reference for evaluating the performance of the proposed estimation approach. Finally, numerical simulations in different scenarios are implemented to validate the effectiveness of the proposed approach.

2. The previous MP mitigation approach has to be operated inside the tracking loop stage of the GNSS receiver. However, this approach cannot be implemented in a commercial off-the-shelf receiver. An MP mitigation technique by dealing with the GNSS PR measurement is taken into account. Considering that non-line-of-sight (NLOS) MP interferences affect position estimation based on GNSS in urban canyons, we propose to model the effects of NLOS MP interferences as mean value jumps contaminating the GNSS PR measurements. The marginalized likelihood ratio test

(MLRT) is then investigated to detect, identify and estimate the corresponding NLOS MP biases. However, the MLRT test statistics is difficult to compute. Thus we consider a Monte Carlo (MC) integration technique based on bias magnitude sampling. Jensen's inequality allows this MC integration to be simplified. The multiple model algorithm is also used to update the prior information for each bias magnitude sample. Some strategies are designed for estimating and correcting the NLOS MP biases. In order to demonstrate the performance of the MLRT, simulations allowing several localization methods to be compared are performed. Finally, results from a measurement campaign conducted in an urban canyon are presented in order to evaluate the performance of the proposed algorithm in a representative environment.

3. Considering that accurate a priori knowledge about the vehicle state can facilitate the detection and consequently the mitigation for MP biases appearing on GNSS PR and DR measurements, a monocular vision sensor and a baro-altimeter aided inertial measurement unit (IMU)/GNSS integration architecture is investigated. The proposed integration architecture aims at exploiting the reliable GNSS measurements in urban environments to ensure the required navigation accuracy and reliability. A hierarchical sensor integration scheme is proposed for state estimation. A quaternion-based UKF is designed to perform the integration of the IMU and other sensors, in which the quaternion normalization constraint is taken into account in the unscented transformation. Finally, results from a measurement campaign conducted in urban canyons are presented in order to evaluate the performance of the proposed approach in practice.

Résumé

Les récepteurs GNSS sont utilisés pour estimer la position et la vitesse d'un véhicule à partir de signaux transmis par des satellites. L'estimation est habituellement réalisée en plusieurs étapes. Les paramètres des signaux qui concernent le délai de propagation, la phase et la fréquence Doppler de la porteuse, sont estimés et exploités pour estimer des mesures de pseudo-distances et de delta-distances. Ces mesures sont ensuite utilisées comme observation de la position et de la vitesse par l'algorithme de navigation qui délivre l'état du véhicule. En environnement GNSS dégradé les signaux émis par les satellites GPS peuvent subir des réflexions, des réfractions, et suivre ainsi des chemins multiples, communément connus sous le nom de multi-trajets. Ces signaux induisent des déformations du signal à différents niveaux dans les récepteurs. En particulier il en résulte une distorsion des fonctions de corrélation et des fonctions de discrimination, ce qui conduit à des erreurs dans les estimées de pseudo-distances et de delta-distances et, en conséquence, à une erreur de positionnement. Bénéficiant d'un état de l'art des approches développées pour l'atténuation des effets des interférences, de nouvelles techniques sont proposées dans cette thèse afin de réduire l'impact des MT sur les performances des récepteurs, et d'améliorer ainsi la précision de positionnement GPS. Les principaux points qui ont été adressés au cours de de cette thèse sont introduits ci-après :

1. Une première approche consiste à traiter le signal dans l'étage de post corrélation du récepteur. Les techniques d'adoucissement des effets des multi-trajets au sein d'un récepteur GNSS peuvent être formulées comme un problème d'estimation de paramètres du signal. Les instants d'apparition et de disparition des multi-trajets, ainsi que leurs caractéristiques, dépendent de nombreux facteurs reliés à l'environnement et au mouvement du véhicule. Il est ainsi difficile d'élaborer un modèle d'évolution statistique des paramètres de ces multi-trajets lorsque le véhicule se déplace en environnement urbain. Il est proposé ici d'utiliser deux approches différentes pour modéliser le signal direct et les signaux de multi-trajets. Par ailleurs l'estimation utilise un modèle d'observation qui dérive d'un banc de corrélateurs dont les sorties décrivent la fonction de corrélation sur tout le domaine d'intérêt. Une technique qui intègre un estimateur de maximum de vraisemblance et un filtre de Kalman sans parfum est proposée pour l'estimation des paramètres des multi-trajets et du trajet direct. La borne de Cramér-Rao a posteriori est calculée pour représenter la borne inférieure de l'erreur quadratique moyenne de l'estimateur, définie en l'absence de signal d'interférence. Elle est utilisée pour évaluer les performances de l'algorithme présenté. Des simulations numériques sont enfin proposées pour comparer cette nouvelle approche, pour différents scénarios, à des approches conventionnelles.

2. L'approche précédente est basée sur des traitements qui doivent être implantés dans l'étage de post-corrélation du récepteur. En pratique cela n'est pas possible lorsqu'un récepteur du commerce

est utilisé. Les techniques d'adoucissement des effets des MT doivent alors adresser les mesures de pseudo-distances et de delta-distances. En considérant que les multi-trajets affectent l'estimation de la position GNSS dans des canyons urbains, leurs effets sont modélisés comme des sauts de moyenne sur les mesures de pseudo-distance. Une méthode au sens du maximum de vraisemblance marginalisé (MLRT) est alors étudiée pour détecter, identifier et estimer les biais induits par des multi-trajets. Le test statistique associé à cette méthode d'estimation est toutefois difficile à calculer. Une intégration par la méthode de Monte Carlo utilisant des tirages aléatoires uniformément distribués de l'amplitude du biais est proposée. L'inégalité de Jensen est exploitée pour faciliter cette intégration. Un algorithme multi-modèles est également étudié pour mettre à jour, pour chaque tirage, l'information a priori. Une estimation et une correction des biais dus aux multi-trajets sont réalisées. Afin de mettre en évidence les performances de cette approche des simulations permettant une comparaison avec d'autres méthodes est réalisée. La solution proposée est ainsi étudiée et évaluée à partir de mesures prélevées dans des canyons urbains au cours d'une campagne de mesure.

3. Les 2 techniques présentées précédemment n'utilisent que des mesures GNSS. Considérant que la connaissance précise a priori de ces mesures GNSS peut faciliter la détection et l'annulation des biais induits par des multi-trajets sur les mesures de pseudo-distance et delta-distance, un schéma d'intégration permettant le couplage d'un système GNSS avec une centrale inertielle bas coût, aidée par un système de vision et un baro-altimètre, est proposé pour améliorer la robustesse et la fiabilité du positionnement dans des milieux urbains. Dans ce contexte, une approche hiérarchique d'intégration de capteurs a été étudiée pour l'estimation des états du véhicule. Une représentation de l'attitude sous forme de quaternion est adoptée et un filtre de Kalman sans parfum est utilisé pour satisfaire la contrainte de norme unité du quaternion. Les performances obtenues ont été évaluées à partir de données expérimentales collectées au cours d'une campagne de mesure réalisée dans un environnement représentatif.

摘 要

全球导航卫星系统（GNSS）接收机通过利用接收到的一组导航卫星信号来解算用户的实时位置，速度及时间等状态信息。在复杂环境中，如城市峡谷或者障碍物密集情况下，卫星信号在到达接收机天线前易受到障碍物的影响，造成信号的折射或散射，这种现象被称为信号的多路径效应。多径干扰会影响接收机中信号处理结果，如造成接收机的相关函数和鉴相函数失真，产生伪距和相位的测量误差，最终影响GNSS的定位精度。多径干扰被认为是GNSS主要的误差源之一，因此本文研究了基于信号处理方法的多径干扰抑制技术。通过分析比较接收机中多径抑制技术的研究现状，提出了基于贝叶斯方法的多径干扰抑制方法，从而减少多径干扰对GNSS接收机的影响，提高GNSS在复杂环境中的定位精度。本文主要工作可概括如下：

1. 提出了基于最大似然准则下的无迹卡尔曼滤波方法，用于实现在多径干扰影响下直达信号参数估计。考虑到多相关器输出可以充分描述多径信号对接收机相关函数的影响，因此将多相关器的输出作为量测信息。分别采用时间相关的一阶马尔科夫模型和静态似然模型来描述直达信号和多径信号参数，然后利用所提方法实现对直达信号和多径信号参数的迭代估计，并推导了卫星信号参数估计的克拉美罗界用于评估所提算法的性能。最后，在不同仿真场景下对所提的多径抑制方法进行了仿真验证。

2. 提出了基于边缘似然比假设检验的非视距多径误差检测，识别与估计方法。考虑到非视距多径干扰常出现在城市峡谷等复杂环境中，造成GNSS接收机输出的伪距量测发生均值跳变。由于边缘似然比统计量不易计算，采用基于均值跳变误差采样的蒙特卡洛积分来获得近似边缘似然比统计量，利用琴生不等式来简化蒙特卡洛积分计算和多模型方法来更新每个均值跳变误差采样的先验信息。通过蒙特卡洛仿真分析了近似边缘似然比统计量的经验分布函数，从而确定了检测门限值。设计了均值跳变误差的估计和校正方法。最后，通过仿真实验分析比较所提方法与其他多径抑制方法，并通过实验数据来评估所提方法对多径干扰的抑制效果。

3. 提出了基于单目视觉传感器和大气压力计辅助的IMU/GNSS组合导航系统，从而确保在多径环境中可以充分利用可靠的GNSS量测并获得准确的定位结果。该系统采用了分级传感器融合架构，首先将单目视觉传感器和大气压力计与IMU进行组合来校正IMU的漂移误差，提高载体状态的估计精度，然后对GNSS伪距和伪距率量测进行检验，最后利用未受到多径干扰的GNSS量测对载体状态进行更新，获得最终的定位结果。为了保证四元数在无迹变换时归一化要求，采用基于四元数的无迹卡尔曼滤波来实现不同传感器信息的融合。由于在城市峡谷环境中多径干扰造成的GNSS伪距和伪距率量测误差较小，因此采用了序贯统计检测方法来处理GNSS伪距和伪距率量测。最后，通过实验数据来验证所提方法的有效性。

Acknowledgement

First and foremost, I would like to express my sincere gratitude to my supervisor, Prof. Jean-Yves TOURNERET, for his continuous support on my thesis. Without his enlightening guidance and immense knowledge, I would not have completed my thesis. Thank you for sharing all your signal processing expertise and wisdom with me and for teaching me how to write a scientific paper. I owe my publications to his careful proofreading and fruitful contribution.

Moreover, I would like to thank my co-supervisor, Dr. Vincent CALMETTES, for his careful guidance on my research work and enthusiastic help on my living in France. His knowledge on the satellite navigation and signal processing has been essential for the development of this thesis. His valuable comments and suggestions have improved the quality of my thesis and publications significantly. I also would like to thank my co-supervisor, Prof. Quan PAN for his support on this joint supervision of Ph.D thesis. His excellent vision and financial support contribute to this international academic exchange and cooperation.

My appreciation is expressed to the jury of this thesis, especially to Prof. André FERRARI and Prof. Min WU, who kindly accepted to review this work and took the time to propose ways of making it more complete. I also greatly appreciate Dr. Mohamed Sahmoudi for opening the road of my research.

It is impossible also not to mention my friends in Toulouse, in particular Paulo ESTEVES who provided huge help for my living and studying in France. You are so reliable and trustworthy. I cannot forget my Portugal trip in my life. Moreover, I would like to thank Syed, Khairol, Remy, Benoît and Gael for their outstanding support.

Finally, I cannot find words to express my gratitude to my family. My parents,my wife and son, thank you for supporting, understanding and accompanying for all these years. Your love motivates me to move forward constantly!

CONTENTS

LIST OF ABBREVIATIONS

ADC	Analog-to-Digital Converter
ADR	Accumulated Delta-Range
BDSS	BeiDou Navigation Satellite System (Chinese GNSS system)
BPSK	Binary Phase Shift Keying Modulation
C/A	Coarse Acquisition (GPS signal)
CDF	Cumulative Distribution Function
CDMA	Code Division Multiple Access
CS	Commercial Service (Galileo service)
DLL	Delay Lock Loop
DR	Delta-Range
DSSS	Direct Sequence Spread Spectrum
E-L	Early minus Late
ECEF	Earth-Centred Earth-Fixed
EKF	Extended Kalman Filter
ELP	Early minus Late Power
FDMA	Frequency Division Multiple Access
FLL	Frequency Lock Loop
GEO	Geostationary Orbit

GLONASS	GLObal Navigation Satellite System (Russian GNSS system)
GLRT	Generalized Likelihood Ratio Test
GNSS	Global Navigation Satellite Systems
GPS	Global Positioning System (US GNSS system)
GSO	Geosynchronous Orbit
HRC	High Resolution Correlator
I&Q	In-phase and Quadrature
IF	Intermediate Frequency
IMU	Inertial Measurement Unit
IRNSS	Indian Regional Navigational Satellite System
KF	Kalman Filter
LEO	Low Earth Orbit
LEX	L-band Experiment (QZSS signal)
LLR	Log-Likelihood Ratio
LOS	Line of Sight
LRT	Likelihood Ratio Test
MAP	Maximum A Posteriori
MC	Monte Carlo
MDR	Multipath-to-Direct Ratio
MEDLL	Multipath Estimating Delay Lock Loop
MEO	Medium Earth Orbit
MET	Multipath Elimination Technology
MLE	Maximum Likelihood Estimation
MLRT	Marginalized Likelihood Ratio Test
MM	Multiple Model

MMT	Multipath Mitigation Technology
MP	Multipath
NCO	Numerically Controlled Oscillator
NED	North-East-Down
NLOS	Non Line of Sight
OS	Open Service (Galileo service)
PAC	Pulse Aperture Correlator
PCRB	Posterior Cramér-Rao Bound
PDF	Probability Density Function
PF	Particle Filter
PFA	Probability of False Alarm
PLL	Phase Lock Loop
PR	Pseudo-Range
PRN	Pseudo Random Noise (spreading code)
PRS	Public Regulated Service (Galileo service)
PSD	Power Spectral Density
PVT	Position, Velocity and Time
QZSS	Quasi-Zenith Satellite System
RF	Radio Frequency
RHCP	Right Handed Circular Polarization
RMSE	Root Mean Square Error
SAIF	Submeter-class Augmentation with Integrity Function (QZSS signal)
SNR	Signal-to-Noise Ratio
UKF	Unscented Kalman Filter
UT	Unscented Transformation

VC	Vision Correlator
WGS-84	World Geodetic System 1984

RÉSUMÉ DES TRAVAUX EN FRANÇAIS

Les récepteurs GNSS sont utilisés pour estimer la position et la vitesse d'un véhicule à partir de signaux transmis par des satellites. L'estimation est habituellement réalisée en plusieurs étapes. Les paramètres des signaux qui concernent le délai de propagation, la phase et la fréquence Doppler de la porteuse, sont estimés et exploités pour estimer des mesures de pseudo-distances et de delta-distances. Ces mesures sont ensuite utilisées comme observation de la position et de la vitesse par l'algorithme de navigation qui délivre l'état du véhicule. En environnement GNSS dégradé les signaux émis par les satellites GPS peuvent subir des réflexions, des réfractions, et suivre ainsi des chemins multiples, communément connus sous le nom de multi-trajets (MT). Ces signaux induisent des déformations du signal à différents niveaux dans les récepteurs. En particulier il en résulte une distorsion des fonctions de corrélation et des fonctions de discrimination, ce qui conduit à des erreurs dans les estimées de pseudo-distances et de delta-distances et, en conséquence, à une erreur de positionnement. Bénéficiant d'un état de l'art des approches développées pour l'atténuation des effets des interférences, de nouvelles techniques sont proposées dans cette thèse afin de réduire l'impact des MT sur les performances des récepteurs, et d'améliorer ainsi la précision de positionnement GPS. Les principaux points qui ont été adressés au cours de de cette thèse ont été identifiés à partir d'un état de l'art qui introduit et analyse différentes approches reliées à des travaux de recherche dans ce domaine. Cette étude bibliographique a ainsi permis d'identifier 3 axes importants pour réduire les effets des multi-trajets dans les récepteurs. Le premier axe concerne le traitement du signal GNSS dans les étages de post-corrélation. Un deuxième axe adresse le problème du traitement statistique des mesures de pseudo-distances et delta-distances utilisées par le navigateur. Une amélioration de cette approche utilisant des capteurs additionnels est enfin proposée.

1 Principe des systems GNSS

La navigation par satellite est basée sur le principe de trilatération qui utilise des mesures de distances par rapport à des balises placées à des positions connues. S'agissant de la navigation par satellite les balises sont des satellites déployés sur des orbites moyennes (30000 Kms) qui transmettent des signaux dans la bande 1.5 GHz. La mesure de distance est basée sur l'estimation du

temps de propagation des signaux transmis. La synchronisation des satellites et la forme des signaux permet de déterminer le temps d'émission qui est le même quel que soit le satellite. La mesure du temps de réception est affecté d'un biais qui correspond à l'écart entre le temps satellite et le temps récepteur. La mesure exploitée est en pratique la mesure de pseudo-distance notée, pour le $i$ème satellite ρ_i

$$\rho_i = c\,\tau_i \tag{1}$$

où τ_i rerésente le temps de propagation, c est la vitesse de la lumière dans le vide. La mesure de pseudo-distance s'exprime en pratique comme étant la mesure de distance affectée du biais de l'horloge du récepteur b_u exprimé en mètre

$$\rho_i = \sqrt{(x_i - x_u)^2 + (y_i - y_u)^2 + (z_i - z_u)^2} + b_u \tag{2}$$

où (x_i, y_i, z_i) et (x_u, y_u, z_u) représentent respectivement les coordonnées du $i$ème satellite et de l'utilisateur, exprimée habituellement dans un repère centré sur la terre, lié à la terre (repère ECEF). Cette équation fait apparaître les 4 inconnues que constituent les coordonnées de l'utilisateur et le biais d'horloge b_u. Le calcul de la position sur la base de ces mesures nécessite donc de bénéficier d'au moins 4 mesures.

Le signal GNSS utilisé pour la mesure du délai de propagation est un signal à spectre étalé obtenu par des méthodes d'étalement de spectre à séquence directe (DSSS). Un code pseudo-aléatoire (PRN) est attribué à chacun des satellites. Il module le signal transmis, permettant un étalement du signal dans une bande de fréquence dépendant du rythme de ce code. L'estimation des paramètres des signaux reçus nécessite la mise en œuvre d'un filtre adapté qui réalise la corrélation du signal reçu avec un signal replica dont les paramètres sont estimés par le récepteur. L'alignement du signal replica avec le signal reçu nécessite d'estimer à la fois le délai de propagation du code transmis, la phase et la fréquence de la porteuse. La fréquence résulte de l'effet Doppler, permettant une observation de la vitesse satellite-récepteur. Par ailleurs une démodulation du signal en sortie du filtre adapté réalise l'extraction du message transmis par le satellite. Ce message contient toutes les informations nécessaires au calcul de la position des satellites, à la synchronization des satellites, à la correction du temps de propagation. Utilisant la position calculée des satellites et les mesures de retard et fréquence, le récepteur élabore le calcul de la position et de la vitesse du récepteur. En particulier l'estimation de la position nécessite la résolution de l'équation (2). L'inversion de ce système d'équations non linéaires est basée sur la méthode des moindres carrés ou sur un filter de Kalman.

2 Impact des interférences sur les performances d'un récepteurs GNSS

2.1 Modèle du signal en presence de multi-trajets

On suppose que le signal reçu résulte du signal direct appelé signal LOS (Line of sight), et de signaux relatifs à des multi-trajets appelés NLOS (Non LOS). Les signaux NLOS parcourant un trajet plus long sont toujours en retard par rapport au signal LOS. Ils sont en général de plus faible amplitude, la polarisation de ces signaux entrainant en particulier une atténuation au niveau de l'antenne de réception. Le signal résultant dépend de l'ensemble des paramètres des signaux reçus, en particulier de leur amplitude, de leur retard, de leur phase. En l'absence de bruit, le signal reçu, échantillonné aux instants nT_s où $n = 1, \ldots, \infty$, est défini ainsi :

$$r(nT_s) = \sum_{m=0}^{M} a_m \, c(nT_s - \tau_0 - \delta\tau_m) \cos\left(2\pi(f_{\mathrm{IF}} + f_m^d) nT_s + \varphi_0 + \delta\varphi_m\right) \tag{3}$$

où M est le nombre de signaux NLOS, $a_m = \sqrt{P_m}$ et f_m^d représentent respectivement l'amplitude et la fréquence Doppler du $m$ème trajet, τ_0 est le délai de propagation du code du LOS, φ_0 est la phase de la porteuse du signal LOS, $\delta\tau_m$ et $\delta\varphi_m$ représente les délais et phases du $m$ème signal NLOS, relatifs à ceux du signal LOS. S'agissant des délais et phases absolus du $m$ème signal NLOS, ils sont notés $\tau_m = \tau_0 + \delta\tau_m$ et $\varphi_m = \varphi_0 + \delta\varphi_m$.

2.2 Effet des signaux d'interférence sur les performances d'un récepteur GNSS

Nous considérons ici la sortie du filtre adapté associé à un canal du récepteur. Ce filtre adapté consiste ici en un corrélateur «en phase». De même les sorties d'un corrélateur «en avance» et d'un corrélateur «en retard», qui sont nécessaires à la mise en œuvre d'un discriminateur de retard, sont analysés. Aux instants de sortie $k = 1, \ldots, \infty$, les sorties du filtre adapté et des corrélateurs en avance et en retard, qui sont des signaux complexes, s'expriment de la manière suivante

$$\begin{aligned}
I_{E,k} &= \sum_{m=0}^{M} a_m \, R\left(\Delta\tilde{\tau}_{0,k} - \delta\tau_{m,k} + \frac{d}{2}T_c\right) \operatorname{sinc}\left(\pi\Delta\tilde{f}_{m,k}^d T_a\right) \cos(\Delta\tilde{\varphi}_{0,k} + \delta\varphi_{m,k}) \\
I_{P,k} &= \sum_{m=0}^{M} a_m \, R\left(\Delta\tilde{\tau}_{0,k} - \delta\tau_{m,k}\right) \operatorname{sinc}\left(\pi\Delta\tilde{f}_{m,k}^d T_a\right) \cos(\Delta\tilde{\varphi}_{0,k} + \delta\varphi_{m,k}) \\
I_{L,k} &= \sum_{m=0}^{M} a_m \, R\left(\Delta\tilde{\tau}_{0,k} - \delta\tau_{m,k} - \frac{d}{2}T_c\right) \operatorname{sinc}\left(\pi\Delta\tilde{f}_{m,k}^d T_a\right) \cos(\Delta\tilde{\varphi}_{0,k} + \delta\varphi_{m,k})
\end{aligned} \tag{4}$$

et

$$
\begin{aligned}
Q_{E,k} &= \sum_{m=0}^{M} a_m\, R\left(\Delta\tilde{\tau}_{0,k} - \delta\tau_{m,k} + \frac{d}{2}T_c\right) \operatorname{sinc}\left(\pi\Delta\tilde{f}^{d}_{m,k}T_a\right) \sin(\Delta\tilde{\varphi}_{0,k} + \delta\varphi_{m,k}) \\
Q_{P,k} &= \sum_{m=0}^{M} a_m\, R\left(\Delta\tilde{\tau}_{0,k} - \delta\tau_{m,k}\right) \operatorname{sinc}\left(\pi\Delta\tilde{f}^{d}_{m,k}T_a\right) \sin(\Delta\tilde{\varphi}_{0,k} + \delta\varphi_{m,k}) \\
Q_{L,k} &= \sum_{m=0}^{m} a_m\, R\left(\Delta\tilde{\tau}_{0,k} - \delta\tau_{m,k} - \frac{d}{2}T_c\right) \operatorname{sinc}\left(\pi\Delta\tilde{f}^{d}_{m,k}T_a\right) \sin(\Delta\tilde{\varphi}_{0,k} + \delta\varphi_{m,k})
\end{aligned}
\tag{5}
$$

où $\operatorname{sinc}(\cdot)$ est la fonction sinus cardinal, $\Delta\tilde{\tau}_{0,k}$ et $\Delta\tilde{\varphi}_{0,k}$ sont les erreurs d'estimation du récepteur, $\Delta\tilde{f}_{m,k}$ est l'erreur de fréquence du $m$ème trajet. Ici la valeur $m = 0$ de l'index indique le signal LOS, tel que $\delta\tau_{0,k} = 0$ and $\delta\varphi_{0,k} = 0$.

Dans le cadre de cette étude on considère le signal LOS et un signal NLOS qui résulte de la somme de tous les signaux NLOS. Dans ces conditions $M = 1$. La Figure 1 représente la fonction d'autocorrélation du signal en présence d'un signal NLOS. Il apparait une distorsion de la fonction d'autocorrélation pour $\delta\tau_1 \neq 0$. La sortie du corrélateur «en phase», représentée à gauche pour un NLOS constructif, à gauche pour un NLOS destructif montre des déformations qui vont induire des erreurs d'estimation positive dans le cas d'un NLOS constructif, négative dans le cas d'un NLOS destructif.

Ceci est mis en évidence à la sortie du discriminateur de retard, Figure 2, qui montre les sorties du discriminateur «avance-retard» en l'absence et en présence de NLOS. On observe que le passage à zéro est décalé vers la droite ou vers la gauche, selon la nature du signal NLOS. La valeur de ce décalage représente l'erreur de mesure qui conduit à une erreur d'estimation du délai, de même valeur.

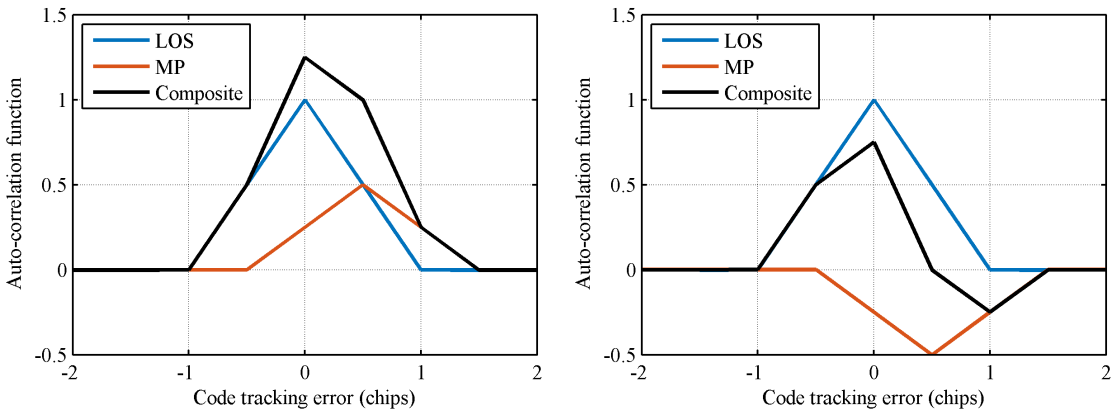

(a) NLOS constructif **(b)** NLOS destructif

Figure 1 – Fonction d'autocorrélation du LOS, du NLOS, du LOS+NLOS pour $\alpha_m = \frac{1}{2}$, $\delta\tau_1 = 0.5$ chip et $\delta\varphi_1 = 0°$ (a) ou 180° (b), pour des signaux à bande infinie.

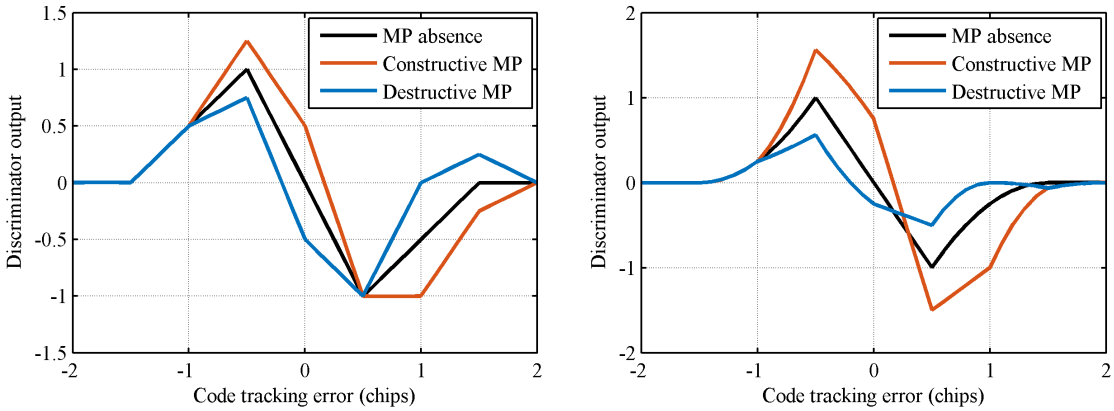

(a) Cohérent E-L discriminateur **(b)** Non-coherent E-L discriminateur

Figure 2 – Sortie du discriminateur avance-retard dans le cas du LOS, du NLOS, du LOS+NLOS, pour $\alpha_m = \frac{1}{2}$, $\delta\tau_1 = 0.5$ chip et $\delta\varphi_1 = 0°$ (a) ou 180° (b), pour des signaux à bande infinie.

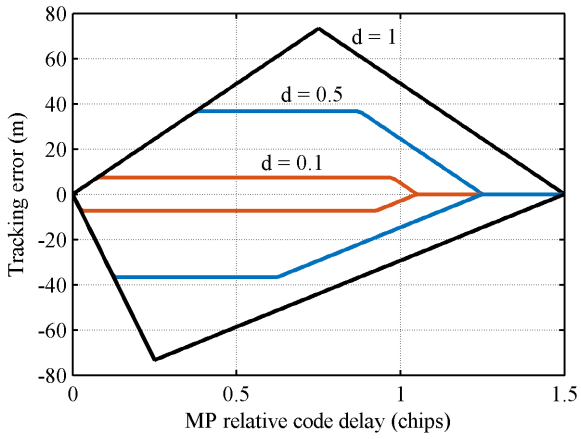

Figure 3 – Enveloppe d'erreur pour $\alpha_m = \frac{1}{2}$, $\delta\tau_1 = 0.5$,$\delta\varphi_1 = 0°$ ou 180°

La Figure 3 montre l'enveloppe d'erreur, qui représente l'erreur d'estimation de délai en fonction de la valeur du retard relatif du signal NLOS, pour un signal NLOS en phase s'agissant de la courbe supérieure, et en opposition de phase s'agissant de la courbe inférieure, pour différentes valeurs de l'espacement entre corrélateurs «avance», «en phase», «retard», d.

Ces enveloppes d'erreur mettent en évidence l'erreur d'estimation de délai pour des retards relatifs du NLOS tel que $\delta\tau \geq (1 + d/2)\, T_c$ où T_c représente la durée d'un chip. L'impact d'un signal NLOS est ainsi limité pour un discriminateur étroit obtenu pour de faible valeur de d.

3 Principales Contributions de la Thèses

Plusieurs approches ont été proposées pour réduire l'impact des signaux d'interférence au sein d'un récepteur.

(1) Le premier axe consiste à traiter le signal dans l'étage de post corrélation du récepteur. Les techniques d'adoucissement des effets des multi-trajets au sein d'un récepteur GNSS peuvent alors être formulées comme un problème d'estimation des paramètres du signal. Les instants d'apparition et de disparition des multi-trajets, ainsi que leurs caractéristiques, dépendent de nombreux facteurs reliés à l'environnement et au mouvement du véhicule. Il est ainsi difficile d'élaborer un modèle d'évolution statistique des paramètres de ces multi-trajets lorsque le véhicule se déplace en environnement urbain. Il est proposé ici d'utiliser deux approches différentes pour modéliser le signal direct et les signaux de multi-trajets. Par ailleurs l'estimation utilise un modèle d'observation qui dérive d'un banc de corrélateurs dont les sorties décrivent la fonction de corrélation sur tout le domaine d'intérêt. Une technique qui intègre un estimateur de maximum de vraisemblance et un filtre de Kalman sans parfum est proposée pour l'estimation des paramètres des multi-trajets et du trajet direct. La borne de Cramér-Rao a posteriori est calculée pour représenter la borne inférieure de l'erreur quadratique moyenne de l'estimateur, définie en l'absence de signal d'interférence. Elle est utilisée pour évaluer les performances de l'algorithme présenté. Des simulations numériques sont enfin proposées pour comparer cette nouvelle approche, pour différents scénarios, à des approches conventionnelles.

(2) L'approche précédente est basée sur des traitements qui doivent être implantés dans l'étage de post-corrélation du récepteur. En pratique cela n'est pas possible lorsqu'un récepteur du commerce est utilisé. Les techniques d'adoucissement des effets des MT doivent alors adresser les mesures de pseudo-distances et de delta-distances. En considérant que les multi-trajets affectent l'estimation de la position GNSS dans des canyons urbains, leurs effets sont modélisés comme des sauts de moyenne sur les mesures de pseudo-distance. Une méthode au sens du maximum de vraisemblance marginalisé (MLRT) est alors étudiée pour détecter, identifier et estimer les biais induits par des multi-trajets. Le test statistique associé à cette méthode d'estimation est toutefois difficile à calculer. Une intégration par la méthode de Monte Carlo utilisant des tirages aléatoires uniformément distribués de l'amplitude du biais est proposée. L'inégalité de Jensen est exploitée pour faciliter cette intégration. Un algorithme multi-modèles est également étudié pour mettre à jour, pour chaque tirage, l'information a priori. Une estimation et une correction des biais dus aux multi-trajets sont réalisées. Afin de mettre en évidence les performances de cette approche des simulations permettant une comparaison avec d'autres méthodes est réalisée. La solution proposée est ainsi étudiée

et évaluée à partir de mesures prélevées dans des canyons urbains au cours d'une campagne de mesure.

(3) Les 2 techniques présentées précédemment n'utilisent que des mesures GNSS. Considérant que la connaissance précise a priori de ces mesures GNSS peut faciliter la détection et l'annulation des biais induits par des multi-trajets sur les mesures de pseudo-distance et delta-distance, un schéma d'intégration permettant le couplage d'un système GNSS avec une centrale inertielle bas coût, aidée par un système de vision et un baro-altimètre, est proposé pour améliorer la robustesse et la fiabilité du positionnement dans des milieux urbains.Dans ce contexte, une approche hiérarchique d'intégration de capteurs a été étudiée pour l'estimation des états du véhicule. Une représentation de l'attitude sous forme de quaternion est adoptée et un filtre de Kalman sans parfum est utilisé pour satisfaire la contrainte de norme unité du quaternion. Les performances obtenues ont été évaluées à partir de données expérimentales collectées au cours d'une campagne de mesure réalisée dans un environnement représentatif.

3.1 Estimateur de Maximum de Vraisemblance basé sur un filter de Kalman sans parfum pour la réduction des effets d'un signal NLOS en sortie d'un banc de corrélateurs

Cet estimateur est basé sur le principe que les évolutions des paramètres du signal LOS sont reliées au mouvement du véhicule, alors que les signaux NLOS subissent des variations très dépendantes de l'environnement dans lequel le récepteur évolue, tout particulièrement dans des canyons urbains. En conséquence il est difficile d'utiliser un modèle de propagation pour décrire précisément la dynamique des paramètres des signaux NLOS dès lors que le véhicule se déplace. Pour cette approche il est proposé d'utiliser 2 modèles, un modèle dynamique déduit du mouvement du véhicule décrivant l'évolution des paramètres du signal LOS, un modèle de vraisemblance relié aux paramètres du signal NLOS. Afin de construire un modèle de mesure qui traduise la distorsion de la fonction d'autocorrélation en présence de signal NLOS, un banc de corrélateurs est utilisé pour échantillonner cette fonction d'autocorrélation autour du point affecté d'une erreur de délai correspondant à l'erreur d'estimation du délai du signal LOS. Un estimateur de maximum de vraisemblance basé sur un filtre de Kalman sans parfum est proposé pour estimer de façon itérative les paramètres des signaux LOS et NLOS. Plus précisément il est proposé de rechercher sur une grille dont le pas correspond à l'écart entre corrélateurs adjacents la valeur du délai du signal NLOS en utilisant l'information a priori obtenue en propageant les paramètres du signal LOS. Un filtre de Kalman sans parfum est implémenté, utilisant un modèle d'observation déduit des estimées des paramètres du NLOS produites par l'estimateur de maximum de vraisemblance, pour mettre à jour les paramètres du signal NLOS.

3.1.1 Formulation du problème

Le vecteur des paramètres du signal reçu $\boldsymbol{x}_k$ peut être partitionné en 2 vecteurs. Le premier vecteur $\boldsymbol{x}_{0,k}$ inclut les paramètres du signal LOS. Le deuxième $(\boldsymbol{x}_{1,k},\ldots,\boldsymbol{x}_{M,k})$ contient les paramètres des signaux NLOS. D'après le théorème de Bayes la densité de probabilité (pdf) a posteriori se définit de la manière suivante

$$\begin{aligned} p(\boldsymbol{x}_k|\boldsymbol{z}_{1:k}) &= p\left(\boldsymbol{x}_{0,k},\boldsymbol{x}_{1,k},\ldots,\boldsymbol{x}_{M,k}|\boldsymbol{z}_{1:k}\right) \\ &\propto p\left(\boldsymbol{z}_k|\boldsymbol{x}_{0,k},\boldsymbol{x}_{1,k},\ldots,\boldsymbol{x}_{M,k},\boldsymbol{z}_{1:k-1}\right)\, p\left(\boldsymbol{x}_{0,k},\boldsymbol{x}_{1,k},\ldots,\boldsymbol{x}_{M,k}|\boldsymbol{z}_{1:k-1}\right) \\ &= p\left(\boldsymbol{z}_k|\boldsymbol{x}_{0,k},\boldsymbol{x}_{1,k},\ldots,\boldsymbol{x}_{M,k},\boldsymbol{z}_{1:k-1}\right)\, p\left(\boldsymbol{x}_{0,k}|\boldsymbol{x}_{1,k},\ldots,\boldsymbol{x}_{M,k},\boldsymbol{z}_{1:k-1}\right)\, p\left(\boldsymbol{x}_{1,k},\ldots,\boldsymbol{x}_{M,k}|\boldsymbol{z}_{1:k-1}\right). \end{aligned} \tag{6}$$

On peut admettre que le vecteur des paramètres du signal LOS et le vecteur des paramètres du signal NLOS sont indépendants. L'équation (6) s'écrit alors :

$$p(\boldsymbol{x}_k|\boldsymbol{z}_{1:k}) \propto p\left(\boldsymbol{z}_k|\boldsymbol{x}_{0,k},\boldsymbol{x}_{1,k},\ldots,\boldsymbol{x}_{M,k},\boldsymbol{z}_{1:k-1}\right)\, p\left(\boldsymbol{x}_{0,k}|\boldsymbol{z}_{1:k-1}\right)\, p\left(\boldsymbol{x}_{1,k},\ldots,\boldsymbol{x}_{M,k}|\boldsymbol{z}_{1:k-1}\right). \tag{7}$$

La pdf a piori associée au vecteur $\boldsymbol{x}_{0,k}$ des paramètres du signal LOS est supposée déterminée, alors que la pdf a piori associée au vecteur des paramètres des signaux NLOS est supposée invariante. Ceci permet de reformuler l'équation (7)

$$p(\boldsymbol{x}_k|\boldsymbol{z}_{1:k}) \propto p\left(\boldsymbol{z}_k|\boldsymbol{x}_{0,k},\boldsymbol{x}_{1,k},\ldots,\boldsymbol{x}_{M,k},\boldsymbol{z}_{1:k-1}\right)\, p\left(\boldsymbol{x}_{0,k}|\boldsymbol{z}_{1:k-1}\right). \tag{8}$$

La résolution de l'équation (8), pour estimer directement le vecteur $\boldsymbol{x}_k$ des paramètres du signal reçu, n'est pas aisée en pratique. Une approche innovante proposée dans cette thèse consiste à construire un estimateur bayésien du vecteur $\boldsymbol{x}_k$ des paramètres. Cette approche est décrite ci-après.

3.1.2 Estimation des paramètres des multi-trajets utilisant l'estimateur de maximum de vraisemblance

On suppose ici que le vecteur $\boldsymbol{x}_{0,k}$ des paramètres du signal LOS est connu à l'instant k. L'équation (6) peut s'écrire

$$\begin{aligned} p(\boldsymbol{x}_k|\boldsymbol{z}_{1:k}) &= p\left(\boldsymbol{x}_{0,k},\boldsymbol{x}_{1,k},\ldots,\boldsymbol{x}_{M,k}|\boldsymbol{z}_{1:k}\right) \\ &= p\left(\boldsymbol{x}_{1,k},\ldots,\boldsymbol{x}_{M,k}|\boldsymbol{x}_{0,k},\boldsymbol{z}_{1:k}\right)\, p\left(\boldsymbol{x}_{0,k}|\boldsymbol{z}_{1:k}\right) \\ &\propto p\left(\boldsymbol{x}_{1,k},\ldots,\boldsymbol{x}_{M,k}|\boldsymbol{z}_{1:k}\right) \end{aligned} \tag{9}$$

où $p\left(\boldsymbol{x}_{1,k},\ldots,\boldsymbol{x}_{M,k}|\boldsymbol{z}_{1:k}\right)$ est la pdf a posteriori du vecteur $(\boldsymbol{x}_{1,k},\ldots,\boldsymbol{x}_{M,k})$ des paramètres des signaux NLOS. Puisque la pdf a priori de ce vecteur est supposée invariante, la pdf a posteriori s'écrit

$$p\left(\boldsymbol{x}_{1,k},\ldots,\boldsymbol{x}_{M,k}|\boldsymbol{z}_{1:k}\right) \propto p\left(\boldsymbol{z}_{1:k}|\boldsymbol{x}_{1,k},\ldots,\boldsymbol{x}_{M,k}\right) \tag{10}$$

où $p\left(\boldsymbol{z}_{1:k}|\boldsymbol{x}_{1,k},\ldots,\boldsymbol{x}_{M,k}\right)$ est la fonction de vraisemblance des observations $\boldsymbol{z}_{1:k}$ élaborées à l'instant k. En conséquence l'estimation de $\boldsymbol{x}_k$, à partir des observations $\boldsymbol{z}_{1:k}$, pour une valeur connue des paramètres du vecteur $\boldsymbol{x}_{0,k}$ des paramètres du signal se ramène à un estimateur de maximum de vraisemblance (MLE).

L'estimateur des paramètres des signaux NLOS est obtenu en maximisant la fonction de vraisemblance définie par l'équation (10), par rapport au vecteur $(\boldsymbol{x}_{1,k},\ldots,\boldsymbol{x}_{M,k})$ des paramètres des signaux NLOS. Ceci est conditionné à la connaissance du vecteur $\boldsymbol{x}_{0,k}$ des paramètres du signal LOS qui n'est pas disponible à l'instant k. L'approche retenue ici propose d'utiliser le modèle d'évolution des paramètres du signal LOS pour dériver la pdf conditionnelle $p\left(\boldsymbol{x}_{0,k}|\boldsymbol{z}_{1:k}\right)$ à l'instant k, permettant d'approximer le vecteur $\boldsymbol{x}_{0,k}$ dans (10). La méthode devient alors très dépendante de la qualité du modèle dynamique décrivant l'évolution des paramètres des signaux NLOS.

3.1.3 Estimation des paramètres du signal LOS basée sur un filtre de Kalman sans parfum

Dans le chapitre 3.1.2 il est décrit une méthode d'estimation des paramètres des signaux NLOS. Si le vecteur $(\boldsymbol{x}_{1,k},\ldots,\boldsymbol{x}_{M,k})$ des paramètres des signaux NLOS est connu à l'instant k, l'équation (6) peut s'écrire ainsi

$$\begin{aligned} p\left(\boldsymbol{x}_k|\boldsymbol{z}_{1:k}\right) &= p\left(\boldsymbol{x}_{0,k},\boldsymbol{x}_{1,k},\ldots,\boldsymbol{x}_{M,k}|\boldsymbol{z}_{1:k}\right) \\ &= p\left(\boldsymbol{x}_{0,k}|\boldsymbol{x}_{1,k},\ldots,\boldsymbol{x}_{M,k},\boldsymbol{z}_{1:k}\right)p\left(\boldsymbol{x}_{1,k},\ldots,\boldsymbol{x}_{M,k}|\boldsymbol{z}_{1:k}\right) \\ &\propto p\left(\boldsymbol{x}_{0,k}|\boldsymbol{z}_{1:k}\right) \\ &\propto p\left(\boldsymbol{z}_k|\boldsymbol{x}_{0,k}\right)\ p\left(\boldsymbol{x}_{0,k}|\boldsymbol{z}_{1:k-1}\right) \end{aligned} \tag{11}$$

où $p\left(\boldsymbol{z}_k|\boldsymbol{x}_{0,k}\right)$ et $p\left(\boldsymbol{x}_{0,k}|\boldsymbol{z}_{1:k-1}\right)$ sont les fonctions de vraisemblance de la $k$ème observation et la pdf conditionnelle du vecteur $\boldsymbol{x}_{0,k}$ des paramètres du signal LOS, conditionnellement aux $k-1$ premières observations $\boldsymbol{z}_{1:k-1}$. Dans ces conditions la loi de densité a posteriori $p\left(\boldsymbol{x}_k|\boldsymbol{z}_{1:k}\right)$, pour une représentation donnée du vecteur des paramètres des signaux NLOS, conduit à une pdf a posteriori du vecteur $\boldsymbol{x}_{0,k}$ des paramètres du signal LOS.

D'après (11), la pdf a posteriori du vecteur $\boldsymbol{x}_{0,k}$ des paramètres du signal LOS peut être décrite comme une fonction du vecteur $(\boldsymbol{x}_{1,k},\ldots,\boldsymbol{x}_{M,k})$ des paramètres des signaux NLOS. Lorsqu'on considère que l'estimateur de maximum de vraisemblance du vecteur des paramètres des signaux NLOS peut être obtenu d'après (10), le vecteur $(\boldsymbol{x}_{1,k},\ldots,\boldsymbol{x}_{M,k})$ qui est utilisé ici peut être approximé par le vecteur obtenu à l'instant k en utilisant l'estimateur de maximum de vraisemblance du vecteur $(\boldsymbol{x}_{1,k},\ldots,\boldsymbol{x}_{M,k})$. Il est proposé ici, étant donné le caractère non linéaire des équations qui régissent le modèle d'observation, d'utiliser un filtre de Kalman sans parfum (UKF) pour obtenir l'estimation a posteriori du vecteur $\boldsymbol{x}_{0,k}$, en fonction du vecteur $(\boldsymbol{x}_{1,k},\ldots,\boldsymbol{x}_{M,k})$.

3.1.4 Résultats

Une analyse réalisée sur des données simulées a permis de mettre en évidence les bonnes performances obtenues. La Figure 4 montre que la méthode proposée offre de très bonne performance, en particulier en présence de résultats. Par ailleurs cette simulation montre la sensibilité de la méthode au nombre de corrélateurs par une comparaison des résultats obtenus avec 11 et 21 corrélateurs.

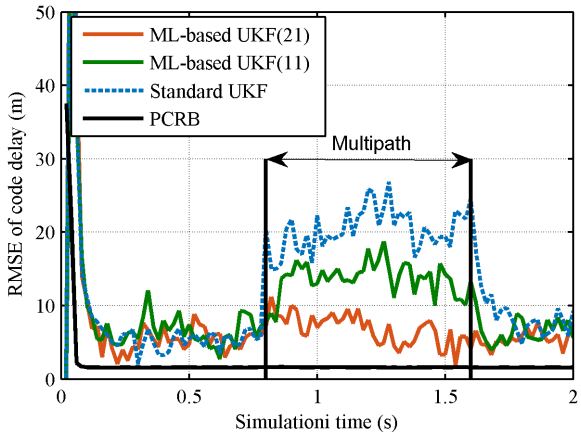

Figure 4 – Erreurs d'estimation

3.2 Définition d'un rapport de maximum de vraisemblance marginalisé pour la détection et l'estimation des biais induits par des multi-trajets sur les mesures GNSS

Dans des canyons urbains, les biais dus à des signaux NLOS induisent des erreurs de position. Ce chapitre propose de modéliser les effets des signaux NLOS sur les mesures de pseudo-distances (PR) par des sauts de moyenne. Le test du rapport de vraisemblance marginalisé (MLRT) est appliqué dans cette thèse pour détecter, identifier et estimer le biais sur les mesures de PR. Le principal problème relié à cette approche est la difficulté de calcul de la statistique du test. Dans le cadre de cette thèse il est proposé d'utiliser une méthode d'intégration de Monte Carlo, basée sur des échantillons du biais obtenus sous l'hypothèse d'une distribution uniforme de ce biais. Un apport important de cette thèse découle de l'application de l'inégalité de Jensen pour simplifier l'intégration de Monte Carlo. Un algorithme multi modèles est aussi utilisé pour mettre à jour l'information a priori pour chaque valeur du biais échantillonnée.

3.2.1 Formulation du problème

Selon la théorie du test d'hypothèses le test du rapport de vraisemblance établi pour la détection de la présence ou de l'absence de saut de moyenne est un test binaire qui compare 2 hypothèses. L'hypothèse H_0 est associée à l'absence de saut de moyenne alors que l'hypothèse H_1 est associée à la présence d'un saut de moyenne. Les 2 hypothèses considérées ici sont donc définies ainsi

H_0 : Pas de saut de moyenne jusqu'à l'instant k,

H_1 : Un saut de moyenne d'amplitude $\upsilon \neq 0$ est apparu à l'instant $\theta < k$.

Le rapport de log-vraisemblance pour ces 2 hypothèses se définit de la manière suivante

$$l_k(\theta, \upsilon) = \ln \frac{p(\boldsymbol{Z}_{1:k}|\mathrm{H}_1(\theta, \upsilon))}{p(\boldsymbol{Z}_{1:k}|\mathrm{H}_0)} \tag{12}$$

où $\boldsymbol{Z}_{1:k} = \{\boldsymbol{Z}_i\}_{i=1}^{k}$ est la séquence des vecteurs de mesure de pseudo-distance obtenue jusqu'à l'instant k avec $\boldsymbol{Z}_i = \left(Z_i^1, \ldots, Z_i^{N_s}\right)$, et N_s est le nombre de satellites en vue. Les fonctions de distribution $p(\boldsymbol{Z}_{1:k}|\mathrm{H}_0)$ and $p(\boldsymbol{Z}_{1:k}|\mathrm{H}_1(\theta, \upsilon))$ sont les pdfs du vecteur de mesure associées respectivement aux hypothèses H_0 and H_1.

Nous supposons ici que la loi de distribution a priori du biais υ sur les mesures de pseudo-distance suit une loi uniforme définie par $p(\upsilon) \sim \mathrm{U}(\upsilon_{\min}, \upsilon_{\max})$ où $\mathrm{U}(\cdot)$ représente la loi uniforme, $\upsilon_{\min}$ et $\upsilon_{\max}$ sont les valeurs minimale et maximale du biais définissant le support de la loi. La marginalisation de l'équation (12) par rapport à υ conduit à

$$l_k(\theta) = \ln \frac{p(\boldsymbol{Z}_{1:k}|\mathrm{H}_1(\theta))}{p(\boldsymbol{Z}_{1:k}|\mathrm{H}_0)} \tag{13}$$

où

$$p(\boldsymbol{Z}_{1:k}|\mathrm{H}_1(\theta)) = \int p(\boldsymbol{Z}_{1:k}|\mathrm{H}_1(\theta, \upsilon))\, p(\upsilon)\, \mathrm{d}\upsilon. \tag{14}$$

Le calcul analytique de l'intégrale (14) étant difficile, une intégration basée sur la méthode de Monte Carlo est proposée. L'intégration de (14) selon la méthode de Monte Carlo est approximée par

$$p(\boldsymbol{Z}_{1:k}|\mathrm{H}_1(\theta)) \approx \sum_{i=1}^{n} \omega^i\, p(\boldsymbol{Z}_{1:k}|\mathrm{H}_1(\theta, \upsilon_i)) \tag{15}$$

où υ_i $(i = 1, \ldots, n)$ est la $i$ème valeur du biais échantillonné sur l'intervalle $(\upsilon_{\min}, \upsilon_{\max})$, et n est le nombre d'échantillons sur cet intervalle. En conséquence un groupe de vecteurs contenant les biais (noté $\boldsymbol{\upsilon}_i = (0, \ldots, \upsilon_i, \ldots, 0)$ pour $i = 1, \ldots, n$), ayant un poids $\omega^i = 1/n$ tel que $\sum_{i=1}^{n} \omega^i = 1$, est généré. En conséquence le test statistique $l_k(\theta)$ MLRT est approximé par

$$l_k(\theta) = \ln \frac{p(\boldsymbol{Z}_{1:k}|\mathrm{H}_1(\theta))}{p(\boldsymbol{Z}_{1:k}|\mathrm{H}_0)} \approx \ln \frac{\sum_{i=1}^{n} \omega^i\, p(\boldsymbol{Z}_{1:k}|\mathrm{H}_1(\theta, \upsilon_i))}{p(\boldsymbol{Z}_{1:k}|\mathrm{H}_0)}. \tag{16}$$

Puisque $v = 0$ pour $k < \theta$, $l_k(\theta)$ peut s'écrire

$$l_k(\theta) = \ln \frac{\sum_{i=1}^{n} \omega^i p(\boldsymbol{Z}_{\theta:k} | \boldsymbol{Z}_{1:\theta-1}, \mathrm{H}_1(\theta, v_i))}{p(\boldsymbol{Z}_{\theta:k} | \boldsymbol{Z}_{1:\theta-1}, \mathrm{H}_0)}. \tag{17}$$

L'estimateur MLE du temps d'apparition θ est

$$\hat{\theta} = \arg\max_{\theta} l_k(\theta). \tag{18}$$

La présence d'un saut de moyenne est détectée à partir de la règle du MLRT suivante

$$l_k\left(\hat{\theta}\right) \underset{\mathrm{H}_0}{\overset{\mathrm{H}_1}{\gtrless}} \varepsilon \tag{19}$$

où ε est un seuil déduit de la probabilité de fausse alarme du test.

3.2.2 Approximation du rapport du MLRT utilisant l'inégalité de Jensen

Selon la théorie du filtre de Kalman, le dénominateur de (17) qui est la fonction de vraisemblance associée à l'hypothèse H_0 peut être défini par

$$p(\boldsymbol{Z}_{\theta:k} | \boldsymbol{Z}_{1:\theta-1}, \mathrm{H}_0) = \prod_{j=\theta}^{k} p\left(\boldsymbol{Z}_j | \boldsymbol{Z}_{1:j-1}, \mathrm{H}_0\right) \tag{20}$$

avec

$$p\left(\boldsymbol{Z}_j | \boldsymbol{Z}_{1:j-1}, \mathrm{H}_0\right) = \mathcal{N}\left(\boldsymbol{Z}_j; \hat{\boldsymbol{Z}}^0_{j/j-1}, \boldsymbol{S}^0_j\right) = p\left(\boldsymbol{\gamma}^0_j | \mathrm{H}_0\right)$$

où $\mathcal{N}\left(\boldsymbol{Z}_j; \hat{\boldsymbol{Z}}^0_{j/j-1}, \boldsymbol{S}^0_j\right)$ est la loi normale de moyenne $\hat{\boldsymbol{Z}}^0_{j/j-1}$ et de matrice de covariance $\boldsymbol{S}^0_j$, $\boldsymbol{\gamma}^0_j = \boldsymbol{Z}_j - \hat{\boldsymbol{Z}}^0_{j/j-1}$ et $\boldsymbol{S}^0_j$ représentent le vecteur innovation et la matrice de covariance de ce vecteur sous l'hypothèse H_0, à l'instant j, $\boldsymbol{Z}_j$ et $\hat{\boldsymbol{Z}}^0_{j/j-1}$ sont les vecteurs des mesures de pseudo-distances et des mesures de pseudo-distances prédites sous l'hypothèse H_0, à l'instant j. Le numérateur de (17) est donc une somme pondérée de fonctions de vraisemblance associées à différentes hypothèses correspondant aux amplitudes v_i $(i = 1, \ldots, n)$. Et la fonction de vraisemblance sous l'hypothèse d'un saut de moyenne d'amplitude v_i est

$$p(\boldsymbol{Z}_{\theta:k} | \boldsymbol{Z}_{1:\theta-1}, \mathrm{H}_1(\theta, v_i)) = \prod_{j=\theta}^{k} p\left(\boldsymbol{Z}_j | \boldsymbol{Z}_{1:j-1}, \mathrm{H}_1(\theta, v_i)\right) \tag{21}$$

avec

$$p\left(\boldsymbol{Z}_j | \boldsymbol{Z}_{1:j-1}, \mathrm{H}_1(\theta, v_i)\right) = \mathcal{N}\left(\boldsymbol{Z}_j; \hat{\boldsymbol{Z}}^i_{j/j-1}, \boldsymbol{S}^i_j\right) = p\left(\tilde{\boldsymbol{\gamma}}^i_j | \mathrm{H}_1(\theta, v_i)\right)$$

où $\tilde{\boldsymbol{\gamma}}^i_j = \boldsymbol{\gamma}^0_j - \boldsymbol{v}_i$ et $\boldsymbol{S}^i_j$ représentent le vecteur innovation et sa matrice de covariance, sous l'hypothèse H_1 associé à un biais d'amplitude v_i à l'instant j. Il est à noter que $\hat{\boldsymbol{Z}}^i_{j/j-1}$ est le vecteur des mesures

prédites sous l'hypothèse H_1 pour un biais d'amplitude v_i à l'instant j.

Une fois utilisés (20) et (21) dans (17), le test statistique du MLRT basé sur une intégration de Monte Carlo (MC) peut s'exprimer comme suit

$$\begin{aligned} l_k(\theta) &= \ln \frac{\sum_{i=1}^{n} \omega^i \prod_{j=\theta}^{k} \mathcal{N}\left(\boldsymbol{Z}_j; \hat{\boldsymbol{Z}}^i_{j/j-1}, \boldsymbol{S}^i_j\right)}{\prod_{j=\theta}^{k} \mathcal{N}\left(\boldsymbol{Z}_j; \hat{\boldsymbol{Z}}^0_{j/j-1}, \boldsymbol{S}^0_j\right)} \\ &= \ln \frac{\sum_{i=1}^{n} \omega^i \prod_{j=\theta}^{k} p\left(\tilde{\boldsymbol{r}}^i_j | \mathrm{H}_1(\theta, v_i)\right)}{\prod_{j=\theta}^{k} p\left(\boldsymbol{r}^0_j | \mathrm{H}_0\right)}. \end{aligned} \tag{22}$$

Dans cette équation (22), il apparait au dénominateur un produit de plusieurs lois normales qui peut être facilement résolu par l'utilisation de la fonction logarithme. Par contre la somme pondérée de lois normales qui constituent le numérateur n'est pas facilement réalisable. Dans le cadre de cette thèse il est proposé d'utiliser l'inégalité de Jensen dans (22). Le test statistique s'écrit

$$l_k(\theta) = \ln \frac{\sum_{i=1}^{n} \omega^i \prod_{j=\theta}^{k} p\left(\tilde{\boldsymbol{r}}^i_j | \mathrm{H}_1(\theta, v_i)\right)}{\prod_{j=\theta}^{k} p\left(\boldsymbol{r}^0_j | \mathrm{H}_0\right)} \geq \sum_{i=1}^{n} \omega^i \ln \prod_{j=\theta}^{k} p\left(\tilde{\boldsymbol{r}}^i_j | \mathrm{H}_1(\theta, v_i)\right) - \ln \prod_{j=\theta}^{k} p\left(\boldsymbol{r}^0_j | \mathrm{H}_0\right) \triangleq \frac{1}{2} \tilde{l}'_k(\theta), \tag{23}$$

i.e.,

$$\tilde{l}'_k(\theta) = \left[\sum_{j=\theta}^{k} \left(\boldsymbol{r}^0_j\right)^{\mathrm{T}} \left(\boldsymbol{S}^0_j\right)^{-1} \left(\boldsymbol{r}^0_j\right) - \sum_{i=1}^{n} \omega^i \sum_{j=\theta}^{k} \left(\tilde{\boldsymbol{r}}^i_j\right)^{\mathrm{T}} \left(\boldsymbol{S}^i_j\right)^{-1} \left(\tilde{\boldsymbol{r}}^i_j\right) \right] + K' \tag{24}$$

où

$$K' = \sum_{j=\theta}^{k} \ln \left| \boldsymbol{S}^0_j \right| - \sum_{i=1}^{n} \omega^i \sum_{j=\theta}^{k} \ln \left| \boldsymbol{S}^i_j \right|$$

est indépendant des mesures. D'après (24), pour obtenir les innovations basées sur n mesures, plusieurs équations de mesure (autant d'équations que de valeurs du biais) doivent être traitées en parallèle et les contributions de toutes ces équations de mesure pondérées par le poids ω^i. Dans la mesure où chaque équation est associée à une valeur de v_i le poids qui lui est attribué dépend directement de la distance $\|v - v_i\|$. Ce poids varie donc dans le temps (chaîne de Markov cachée) et est notée $\tilde{\omega}^i_j$ (poids de la $i$ème mesure à l'instant j).

En remplaçant ω^i par $\tilde{\omega}^i_j$ dans (24), cette équation devient

$$\tilde{l}_k(\theta) = \sum_{j=\theta}^{k} \left[\left(\boldsymbol{r}^0_j\right)^{\mathrm{T}} \left(\boldsymbol{S}^0_j\right)^{-1} \left(\boldsymbol{r}^0_j\right) - \sum_{i=1}^{n} \tilde{\omega}^i_j \left(\tilde{\boldsymbol{r}}^i_j\right)^{\mathrm{T}} \left(\boldsymbol{S}^i_j\right)^{-1} \left(\tilde{\boldsymbol{r}}^i_j\right) \right] + K \tag{25}$$

où

$$K = \sum_{j=\theta}^{k} \left[\ln \left| \boldsymbol{S}^0_j \right| - \sum_{i=1}^{n} \tilde{\omega}^i_j \ln \left| \boldsymbol{S}^i_j \right| \right].$$

Et la présence d'un saut de valeur moyenne est acceptée ou rejetée d'après la règle suivante

$$\tilde{l}_k(\theta) \underset{\mathrm{H}_0}{\overset{\mathrm{H}_1}{\gtrless}} \varepsilon' \tag{26}$$

où ε' est un seuil dont la valeur dépend de la probabilité de fausse alarme du test. Le paramètre θ est alors remplacé par le paramètre $\hat{\theta}$ délivré par l'estimateur MLE tel que

$$\hat{\theta} = \arg\max_{\theta} \tilde{l}_k(\theta). \tag{27}$$

3.2.3 Résultats

La Figure 5 montre les résultats obtenus à partir de données collectées dans le centre de Toulouse. La méthode proposée permet de vérifier les bonnes performances de l'algorithme en présence de NLOS, alors que le véhicule est à l'arrêt.

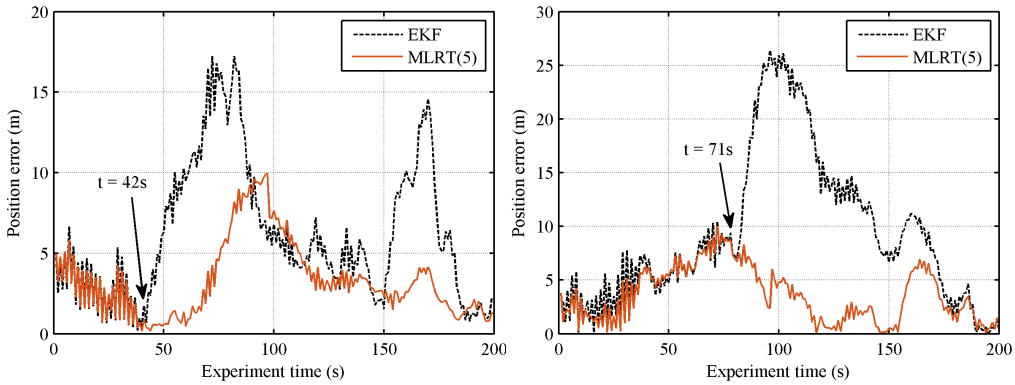

(a) Horizontal error **(b)** Vertical error

i) Positioning errors versus time.

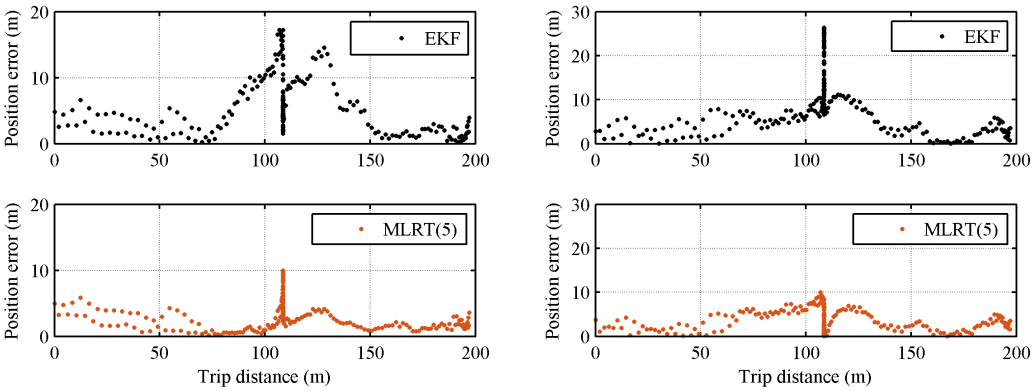

(c) Horizontal error **(d)** Vertical error

ii) Positioning errors versus trip distance.

Figure 5 – Erreurs de position horizontales et verticales.

3.3 Architecture multi-capteurs pour un positionnement efficace en environnement urbain

Ce chapitre analyse l'apport de capteurs complémentaires qui sont utilisés ici pour améliorer l'information a priori sur l'état du véhicule et faciliter le traitement des mesures GNSS en environnement urbain, permettant de bonnes performances en terme de précision et de robustesse. Une architecture multi-capteurs qui intègre une caméra monoculaire, un baro-altimètre, une centrale inertielle, et un récepteur GNSS est étudiée. Afin d'améliorer les performances en permettant une meilleure détection des biais sur les mesures de pseudo-distances (PR) et de fréquence Doppler (DR), la caméra et le baro-altimètre sont utilisés pour calibrer la centrale inertielle. Cette calibration réalisée avant la mise à jour de la centrale inertielle au moyen du récepteur GNSS permet d'améliorer la qualité de l'information a priori. Il en résulte une meilleure détection de mesures GNSS contaminées due à la réduction du bruit sur les innovations.

Alors que la caméra délivre des mesures de flot optique qui permettent de réduire la dérive de la centrale inertielle, les mesures GNSS sont utilisées ici pour borner l'erreur sur l'état du véhicule qui contient la position, la vitesse et l'attitude représentée par les quaternions. Un filtre UKF est spécifié pour réaliser l'intégration de ces différents capteurs. La représentation utilisée permet d'adresser le problème de normalisation des quaternions.

3.3.1 Architecture du système de navigation

L'architecture étudiée consiste en une centrale inertielle (INS) calibrée par une caméra monoculaire, un capteur de pression et un récepteur GNSS. Elle est représentée Figure 6. Une approche hiérarchique est proposée pour cette intégration. L'algorithme qui délivre la position, la vitesse et l'attitude du véhicule est implanté sur plusieurs étages comme le montre cette figure.

(1) L'état du véhicule représenté par la position, la vitesse et l'attitude, est propagé en utilisant les mesures inertielles délivrées par le module inertiel (IMU), qui sont exploitée par l'INS sur la base d'équations non linéaires qui résultent des lois de la mécanique.

(2) L'INS est intégrée avec la caméra et le capteur de pression afin de réduire la dérive de l'INS qui résulte des bruits induits par l'IMU, permettant de réduire la covariance de l'erreur sur l'état du véhicule.

(3) Cette réduction de la covariance permet de réduire la covariance des innovations sur les mesures de PR et DR, facilitant la détection de mesures GNSS contaminées (mesures de PR et de DR).

(4) Les mesures GNSS non contaminées sont enfin utilisées. Indépendantes des mesures délivrées par les autres capteurs, elles sont utilisées indépendamment par le filtre UKF.

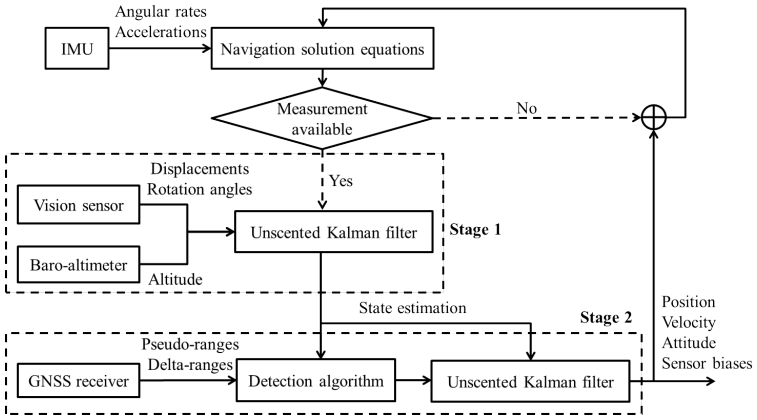

Figure 6 – Architecture du sysème de navigation multi-capteurs.

3.3.2 Traitement des mesures GNSS

En améliorant l'estimation de l'état a priori les capteurs complémentaires s'avèrent intéressant puisqu'ils facilitent la détection de mesures GNSS contaminées. En pratique les erreurs sur les mesures GNSS dépendent du mouvement du récepteur. Pour des vitesses élevées du véhicule les signaux NLOS sont portées par des fréquences qui permettent un filtrage de ces signaux. Au contraire, pour des mouvements lents du véhicule, les signaux NLOS apparaissent à une fréquence très proche de celle du signal LOS. Les signaux NLOS dégradent alors les mesures de PR alors que les mesures de DR sont faiblement contaminées. Il est donc proposé un algorithme de détection de mesures contaminées qui opère sur 2 étages. Cette algorithme est représenté Figure 7.

- **Premier étage** (Détection de mesures de PR biaisées) : Les mesures de PR sont éliminées si le test statistique réalisé sur l'innovation relative à une mesure de PR excède un seuil déterminé à partir du bruit sur cette innovation et de la probabilité de fausse alarme. Les mesures Doppler sont alors analysées.

- **Deuxième étage** (Détection de mesures de DR biaisées) : Les mesures de DR, relatives aux satellites dont les mesures de PR sont contaminées, sont testées. Elles sont éliminées si le test statistique réalisé sur l'innovation relative à une mesure de DR excède un seuil déterminé à partir du bruit sur cette innovation et de la probabilité de fausse alarme.

Cette approche permet de n'exploiter que les mesures GNSS jugées pertinentes. Dans le cadre de ce projet, dans la mesure où les mesures de PR et DR sont corrélées, le choix a été fait de ne conserver qu'une de ces 2 mesures pour un satellite donné, en privilégiant lorsque cela était possible la mesure de PR qui est reliée à la position du véhicule.

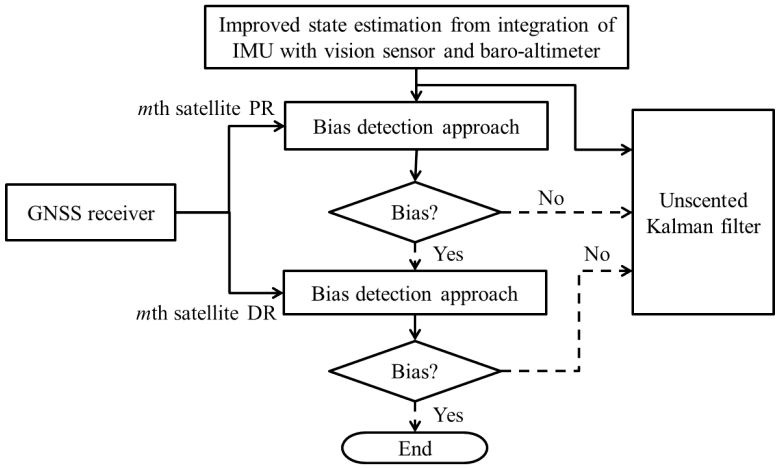

Figure 7 – Détection de mesures GNSS contaminées.

3.3.3 Résultats

La Figure 8 montre les performances obtenues à partir de mesures collectées sur le terrain. Les mesures de l'IMU et d'un récepteur GPS sont délivrées par une INS IMAR dont les performances ont été dégradées pour simuler une centrale équipée de capteurs de technologie MEMS. Les mesures de flot optique de la caméra et de pression du baro-altimètre ont été simulées. La trajectoire estimée est représentée pour 3 approches. La trajectoire blanche est la trajectoire de référence. La trajectoire jaune est la trajectoire obtenue avec une solution GPS qui ne réalise aucun traitement des mesures. La trajectoire verte est également obtenue avec un récepteur GNSS seul mais le traitement visant à exclure des mesures contaminées est réalisé. Enfin la trajectoire rouge est la trajectoire obtenue en utilisant l'architecture multi-capteurs présentée ici. Il apparait clairement que cette solution, plus couteuse puisqu'elle intègre des capteurs complémentaires, délivre les meilleures performances.

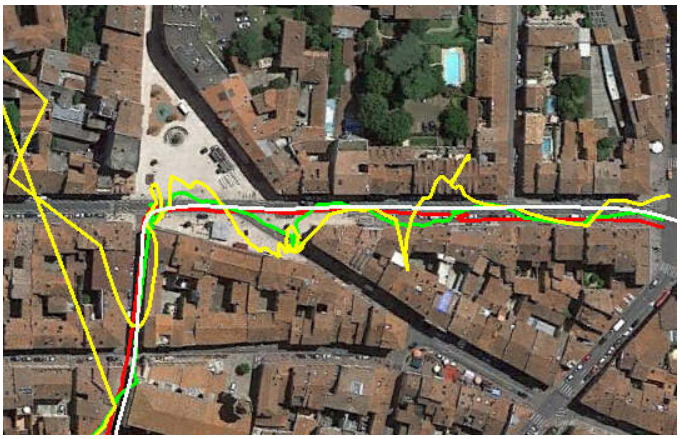

Figure 8 – Trajectoire estimée.

4 Conclusions and Perspectives

La navigation par satellite navigation tient un rôle de plus en plus important dans notre société. Les applications sont nombreuses et adressent tout particulièrement le problème du positionnement dans les villes. Ces nouvelles applications induisent de nouveaux challenges. Cette thèse étudie des solutions pour le traitement de signaux d'interférence. Après une introduction et un état de l'art des méthodes existantes, cette thèse propose plusieurs approches qui se positionnent en différents points du récepteur. Les méthodes étudiées sont résumées ici. Des perspectives d'amélioration de ces techniques sont également proposées.

4.1 Conclusions sur ces travaux

Estimateur de maximum de vraisemblance basé sur un filtre UKF pour la réduction des effets des signaux NLOS au sein d'un récepteur équipé d'un banc de corrélateurs Cet estimateur, décrit dans le chapitre 3, permet en particulier d'estimer les paramètres du signal LOS en présence de signaux NLOS. Cette approche a été évalué en considérant comme modèle d'observation les sorties de corrélateurs décalés, explorant la fonction d'autocorrélation en plusieurs points autour du point correspondant au délai estimé du signal LOS. L'approche considère un modèle dynamique pour traduire l'évolution du vecteur des paramètres du signal LOS, alors qu'un modèle de vraisemblance est utilisé pour décrire le vecteur des paramètres des signaux NLOS. Une approche itérative a été proposée pour estimer à chaque étape les paramètres des signaux LOS et NLOS. La connaissance des paramètres du signal LOS, obtenue sur la base du modèle dynamique, est d'abord exploitée pour estimer les paramètres des signaux NLOS selon le principe du maximum de vraisemblance. L'estimation des paramètres du signal LOS est ensuite réalisée au moyen d'un filtre UKF utilisant comme modèle d'observation les sorties des corrélateurs corrigées des effets des signaux NLOS. Les simulations réalisées ont montré l'intérêt de cette approche en présence de signaux NLOS, tout particulièrement en présence de variations brusques de ces signaux NLOS. Elles ont permis de vérifier la robustesse de l'algorithme proposé.

Test MLRT pour la détection et l'estimation de biais affectant les mesures de pseudo-distances Dans le chapitre 4, une approximation du test du MLRT utilisant l'inégalité de Jensen a été proposée pour détecter, identifier et estimer les biais induits par un NLOS sur les mesures de pseudo-distances. Les effets des signaux NLOS ont été modélisés par des sauts de moyenne. L'approche proposée est basée sur un test du rapport de vraisemblance marginalisé. Ce test est approximé par une intégration de Monte Carlo en utilisant l'inégalité Jensen. Un algorithme à modèles multiples a été présenté. Il réalise la mise à jour de l'information a priori pour chaque valeur échantillonné du biais afin d'améliorer les performances du détecteur. Les performances de cet algorithme ont été évaluées. En particulier une comparaison des résultats obtenus avec cette approche à ceux ob-

tenus par le test du GLRT a permis de mettre en évidence l'intérêt de la méthode introduite dans cette thèse. En particulier la probabilité de bonne détection a été améliorée de manière significative. Ceci met en évidence l'intérêt de l'information a priori pour caractériser l'amplitude du biais. Par ailleurs, en comparaison avec un filtre de Kalman étendu, la solution proposée ici offre une meilleure précision. Enfin des données prélevées au cours d'une campagne de mesure conduite dans le centre de Toulouse ont permis de vérifier l'efficacité de l'approche proposée dans des zones qui induisent des signaux NLOS. Les résultats ont montré que la détection et la correction des effets des multi-trajets permettaient un positionnement précis dans ces situations.

Architecture d'intégration multi-capteurs pour un positionnement performant en environnement urbain Dans le chapitre 5, une architecture multi-capteurs, basée sur une IMU calibrée par une caméra, un capteur de pression et un récepteur GNSS, est étudiée. Cette solution est analysée en environnement urbain, en présence de signaux NLOS. L'approche proposée utilise les capteurs de manière hiérarchique. Le capteur de vision et le baro-altimètre sont utilisés pour réduire la covariance sur les innovations relatives aux mesures délivrées par le récepteur GNSS. Les mesures GNSS sont ensuite testées. Un premier test adresse les mesures de PR. Les mesures de PR des satellites qui satisfont ce test sont exploitées pour mettre à jour l'INS. Les mesures de DR des autres satellites sont ensuite soumises à un 2ème test visant à ne conserver que les mesures de DR jugées pertinentes. L'algorithme est basé sur un filtre UKF qui évite de calculer la matrice jacobienne du modèle d'état. Ce modèle est en effet fondé sur les équations non linéaires qui régissent l'INS. Une représentation de l'attitude basée sur les quaternions est proposée ici. Cette représentation satisfait la contrainte de normalisation des quaternions. Une campagne de mesure a été conduite pour évaluer les performances de cette approche. Les résultats obtenus ont mis en évidence l'apport de capteurs supplémentaires en environnement urbain.

4.2 Perspectives

Les voies explorées au cours de cette thèse, à la vue des résultats obtenus, amènent à proposer des études dans la continuité de ce travail :

- Dans le chapitre 3, la recherche de la valeur du délai du signal résultant des signaux NLOS est réalisée en explorant une grille dont le pas dépend de l'espacement entre les différents corrélateurs. Cette approche présente 2 inconvénients. Le premier inconvénient est une mauvaise précision du délai estimé, ce délai étant affecté de la valeur du délai du corrélateur le plus proche. Le deuxième est une charge de calcul importante, l'estimateur (MLE) étant élaboré pour chaque valeur du délai. Une méthode plus performante basée sur des méthodes d'optimisation telle que la méthode itérative de Newton ou l'algorithme « espérance-maximisation » pourrait être analysée pour déterminer la valeur du délai du signal résultant des signaux NLOS. Enfin l'évaluation de cette solution au sein d'une architecture vectorielle permettrait d'une part d'améliorer le modèle dynamique décrivant l'évolution du signal LOS, d'autre part de réduire la corrélation entre les paramètres des signaux LOS et NLOS.

- Dans le chapitre 4, il est admis que le biais induit par la présence de signaux NLOS suit une loi uniforme sur une plage qui dépend de l'environnement. En pratique des campagnes de mesure ont montré que le délai suit une loi de Rayleigh dans des environnements très contraint. Cette loi de distribution pourrait être admise pour définir le test du rapport de maximum de vraisemblance marginalisé. L'impact de cette hypothèse sur la complexité et les performances pourrait être regardé.

- Dans le chapitre 5, l'architecture « multi-capteurs » proposée a été évaluée en post traitement à partir de données issues d'une campagne de mesure. Une application temps réel de cette approche intégrant un capteur d'images permettrait une évaluation sur le terrain de l'algorithme proposé. Par ailleurs l'approche analysée ici est basée sur une mesure de flot optique qui ne nécessite pas la sauvegarde de points d'intérêt. Cette mesure est reliée au mouvement du véhicule. Des méthodes délivrant des mesures absolues, associées à des techniques de classification des biais issus de signaux NLOS, dépendante de l'environnement, pourrait être explorées et évaluées sur la base de mesures faites sur le terrain.

RÉSUMÉ DES TRAVAUX EN CHINOIS

目前，全球导航卫星系统（GNSS）已在军事和民用等诸多领域得到广泛应用。现有的全球导航卫星系统（GNSS）包括了美国全球定位系统（GPS），俄罗斯格洛纳斯系统（GLONASS），欧盟伽利略系统（Galileo），中国北斗导航卫星系统（BDS），印度区域卫星导航系统（IRNSS）以及日本准天顶卫星系统（QZSS）。随着GNSS接收机被更多的应用在例如城市峡谷或其他障碍物密集的复杂环境中，当卫星信号到达接收机天线前，易受到障碍物的影响造成信号的折射或散射，从而使得载体位置，速度和时间的解算产生误差，这种现象被称为信号的多路径效应。多径误差被认为是GNSS系统的主要误差源之一。本文尝试在GNSS接收机中采用不同信号处理方法来的抑制多径误差。

1 GNSS系统原理

卫星导航系统的定位原理是基于三角测量方法，也就是说在几何空间中任意一个未知点的位置可以由在同一空间中一组位置已知的坐标点相对于未知点的距离推算得出。一般来说，导航卫星相对于接收机的距离，也被称为伪距（pseudo-range），可以通过信号的传播时间计算得到

$$\rho_i = c\tau_i \tag{1}$$

其中，τ_i是信号传播时间，c是光在真空中的传播速度。假设接收机与导航卫星时钟对准，通过式(1)可以直接得到卫星与接收机之间的几何距离。但是，由于接收机与导航卫星的时钟间总存在偏差Δb且无法预先消除。因此，GNSS导航方程式定义如下

$$\rho_i = r_i + c\Delta b = \sqrt{(x_i - x_u)^2 + (y_i - y_u)^2 + (z_i - z_u)^2} + b_u \tag{2}$$

其中，ρ_i 为接收机与第i颗导航卫星之间的伪距，(x_i, y_i, z_i)和(x_u, y_u, z_u)分别代表第i颗导航卫星和接收机在地心坐标系(ECEF)中的位置向量，$b_u = c\Delta b$是由接收机相对于导航卫星时钟偏差产生的距离误差。因此，需要利用4个导航方程来确定包括载体位置向量和接收机时钟偏差在内的四个未知参数。

GNSS接收机采用直接序列扩频（DSSS）技术来估计第i颗导航卫星与接收机之间的信号传播时间τ_i，从而获得相应的伪距量测。鉴于每一颗导航卫星利用特定的伪随机噪声（PRN）码来调制发射信号，GNSS接收机产生本地伪随机码并与接收到的卫星伪随机码实现同步，从而

估计出卫星信号到达接收机的时间，再通过解调接收到的卫星信号来获得信号的发送时刻并最终确定信号的传播时间。另外，GNSS接收机利用本地信号与卫星信号的载波同步来估计卫星信号的多普勒频率。通过解调导航卫星信号，还可以得到导航卫星的开普雷轨道参数和相关的星历数据以及GNSS系统时间误差和电离层延迟等模型参数，这些参数被用于构建导航方程式(2)。最后，通过最小二乘或者基于卡尔曼滤波的方法来解算一组导航方程，从而得到载体的位置向量。

2 多径干扰对GNSS接收机性能影响

2.1 多径信号模型

当存在多径干扰时，接收到的GNSS信号包含了一个直达信号（LOS signal）和多个多径信号（MP signals）。此时，由于多径信号经过的路径总是比直达信号更长，因而相对于直达信号而言多径信号的到达总是存在延迟，另外，由于障碍物的折射或遮挡，使得多径信号存在额外的功率衰减，所以多径信号的功率总是低于直达信号。因此，多径信号对直达信号的影响取决于其相对于直达信号的功率，伪随机码延迟，载波相位和多普勒频率。在导频信道中，不考虑随机噪声影响，包含有直达和多径信号的GNSS信号可以表示为

$$r(nT_s)=\sum_{m=0}^{M} a_m\, c(nT_s-\tau_0-\delta\tau_m)\cos\left(2\pi(f_{\mathrm{IF}}+f_m^d)nT_s+\varphi_0+\delta\varphi_m\right) \tag{3}$$

其中nT_s为采样时刻（$n=1,\ldots,\infty$），M为多径信号数量，$a_m=\sqrt{P_m}$和f_m^d是第m个信号的平均功率与载波多普勒频率，τ_0和φ_0为直达信号的伪随机码延迟和载波相位，$\delta\tau_m$和$\delta\varphi_m$是第m个多径信号相对于直达信号的时间延时和相对载波相位。因此，第m个多径信号的绝对时间延迟和载波相位可以表示为$\tau_m=\tau_0+\delta\tau_m$和$\varphi_m=\varphi_0+\delta\varphi_m$。

2.2 多径干扰对接收机性能影响分析

当多径信号存在时，接收机中产生的同相（I）和正交相（Q）相关器输出如下

$$\begin{aligned}
I_{E,k}&=\sum_{m=0}^{M} a_m\, R\left(\Delta\tilde{\tau}_{0,k}-\delta\tau_{m,k}+\frac{d}{2}T_c\right)\operatorname{sinc}\left(\pi\Delta\tilde{f}_{m,k}^d T_a\right)\cos(\Delta\tilde{\varphi}_{0,k}+\delta\varphi_{m,k})\\
I_{P,k}&=\sum_{m=0}^{M} a_m\, R\left(\Delta\tilde{\tau}_{0,k}-\delta\tau_{m,k}\right)\operatorname{sinc}\left(\pi\Delta\tilde{f}_{m,k}^d T_a\right)\cos(\Delta\tilde{\varphi}_{0,k}+\delta\varphi_{m,k})\\
I_{L,k}&=\sum_{m=0}^{M} a_m\, R\left(\Delta\tilde{\tau}_{0,k}-\delta\tau_{m,k}-\frac{d}{2}T_c\right)\operatorname{sinc}\left(\pi\Delta\tilde{f}_{m,k}^d T_a\right)\cos(\Delta\tilde{\varphi}_{0,k}+\delta\varphi_{m,k})
\end{aligned} \tag{4}$$

与

$$
\begin{aligned}
Q_{E,k} &= \sum_{m=0}^{M} a_m\, R\left(\Delta\tilde{\tau}_{0,k} - \delta\tau_{m,k} + \frac{d}{2}T_c\right) \operatorname{sinc}\left(\pi\Delta\tilde{f}_{m,k}^{d} T_a\right) \sin(\Delta\tilde{\varphi}_{0,k} + \delta\varphi_{m,k}) \\
Q_{P,k} &= \sum_{m=0}^{M} a_m\, R\left(\Delta\tilde{\tau}_{0,k} - \delta\tau_{m,k}\right) \operatorname{sinc}\left(\pi\Delta\tilde{f}_{m,k}^{d} T_a\right) \sin(\Delta\tilde{\varphi}_{0,k} + \delta\varphi_{m,k}) \\
Q_{L,k} &= \sum_{m=0}^{m} a_m\, R\left(\Delta\tilde{\tau}_{0,k} - \delta\tau_{m,k} - \frac{d}{2}T_c\right) \operatorname{sinc}\left(\pi\Delta\tilde{f}_{m,k}^{d} T_a\right) \sin(\Delta\tilde{\varphi}_{0,k} + \delta\varphi_{m,k})
\end{aligned}
\tag{5}
$$

其中，$\operatorname{sinc}(\cdot)$是Sinc函数，$\Delta\tilde{\tau}_{0,k}$和$\Delta\tilde{\varphi}_{0,k}$为接收机中产生的本地信号与接收到直达信号间的伪随机码和载波相位偏差，$\Delta\tilde{f}_{m,k}$是本地信号与第m个信号间的载波多普勒频率偏差。由于下标$m=0$代表直达信号，因此$\delta\tau_{0,k}=0$且$\delta\varphi_{0,k}=0$。

假设在接收机中接收到的GNSS信号由一个直达信号和一个多径信号组成，也就是说$f_0^d = f_m^d$且$M=1$。图1分别显示了GNSS接收机中直达，多径以及复合信号的相关函数输出。可以看出，同相多径使得延迟估计滞后，增大伪距量测值；而反相多径的使得延迟估计超前，减小伪距量测值。因此，多径信号相对延迟$\delta\tau$决定多径干扰对于直达信号的影响程度。当相对延迟满足$\delta\tau \geq (1+d/2)\,T_c$条件时，多径信号将不会对直达信号的相关函数产生影响，因而也不会产生伪距误差。因此，缩小GNSS信号中的伪随机码码片宽度T_c或者减小接收机中相关器间隔d有助于削弱多径干扰对于GNSS接收机的影响。

图2分别显示当存在或缺少多径干扰时GNSS接收机中相干点积延迟锁定环鉴别器（E-L）和非相干超前减滞后延迟锁定环鉴别器（ELP）的输出。当存在同相多径干扰时，鉴相器的输出向右侧发生了偏移；当存在反相多径干扰时，鉴相器的输出向左侧发生了偏移；因此，鉴相器输出偏移会造成相应的伪距误差。

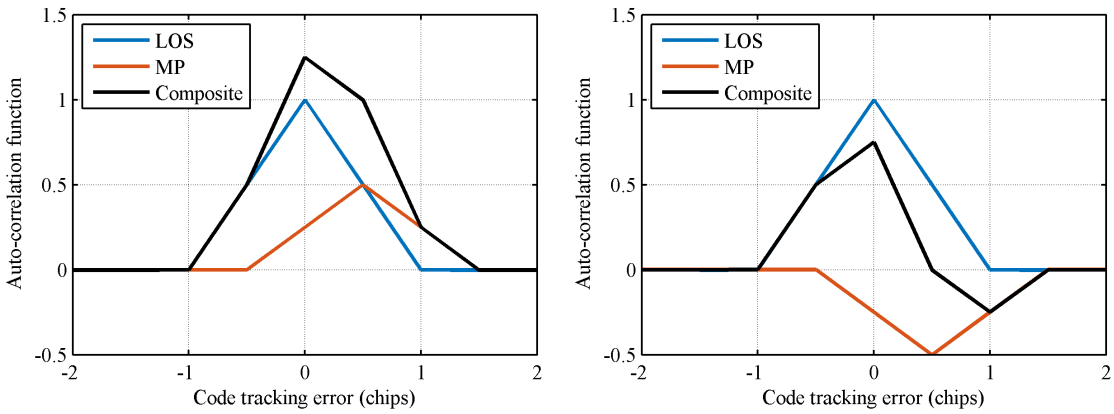

(a) 同相多径干扰　　**(b)** 反向多径干扰

图 **1** – 直达、多径和复合信号的相关函数，其中，$\alpha_m = \frac{1}{2}$，$\delta\tau_1 = 0.5$，$\delta\varphi_1 = 0°$或$180°$，忽略预相关带宽

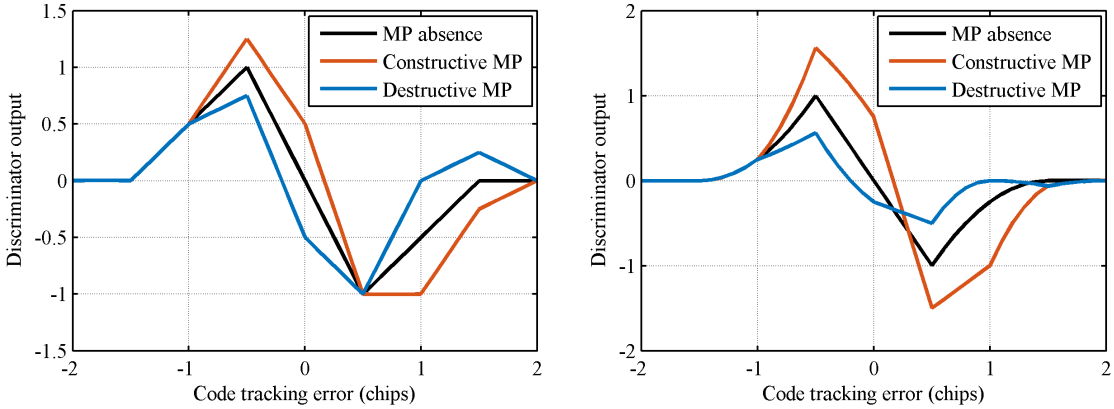

(a) 相干点积鉴别器　　**(b)** 非相干超前减滞后鉴别器

图 **2** – 存在或缺少多径干扰时延迟锁定环鉴别器输出，其中，$\alpha_m = \frac{1}{2}$，$\delta\tau_1 = 0.5$，$\delta\varphi_1 = 0°$或$180°$

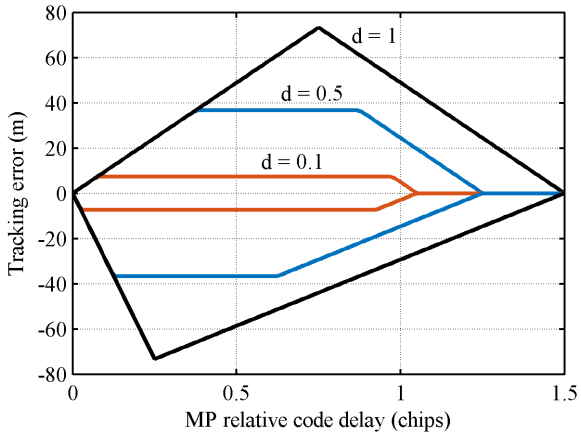

图 **3** – GNSS接收机不同相关器间隔的跟踪误差包络，其中，$\alpha_m = \frac{1}{2}$, $\delta\tau_1 = 0.5$，$\delta\varphi_1 = 0°$或$180°$，且忽略预相关带宽

图3显示了在GNSS接收机中不同相关器间隔d的跟踪误差包络，其中，上包络表示同相多径干扰（$\delta\varphi_1 = 0°$）造成的跟踪误差，而下包络表示反向多径干扰（$\delta\varphi_1 = 180°$）造成的跟踪误差。由图3可以看出，相关器间隔越小，多径信号引起的跟踪误差就越小。此外，当多径信号相对延迟$\delta\tau$满足$\delta\tau \geq (1 + d/2)\,T_c$时，多径信号不会造成跟踪误差。

3 论文主要贡献点概述

通过论文第2章对GNSS接收机中多径抑制方法的归纳与分析，本文提出了基于贝叶斯方法的多径干扰抑制方法，从而减小多径干扰对GNSS接收机的影响，提高GNSS在复杂环境中的定位精度，主要贡献点概括如下：

- 提出基于最大似然准则的无源卡尔曼滤波（UKF），实现在多径干扰情况下对直达信号参数的估计。
- 提出近似边缘似然比假设检验，实现对非视距多径偏差的检测与估计。
- 提出多传感器信息融合架构，实现对多径误差的检测并提高在多径环境下的定位精度。

3.1 多相关器GNSS接收机中基于最大似然准则无源卡尔曼滤波的多径干扰抑制方法

鉴于多径信号出现与消失取决于接收机与导航卫星间的相对运动以及接收机所处的环境等多种因素，在城市峡谷等复杂环境中，很难用一个确定的先验统计模型来描述多径信号参数的动态变化。因此，利用两类不同模型来分别描述直达和多径信号参数，即首先采用时间相关的一阶马尔科夫模型来描述直达信号参数，而采用静态似然模型来描述多径信号参数。考虑到多相关器输出可以充分描述多径信号对接收机相关函数的影响，因此将多相关器的输出作为量测信息，提出基于最大似然准则下的无迹卡尔曼滤波实现对直达信号与多径信号参数的迭代估计，也就是说，首先基于直达信号的先验信息来实现对多径信号参数的最大似然估计，然后再利用多径信号的最大似然估计值来实现直达信号参数的后验估计。

3.1.1 问题描述

当存在多径干扰时，进入GNSS接收机的信号参数向量$\boldsymbol{x}_k$由两部分组成：直达信号参数向量$\boldsymbol{x}_{0,k}$和多径信号参数向量$(\boldsymbol{x}_{1,k},\ldots,\boldsymbol{x}_{M,k})$，根据贝叶斯定理，信号参数向量$\boldsymbol{x}_k$的后验概率密度函数为

$$\begin{aligned}
p(\boldsymbol{x}_k|\boldsymbol{z}_{1:k}) &= p\left(\boldsymbol{x}_{0,k},\boldsymbol{x}_{1,k},\ldots,\boldsymbol{x}_{M,k}|\boldsymbol{z}_{1:k}\right) \\
&\propto p\left(\boldsymbol{z}_k|\boldsymbol{x}_{0,k},\boldsymbol{x}_{1,k},\ldots,\boldsymbol{x}_{M,k},\boldsymbol{z}_{1:k-1}\right)\, p\left(\boldsymbol{x}_{0,k},\boldsymbol{x}_{1,k},\ldots,\boldsymbol{x}_{M,k}|\boldsymbol{z}_{1:k-1}\right) \\
&= p\left(\boldsymbol{z}_k|\boldsymbol{x}_{0,k},\boldsymbol{x}_{1,k},\ldots,\boldsymbol{x}_{M,k},\boldsymbol{z}_{1:k-1}\right)\, p\left(\boldsymbol{x}_{0,k}|\boldsymbol{x}_{1,k},\ldots,\boldsymbol{x}_{M,k},\boldsymbol{z}_{1:k-1}\right)\, p\left(\boldsymbol{x}_{1,k},\ldots,\boldsymbol{x}_{M,k}|\boldsymbol{z}_{1:k-1}\right)
\end{aligned} \tag{6}$$

一般情况下，可以假设直达信号和多径信号相互独立，因此，式(6)可以写成

$$p(\boldsymbol{x}_k|\boldsymbol{z}_{1:k}) \propto p\left(\boldsymbol{z}_k|\boldsymbol{x}_{0,k},\boldsymbol{x}_{1,k},\ldots,\boldsymbol{x}_{M,k},\boldsymbol{z}_{1:k-1}\right)\, p\left(\boldsymbol{x}_{0,k}|\boldsymbol{z}_{1:k-1}\right)\, p\left(\boldsymbol{x}_{1,k},\ldots,\boldsymbol{x}_{M,k}|\boldsymbol{z}_{1:k-1}\right) \tag{7}$$

假设直达信号参数向量的先验信息已知，而多径信号参数向量先验信息为常数（即不存在先验

信息），因此，式(7)可以写成

$$p(\boldsymbol{x}_k|\boldsymbol{z}_{1:k}) \propto p\left(\boldsymbol{z}_k|\boldsymbol{x}_{0,k},\boldsymbol{x}_{1,k},\ldots,\boldsymbol{x}_{M,k},\boldsymbol{z}_{1:k-1}\right)\ p\left(\boldsymbol{x}_{0,k}|\boldsymbol{z}_{1:k-1}\right) \tag{8}$$

由于很难直接获得式(8)的闭合解，无法根据式(8)得到信号参数向量$\boldsymbol{x}_k$的估计值。因而提出了一个迭代估计方法来获得信号参数向量$\boldsymbol{x}_k$的贝叶斯估计。

3.1.2 基于最大似然准则的多径信号参数估计

假设直达信号参数向量$\boldsymbol{x}_{0,k}$在k时刻已知，此时，式(6)可写为

$$\begin{aligned} p(\boldsymbol{x}_k|\boldsymbol{z}_{1:k}) &= p\left(\boldsymbol{x}_{0,k},\boldsymbol{x}_{1,k},\ldots,\boldsymbol{x}_{M,k}|\boldsymbol{z}_{1:k}\right) \\ &= p\left(\boldsymbol{x}_{1,k},\ldots,\boldsymbol{x}_{M,k}|\boldsymbol{x}_{0,k},\boldsymbol{z}_{1:k}\right)\ p\left(\boldsymbol{x}_{0,k}|\boldsymbol{z}_{1:k}\right) \\ &\propto p\left(\boldsymbol{x}_{1,k},\ldots,\boldsymbol{x}_{M,k}|\boldsymbol{z}_{1:k}\right) \end{aligned} \tag{9}$$

其中，$p\left(\boldsymbol{x}_{1,k},\ldots,\boldsymbol{x}_{M,k}|\boldsymbol{z}_{1:k}\right)$是多径信号参数向量$(\boldsymbol{x}_{1,k},\ldots,\boldsymbol{x}_{M,k})$的后验概率密度函数。假设多径信号参数向量的先验分布未知，因此，其后验概率密度函数可表示为

$$p\left(\boldsymbol{x}_{1,k},\ldots,\boldsymbol{x}_{M,k}|\boldsymbol{z}_{1:k}\right) \propto p\left(\boldsymbol{z}_{1:k}|\boldsymbol{x}_{1,k},\ldots,\boldsymbol{x}_{M,k}\right) \tag{10}$$

其中，$p\left(\boldsymbol{z}_{1:k}|\boldsymbol{x}_{1,k},\ldots,\boldsymbol{x}_{M,k}\right)$是在$k$时刻给定量测向量$\boldsymbol{z}_{1:k}$情况下的似然函数。因此，当给定量测向量$\boldsymbol{z}_{1:k}$以及直达信号参数向量$\boldsymbol{x}_{0,k}$时，对于信号参数向量$\boldsymbol{x}_k$的估计可以转换为多径信号参数向量$(\boldsymbol{x}_{1,k},\ldots,\boldsymbol{x}_{M,k})$的最大似然估计。

因此，多径信号参数的估计可以通过最大化式(10)来获得。尽管如此，在k时刻，这个最大化过程需要利用直达信号参数向量$\boldsymbol{x}_{0,k}$。由于直达信号参数向量$\boldsymbol{x}_{0,k}$在k时刻未知，可以通过直达信号参数传递模型来获得其在k时刻的预测值$\boldsymbol{x}_{0,k|k-1}$，从而近似式(10)中所需的$\boldsymbol{x}_{0,k}$。

3.1.3 基于无源卡尔曼滤波的直达信号参数估计

假设多径信号参数向量$(\boldsymbol{x}_{1,k},\ldots,\boldsymbol{x}_{M,k})$在$k$时刻已知，此时，式(6)可写为

$$\begin{aligned} p(\boldsymbol{x}_k|\boldsymbol{z}_{1:k}) &= p\left(\boldsymbol{x}_{0,k},\boldsymbol{x}_{1,k},\ldots,\boldsymbol{x}_{M,k}|\boldsymbol{z}_{1:k}\right) \\ &= p\left(\boldsymbol{x}_{0,k}|\boldsymbol{x}_{1,k},\ldots,\boldsymbol{x}_{M,k},\boldsymbol{z}_{1:k}\right)p\left(\boldsymbol{x}_{1,k},\ldots,\boldsymbol{x}_{M,k}|\boldsymbol{z}_{1:k}\right) \\ &\propto p\left(\boldsymbol{x}_{0,k}|\boldsymbol{z}_{1:k}\right) \\ &\propto p\left(\boldsymbol{z}_k|\boldsymbol{x}_{0,k}\right)\ p\left(\boldsymbol{x}_{0,k}|\boldsymbol{z}_{1:k-1}\right) \end{aligned} \tag{11}$$

其中，$p\left(\boldsymbol{z}_k|\boldsymbol{x}_{0,k}\right)$和$p\left(\boldsymbol{x}_{0,k}|\boldsymbol{z}_{1:k-1}\right)$分别是直达信号参数向量$\boldsymbol{x}_{0,k}$基于$k$时刻量测的似然函数和基于$k-1$时刻量测的条件概率密度函数。因此，当给定多径信号参数向量时，对于信号参数向量$\boldsymbol{x}_k$的估计可以转换为求解直达信号参数向量$\boldsymbol{x}_{0,k}$的后验概率密度函数。

由式(11)可知，直达信号$\boldsymbol{x}_{0,k}$的后验概率密度函数是多径信号参数向量$(\boldsymbol{x}_{1,k},\ldots,\boldsymbol{x}_{M,k})$的函数。由于多径信号参数的最大似然估计可由式(10)得到，因此在求解直达信号参数向量$\boldsymbol{x}_{0,k}$的后验概率密度函数时，所需的多径信号参数向量可以由其最大似然估计值代替。由于量测模型是一个强非线性模型，因此采用基于无源变换（UT）的无源卡尔曼滤波来实现对直达信号参数的估计。

3.1.4 仿真结果

图4显示了在仿真环境下不同方法的伪随机码延迟估计误差。仿真结果表明，所提方法的估计精度明显优于标准无源卡尔曼滤波。此外，所提方法的估计精度取决于接收机中相关器的数目。

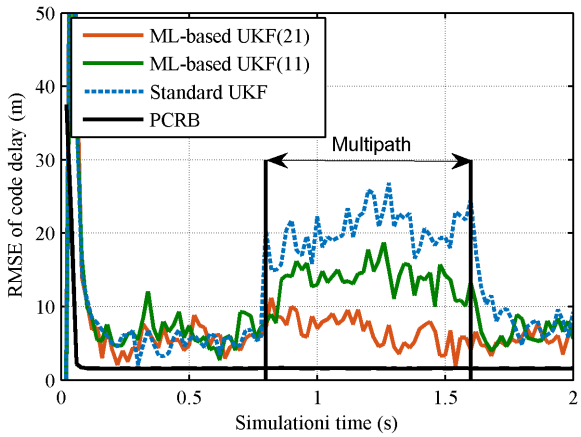

图 **4** – 伪随机码延迟估计误差

3.2 基于边缘似然比假设检验的多径偏差检测与估计

考虑到非视距多径干扰常出现在城市峡谷等复杂环境中，造成GNSS接收机输出的伪距量测发生跳变。提出了基于边缘似然比假设检验的非视距多径误差检测，识别与估计方法。由于边缘似然比统计量不易计算，采用基于均值跳变误差采样的蒙特卡洛积分来构造近似的边缘似然比统计量，然后利用琴生不等式简化构造的似然比统计量并运用多模型方法更新每个跳变误差采样的先验信息，通过蒙特卡洛仿真分析了近似边缘似然比统计量的经验分布函数，从而确定了检测门限值。最后设计了均值跳变误差的估计和校正方法。

3.2.1 问题描述

根据假设检验理论，对于均值跳变的似然比假设检验可以被认为是一种二元假设检验，因

此，对于多径干扰引起的GNSS伪距量测跳变的二元假设检验定义如下：

$$\text{原假设}\mathrm{H}_0:\text{截止至}k\text{时刻无均值跳变}$$
$$\text{备择假设}\mathrm{H}_1:\text{在}\theta<k\text{时刻发生了幅值为}v\neq 0\text{的均值跳变}$$

因此，对数似然比统计量可定义如下：

$$l_k(\theta,v)=\ln\frac{p(\boldsymbol{Z}_{1:k}|\mathrm{H}_1(\theta,v))}{p(\boldsymbol{Z}_{1:k}|\mathrm{H}_0)} \tag{12}$$

其中，$\boldsymbol{Z}_{1:k}=\{\boldsymbol{Z}_i\}_{i=1}^k$是前$k$个伪距量测序列且$\boldsymbol{Z}_i=\left(Z_i^1,\ldots,Z_i^{N_s}\right)$，$N_s$是可见的导航卫星数目。$p(\boldsymbol{Z}_{1:k}|\mathrm{H}_0)$和$p(\boldsymbol{Z}_{1:k}|\mathrm{H}_1(\theta,v))$分别为当原假设$\mathrm{H}_0$和备择假设$\mathrm{H}_1$成立时相应的似然函数。

假设由多径干扰引起的伪距量测均值跳变误差的幅值v服从均匀分布，也就是说$p(v)\sim\mathrm{U}(v_{\min},v_{\max})$，其中，$\mathrm{U}(\cdot)$代表均匀分布函数，$v_{\min}$和$v_{\max}$分别代表均值跳变可能的上下界。因此，式(12)相对于幅值v的边缘积分可写为

$$l_k(\theta)=\ln\frac{p(\boldsymbol{Z}_{1:k}|\mathrm{H}_1(\theta))}{p(\boldsymbol{Z}_{1:k}|\mathrm{H}_0)} \tag{13}$$

其中

$$p(\boldsymbol{Z}_{1:k}|\mathrm{H}_1(\theta))=\int p(\boldsymbol{Z}_{1:k}|\mathrm{H}_1(\theta,v))\,p(v)\,\mathrm{d}v \tag{14}$$

由于无法得到式(14)的解析解，因此采用蒙特卡洛积分的方法获得式(14)的近似解为

$$p(\boldsymbol{Z}_{1:k}|\mathrm{H}_1(\theta))\approx\sum_{i=1}^{n}\omega^i p(\boldsymbol{Z}_{1:k}|\mathrm{H}_1(\theta,v_i)) \tag{15}$$

其中，v_i（$i=1,\ldots,n$）是多径干扰引起的伪距量测均值跳变误差幅值的第i个采样值，n是采样个数。相应的，一组的均值跳变误差采样向量可定义为$\boldsymbol{v}_i=(0,\ldots,v_i,\ldots,0)$（$i=1,\ldots,n$），其中每个向量的权值为$\omega^i=1/n$且$\sum_{i=1}^n\omega^i=1$。因此，边缘似然比统计量$l_k(\theta)$可近似为

$$l_k(\theta)=\ln\frac{p(\boldsymbol{Z}_{1:k}|\mathrm{H}_1(\theta))}{p(\boldsymbol{Z}_{1:k}|\mathrm{H}_0)}\approx\ln\frac{\sum_{i=1}^n\omega^i p(\boldsymbol{Z}_{1:k}|\mathrm{H}_1(\theta,v_i))}{p(\boldsymbol{Z}_{1:k}|\mathrm{H}_0)} \tag{16}$$

当$k<\theta$时$v=0$, $l_k(\theta)$可以表示为

$$l_k(\theta)=\ln\frac{\sum_{i=1}^n\omega^i p(\boldsymbol{Z}_{\theta:k}|\boldsymbol{Z}_{1:\theta-1},\mathrm{H}_1(\theta,v_i))}{p(\boldsymbol{Z}_{\theta:k}|\boldsymbol{Z}_{1:\theta-1},\mathrm{H}_0)} \tag{17}$$

因此，跳变发生时刻θ的最大似然估计为

$$\hat{\theta}=\arg\max_{\theta} l_k(\theta) \tag{18}$$

而判定均值跳变是否发生的条件为

$$l_k\left(\hat{\theta}\right) \underset{\mathrm{H}_0}{\overset{\mathrm{H}_1}{\gtrless}} \boldsymbol{\varepsilon} \tag{19}$$

其中，$\boldsymbol{\varepsilon}$是相应的检测门限值。

3.2.2 基于琴生不等式的近似边缘似然比假设检验

由(17)可知，$p(\boldsymbol{Z}_{\theta:k}|\boldsymbol{Z}_{1:\theta-1},\mathrm{H}_0)$是当原假设$\mathrm{H}_0$成立时相应的似然函数。根据卡尔曼滤波理论，可以表示为

$$p(\boldsymbol{Z}_{\theta:k}|\boldsymbol{Z}_{1:\theta-1},\mathrm{H}_0)=\prod_{j=\theta}^{k} p\left(\boldsymbol{Z}_j|\boldsymbol{Z}_{1:j-1},\mathrm{H}_0\right) \tag{20}$$

且

$$p\left(\boldsymbol{Z}_j|\boldsymbol{Z}_{1:j-1},\mathrm{H}_0\right)=\mathcal{N}\left(\boldsymbol{Z}_j;\hat{\boldsymbol{Z}}^0_{j/j-1},\boldsymbol{S}^0_j\right)=p\left(\boldsymbol{\gamma}^0_j|\mathrm{H}_0\right)$$

其中，$\mathcal{N}\left(\boldsymbol{Z}_j;\hat{\boldsymbol{Z}}^0_{j/j-1},\boldsymbol{S}^0_j\right)$为均值是$\hat{\boldsymbol{Z}}^0_{j/j-1}$、方差是$\boldsymbol{S}^0_j$的正态分布函数。$\boldsymbol{\gamma}^0_j=\boldsymbol{Z}_j-\hat{\boldsymbol{Z}}^0_{j/j-1}$和$\boldsymbol{S}^0_j$是$j$时刻当原假设$\mathrm{H}_0$成立时相应的滤波残差向量以及其协方差矩阵，$\boldsymbol{Z}_j$和$\hat{\boldsymbol{Z}}^0_{j/j-1}$分别是$j$时刻当原假设$\mathrm{H}_0$成立时实际的和预测的伪距量测向量。因此，式(17)的分子部分是由一组带有不同均值跳变采样误差采样的备择假设H_1成立时相应似然函数的加权和组成。当与第i个均值跳变误差采样对应的备择假设H_1成立时，相应的似然函数可以表示为

$$p(\boldsymbol{Z}_{\theta:k}|\boldsymbol{Z}_{1:\theta-1},\mathrm{H}_1(\theta,v_i))=\prod_{j=\theta}^{k} p\left(\boldsymbol{Z}_j|\boldsymbol{Z}_{1:j-1},\mathrm{H}_1(\theta,v_i)\right) \tag{21}$$

且

$$p\left(\boldsymbol{Z}_j|\boldsymbol{Z}_{1:j-1},\mathrm{H}_1(\theta,v_i)\right)=\mathcal{N}\left(\boldsymbol{Z}_j;\hat{\boldsymbol{Z}}^i_{j/j-1},\boldsymbol{S}^i_j\right)=p\left(\tilde{\boldsymbol{\gamma}}^i_j|\mathrm{H}_1(\theta,v_i)\right),$$

其中，$\tilde{\boldsymbol{\gamma}}^i_j=\boldsymbol{\gamma}^0_j-\boldsymbol{v}_i$和$\boldsymbol{S}^i_j$是$j$时刻与第$i$个均值跳变误差采样相关的备择假设$\mathrm{H}_1$成立时的滤波残差向量和相应的协方差矩阵，$\hat{\boldsymbol{Z}}^i_{j/j-1}$是$j$时刻与第$i$个均值跳变误差采样相关的备择假设$\mathrm{H}_1$成立时的预测伪距量测向量。

将(20)和(21)代入(17)，基于蒙特卡洛积分的近似边缘似然比假设检验统计量可以表示为

$$\begin{aligned} l_k(\theta)&=\ln\frac{\sum_{i=1}^{n}\omega^i\prod_{j=\theta}^{k}\mathcal{N}\left(\boldsymbol{Z}_j;\hat{\boldsymbol{Z}}^i_{j/j-1},\boldsymbol{S}^i_j\right)}{\prod_{j=\theta}^{k}\mathcal{N}\left(\boldsymbol{Z}_j;\hat{\boldsymbol{Z}}^0_{j/j-1},\boldsymbol{S}^0_j\right)}\\ &=\ln\frac{\sum_{i=1}^{n}\omega^i\prod_{j=\theta}^{k}p\left(\tilde{\boldsymbol{\gamma}}^i_j|\mathrm{H}_1(\theta,v_i)\right)}{\prod_{j=\theta}^{k}p\left(\boldsymbol{\gamma}^0_j|\mathrm{H}_0\right)} \end{aligned} \tag{22}$$

由式(22)可知，其分母部分由多个正态分布的乘积组成，因此便于对数函数的计算。而其分子部分由多个正态分布乘积的加权和组成，因此不便于对数函数的计算。将琴生不等式应用到

式(22)中可得

$$l_k(\theta)=\ln\frac{\sum_{i=1}^{n}\omega^i\prod_{j=\theta}^{k}p\left(\tilde{\boldsymbol{r}}_j^i|\mathrm{H}_1(\theta,v_i)\right)}{\prod_{j=\theta}^{k}p\left(\boldsymbol{r}_j^0|\mathrm{H}_0\right)}\geq\sum_{i=1}^{n}\omega^i\ln\prod_{j=\theta}^{k}p\left(\tilde{\boldsymbol{r}}_j^i|\mathrm{H}_1(\theta,v_i)\right)-\ln\prod_{j=\theta}^{k}p\left(\boldsymbol{r}_j^0|\mathrm{H}_0\right)\triangleq\frac{1}{2}\tilde{l}_k'(\theta) \tag{23}$$

也就是说

$$\tilde{l}_k'(\theta)=\left[\sum_{j=\theta}^{k}\left(\boldsymbol{r}_j^0\right)^{\mathrm{T}}\left(\boldsymbol{S}_j^0\right)^{-1}\left(\boldsymbol{r}_j^0\right)-\sum_{i=1}^{n}\omega^i\sum_{j=\theta}^{k}\left(\tilde{\boldsymbol{r}}_j^i\right)^{\mathrm{T}}\left(\boldsymbol{S}_j^i\right)^{-1}\left(\tilde{\boldsymbol{r}}_j^i\right)\right]+K' \tag{24}$$

其中

$$K'=\sum_{j=\theta}^{k}\ln\left|\boldsymbol{S}_j^0\right|-\sum_{i=1}^{n}\omega^i\sum_{j=\theta}^{k}\ln\left|\boldsymbol{S}_j^i\right|$$

与伪距量测无关。由式(24)可知，为了得到n个滤波残差向量，量测方程的数目需要与均值跳变误差采样数目相同并且每一个量测方程的权重值为ω^i。虽然每一个均值跳变误差采样值对应一个量测方程，但其权重值取决于均值跳变采样值与真实跳变值的接近程度。因此，与每一个量测方程相关的权重值可以被看做是一个隐马尔科夫链并且可以被定义为$\tilde{\omega}_j^i$（j时刻第i个量测方程的权重值）。将ω^i应用于式(24)中，近似边缘似然比假设检验统计量可写为

$$\tilde{l}_k(\theta)=\sum_{j=\theta}^{k}\left[\left(\boldsymbol{r}_j^0\right)^{\mathrm{T}}\left(\boldsymbol{S}_j^0\right)^{-1}\left(\boldsymbol{r}_j^0\right)-\sum_{i=1}^{n}\tilde{\omega}_j^i\left(\tilde{\boldsymbol{r}}_j^i\right)^{\mathrm{T}}\left(\boldsymbol{S}_j^i\right)^{-1}\left(\tilde{\boldsymbol{r}}_j^i\right)\right]+K \tag{25}$$

其中

$$K=\sum_{j=\theta}^{k}\left[\ln\left|\boldsymbol{S}_j^0\right|-\sum_{i=1}^{n}\tilde{\omega}_j^i\ln\left|\boldsymbol{S}_j^i\right|\right]$$

最后，均值跳变出现或消失的判定条件可定义如下：

$$\tilde{l}_k(\theta)\underset{\mathrm{H}_0}{\overset{\mathrm{H}_1}{\gtrless}}\varepsilon' \tag{26}$$

其中ε'是相应的检测门限值。 同时，跳变出现时刻的最大似然估计为

$$\hat{\theta}=\arg\max_{\theta}\tilde{l}_k(\theta) \tag{27}$$

3.2.3 实验结果

图5显示了在真实城市峡谷环境中不同方法的位置估计误差。实验结果表明，所提方法可以有效的抑制多径干扰，从而载体的提高定位精度。

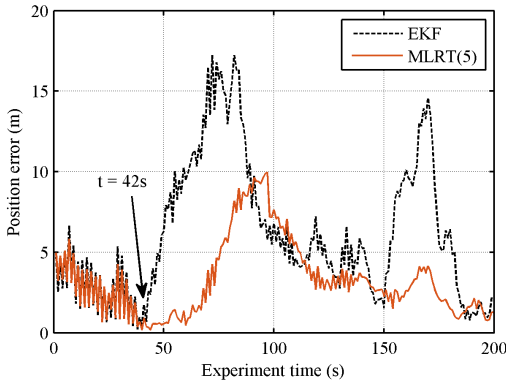

(a) Horizontal error

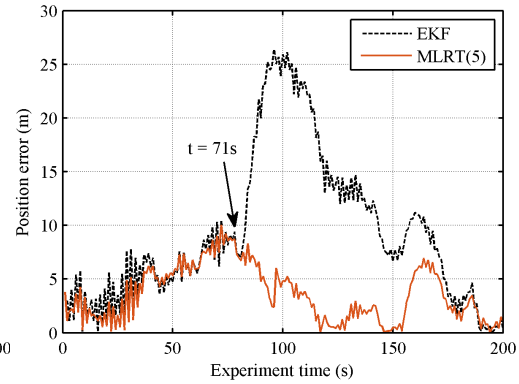

(b) Vertical error

i) Positioning errors versus time.

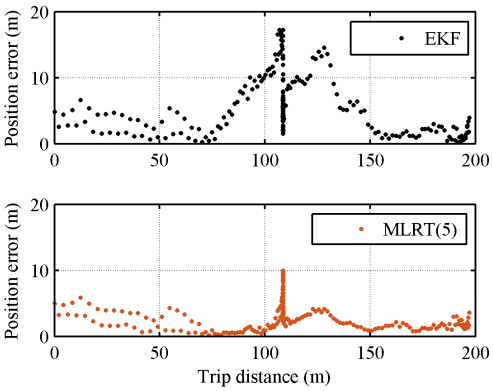

(c) Horizontal error

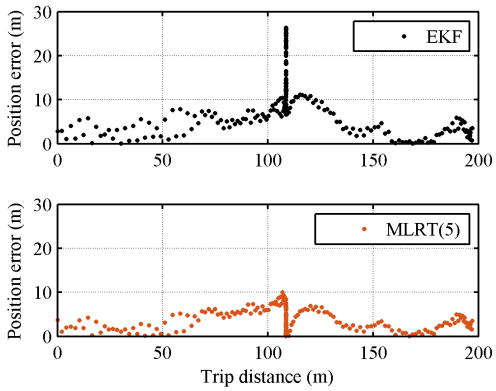

(d) Vertical error

ii) Positioning errors versus trip distance.

图 **5** – 位置估计误差

3.3 多径环境下基于视觉传感器辅助的**IMU/GNSS**组合导航系统

考虑到多传感器间的信息互补有利于多径干扰引起的GNSS伪距和伪距率量测误差的检测，提出了基于单目视觉传感器和大气压力计辅助的惯性测量单元（IMU）/GNSS组合导航系统，从而确保在多径环境中可以充分利用可靠的GNSS量测信息并获得准确的定位结果。该系统采用了分级传感器融合架构，首先将单目视觉传感器和大气压力计与IMU进行组合来校正IMU的漂移误差，提高载体状态的估计精度，然后对GNSS伪距和伪距率量测进行检验，最后利用未受到多径干扰的GNSS量测对载体状态进行更新，获得最终的定位结果。为了保证四元数在无迹变换时归一化要求，采用基于四元数的无迹卡尔曼滤波来实现不同传感器信息的融合。由于在城市峡谷环境中多径干扰造成的GNSS伪距和伪距率量测误差较小，因此采用了序贯统计检测方法来处理GNSS伪距和伪距率量测。

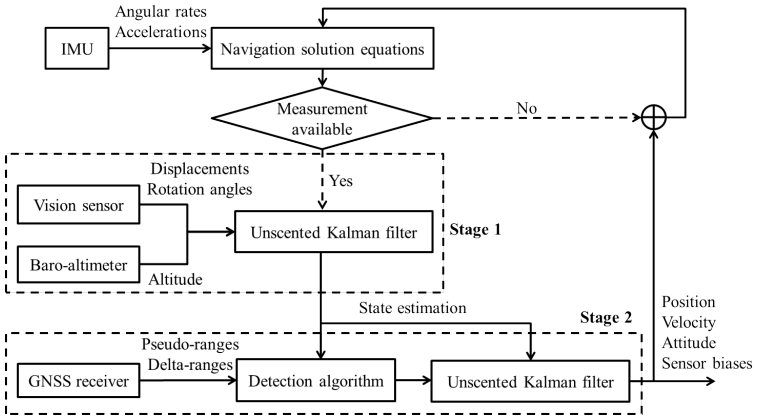

图 **6** – 基于视觉传感器和大气压力计辅助的IMU/GNSS组合导航系统结构图

3.3.1 组合导航系统架构

图6显示了基于视觉传感器和大气压力计辅助的IMU/GNSS组合导航系统的结构，其中，分级传感器融合步骤如下：

(1) 基于IMU测量输出，利用惯性导航解算模型递推获得载体的位置，速度和姿态等状态信息

(2) 利用基于四元数的无迹卡尔曼滤波将递推得到的载体状态信息与视觉传感器和大气压力计的量测进行融合，从而改进载体状态信息

(3) 利用改进的载体状态信息来对GNSS伪距和伪距率量测进行检测，筛选出未受到多径干扰的GNSS量测

(4) 利用未受到多径干扰的GNSS量测对载体状态进行更新并获得最终的定位结果

3.3.2 GNSS量测处理方法

考虑到在慢衰落信道中，相干多径干扰对于GNSS量测的影响取决于载体相对于卫星的运动方向，此时，多径干扰会对GNSS伪距量测造成影响，而相应的伪距率量测不会受到多径干扰的影响。因此，图7显示了对于GNSS伪距和伪距率量测的两步检测方案，

- 步骤一 （伪距检测）：当检测统计量$l_{m,t}^{\mathrm{PR}}$超过检测门限值时，认为该伪距量测受到多径干扰，将此伪距量测剔除并在第二步中对同一卫星的伪距率量测进行检测
- 步骤二 （伪距率检测）：当检测统计量$l_{m,t}^{\mathrm{DR}}$超过检测门限值时，认为该伪距率量测受到多径干扰，将此伪距率量测剔除

通过以上方案，可以筛选出未收到多径干扰的GNSS量测。鉴于GNSS伪距量测与伪距率量测高度相关，因此只选择一个量测用于组合导航系统中。

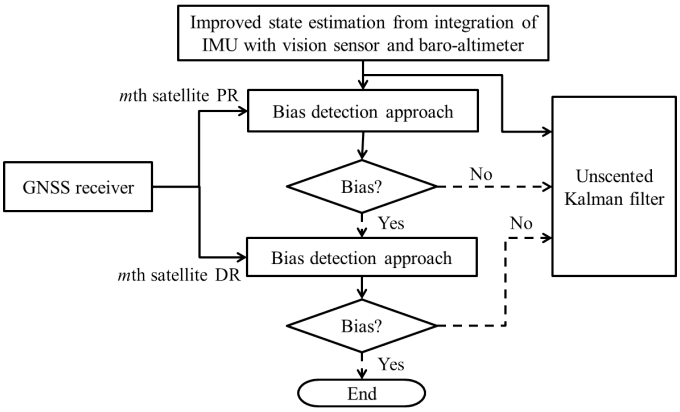

图 **7** – GNSS伪距和伪距率检测方案

3.3.3 实验结果

图5显示了在真实城市峡谷环境中不同方法的定位结果，图中，红线代表所提方法的定位结果。试验结果表明，所提方法的定位结果明显优于其他方法。

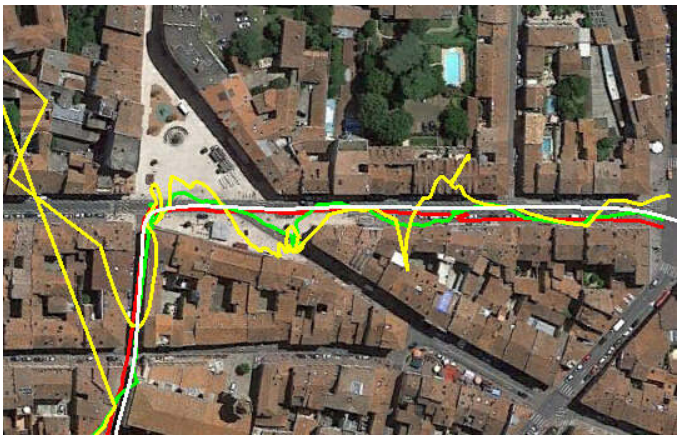

图 **8** – 定位结果

4 总结与展望

4.1 论文工作总结

本研究尝试采用不同信号处理方法来的抑制多径干扰对与GNSS定位结果的影响。通过论文第2章对GNSS接收机中多径抑制方法的归纳与分析，本研究的三个主要贡献点总结如下：

1. 多相关器GNSS接收机中基于最大似然准则无源卡尔曼滤波的多径干扰抑制方法

第三章提出了基于最大似然准则下的无迹卡尔曼滤波方法，用于实现在多径干扰影响下的直达信号参数估计。考虑到多相关器输出可以充分描述多径信号对接收机相关函数的影响，因此将多相关器的输出作为量测信息。分别采用时间相关的一阶马尔科夫模型和静态似然模型来描述直达信号和多径信号参数。然后利用所提方法实现对直达信号和多径信号参数的迭代估计，首先基于直达信号的先验信息来实现对多径信号参数的最大似然估计，然后再基于多径信号的最大似然估计值来实现直达信号参数的后验估计。最后与标准无源卡尔曼滤波进行仿真比较，仿真结果表明，当没有多径干扰时，所提方法等价于标准的无源卡尔曼滤波；而当存在多径干扰时，所提方法比标准的无源卡尔曼滤波更加鲁棒，并且可以明显提高直达信号参数的估计精度。

2. 在多径干扰下基于边缘似然比假设检验的伪距偏差检测与估计方法

第四章提出了基于边缘似然比假设检验的非视距多径误差检测，识别与估计方法。考虑到非视距多径干扰常出现在城市峡谷等复杂环境中，造成GNSS接收机输出的伪距量测发生跳变。由于边缘似然比统计量不易计算，采用基于均值跳变误差采样的蒙特卡洛积分来获得近似边缘似然比统计量，利用琴生不等式来简化蒙特卡洛积分计算和多模型方法来更新每个均值跳变误差采样的先验信息。仿真结果表明，尽管所提方法的检测延迟略大于其他方法，但是对于均值跳变的检测率有着明显的提高。实验结果表明，所提方法可以有效的检测和抑制由多径干扰引起的GNSS伪距均值跳变误差，从而提高载体定位精度。

3. 多径环境下基于视觉传感器辅助的IMU/GNSS组合导航系统

第五章提出了基于单目视觉传感器和大气压力计辅助的惯性测量单元/GNSS组合导航系统，从而确保在多径环境中可以充分利用可靠的GNSS量测并获得准确的定位结果。组合导航系统采用了分级传感器融合架构，1)将单目视觉传感器和大气压力计与IMU进行组合来校正IMU的漂移误差，提高载体状态的估计精度，2)对GNSS伪距和伪距率量测进行检验，3)利用未受到多径干扰的GNSS量测对载体状态进行更新并获得最终的定位结果。为了保证四元数在无迹变换时归一化要求，采用基于四元数的无迹卡尔曼滤波来实现不同传感器信息的融合。由于在城市峡谷环境中多径干扰造成的GNSS伪距和伪距率量测误差较小，因此采用了序贯统计检测方法来处理GNSS伪距和伪距率量测。实验结果表明，所提方法在多径环境中可以有效的检测和筛选受到多径干扰影响的GNSS量测，并且可以明显的提高载体定位精度。

4.2 工作展望

本文深入研究了基于贝叶斯方法的GNSS多径干扰抑制方法，但是，仍有一些问题需要进一步深入研究

- 在第三章中，网格搜索方法被用于估计多径信号伪随机码延迟。这种方法的计算量不仅较高，而且由于实际伪随机码延迟被近似为最邻近的相关器延迟，会存在相应的近似误差，因此所得到的估计结果并不是最优结果。需要进一步研究如牛顿迭代，期望最大化等最优的估计方法。

- 在第四章中，假设由多径干扰引起的伪距量测均值跳变误差的幅值服从均匀分布。但在一些情况下，均值跳变误差的幅值可能服从瑞利分布。因此，需要进一步研究基于瑞利分布的近似边缘似然比假设检验方法。

- 在第五章中，利用测量数据后处理的方式对所提的组合导航系统进行验证，而采用实时测量数据会更有利于系统性能的评估。另外，需要进一步研究在复杂环境中对于多径干扰引起的GNSS量测误差的分类方法，从而提高多径误差的检测率。

CHAPTER

ONE

INTRODUCTION

Global navigation satellite systems (GNSS) have been widely used in many military and civilian applications, such as various kinds of aerial/landing vehicles. The GNSS systems which support these applications, include the well-known United States Global Positioning System (GPS), the Russian GLONASS, the European Galileo, and the new-emerging China BeiDou Navigation Satellite System (BDS), the Indian Regional Navigational Satellite System (IRNSS) and the Japan Quasi-Zenith Satellite System (QZSS).

With the new application requirements for GNSS systems in a complex environment, such as in urban canyons or other intensive obstruction scenarios, new challenges have also risen which had not been foreseen in the beginnings of GPS and GNSS. Indeed, the urban canyon environment leads to masking effect, reflection and diffraction which degrade the received signal. Thus one of the largest challenges is to address the impact of multipath (MP) interferences on positioning based GNSS. MP interferences are mainly due to the fact that a signal transmitted by a satellite is very likely to be reflected or diffracted and can follow different paths before arriving at the GNSS receiver. When the MP interference mitigation needs to be performed, a signal processing method within the receiver is more sophisticated than in open-air environments. In this thesis, the issue of MP mitigation at different signal processing stages of the GNSS receiver is discussed.

In this introductive chapter, the first section provides a brief overview of GNSS systems including their working principle and a description of the currently available and future planned systems worldwide. In the following section, the interests of the research that is conducted in this thesis is introduced. The final section summarizes the approaches that will be investigated in this thesis and outlines the contribution of each chapter to the thesis objective.

1.1 GNSS Systems Overview

1.1.1 Working Principle

Positioning for any satellite navigation system is based on a principle called trilateration in which a position in a given geometric space can be inferred by calculating distances to a set of landmarks with a known position in this same space. Generally, the distance, which is commonly known as pseudo-range (PR), can be calculated from the propagation time of the signal from the satellite to the user [1–3]

$$\rho_i = c\tau_i \tag{1.1}$$

where τ_i represents the signal propagation time and c is the speed of light in the vacuum. This equation provides directly the satellite-user geometric range assuming that the user and satellite clocks has been synchronized beforehand. However, the clock bias Δb between the user and the satellite always exists and cannot be determined a priori. As a consequence, the key equation in satellite navigation, also known as the navigation equation, is defined as [4–6]

$$\rho_i = r_i + c\Delta b = \sqrt{(x_i - x_u)^2 + (y_i - y_u)^2 + (z_i - z_u)^2} + b_u \tag{1.2}$$

where ρ_i is known as the PR measurement between the user and the ith satellite, $(x_i,\ y_i,\ z_i)$ and $(x_u,\ y_u,\ z_u)$ are the ith satellite and the user positions in the earth-centered earth-fixed (ECEF) frame and $b_u = c\Delta b$ is the user clock bias expressed in distance. It is clear that there are four unknown parameters, including the coordinates of the 3D user position in meters and the clock bias that need to be determined using the PR measurements. As a consequence, the minimum number of satellite measurements for obtaining a navigation solution is at least four.

The estimation of the signal propagation time τ_i from the navigation satellite to the user, for the calculation of PR measurement, is implemented using direct-sequence spread-spectrum (DSSS) demodulation techniques [7, 8]. A specific pseudo-random noise (PRN) code associated with each navigation satellite is used to modulate the satellite signal. In order to determine the parameters of the received satellite signal inside the receiver, the code synchronization is performed by aligning a local generated signal replica with the received signal. Code alignment allows the arrival time of satellite signals to be estimated. The propagation time is then obtained by considering the time instant when the signal is transmitted by the navigation satellite. Carrier alignment can also be used to estimate the signal Doppler frequency which is related to the satellite-user velocity. Moreover, the demodulation of the navigation data contained in received satellite signals is necessary to obtain the satellite Keplerian orbit information, such as the satellite position in the ECEF frame at the time instant when the signal is transmitted by the satellite, the satellite ephemeris and the model parameters of the satellite system time error and of the ionospheric delay error. Each of these pa-

rameters are essential to develop the equation (1.2). Finally, the set of navigation equations is solved by a least-squares method or a Kalman filtering-based approach [4–6, 9].

1.1.2 GNSS Systems Worldwide

Various GNSS systems are operational and under deployment around the globe. These include the United States' (US) Global Positioning System (GPS), the Russian GLObal NAvigation Satellite System (GLONASS), the European Galileo, the Chinese BeiDou, the Indian Regional Navigational Satellite System (IRNSS) and the Japanese Quasi-Zenith Satellite System (QZSS). A brief overview of these systems, and their services and signals is provided next.

Global Positioning System (GPS) GPS is the most well-known GNSS system worldwide. It was developed by the U.S. government as a military program in 1973. After two decades of planning and construction, it has been fully operational since 1995. Before May 2000, civilian usage of the GPS signals was degraded to the order of 100 m by selective availability technique, that was cut off on 2000. From then on, the civilian GPS became has a wide-application. As of beginning 2014, the GPS constellation consists of 32 satellites arranged into 6 equally-spaced orbital planes at an altitude of approximately 20.200 km corresponding to a Medium Earth Orbit (MEO), which circle the Earth twice per day. Currently, three civil signals are being transmitted by GPS satellites, in three different frequency bands, and a fourth one will be included in the new generation of GPS satellites [1, 2, 4–6, 9, 10].

The most commonly used GPS signal is known as the GPS Coarse/Acquisition (C/A) signal, transmitted at the L1 spectrum band (1575.42 MHz). This signal is transmitted by all GPS satellites currently in orbit and is available for public use. Each satellite transmits a unique PRN Gold code of length 1023 chips, repeating itself every 1 ms. The navigation data contained in this signal is transmitted at a rate 20 times lower than the code pseudo-period, meaning that each navigation data bit spans over 20 code pseudo-periods of the PRN code. One other signal that has also been transmitted since the origins of the GPS program, is known as the Precise (P) code signal. Given that the actual P code is encrypted using the Y code, this signal is usually referred to as the P(Y) signal. This code is not available for civilian users and is primarily used by the US military. This code is transmitted on both the L1 and L2 (1227.6 MHz) bands [2, 11, 12].

Three new civil signals have been conceived in the modernization phase of GPS undertaken since the early 2000s. The second civil signal, transmitted in the L2 band, and known as L2 Civil (L2C) signal, started being transmitted in 2005 and as of December 2013 was broadcast by 11 satellites. The third civil signal is intended for the support of safety-critical civil aviation operations and is transmitted at the L5 band (1176.45 MHz), a band highly protected for Aeronautical Radio Navigation Services. This signal started to be used in 2010 and is currently being transmitted by four GPS

satellites. The fourth civil signal, also transmitted in the L1 band, and known as L1 Civil (L1C) was designed to enable interoperability between GPS and other GNSS systems. This signal is intended to be transmitted in 2015 [2, 12–14].

Global Navigation Satellite System (GLONASS) The GLONASS system was initially developed in the 1970s, in parallel to GPS, and was designed to offer both a civil and a military positioning service. After decade of construction, a full satellite constellation, i.e., 24 satellites, was achieved in 1995. Due to financial problems, the Russian government led to a decay of the number of operational satellites, which reached a minimum of seven operational satellites by 2001. From 2001, a modernization program was proposed and rebuilding the constellation of 23 operational spacecraft was achieved by April 2013. These satellites are placed in three orbital planes at an orbital altitude of approximately 19.100 km (MEO) [2, 9, 15].

While the legacy GLONASS satellites broadcast navigation signals in the L1 (standard and high accuracy signals) and L2 (high accuracy signal) bands, the modernized satellites will transmit in the L3/L5 band as well. Several signals are currently planned for these bands, both employing Frequency Division Multiple Access (FDMA) and Code Division Multiple Access (CDMA) for sharing the spectrum between the different satellites [9, 15–17].

Galileo Development of the Galileo satellite navigation system was initiated in 1999 by the European Union and European Space Agency. The Galileo is the first system to be conceived and developed under civilian control. Once fully deployed, the complete Galileo constellation will consist of 30 satellites in three orbital planes at an approximate orbital altitude of 23.200 km, completing an orbit around the Earth every 14 hours. Until 2014, the Galileo constellation consisted of four operational satellites.

Galileo offers three main navigation services. The Galileo Open Service (OS) is a free-of-charge service suitable for mass-market applications and is accessible at the L1/E1 and E5 (1191.795 MHz) bands. It will offer a performance level similar to the modernized standard GPS service. The Public Regulate Service (PRS) will provide position and timing restricted to government-authorized users and is intended for security and strategic infrastructure. This service is broadcast in the E1 and E6 (1278.75 MHz) bands. The third service, Commercial Service (CS), is aimed at market applications requiring higher performance than this offered by the OS. This service is based on the OS and is complemented by two signals at the E6 band (1278.75 MHz) [18, 19]. The services dedicated to the civil aviation commercially are also supported. They will be broadcasted in the E5 band.

BeiDou Navigation Satellite System (BDSS) The BDSS is equally a global system which in its full operating capability will incorporate 35 satellites (five in Geostationary orbit (GEO), 37 in MEO at an altitude of 21.528km, and three in an inclined Geosynchronous orbit (GSO)). Two civil signals

are currently described in the BDSS Interface Control Document, the B1I and B2I signals in the E2 (1561.098MHz) and E5B (1207.14 MHz) bands. With a constellation of 14 operational systems, the system has been declared fully operational over the Asia-Pacific region since December 2012 [20, 21]. At the beginning of 2015, the 17th Beidou satellite was successfully launched in order to carry out new type of navigation signal system validation and inter-satellite link demonstration, which build technology basis for the BDS global service [22].

Indian Regional Navigational Satellite System (IRNSS) The IRNSS is an independent regional navigation satellite system that will consist of seven satellites (three satellites in GEO, and two satellites in GSO). The IRNSS will provide two signals in the L5 and S (2492.03 MHz) bands providing two services: the Standard Positioning Service for common civilian users, and the Restricted Service for special authorized users. The first satellite has been launched in July 2013 and the full constellation is expected to be deployed by 2016 [23, 24].

Quasi-Zenith Satellite System (QZSS) The QZSS system is under development by Japan and will be composed of satellites in quasi-zenith orbits, appropriate for signal reception over Japan. This system is intended to at first augment GPS with a four-satellite constellation by 2018, and to have in the future a full constellation of seven satellites. The QZSS system will provide signals similar to GPS's L1 C/A, L1C, L2C, and L5, as well as two augmentation signals, the Submeter-class Augmentation with Integrity Function (SAIF) in the L1 band and the L-band Experiment (LEX) in the L6/E6 band [25, 26].

1.2 Research Significance on GNSS MP Mitigation

With the development and modernization of GNSS, many error sources for GNSS, such as satellite clock errors, ephemeris and troposphere delay errors, can be reduced using appropriate techniques. Therefore, the MP error can be considered as a dominant error source in some situations, such as in urban canyons or other intensive obstruction scenarios. Generally, the MP signals are mainly due to the fact that a signal transmitted by a satellite is very likely to be reflected or diffracted and can follow different paths before arriving at the GNSS receiver. The presence or absence of MP signals not only depends on the relative position between the navigation satellite and the GNSS receiver, but also on the environment where the GNSS receiver is located. When the receiver moves with time, MP parameters also change and the change rate depends on the vehicle speed. As a consequence, it is difficult to accurately describe the changes in MP signals by using a mathematical model, increasing the difficulty to perform an efficient approach for mitigating MP interferences.

Until now, the research on MP mitigation techniques remains an area of active interest. With regard to MP mitigation approaches, many factors need to be considered, such as the performance

and robustness in different kinds of MP scenarios, the implementation complexity and feasibility in the employed GNSS receiver. Unfortunately, most of the existing MP mitigation techniques are hard to fully satisfy these requirements, resulting in increased receiver complexity and poor performance with regard to noise and interference. Thus it is a great challenge for proposing a new MP mitigation approach to satisfy these requirements as much as possible.

1.3 Thesis Objectives, Main Contributions and Overview

This thesis addresses MP mitigation techniques based on signal processing methods at different stages of the GNSS receiver. Other MP mitigation approaches, such as antenna array based approaches [27, 28] or using a 3D model of environment [29, 30] are not considered in this thesis. The main objective of our research is to propose innovative MP mitigation approaches with regard to the problems obtained from a start-of-the-art review presented in Chapter 2. The contributions of this work related to MP mitigation issues are described below.

Chapter 3: LOS Signal Parameter Estimation in the Presence of MP Interferences In MP environments, the correlator outputs are distorted as the line-of-sight (LOS) signal entering the receiver is combined with MP signals. This results in tracking errors which introduce biases in pseudorange, carrier phase and Doppler frequency measurements. Thus MP mitigation techniques inside the GNSS receiver can be formulated as a problem of signal parameter estimation in order to reduce the impact of MP signals for obtaining an accurate LOS parameter estimator. Considering that the presence and absence of MP signals depend on several factors related to the vehicle environment and motion, it is difficult to use a specific propagation model for the MP signal parameters when the vehicle is moving. Thus we propose to use two kinds of models for describing the LOS and MP signal parameters: a dynamic model associated with the time propagation of LOS signal parameters and a likelihood model associated with the MP signal parameters. Moreover, a multi-correlator based receiver is exploited with the advantage to fully characterize the impact of MP signals on the correlation function by providing samples of the whole correlation function. A maximum likelihood-based unscented Kalman filter (UKF) is then investigated to estimate the LOS signal parameters and MP signal parameters iteratively. The posterior Cramér-Rao bound of the LOS signal parameter estimation in the absence of MP interferences is derived and used as the reference for evaluating the performance of the proposed estimation approach. Finally, numerical simulations in different scenarios are implemented to validate the effectiveness of the proposed approach.

Chapter 4: Detection, Estimation and Correction of NLOS MP Biases In urban canyons, non-line-of-sight (NLOS) MP interferences affect position estimation based on GNSS. We propose to

model the effects of NLOS MP interferences as mean value jumps contaminating the GNSS PR measurements. The marginalized likelihood ratio test (MLRT) is then investigated to detect, identify and estimate the corresponding NLOS MP biases. However, the MLRT test statistics is difficult to compute. In this work, we consider a Monte Carlo (MC) integration technique based on bias magnitude sampling. Jensen's inequality allows this MC integration to be simplified. The multiple model algorithm is also used to update the prior information for each bias magnitude sample. Some strategies are designed for estimating and correcting the NLOS MP biases. Moreover, the empirical cumulative distribution function of the approximate test statistic is analyzed and the corresponding detection threshold is determined via MC simulations. Finally, results from a measurement campaign conducted in an urban canyon are presented in order to evaluate the performance of the proposed algorithm in a representative environment.

Chapter 5: Multi-sensor Integration for Reliable Positioning in MP Environments A multi-sensor integration architecture, which consists of a monocular vision sensor and a baro-altimeter aided inertial measurement unit (IMU)/GNSS integration, is investigated. The proposed approach aims at exploiting the reliable GNSS measurements in urban environments to ensure the required navigation accuracy and reliability. Thus the implementation of this method mainly consists of three steps: 1) the integration of an IMU, a monocular vision sensor and a baro-altimeter is performed in order to calibrate the IMU solution drift so as to improve the a priori estimate of the vehicle state; 2) GNSS measurements are processed for detecting the measurements contaminated by the MP interferences and 3) reliable GNSS measurements and IMU data are combined to provide the final vehicle state estimation. A quaternion-based UKF is designed to perform the integration of the IMU and other sensors, in which the quaternion normalization constraint is satisfied in the unscented transformation. Finally, results from a measurement campaign conducted in an urban canyon are presented in order to evaluate the availability of the proposed approach.

Thesis Structure The remainder of this manuscript is organized in 5 chapters. In Chapter 2, the structure of the GNSS receiver is described briefly, and the impacts of MP interferences on the different stages of the GNSS receiver are discussed. Moreover, the state-of-the-art MP mitigation approaches to be implemented inside the GNSS receivers are reviewed. In light of this state-of-the-art review, the research objectives are also justified.

In chapters 3 to 5, the main contributions of this thesis are described. Finally, Chapter 6 concludes this thesis, and provides considerations about directions for future work based on the algorithms developed.

1.4 List of Publications

International Conferences

(1) C. Cheng, V. Calmettes, B. Priot, Q. Pan and J.-Y. Tourneret, "Vision aided INS/GNSS integration for improving the robustness of a navigation system for mini unmanned aerial vehicles," in *Proceedings of 2013 International Technical Meeting of The Institute of Navigation (ION ITM 2013)*, San Diego, CA, USA, 2013.

(2) C. Cheng, J.-Y. Tourneret, Q. Pan and V. Calmettes, "A marginalized likelihood ratio approach for detecting and estimating multipath biases on GNSS measurements," in *Proceedings of the* 17th *International Conference on Information Fusion (FUSION 2014)*, Salamanca, Spain, 2014.

International Journals

(3) C. Cheng, J.-Y. Tourneret, Q. Pan and V. Calmettes, "Detecting, estimating and correcting multipath biases affecting GNSS signals using a marginalized likelihood ratio-based method," To appear in *Elsevier Signal Processing* in 2015.

CHAPTER

TWO

STATE-OF-THE-ART MULTIPATH MITIGATION IN GNSS RECEIVERS

GNSS receivers are used to process the signals transmitted by the satellites. This processing includes GNSS signal down-conversion, acquisition and tracking. These operations allow GNSS signal parameters to be estimated and then to determine the user position, velocity and time. A signal transmitted by a satellite can be reflected or diffracted and can follow different paths which are commonly known as multipath (MP) signals, before arriving at the GNSS receiver antenna. Generally, due to the structure of the signal, MP issue can readily be resolved inside the receiver when the time delay of MP interferences, relative to the direct path delay, is large enough. In this particular case, MP interferences have little influence on the receiver. However, in some situations, such as in urban canyons where the relative time delay of the MP is short, MP interferences affect the signal processing results at different stages in the receiver. For instance, MP signals can modify the correlation and discriminator functions and can introduce biases in pseudo-range and carrier phase measurements, and severely impair the positioning solution based on GNSS.

In Section 2.1, the structure of the GNSS receiver is described briefly. In Section 2.2, the impacts of MP interferences on the GNSS receiver are discussed. Then state-of-the-art MP mitigation approaches, inside a GNSS receiver, are reviewed in Section 2.3. According to the state-of-the-art review, the last section justifies the research topics that have been pursued during this doctoral research.

2.1 Principle of the GNSS Receiver

Generally, a typical GNSS receiver is composed of three functional blocks: 1) antenna and front-end block; 2) baseband signal processing block; 3) navigation processor block. The architecture of these blocks [4] is shown in Figure 2.1. In this section, each block of the receiver, especially tracking loops which play an important part of the baseband signal processing block, is introduced briefly.

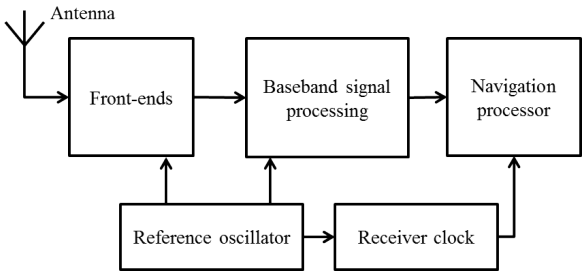

Figure 2.1 – GNSS receiver architecture.

2.1.1 Antenna and Front-end Block

In GNSS systems, the signals transmitted by the GNSS satellites are composed of a direct spread spectrum sequence, a binary navigation data and a carrier waveform [1,7]. The direct spread spectrum sequence is obtained by a linear modulation of a sequence of pulses $p(t - nT_c)$, which are commonly known as chips with a duration T_c, by a pseudo-random noise (PRN) code c_n, i.e.,

$$c(t) = \sum_{n=0}^{N-1} c_n \, p(t - nT_c) \tag{2.1}$$

where N is the length of the PRN code. The spread spectrum sequence is then used to modulate a binary navigation data sequence $d(t) = \pm 1$, which is typically at a much lower rate than $c(t)$, leading to

$$q(t) = \sum_{i=-\infty}^{i=+\infty} d(i) \, c(t - iT) \tag{2.2}$$

where $T = NT_c$ is the code pseudo-period. This modulation is also referred to as a direct-sequence spread-spectrum (DS-SS) technique [8]. Finally, GNSS signals are obtained by mixing the signal $q(t)$ with a carrier waveform of frequency f_c, carrier phase φ and power P_s, using binary phase-shift keying (BPSK) modulation technique [4],

$$s(t) = \sqrt{P_s} \, d(t) \, c(t) \cos(2\pi f_c t + \varphi). \tag{2.3}$$

This signal structure is widely recognized as the structure of the GPS L1 C/A signal, in which the chip rate is $f_c = 1/T_c = 1.023$ MHz and the length of the PRN code is $N = 1023$, resulting in a code

period of 1 ms. This signal structure is the basis for most current and planned GNSS signals, and is considered as the signal model to be treated in this section.

The receiver antenna of the GNSS receiver, which converts an electromagnetic signal into an electrical signal so that it may be processed by the GNSS receiver, should be sensitive only to right-handed circular polarization (RHCP) signals [4]. The corresponding power of the received signal depends on the incident angle of the GNSS signal. However, it changes very less with the elevation angle of the GNSS signal, e.g., the received signal power varies only 3 dB when the elevation angle changes from 5° to 90° [2].

The receiver front-end block down-converts the received signal carrier frequency from the original L-band radio frequency (RF) to a lower intermediate frequency (IF) and then digitizes the signal which is further treated by the baseband signal processing block. This processing is called "signal conditioning". A typical front-end consists of a radio frequency processing stage, followed by two IF down-conversion stages, and then the analog-to-digital converter (ADC). The bandwidth of the conditioned signals entering the ADC is known as the pre-correlation bandwidth [9]. The minimum double-sided bandwidth is about twice the chip rate for a BPSK signal. It is assumed that $f_s = 1/T_s$ is the single-side pre-correlation bandwidth (sampling frequency) in the front-end of GNSS receiver. In a pilot channel, the received GNSS signal, sampled at time instants nT_s where $n = 1, \ldots, \infty$, can be defined as [5]

$$r(nT_s) = \sqrt{P}\, c(nT_s - \tau)\, \cos\big(2\pi(f_{\mathrm{IF}} + f^d)nT_s + \varphi\big) + \omega(nT_s) \tag{2.4}$$

where P is the mean power of the received GNSS signal, τ is the propagation delay of the signal transmitted by the given GNSS satellite, f_{IF} is the intermediate frequency of the front-end and f^d is the carrier Doppler frequency due to the relative motion of the given GNSS satellite and the antenna in the GNSS receiver. Finally, φ is the carrier phase (which depends on the Doppler frequency drift) and $\omega(nT_s)$ is the additive white noise affecting the GNSS signal. Note that $\omega(nT_s)$ denotes the overall noise which consists of external noise entering the receiver through the antenna, the noise generated in the front-end block and the noises due to the cross correlation between different satellite codes.

2.1.2 Baseband Signal Processing Block

In the baseband signal processing block, the digitized IF signal which is provided by the receiver front-end, is demodulated by mixing this signal with a local generated replica of the carrier signal. A de-spread operation is performed by correlating the demodulated signal with a local generated replica of the PRN code. Then the de-spread signal is accumulated over a time interval. This procedure is commonly known as "signal correlation". Since the rate of the correlation output is much lower than the signal sampling frequency, the correlation outputs are usually used to acquire and

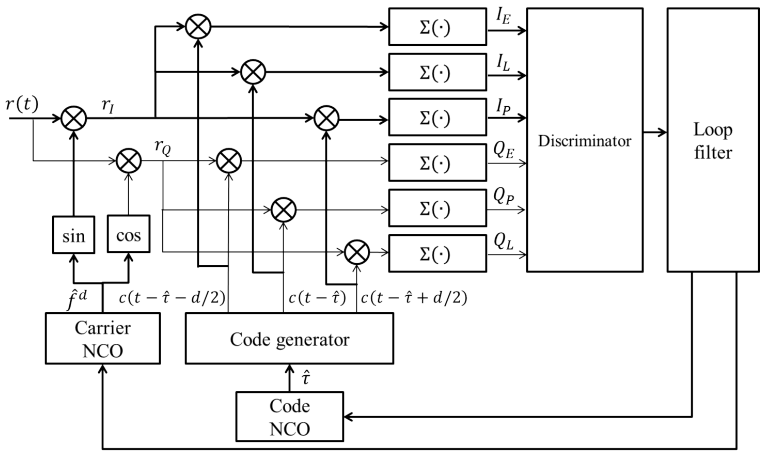

Figure 2.2 – GNSS baseband signal processing channel [4].

track each in-view satellite signal. The signal acquisition and tracking are the processes, consisting of estimating the PRN code delay time, the carrier phase and Doppler frequency which allows the local generated signal replica to be synchronized with the received signal. In most receivers, the tracking process is achieved by using tracking loops known as delay tracking loop (DLL), phase tracking loop (PLL), frequency tracking loop (FLL). In addition, the GNSS measurements which consist of the pseudo-range (PR), delta-range (DR) and accumulated delta-range (ADR) can be estimated from above mentioned signal parameters [4]. Thus the baseband signal processor is divided into a set of parallel channels, one for each in-view satellite signal processing. The Figure 2.2 shows an architecture of a typical GNSS baseband signal processing channel.

In the correlators, each channel decomposes the corresponding received GNSS signal into its in-phase (I) and quadrature (Q) components. In practice, several samples of the correlation function are necessary to implement the signal acquisition and tracking. The simplest receivers are based on three correlators for each channel, which are known as early correlator for the code advanced replica, prompt correlator for the in-phase code with replica, and late correlator for the code delayed replica. Each correlation is performed over a time interval T_a, such as 1 ms at least for the GPS L1 C/A code, in order to obtain the integration outputs of the I and Q components with early, prompt and late correlation. This stage is known as "integrate and dump". The prompt in-phase component of the local generated signal replica can be defined as

$$\tilde{r}_{IP}(nT_s) = c(nT_s - \tilde{\tau}) \cos\left(2\pi(f_{\mathrm{IF}} + \tilde{f}^d)nT_s + \tilde{\varphi}\right). \tag{2.5}$$

Similarly, the prompt quadrature component is

$$\tilde{r}_{QP}(nT_s) = c(nT_s - \tilde{\tau}) \sin\left(2\pi(f_{\mathrm{IF}} + \tilde{f}^d)nT_s + \tilde{\varphi}\right) \tag{2.6}$$

where $\tilde{\tau}$, $\tilde{\varphi}$ and $\tilde{f}^d$ are the PRN code delay, carrier phase and Doppler frequency of the local generated signals. Thus, considering the early, prompt and late correlator, the outputs of the I and Q components, sampled at time instants $k = 1, \ldots, \infty$, are defined as

$$\begin{aligned}
I_{E,k} &= \frac{1}{N_s}\sqrt{P}\, R\left(\Delta\tilde{\tau}_k + \frac{d}{2}T_c\right)\frac{\sin(\pi\Delta\tilde{f}_k^d T_a)}{\sin(\pi\Delta\tilde{f}_k^d T_s)}\cos(\Delta\tilde{\varphi}_k) + \omega_I(nT_s)\\
I_{P,k} &= \frac{1}{N_s}\sqrt{P}\, R(\Delta\tilde{\tau}_k)\frac{\sin(\pi\Delta\tilde{f}_k^d T_a)}{\sin(\pi\Delta\tilde{f}_k^d T_s)}\cos(\Delta\tilde{\varphi}_k) + \omega_I(nT_s)\\
I_{L,k} &= \frac{1}{N_s}\sqrt{P}\, R\left(\Delta\tilde{\tau}_k - \frac{d}{2}T_c\right)\frac{\sin(\pi\Delta\tilde{f}_k^d T_a)}{\sin(\pi\Delta\tilde{f}_k^d T_s)}\cos(\Delta\tilde{\varphi}_k) + \omega_I(nT_s)
\end{aligned} \tag{2.7}$$

and

$$\begin{aligned}
Q_{E,k} &= \frac{1}{N_s}\sqrt{P}\, R\left(\Delta\tilde{\tau}_k + \frac{d}{2}T_c\right)\frac{\sin(\pi\Delta\tilde{f}_k^d T_a)}{\sin(\pi\Delta\tilde{f}_k^d T_s)}\sin(\Delta\tilde{\varphi}_k) + \omega_Q(nT_s)\\
Q_{P,k} &= \frac{1}{N_s}\sqrt{P}\, R(\Delta\tilde{\tau}_k)\frac{\sin(\pi\Delta\tilde{f}_k^d T_a)}{\sin(\pi\Delta\tilde{f}_k^d T_s)}\sin(\Delta\tilde{\varphi}_k) + \omega_Q(nT_s)\\
Q_{L,k} &= \frac{1}{N_s}\sqrt{P}\, R\left(\Delta\tilde{\tau}_k - \frac{d}{2}T_c\right)\frac{\sin(\pi\Delta\tilde{f}_k^d T_a)}{\sin(\pi\Delta\tilde{f}_k^d T_s)}\sin(\Delta\tilde{\varphi}_k) + \omega_Q(nT_s)
\end{aligned} \tag{2.8}$$

with

$$R(\Delta\tilde{\tau}_k) \approx \begin{cases} 1 - |\Delta\tilde{\tau}| & |\Delta\tilde{\tau}| < T_c \\ 0 & |\Delta\tilde{\tau}| \geq T_c \end{cases}$$

and

$$\Delta\tilde{\varphi}_k - \Delta\tilde{\varphi}_{k-1} = 2\pi\Delta\tilde{f}_k^d T_a$$

where $T_a = N_s T_s$ and N_s is the number of correlated samples during an integration interval, d is the correlator spacing in chips between the early and late replicas, $\Delta\tilde{\tau}_k$, $\Delta\tilde{\varphi}$ and $\Delta\tilde{f}_k^d$ are tracking errors between actual and local generated code delay, carrier phase and Doppler frequency, $R(\cdot)$ is the auto-correlation function of the PRN code (which is defined here by neglecting pre-correlation band-limiting effect), $\omega_I(nT_s)$ and $\omega_Q(nT_s)$ are the noises with a constant power spectral density (PSD) N_0 associated with the in-phase and quadrature signals. Generally, the noise can be considered as a zero mean additive white noise and the corresponding variance is N_0/T_a. Thus longer integration time T_a results in a reduction of the noise power.

The I and Q components are used within the receiver for estimating the received GNSS signal parameters. This estimation includes 1) the signal acquisition which is a global search for obtaining the approximate estimation of the considered parameters, 2) the signal tracking which allows an accurate parameter estimation to be performed [1]. In the signal acquisition stage, a two dimensional search involves simultaneously finding the rough estimation of the code delay τ and the Doppler frequency f^d. The search steps for the code delay time and the carrier Doppler frequency are set

as $T_c/2$ and $1/2T_a$ respectively. Thus each combination of the two parameters is termed as a cell. When the two PRN codes of the received and estimated signals are aligned enough and the local generated carrier Doppler frequency matches sufficiently that of the received signal, a maximum test statistic in the cell set, which is based on the power of the complex $I + jQ$ signal, exceeds a given threshold. At this time, the acquisition stage can be considered as completed.

Since the signal acquisition provides rough estimations of the PRN code delay and carrier Doppler frequency, the tracking loops in the signal tracking stage are used to obtain the accurate parameter estimations. Generally, three different lock loops leading to different parameter estimations are implemented in the GNSS receiver [1]:

- Delay lock loop (DLL): tracking the PRN code delay,
- Frequency lock loop (FLL): tracking the Doppler frequency and the Doppler frequency drift,
- Phase lock loop (PLL): tracking the carrier phase and the Doppler frequency.

Each lock loop consists of four components: 1) discriminator function; 2) loop filter; 3) numerically controlled oscillator (NCO); 4) code generator. Accordingly, the parameter estimation can be carried out through the following steps,

(1) Tracking errors associated with signal parameters can be extracted by the corresponding discriminators using the integration outputs of the I and Q components,

(2) The estimation of the different signal parameters is updated using the extracted tracking errors inside the loop filter,

(3) The filter outputs are used to control the frequency of the NCOs which generate the code and carrier replica.

Some common code delay and carrier phase discriminators are recalled in Tables 2.1 and 2.2, respectively [2]. Theoretically, the received GNSS signal is considered to be tracked by the receiver when the discriminator outputs (tracking error) are zero, i.e., when the local replica PRN code generated in the receiver is aligned in time with the PRN code of the received signal and the carrier replica signal is in phase with the received carrier signal, or at least at the same frequency. However, the noises in the received signal lead to tracking random errors. As a consequence, errors in the PRN code delay result in PR measurement random errors, and errors on the carrier phase affect the accuracy of DR and ADR measurements.

2.1.3 Navigation Processor Block

When the carrier phase loop is locked, the navigation data message is demodulated in order to obtain the satellite Keplerian orbit information such as the satellite position and velocity in the earth-

Table 2.1 – Code delay discriminator function.

Type	Discriminator function	Characteristics
Non-coherent	$\sqrt{(I_E^2+Q_E^2)}-\sqrt{(I_L^2+Q_L^2)}$	Early minus late envelope Normalizing factor: $\sqrt{(I_E^2+Q_E^2)}+\sqrt{(I_L^2+Q_L^2)}$
	$(I_E^2+Q_E^2)-(I_L^2+Q_L^2)$	Early minus late power Normalizing factor: $(I_E^2+Q_E^2)+(I_L^2+Q_L^2)$
	$(I_E-I_L)I_P+(Q_E-Q_L)Q_P$	Dot product power Normalizing factor: I_P^2 and I_Q^2
Coherent	$\text{sign}(I_P)(I_E-I_L)$	Dot product Normalizing factor: I_P^2

Table 2.2 – Carrier phase discriminator function.

Discriminator function	Output	Characteristics
$\frac{Q_p}{I_p}$	$\tan(\varphi)$	Independence of signal amplitude for function slope Divide by zero error at ±90°
$\arctan\left(\frac{Q_p}{I_p}\right)$	φ	Independence of signal amplitude for function slope Usually table lookup implementation

centred earth-fixed (ECEF) frame, and the parameters used to describe different GNSS system errors such as the system time error and the ionospheric delay error. Then three different GNSS measurements, including PR, DR and ADR measurements, are calculated by using estimation methods applied to the received signal resulting from the tracking loop and the navigation data message [5,6]. Finally, the navigation processor solves the user position, velocity and time (PVT) from these GNSS measurements.

2.2 Impact of MP Interferences on the GNSS Receiver

Generally, multipath (MP) interferences can be divided into two classes [2, 31, 32]:

- line-of-sight (LOS) MP interferences: the sum of the direct signal (LOS signal) and delayed reflected signals (MP signals) are processed within the GNSS receiver. In this case, the MP interferences which arrive in the receiver antenna are assumed to be at a frequency that is different from the frequency of the LOS signal.

- non-line-of-sight (NLOS) MP interferences: a unique reflected signal is received and tracked within the GNSS receiver due to the fact that the direct signal is masked and blocked by the obstructions, or is so attenuated by foliage that its power is even lower than the power of

reflected MP signals. In addition, this case can also reflect what is happening when the LOS signal and MP signal arrive in the receiver antenna at the same frequency.

In order to analyse the impact of MP interferences on the performance of the GNSS receiver, the received GNSS signal that consists of the LOS and MP signals in a noise-free situation is considered in this section. In this case, the MP signals are always delayed and have lower amplitudes with respect to the LOS signal due to the fact that the propagation path of the reflected signal is always longer than that of the LOS signal [33,34]. In general, the impact of MP signals on the LOS signal depends on the amplitude, the PRN code delay time, the carrier phase and Doppler frequency relative to those of the LOS signal.

2.2.1 MP Signal Model

In the presence of LOS MP interferences, the received GNSS signal in the receiver consists of a LOS signal and MP signals. In a pilot channel, the LOS and MP signals in a noise-free situation, sampled at time instants nT_s where $n = 1, \ldots, \infty$, can be defined as [2,35]

$$r(nT_s) = \sum_{m=0}^{M} a_m \, c(nT_s - \tau_0 - \delta\tau_m) \cos\left(2\pi(f_{\mathrm{IF}} + f_m^d)nT_s + \varphi_0 + \delta\varphi_m\right) \tag{2.9}$$

where M is the number of MP signals, $a_m = \sqrt{P_m}$ and f_m^d are the mean power and carrier Doppler frequency associated with the mth signal path respectively, τ_0 and φ_0 are the PRN code delay time and the carrier phase of the LOS signal, $\delta\tau_m$ and $\delta\varphi_m$ are the delay time and the carrier phase of the mth MP signal relative to the LOS signal. Thus the absolute delay time and the carrier phase of the mth MP signal are denoted as $\tau_m = \tau_0 + \delta\tau_m$ and $\varphi_m = \varphi_0 + \delta\varphi_m$.

Due to the signal reflection, the MP signal arrives at the receiver later than the LOS signal and have some power attenuation leading to an MP signal magnitude lower than that of the LOS signal. Therefore, we have $\tau_0 > \tau_m$, $a_0 > a_m$, and $\alpha_m = \frac{a_m}{a_0} < 1$, where $m = 1, \ldots, M$ and α_m represents the multipath-to-direct ratio (MDR) [36]. In addition, the MP signal can be classified in two categories depending on the value of its carrier phase. When the relative carrier phase is $-90° \leq \delta\varphi_m \leq 90°$, the MP signal is referred to as a constructive interference such that the LOS signal is strengthened by the MP signals; on a contrary, the MP signal is a destructive interference when the relative carrier phase satisfies the condition $-180° \leq \delta\varphi_m \leq -90°$ or $90° \leq \delta\varphi_m \leq 180°$. At this time, the LOS signal is weakened by the MP signals. Tracking errors due to MP interferences are maximized when the relative carrier phase is 0° (in-phase with the LOS signal) and 180° (out-of-phase with the LOS signal) [2,37].

2.2.2 Effect of MP Interferences on the Receiver Performance

According to (2.7) and (2.8), the in-phase and quadrature integration outputs combining LOS and MP signals, sampled at time instants $k = 1, \ldots, \infty$, can be defined as [1] [9, 38]

$$\begin{aligned}
I_{E,k} &= \sum_{m=0}^{M} a_m\, R\left(\Delta\tilde{\tau}_{0,k} - \delta\tau_{m,k} + \frac{d}{2}T_c\right) \operatorname{sinc}\left(\pi\Delta\tilde{f}^d_{m,k}T_a\right) \cos(\Delta\tilde{\varphi}_{0,k} + \delta\varphi_{m,k}) \\
I_{P,k} &= \sum_{m=0}^{M} a_m\, R\left(\Delta\tilde{\tau}_{0,k} - \delta\tau_{m,k}\right) \operatorname{sinc}\left(\pi\Delta\tilde{f}^d_{m,k}T_a\right) \cos(\Delta\tilde{\varphi}_{0,k} + \delta\varphi_{m,k}) \\
I_{L,k} &= \sum_{m=0}^{M} a_m\, R\left(\Delta\tilde{\tau}_{0,k} - \delta\tau_{m,k} - \frac{d}{2}T_c\right) \operatorname{sinc}\left(\pi\Delta\tilde{f}^d_{m,k}T_a\right) \cos(\Delta\tilde{\varphi}_{0,k} + \delta\varphi_{m,k})
\end{aligned} \tag{2.10}$$

and

$$\begin{aligned}
Q_{E,k} &= \sum_{m=0}^{M} a_m\, R\left(\Delta\tilde{\tau}_{0,k} - \delta\tau_{m,k} + \frac{d}{2}T_c\right) \operatorname{sinc}\left(\pi\Delta\tilde{f}^d_{m,k}T_a\right) \sin(\Delta\tilde{\varphi}_{0,k} + \delta\varphi_{m,k}) \\
Q_{P,k} &= \sum_{m=0}^{M} a_m\, R\left(\Delta\tilde{\tau}_{0,k} - \delta\tau_{m,k}\right) \operatorname{sinc}\left(\pi\Delta\tilde{f}^d_{m,k}T_a\right) \sin(\Delta\tilde{\varphi}_{0,k} + \delta\varphi_{m,k}) \\
Q_{L,k} &= \sum_{m=0}^{m} a_m\, R\left(\Delta\tilde{\tau}_{0,k} - \delta\tau_{m,k} - \frac{d}{2}T_c\right) \operatorname{sinc}\left(\pi\Delta\tilde{f}^d_{m,k}T_a\right) \sin(\Delta\tilde{\varphi}_{0,k} + \delta\varphi_{m,k})
\end{aligned} \tag{2.11}$$

where $\operatorname{sinc}(\cdot)$ is the cardinal sine function, $\Delta\tilde{\tau}_{0,k}$ and $\Delta\tilde{\varphi}_{0,k}$ are the differences between the code delay, the carrier phase of the received LOS signal and the same parameters of the local replica signal which is generated in the receiver, $\Delta\tilde{f}_{m,k}$ is the difference between the carrier Doppler frequency of the mth signal path and that of the local replica signal. Here the subscript $m = 0$ denotes the LOS signal, and $\delta\tau_{0,k} = 0$ and $\delta\varphi_{0,k} = 0$.

In order to analyze the impact of MP interferences on receiver performance, the following assumptions have been made

Hypothesis 1 the received signal in the receiver is composed of a LOS signal and an NLOS MP signal, i.e., $f^d_0 = f^d_m$ and $M = 1$.

Hypothesis 2 the local generated signal replica in the receiver is aligned with the LOS signal, i.e., the code delay, carrier phase and Doppler frequency of the local generated signal replica are identical to those of the received LOS signal.

Figure 2.3 displays the composite correlation function defined as the correlation functions due to the LOS and MP signals. It is clear that the correlation function is distorted by the relative delay time $\delta\tau_1$. The prompt correlator sample is shifted to the right due to the constructive MP signal and the

[1] In practice, $\pi\Delta\tilde{f}^d_{m,k}T_s \ll 1$, thus $\dfrac{\sin(\pi\Delta\tilde{f}^d_{m,k}T_a)}{\sin(\pi\Delta\tilde{f}^d_{m,k}T_s)} \approx \dfrac{\sin(\pi\Delta\tilde{f}^d_{m,k}T_a)}{\pi\Delta\tilde{f}^d_{m,k}T_a}\dfrac{T_a}{T_s}$.

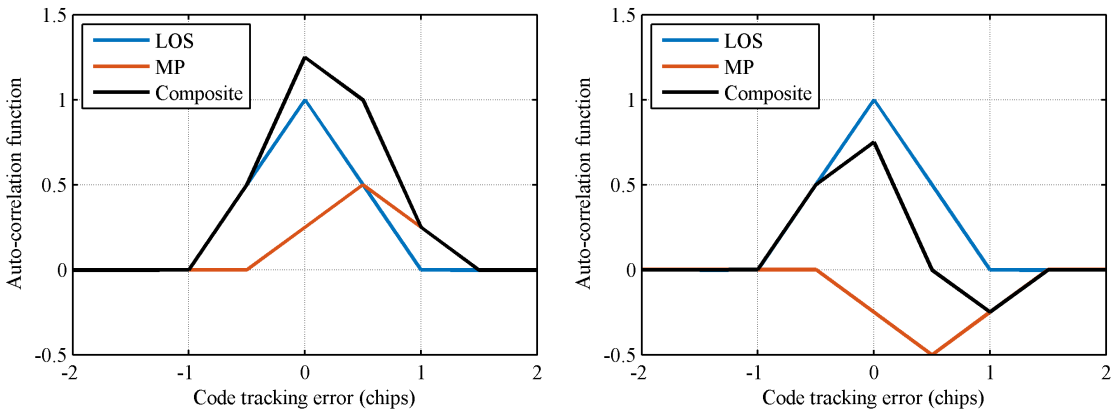

(a) Constructive MP interference **(b)** Destructive MP interference

Figure 2.3 – LOS, MP and composite signal correlation functions for $\alpha_m = \frac{1}{2}$, $\delta\tau_1 = 0.5$ chip and $\delta\varphi_1 = 0°$ and 180° (neglecting pre-correlation band-limiting).

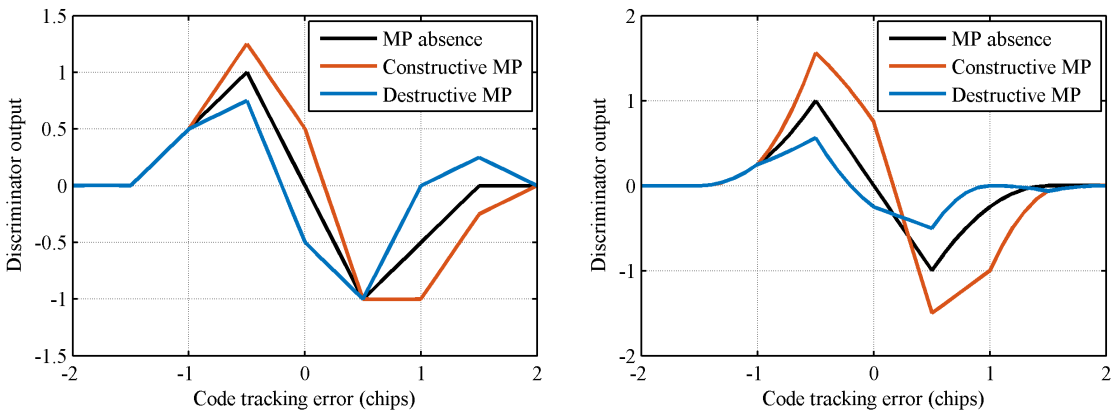

(a) Coherent E-L discriminator **(b)** Non-coherent ELP discriminator

Figure 2.4 – Discriminator output in absence/presence of MP interferences ($\alpha_m = \frac{1}{2}$, $\delta\tau_1 = 0.5$ chip and $\delta\varphi_1 = 0°$ and 180°).

corresponding measured PR is longer than the actual one; similarly, the prompt correlator sample is shifted to the left due to the destructive MP signal and the corresponding measured PR is shorter than the actual one. Thus the relative delay time $\delta\tau$ determines how much the MP interference affects the LOS signal. If the relative delay time satisfies $\delta\tau \geq (1 + d/2)\,T_c$, the MP signals will not impact the late correlator sample of the LOS signal at this time. As a consequence, no bias appears on the corresponding PR measurement. Therefore, a short chip duration T_c for the PRN code on GNSS signal or a narrow correlator spacing d in the GNSS receiver can effectively reduce the impact of the MP interferences.

Figure 2.4 displays the output functions of the coherent early minus late (E-L) and non-coherent early minus late power (ELP) discriminators in the absence and presence of the MP signal. It is clear

that the discriminator function passes through zero in the absence of MP interference. However, in the presence of MP interferences, the discriminator function is distorted and has a zero-crossing at a non-zero value of the code tracking error leading to a local generated PRN code ahead (constructive interference) to or behind (destructive interference) the received LOS signal. Accordingly, the tracking error generates a PR error in the GNSS measurement. The PR error envelope for different correlator spacings d versus the relative delay time of the MP signal is shown in Figure 2.5. The upper envelope corresponds to errors resulting from constructive interferences ($\delta\varphi_1 = 0$), whereas the lower one to errors from destructive interferences ($\delta\varphi_1 = \pi$). It is clear that the PR error envelope with a narrower correlator spacing is smaller than that obtained with a larger spacing. In addition, the PR error converges to zero when the relative delay time $\delta\tau$ is increasing and becomes zero when $\delta\tau \geq (1 + d/2)\, T_c$.

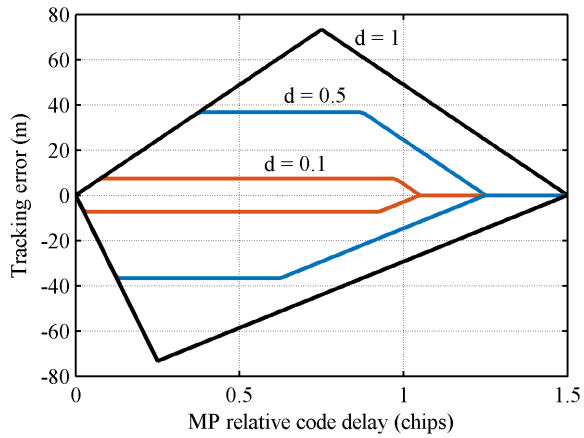

Figure 2.5 – Error envelope of tracking error due to MP relative code delay for $\alpha_m = \frac{1}{2}$, $\delta\tau_1 = 0.5$ chip and $\delta\varphi_1 = 0°$ and 180° (neglecting pre-correlation band-limiting).

2.3 State-of-the-art MP Mitigation Approaches in the Receiver

In some applications, the MP interference is one of the largest sources of GNSS errors. According to the analysis made in Section 2.2, the MP interferences result in tracking errors due to the fact that the correlation and discriminator functions are distorted. Moreover, the tracking errors lead to biases appearing on the GNSS measurements. In recent years, different kinds of signal processing approaches can be found in the literature for mitigating MP interference in the GNSS receiver. These approaches can be mainly divided into two classes: 1) tracking loop-based techniques which aim at mitigating the effects of MP interferences on correlation and discriminator functions inside the tracking loop stage; 2) GNSS measurement processing which consists of detecting and correcting the GNSS measurement errors resulting from the MP interferences. Some state-of-the-art related to these two MP mitigation approaches are proposed in the rest of this section.

2.3.1 Tracking Loop-Based Techniques

Tracking loop-based techniques attempt to mitigate MP interferences by using signal processing approaches inside the lock loop. Existing approaches are based on non-parametric and parametric processing. Non-parametric-based processing uses correlator or discriminator designs that are less sensitive to MP-induced errors, while parametric-based processing attempts to model and estimate the unknown parameters associated with LOS and MP signals by using statistical signal processing theory.

1. Non-parametric processing Non-parametric techniques attempt to design discriminator functions which consist of a narrow-correlator or a bank of correlators with different spacings in order to reduce the sensitivity of the discriminator to MP interferences [39]. Until now, some techniques have been developed and implemented in different brands of receivers [35]. The first approach to mitigate MP interference was a narrow correlation technique [40] which has been implemented into GPS receivers by NovAtel Inc.. This approach proposed to use a narrow correlator spacing, such as $d = 0.1$, instead of a standard correlator ($d = 1$). The early-late slope technique [33], also known as MP elimination technology (MET), determines a PR correction by analysing the horizontal distance from the intersection point between the slopes of both sides of the auto-correlation function to zero. The "Double Delta Correlator" is a general concept leading to define a kind of discriminator which is formed by computing two pairs of early and late correlations with different early-late spacings. The concept was first proposed for the strobe & edge correlator [41] which has been implemented in Ashtech's receiver, and then similar correlators with the same concept were proposed in high resolution correlator (HRC) [42, 43] and pulse aperture correlator (PAC) [44]. Since the auto-correlation function is distorted by MP interference, the early 1 - early 2 tracking concept [45], in which two correlators are located on the early slope of the auto-correlation function, was proposed to determine a point on the auto-correlation function which is not distorted by MP interference. Similarly, an MP insensitive delay lock loop [46, 47] was implemented by determining an invariant point in the standard discriminator output in the absence/presence of MP interferences and then tracking this stable point.

The advantage of the non-parametric processing techniques is that they are easily implemented and independent of the number of MP. However, their benefits are off-set to some degree by worse performance compared with those of a conventional discriminator, due to the fact that a narrow correlator can easily lead to a loss of lock of the code in the case of a low signal-to-noise ratio situation [37].

2. Parametric processing As mentioned above, the received GNSS signal in the receiver is composed of a LOS signal and MP signals in the presence of MP interferences. Accordingly, a model

of the received signal observation including the unknown parameters of LOS and MP signals can be represented as a measurement equation. Thus the parametric-based approaches consist of determining the unknown signal parameters by using estimation methods. Basically, the signal parameter estimation techniques can be divided into static and dynamic classes, which depend on whether a prior information about the unknown signal parameters is taken into account or not.

Static estimation Several MP mitigation methods proposed in recent years are based on the maximum likelihood estimation (MLE) principle. The basic idea behind the MLE is to determine the parameters that maximize a likelihood function of the unknown signal parameters given the measurements [48]. This estimation method does not require a priori information and assumes that the unknown signal parameters are constant over an observation period. An MP estimating DLL (MEDLL) [34,49] was the first widely known and practical MP mitigation approach based on the MLE principle. The partial derivatives of the likelihood function with respect to the unknown signal parameters setting to zero leads to a set of non-linear equations (cross-correlation function) whose solution is difficult to be obtained. Thus the MEDLL proposed to use a bank of correlator outputs with certain code delay and carrier phase to approximate the overall cross-correlation functions. A large computation load resulting from a bank of correlators impacts the real-time application of MEDLL [50]. Moreover, the MLE principle contained in the MEDLL has inspired many related MP mitigation algorithms, the MP mitigation technology (MMT) [51] and the vision correlator (VC) [52] being the most famous. In order to increase the MLE computational efficiency, the MMT assumes that only one MP exists in the received signal and performs a non-linear transformation on the six signal parameters to obtain four new parameters. As a consequence, the final maximization of the likelihood function requires a search in only two dimensions. Moreover, the MMT was used as the fundamental MP mitigation approach in the vision correlator. Further hardware improvements and optimizations were developed at a manufacturer in the course of commercializing the vision correlator.

In order to obtain more robust and efficient MLE-based MP mitigation approaches, such as the Newton iteration method [53], the grid search approach, the data compression [54–56] or interpolation [57] method, have been implemented in the literature. A fast iterative maximum-likelihood algorithm (FIMLA) [58] computes the gradient and Hessian matrices by using the Newton iteration method. In order to overcome the convergence problem that exists in the iterative algorithms, a closed-form solution based on a grid search approach was proposed in [59] to maximize the log-likelihood function by restricting the estimation of the code delay to a set of discrete values defined by a bank of correlators with different spacings. The data interpolation [60] was introduced to restrict the number of correlators so as to decrease the computational complexity.

In addition, other approaches were proposed to simplify or approximate MLE-based MP mitigation approaches, such as the non-linear least-squares algorithm [61] or the

expectation-maximization algorithm [62]. An MP mitigation approach based on the Levenberg-Marquardt algorithm was implemented using an iterative best-fit solution to estimate the received signal parameters. A space-alternating generalized expectation-maximization algorithm was also proposed in [63] to approximate the MLE by simplifying the global optimization problem into a number of decoupled local optimization problems. In this case, the estimation of signal parameters is divided into several one-dimensional optimization problems which can be easily solved by the gradient computation and interpolation.

Finally, it is interesting to note that the MLE-based approaches are based on assumption that the signal parameters are not time varying over the time period. Thus parameter estimations associated with adjacent observation period are independent and do not exploit any dynamic information for the signal parameters. Methods accounting for the dynamic information are presented in the next section.

Dynamic estimation Some approaches assume that the time propagation associated with the unknown parameters of LOS and MP signals can be modelled by a first-order Markov model, which provides the time-dependent prior probability density distribution for the unknown parameters [64–66]. The objective is then to estimate recursively the posterior probability density function of the unknown parameters given all observations. Estimating the unknown parameters of LOS and MP signals can be formulated as a sequential Bayesian estimation problem.

Considering that the GNSS observation are related to the unknown parameters by highly non-linear equations, the particle filter (PF) has been proposed to estimate the parameters [67, 68]. In order to reduce the dimensionality of this non-linear estimation, a Rao-blackwellized method was used to marginalize the linear and non-linear parts of the unknown signal parameters, and to implement in parallel a standard Kalman filter and a particle filter for processing the two parts [38]. Moreover, an importance density based on a Laplace approximation, which is used to propagate samples of the non-linear unknown parameters, was proposed to improve the efficiency of the PF approach [69]. The data compression method based on the MLE was also used to decrease the dimension of observation so as to reduce the complexity of the MP mitigation technique [70, 71]. In above MP mitigation approaches, the number of reflected signal path is assumed to be known and the determination of this number was not addressed. A two-fold marginalized Bayesian filter was proposed in [72] to estimate the number of reflected path and the corresponding signal parameters.

Although many approaches have been addressed to improve the efficiency of Bayesian estimation, a high computational load hinders the real-time application of PF-based MP mitigation approaches. In addition, the presence or absence of MP signals not only depends on the relative position of the receiver and GNSS satellites, but also on the environment where the receiver is located. Thus it is difficult to use a specific propagation model for the MP signal parameters when the receiver is moving.

2.3.2 GNSS Measurement Processing

The tracking errors resulting from MP interferences lead to errors appearing on the GNSS PR measurements. In addition, when the LOS signal is masked and blocked by the obstructions, or is so attenuated by the foliage that its power is even lower than the powers of reflected MP signals, the MP interferences can be hardly mitigated by the strategies based on tracking loops. Thus GNSS measurement processing techniques, which aims at detecting and mitigating the PR measurement errors by using statistical methods when the prior statistical information about the MP errors are available, are of high interest [73]. In these methods, a prior distribution for an MP error appearing on the PR measurement can be defined and compared with the actual error obtained from the PR measurements within an observation window. Different kinds of MP error mitigation approaches with different priors can be found in the literature. Some of them are recalled below.

One assumption is that the MP error can be considered as a constant bias appearing on the PR measurement within a certain observation window. Thus the bias detection and estimation approaches based on hypothesis tests including the generalized likelihood ratio test or the marginalized likelihood ratio test, were implemented. Other aided methods including a fix-lag Rao-blackwellized particle filter or multiple models have been exploited in order to improve the detection performance [74, 75]. In addition, for detecting the MP error in different scenarios, different models [76] are used to describe the MP error depending on the availability of LOS signals. The MP error appearing on the PR measurement can be assumed to be described by a kind of stationary error model, i.e., the MP errors follow a fixed deterministic distribution within a certain observation window. Random models [77, 78] or non-parametric approaches [79, 80] modelling the MP errors have been proposed in order to more accurately describe the statistical property of the MP error appearing on the PR measurement, especially in the very constricted environment (like an urban or city canyon).

Measurement processing techniques attempt to mitigate the MP interferences by processing the GNSS measurements. One potential advantage is that the influence of these techniques on the receiver internal architecture is less than that of the tracking loop-based techniques. However, the performance of the measurement processing techniques mainly depends on the number of available GNSS PR measurements and the corresponding random noise intensity. Thus these factors restrict the application scope of these approaches.

2.4 Discussion

In this chapter, the principles of the GNSS receiver, the impact of MP interferences on the receiver and the state-of-the-art MP mitigation approaches inside GNSS receiver have been reviewed. Regarding MP mitigation techniques, the topics approached in this subject can be summarized in a

very minimal and simplified way as follows (for more details refer to all previous sections):

Non-parametric processing inside the tracking loop stage is easily implemented and independent of the number of MP. Moreover, the performance resulting from these techniques can be worse than conventional tracking loops in low signal-to-noise ratio (SNR) situations.

Static parametric processing inside the tracking loop stage can be implemented to compute the MLE of the unknown parameters. Moreover, the dynamic information of signal parameters is not taken into account and the signal parameters are assumed to be time-invariant over each time period.

Dynamic parametric processing inside the tracking loop stage considers a prior information for the unknown parameters of LOS and MP signals. Moreover, using a propagation model hardly reflects the dynamics of MP parameters in a constricted environment and a high computational load of PF-based approaches makes the real-time application more difficult.

Measurement Processing has a minor influence on the receiver internal architecture. Moreover, its performance depends on the number of available GNSS PR measurements and the corresponding random noise intensity.

Based on the above analysis of MP mitigation approaches which can be implemented inside a GNSS receiver, the number of interesting aspects which could have been targeted during this doctoral research on MP mitigation is considerably large. Thus the selection of research subjects in this thesis were object of careful consideration throughout the research period. Finally, the research directions that were defined as relevant for MP mitigation in the GNSS receivers, both from a scientific and practical engineering standpoint (and that are analyzed in detail in the remainder of this thesis) are:

- A maximum likelihood-based unscented Kalman filter (UKF) for estimating the LOS signal parameters in the presence of MP interferences - Chapter 3.
- A marginalized likelihood ratio-based method for NLOS MP bias detection and estimation - Chapter 4.
- A GNSS measurement processing aided with other sensor data for improving MP interference detection and providing reliable positioning in MP environments - Chapter 5.

These choices were motivated by the relevance of these topics and by the opportunities for meaningful contributions during the limited doctoral research period.

CHAPTER

THREE

A MAXIMUM LIKELIHOOD-BASED UKF FOR MULTIPATH MITIGATION IN A MULTI-CORRELATOR BASED GNSS RECEIVER

In multipath (MP) environments, the correlator outputs are distorted as the LOS signal entering the receiver is combined with MP signals. This results in tracking errors which introduce biases in pseudo-range, carrier phase and Doppler frequency measurements. Thus MP mitigation techniques inside the GNSS receiver can be formulated as a problem of signal parameter estimation. The main issue of this chapter is to reduce the impact of MP signals for obtaining an accurate LOS parameter estimator.

Since the presence and absence of MP signals depend on several factors related to the vehicle environment and motion, it is difficult to use a specific propagation model for the MP signal parameters when the receiver is moving. Thus this chapter proposes to use two kinds of models for describing the LOS and MP signal parameters: a dynamic model associated with the time propagation of LOS signal parameters and a likelihood model associated with the MP signal parameters. Moreover, a multi-correlator based receiver is exploited with the advantage to fully characterize the impact of MP signals on the correlation function by providing samples of the whole correlation function. A maximum likelihood-based unscented Kalman filter is then investigated to estimate the LOS signal parameters and MP signal parameters iteratively. The posterior Cramér-Rao bound of the LOS signal parameter estimation in the absence of MP interferences is derived and used as the reference for evaluating the performance of the proposed estimation approach. Finally, several numerical simulations in different scenarios are implemented to validate the effectiveness of the proposed approach.

3.1 Introduction

In the presence of MP interferences, the received signal consisting of a line-of-sight (LOS) signal and of MP signals is processed in the GNSS receiver. As a consequence, the correlation function of the LOS signal is distorted by the MP signals, and this distortion results in tracking errors which introduce biases in pseudo-range (PR), carrier phase and Doppler frequency measurements as mentioned in Section 2.2. In this context, the MP mitigation technique inside the GNSS receiver can be formulated as a statistical estimation problem so as to reduce the impact of the correlator output distortion resulting from the presence of MP signals. Bayesian-based methods, such as Kalman filter [38,64] or Particle filter [69,72] approaches that require to define a state-space model, are usually exploited to solve this estimation problem.

In practice, the presence or absence of MP signals not only depends on the relative position between the receiver and GNSS satellites, but also on the environment where the receiver is located, especially in an urban canyon. Thus it is difficult to use a specific MP parameter propagation model to accurately capture the dynamics of MP parameters when the receiver is moving. In this chapter, we propose to use two kinds of models for describing the LOS and MP signal parameters: a dynamic model associated with the time propagation of LOS signal parameters (since this propagation is related to the vehicle motion), and a likelihood model associated with the MP signal parameters. In order to fully characterize the impact of MP interferences on the correlation function, a multi-correlator based receiver, which allows a complete sampling of the whole useful part of the correlation function, is considered. A maximum likelihood-based unscented Kalman filter (UKF) is investigated to estimate the LOS and MP signal parameters iteratively. More precisely, an interval grid search based on the maximum likelihood principle is implemented to estimate the MP signal parameters by using the prior information about LOS signal, and then an UKF is implemented to estimate the LOS signal parameters based on the maximum likelihood estimation (MLE) of the MP signal parameters. The posterior Cramér-Rao bound of the LOS signal parameter estimation in the absence of MP interferences is derived and used as the reference for evaluating the performance of the proposed estimation approach. Finally, several numerical simulations associated with different scenarios are implemented to validate the effectiveness of the proposed approach.

3.2 GNSS Signal Model in the Presence of MP Interferences

3.2.1 Measurement Model for Multi-correlator Based Receiver

In a pilot channel, the received complex baseband signal associated with the given GNSS satellite affected by M MP signals can be written as follows [1, 69]

$$r(t) = \sum_{m=0}^{M} a_m \, c(t-\tau_m) \exp\left(j\varphi_m\right) + \omega(t) \tag{3.1}$$

with

$$\frac{\mathrm{d}\varphi_m}{\mathrm{d}t} = 2\pi f_m^d$$

where $m = 0, \ldots, M$ and M is the number of signal paths. Here the subscript $m = 0$ denotes the LOS signal, $a_m = \sqrt{P_m}$ is the signal amplitude associated with the mth signal path and P_m is the corresponding mean power of the mth signal path, $c(t)$ is the pseudo-random noise (PRN) code associated with the given GNSS signal, τ_m, φ_m and f_m^d are the code delay, carrier phase and Doppler frequency associated with the mth signal path and $\omega(t)$ is an additive white Gaussian noise affecting the GNSS signal. We denote as $f_s = 1/T_s$ the sampling frequency of the digitizer which provides samples of the front-end output in a GNSS receiver. The received complex baseband signal, sampled at time instants nT_s where $n = 1, \ldots, \infty$, is defined as

$$r(nT_s) = \sum_{m=0}^{M} a_m \, c(nT_s-\tau_m) \exp\left(j\varphi_m\right) + \omega(nT_s) \tag{3.2}$$

where $\omega(nT_s)$ is a zero mean additive Gaussian white noise with a variance $N_0 f_s$ where N_0 is the noise power spectral density (PSD).

In general, a typical GNSS receiver consists of baseband signal processing channels, each of them being driven by two pairs of correlator outputs. In this work, a multi-correlator based receiver is considered. For each channel in this kind of receiver, correlation outputs of the received signal with a bank of local generated signal replicas are exploited for estimating the GNSS signal parameters. The architecture of such a receiver is illustrated in Figure 3.1 (also available in [38]). Firstly, the received signal associated with the given satellite is decomposed into its in-phase (I) and quadrature (Q) components after being multiplied by the in-phase and quadrature local generated carrier. Then each component is correlated with $2J+1$ replicas of the PRN code for obtaining a multi-correlator structure. Thus the jth in-phase and quadrature integration outputs $I_{\theta_j,k}$ and

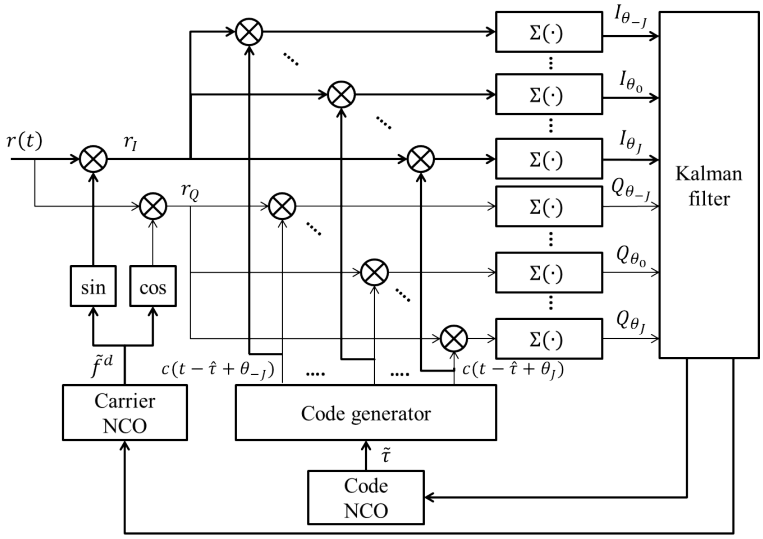

Figure 3.1 – GNSS baseband signal processing channel with a multi-correlator.

$Q_{\theta_j,k}$ resulting from an integration over an interval T_a can be defined as

$$\begin{aligned} I_{\theta_j,k} &= \sum_{m=0}^{M} a_{m,k}\, R\left(\Delta\tilde{\tau}_{m,k}+\theta_j\right) \operatorname{sinc}\left(\pi\Delta\tilde{f}^d_{m,k}T_a\right) \cos(\Delta\tilde{\varphi}_{m,k}) + n_{I_{\theta_j},k} \\ Q_{\theta_j,k} &= \sum_{m=0}^{M} a_{m,k}\, R\left(\Delta\tilde{\tau}_{m,k}+\theta_j\right) \operatorname{sinc}\left(\pi\Delta\tilde{f}^d_{m,k}T_a\right) \sin(\Delta\tilde{\varphi}_{m,k}) + n_{Q_{\theta_j},k} \end{aligned} \tag{3.3}$$

with

$$R\left(\Delta\tilde{\tau}_{m,k}\right) \approx \begin{cases} 1-\left|\Delta\tilde{\tau}_{m,k}\right| & \left|\Delta\tilde{\tau}_{m,k}\right| < 1 \\ 0 & \left|\Delta\tilde{\tau}_{m,k}\right| \geq 1 \end{cases}$$

and

$$\begin{aligned} \Delta\tilde{\tau}_{m,k} &= \tau_{m,k} - \tilde{\tau}_k \\ \Delta\tilde{\varphi}_{m,k} &= \varphi_{m,k} - \tilde{\varphi}_k \\ \Delta\tilde{f}^d_{m,k} &= f^d_{m,k} - \tilde{f}^d_k \end{aligned}$$

where $T_a = N_s T_s$ and N_s is the number of GNSS signal samples in an integration interval T_a, $\operatorname{sinc}(\cdot)$ is the cardinal sine function, $\theta_j = j\Delta\theta$ is the jth correlator delay expressed in chips where $\Delta\theta = \theta_{j+1} - \theta_j > 0$ $(j = -J, \ldots, 0, \ldots, J)$ is a correlation spacing between adjacent correlators. Note that $\theta_0 = 0$, $\theta_{j<0}$ and $\theta_{j>0}$ correspond to the prompt, early and late correlation, respectively. $R(\cdot)$ is the auto-correlation function of the PRN code obtained after neglecting pre-correlation band-limiting effect, $\Delta\tilde{\tau}_{m,k}$, $\Delta\tilde{\varphi}_{m,k}$ and $\Delta\tilde{f}^d_{m,k}$ denote differences between the code delay, carrier phase and Doppler frequency of the mth signal path $(\tau_{m,k},\ \varphi_{m,k},\ f^d_{m,k})$ and those of local generated replicas $(\tilde{\tau}_k,\ \tilde{\varphi}_k,\ \tilde{f}^d_k)$. Note that the units of the code delay, carrier phase and Doppler frequency in this

work are chips, cycle and hertz (Hz), and that $n_{I_{\theta_j},k}$ and $n_{Q_{\theta_j},k}$ are both zero mean Gaussian white noises with PSD N_0 associated with the jth in-phase and quadrature correlation function samples. Accordingly, the measurement equation at time k can be defined as

$$\boldsymbol{z}_k = \mathbf{h}(\boldsymbol{x}_k) + \boldsymbol{n}_k \tag{3.4}$$

with

$$\begin{aligned}
\boldsymbol{z}_k &= \left(I_{\theta_{-J},k},\ \ldots,\ I_{\theta_0,k},\ \ldots\ I_{\theta_J,k},\ Q_{\theta_{-J},k},\ldots,\ Q_{\theta_0,k},\ \ldots,\ Q_{\theta_J,k}\right)^{\mathrm{T}} \\
\boldsymbol{x}_k &= \left(\boldsymbol{x}_{0,k},\ \ldots,\ \boldsymbol{x}_{M,k}\right)^{\mathrm{T}} \\
\boldsymbol{n}_k &= \left(n_{I_{\theta_{-J}},k},\ \ldots,\ n_{I_{\theta_0},k},\ \ldots\ n_{I_{\theta_J},k},\ n_{Q_{\theta_{-J}},k},\ \ldots,\ n_{Q_{\theta_0},k},\ \ldots\ n_{Q_{\theta_J},k}\right)^{\mathrm{T}}
\end{aligned}$$

and

$$\begin{aligned}
\boldsymbol{x}_{0,k} &= \left(a_{0,k},\ \tau_{0,k},\ \varphi_{0,k},\ f^d_{0,k},\ \xi^d_{0,k}\right)^{\mathrm{T}} \\
\boldsymbol{x}_{m,k} &= \left(a_{m,k},\ \tau_{m,k},\ \varphi_{m,k},\ f^d_{m,k}\right)^{\mathrm{T}}
\end{aligned}$$

where $m = 1,\ldots,M$ and $k = 1,\ldots,K$ denotes the kth time instant of the correlator integration output, $\mathbf{h}(\cdot)$ contains the in-phase and quadrature components resulting from (3.3) and thus is a non-linear function of the state vector $\boldsymbol{x}_k$ (which contains the LOS parameter vector $\boldsymbol{x}_{0,k}$ and the MP signal parameter vectors $(\boldsymbol{x}_{1,k},\ldots,\boldsymbol{x}_{M,k})$ at time k), and $\xi^d_{0,k}$ denotes a drift associated with the carrier Doppler frequency $f^d_{0,k}$. It is important to note that the noise terms $n_{I_{\theta_j},k}$ (or $n_{Q_{\theta_j},k}$) for $j = -J,\ \ldots,\ J$ of the in-phase (or quadrature phase) correlation function samples are correlated with the following covariance matrix

$$\boldsymbol{R}_k = \sigma^2 \begin{pmatrix} \boldsymbol{R}_I & \mathbf{0} \\ \mathbf{0} & \boldsymbol{R}_Q \end{pmatrix} \tag{3.5}$$

with

$$\boldsymbol{R}_I = \boldsymbol{R}_Q = \begin{pmatrix} \lambda_{(-J,-J)} & \lambda_{(-J,-J+1)} & \cdots & \lambda_{(-J,\,J)} \\ \lambda_{(-J+1,-J)} & \lambda_{(-J+1,-J+1)} & \cdots & \lambda_{(-J+1,\,J)} \\ \vdots & \cdots & \ddots & \vdots \\ \lambda_{(J,-J)} & \lambda_{(J,-J+1)} & \cdots & \lambda_{(J,\,J)} \end{pmatrix}_{(2J+1)\times(2J+1)}$$

where

$$\lambda_{(j,\,n)} = 1 - \left|\theta_j - \theta_n\right| = \begin{cases} 1 - \left|j-n\right|\Delta\theta & \left|j-n\right|\Delta\theta < 1 \\ 0 & \left|j-n\right| \geq 1 \end{cases}$$

and where $\sigma^2 = N_0/2T_a$ depends on the signal PSD and on the integration time T_a.

3.2.2 Propagation Model for LOS Parameters

When the GNSS signal has been locked inside the receiver, we can define a time propagation model for the LOS signal parameters. The parameter vector for describing the LOS signal is defined as [72, 81]

$$\boldsymbol{x}_{0,k} = \left(a_{0,k},\ \tau_{0,k},\ \varphi_{0,k},\ f^d_{0,k},\ \xi^d_{0,k}\right)^{\mathrm{T}} \tag{3.6}$$

where $a_{0,k}$, $\tau_{0,k}$ and $\varphi_{0,k}$ denote the amplitude, delay time of the PRN code, and carrier phase of the LOS signal, $f^d_{0,k}$ and $\xi^d_{0,k}$ denote the carrier Doppler frequency and its drift at time k, respectively. Assuming that the GNSS signal has been locked, the LOS signal amplitude a_0 can be reasonably modelled as a random walk, i.e., $\dot{a}_0 = \omega_a$ where ω_a is a zero mean Gaussian white noise of variance σ^2_a. In addition, a propagation model for τ_0 and φ_0 can be defined by using the Doppler frequency, i.e., $\dot{\tau}_0 = k_c f^d_0 + \omega_\tau$ and $k_c = f_{\mathrm{co}}/f_{\mathrm{ca}}$ is a scale factor converting the carrier Doppler frequency to the code Doppler frequency, where f_{co} and f_{ca} are the PRN code and the GNSS signal carrier frequencies. Similarly, $\dot{\varphi}_0 = f^d_0 + \omega_\varphi$ where ω_τ and ω_φ are zero mean Gaussian white noises of variances σ^2_τ and σ^2_φ. Moreover, f^d_0 and ξ^d_0 depend on the velocity and acceleration of the vehicle, i.e., $f^d_0 = -\left(f_{\mathrm{ca}}/c\right)v$ where c is the speed of light and v is the vehicle velocity. Thus the carrier Doppler frequency and its drift can be also modelled as random walks, i.e., $\dot{f}_0 = \xi_0 + \omega_f$ and $\dot{\xi}_0 = \omega_\xi$ where ω_f and ω_ξ are zero-mean Gaussian white noises of variance σ^2_f and σ^2_ξ. Based on the above assumptions, a discrete-time state model which describes the time propagation of LOS parameter vector $\boldsymbol{x}_{0,k}$ at time k can be formulated as

$$\boldsymbol{x}_{0,k} = \boldsymbol{F}_{k|k-1}\boldsymbol{x}_{0,k-1} + \boldsymbol{\Gamma}_{k-1}\boldsymbol{\omega}_{k-1} \tag{3.7}$$

where

$$\boldsymbol{\omega}_{k-1} = \left(\omega_{a,k-1},\ \omega_{\tau,k-1},\ \omega_{\varphi,k-1},\ \omega_{f,k-1},\ \omega_{\xi,k-1}\right)^{\mathrm{T}}$$

and where $k = 1, \ldots, K$ denotes the kth time instant, $\boldsymbol{\omega}_{k-1}$ is a zero mean Gaussian white noise vector of covariance matrix $\boldsymbol{q}_{k-1}$ where

$$\boldsymbol{q}_{k-1} = \begin{pmatrix} \sigma^2_a & 0 & 0 & 0 & 0 \\ 0 & \sigma^2_\tau & 0 & 0 & 0 \\ 0 & 0 & \sigma^2_\varphi & 0 & 0 \\ 0 & 0 & 0 & \sigma^2_f & 0 \\ 0 & 0 & 0 & 0 & \sigma^2_\xi \end{pmatrix}.$$

More precisely, the matrices $\boldsymbol{F}_{k|k-1}$ and $\boldsymbol{\Gamma}_{k-1}$ can be defined as follows

$$\boldsymbol{F}_{k|k-1} = \begin{pmatrix} 1 & 0 & 0 & 0 & 0 \\ 0 & 1 & 0 & k_c T_a & \frac{k_c T_a^2}{2} \\ 0 & 0 & 1 & T_a & \frac{T_a^2}{2} \\ 0 & 0 & 0 & 1 & T_a \\ 0 & 0 & 0 & 0 & 1 \end{pmatrix} \text{ and } \boldsymbol{\Gamma}_{k-1} = \begin{pmatrix} T_a & 0 & 0 & 0 & 0 \\ 0 & T_a & 0 & \frac{k_c T_a^2}{2} & \frac{k_c T_a^3}{6} \\ 0 & 0 & T_a & \frac{T_a^2}{2} & \frac{T_a^3}{6} \\ 0 & 0 & 0 & T_a & \frac{T_a^2}{2} \\ 0 & 0 & 0 & 0 & T_a \end{pmatrix}.$$

As a consequence, the process noise covariance matrix $\boldsymbol{Q}_{k-1}$ for the state equation (3.7) can be computed as follow

$$\begin{aligned} \boldsymbol{Q}_{k-1} &= \mathrm{E}\left[(\boldsymbol{\Gamma}_{k-1}\boldsymbol{\omega}_{k-1})(\boldsymbol{\Gamma}_{k-1}\boldsymbol{\omega}_{k-1})^{\mathrm{T}}\right] = \boldsymbol{\Gamma}_{k-1}\boldsymbol{q}_{k-1}\boldsymbol{\Gamma}_{k-1}^{\mathrm{T}} \\ &= \begin{pmatrix} \sigma_a^2 T_a^2 & 0 & 0 & 0 & 0 \\ 0 & \sigma_\tau^2 T_a^2 + \sigma_f^2 \frac{k_c^2 T_a^4}{4} + \sigma_\xi^2 \frac{k_c^2 T_a^6}{36} & \sigma_f^2 \frac{k_c T_a^4}{4} + \sigma_\xi^2 \frac{k_c T_a^6}{36} & \sigma_f^2 \frac{k_c T_a^3}{2} + \sigma_\xi^2 \frac{k_c T_a^5}{12} & \sigma_\xi^2 \frac{k_c T_a^4}{6} \\ 0 & \sigma_f^2 \frac{k_c T_a^4}{4} + \sigma_\xi^2 \frac{k_c T_a^6}{36} & \sigma_\varphi^2 T_a^2 + \sigma_f^2 \frac{T_a^4}{4} + \sigma_\xi^2 \frac{T_a^6}{36} & \sigma_f^2 \frac{T_a^3}{2} + \sigma_\xi^2 \frac{T_a^5}{12} & \sigma_\xi^2 \frac{T_a^4}{6} \\ 0 & \sigma_f^2 \frac{k_c T_a^3}{2} + \sigma_\xi^2 \frac{k_c T_a^5}{12} & \sigma_f^2 \frac{T_a^3}{2} + \sigma_\xi^2 \frac{T_a^5}{12} & \sigma_f^2 T_a^2 + \sigma_\xi^2 \frac{T_a^3}{4} & \sigma_\xi^2 \frac{T_a^3}{2} \\ 0 & \sigma_\xi^2 \frac{k_c T_a^4}{6} & \sigma_\xi^2 \frac{T_a^4}{6} & \sigma_\xi^2 \frac{T_a^3}{2} & \sigma_\xi^2 T_a^2 \end{pmatrix} \end{aligned}$$

where $\mathrm{E}[\cdot]$ denotes the expectation function.

3.2.3 Likelihood Model for MP Parameters

As mentioned above, the presence or absence of MP signals not only depends on the relative position between the receiver and GNSS satellites, but also on the environment where the receiver is located. Thus it is difficult to use a specific propagation model for the MP parameters when the receiver is moving. However, a likelihood function of the observation provided by the bank of correlators can be defined to construct an estimator of the unknown MP signal parameters. The parameter vector for describing the MP signals is defined as [66, 71]

$$\boldsymbol{x}_{m,k} = \left(a_{m,k},\ \tau_{m,k},\ \varphi_{m,k},\ f_{m,k}^d\right)^{\mathrm{T}} \tag{3.8}$$

where $m = 1, \ldots, M$ and $a_{m,k}$, $\tau_{m,k}$, $\varphi_{m,k}$, $f_{m,k}^d$ denote the amplitude, code delay, carrier phase and Doppler frequency of the mth MP signal, respectively. According to (3.4), a function of the MP parameter vectors $(\boldsymbol{x}_{1,k}, \ldots, \boldsymbol{x}_{M,k})$ and the correlation function samples at time k can be written as

$$\boldsymbol{z}_k = \mathbf{h}_0\left(\boldsymbol{x}_{0,k}\right) + \mathbf{h}_1\left(\boldsymbol{x}_{1,k},\ \ldots\ \boldsymbol{x}_{M,k}\right) + \boldsymbol{n}_k \tag{3.9}$$

where $k = 1, \ldots, K$ denotes the kth time instant of the correlator integration output. The LOS parameter vector $\boldsymbol{x}_{0,k}$ is first assumed to be known (the unknown case will be discussed in next sec-

tion). Replacing (3.3) in (3.9) leads to

$$\boldsymbol{z}'_k = \boldsymbol{\Phi}_k(\boldsymbol{\tau})\,\boldsymbol{\Lambda}_k\left(\boldsymbol{a},\,\boldsymbol{\varphi},\,\boldsymbol{f}^d\right) + \boldsymbol{n}_k \tag{3.10}$$

with

$$\boldsymbol{z}'_k = \boldsymbol{z}_k - \mathbf{h}_0\left(\boldsymbol{x}_{0,k}\right)$$

where the parameter vectors $\boldsymbol{\tau}_k = \left(\tau_{1,k},\,\ldots,\,\tau_{M,k}\right)^{\mathrm{T}}$, $\boldsymbol{a}_k = \left(a_{1,k},\,\ldots,\,a_{M,k}\right)^{\mathrm{T}}$, $\boldsymbol{\varphi}_k = \left(\varphi_{1,k},\,\ldots,\,\varphi_{M,k}\right)^{\mathrm{T}}$ and $\boldsymbol{f}_k = \left(f_{1,k},\,\ldots,\,f_{M,k}\right)^{\mathrm{T}}$ are the code delays, the amplitudes, the carrier phases and Doppler frequencies of the MP signals at time k, respectively. Moreover, the matrix $\boldsymbol{\Phi}_k$ only depends on the code delays of the MP signals and is defined as

$$\boldsymbol{\Phi}_k = \begin{pmatrix} \boldsymbol{\Phi}_{I,k} & \mathbf{0} \\ \mathbf{0} & \boldsymbol{\Phi}_{Q,k} \end{pmatrix} \tag{3.11}$$

with

$$\boldsymbol{\Phi}_{I,k} = \boldsymbol{\Phi}_{Q,k} = \begin{pmatrix} R\left(\Delta\tilde{\tau}_{1,k} + \theta_{-J}\right) & \ldots & R\left(\Delta\tilde{\tau}_{M,k} + \theta_{-J}\right) \\ R\left(\Delta\tilde{\tau}_{1,k} + \theta_{-J+1}\right) & \ldots & R\left(\Delta\tilde{\tau}_{M,k} + \theta_{-J+1}\right) \\ \vdots & \ddots & \vdots \\ R\left(\Delta\tilde{\tau}_{1,k} + \theta_{J}\right) & \ldots & R\left(\Delta\tilde{\tau}_{M,k} + \theta_{J}\right) \end{pmatrix}_{(2J+1)\times M}.$$

The vector $\boldsymbol{\Lambda}_k$ containing the unknown MP signal parameters is defined as

$$\boldsymbol{\Lambda}_k = \left(a'_{1,k}\cos\left(\Delta\tilde{\varphi}_{1,k}\right),\,\ldots,\,a'_{M,k}\cos\left(\Delta\tilde{\varphi}_{M,k}\right),\,a'_{1,k}\sin\left(\Delta\tilde{\varphi}_{1,k}\right),\,\ldots,\,a'_{M,k}\sin\left(\Delta\tilde{\varphi}_{M,k}\right)\right)^{\mathrm{T}} \tag{3.12}$$

with

$$a'_{m,k} = a_{m,k}\operatorname{sinc}\left(\pi\Delta\tilde{f}^d_{m,k}T_a\right)$$

where $m = 1,\ldots,M$. Considering that the vector $\boldsymbol{n}_k$ is an additive Gaussian white noise vector, the likelihood function of the MP signal parameters defined from the correlation function samples, under the assumption of known LOS signal parameters, is written as

$$p\left(\boldsymbol{z}'_k|\boldsymbol{x}_{1,k},\,\ldots,\,\boldsymbol{x}_{M,k}\right) = \frac{1}{\pi^{2J+1}\left|\boldsymbol{R}_k\right|}\exp\left(-\frac{1}{2}\left(\boldsymbol{z}'_k - \boldsymbol{\Phi}_k\boldsymbol{\Lambda}_k\right)^{\mathrm{T}}\boldsymbol{R}_k^{-1}\left(\boldsymbol{z}'_k - \boldsymbol{\Phi}_k\boldsymbol{\Lambda}_k\right)\right). \tag{3.13}$$

It is clear that the MP parameter vectors are highly non-linear functions of the multi-correlator measurements, thus they cannot be estimated with closed-form expressions. However, the MP parameter vectors can be estimated by using the maximum likelihood principle, i.e., by maximizing the likelihood function defined in (3.13) with respect to the MP signal parameters.

3.3 The Maximum Likelihood-Based UKF for MP Mitigation

3.3.1 Problem Formulation

In the presence of MP interferences, the MP mitigation problem can be formulated as how to accurately estimate the LOS signal parameters when the correlation function in the receiver is distorted by the MP signals. As mentioned in Section 3.2, we propose to use two kinds of models for describing the LOS and MP signal parameters: a dynamic model associated with the time propagation of LOS signal parameters and a static model associated with the MP signal parameters. Accordingly, this work studies a maximum likelihood-based unscented Kalman filter (UKF) approach to estimate the LOS signal parameters in the presence of MP signals. In this approach, the estimation of the MP parameter vectors is implemented by using a maximum likelihood principle and then the estimation of the LOS signal parameter vector is implemented by using the UKF method after eliminating the impact of MP signals on the correlation function. According to Section 3.2.1, the received signal parameter vector $\boldsymbol{x}_k$ can be partitioned into a LOS signal parameter vector $\boldsymbol{x}_{0,k}$ and MP parameter vectors $(\boldsymbol{x}_{1,k},\ldots,\boldsymbol{x}_{M,k})$. Using Bayes theorem, the posterior probability density function (pdf) of the parameter vector $\boldsymbol{x}_k$ is defined as

$$\begin{aligned} p(\boldsymbol{x}_k|\boldsymbol{z}_{1:k}) &= p\left(\boldsymbol{x}_{0,k},\boldsymbol{x}_{1,k},\ldots,\boldsymbol{x}_{M,k}|\boldsymbol{z}_{1:k}\right) \\ &\propto p\left(\boldsymbol{z}_k|\boldsymbol{x}_{0,k},\boldsymbol{x}_{1,k},\ldots,\boldsymbol{x}_{M,k},\boldsymbol{z}_{1:k-1}\right)\, p\left(\boldsymbol{x}_{0,k},\boldsymbol{x}_{1,k},\ldots,\boldsymbol{x}_{M,k}|\boldsymbol{z}_{1:k-1}\right) \\ &= p\left(\boldsymbol{z}_k|\boldsymbol{x}_{0,k},\boldsymbol{x}_{1,k},\ldots,\boldsymbol{x}_{M,k},\boldsymbol{z}_{1:k-1}\right)\, p\left(\boldsymbol{x}_{0,k}|\boldsymbol{x}_{1,k},\ldots,\boldsymbol{x}_{M,k},\boldsymbol{z}_{1:k-1}\right)\, p\left(\boldsymbol{x}_{1,k},\ldots,\boldsymbol{x}_{M,k}|\boldsymbol{z}_{1:k-1}\right). \end{aligned} \tag{3.14}$$

Generally, it can be assumed that the parameter vectors of the LOS and MP signals are pairwise independent. As a consequence, (3.14) can be rewritten as

$$p(\boldsymbol{x}_k|\boldsymbol{z}_{1:k}) \propto p\left(\boldsymbol{z}_k|\boldsymbol{x}_{0,k},\boldsymbol{x}_{1,k},\ldots,\boldsymbol{x}_{M,k},\boldsymbol{z}_{1:k-1}\right)\, p\left(\boldsymbol{x}_{0,k}|\boldsymbol{z}_{1:k-1}\right)\, p\left(\boldsymbol{x}_{1,k},\ldots,\boldsymbol{x}_{M,k}|\boldsymbol{z}_{1:k-1}\right) \tag{3.15}$$

where $p\left(\boldsymbol{z}_k|\boldsymbol{x}_{0,k},\boldsymbol{x}_{1,k},\ldots,\boldsymbol{x}_{M,k},\boldsymbol{z}_{1:k-1}\right)$ denotes the likelihood function of the received signal parameter vector $\boldsymbol{x}_k$ defined from the correlation function samples, $p\left(\boldsymbol{x}_{0,k}|\boldsymbol{z}_{1:k-1}\right)$ and $p\left(\boldsymbol{x}_{1,k},\ldots,\boldsymbol{x}_{M,k}|\boldsymbol{z}_{1:k-1}\right)$ are the pdfs of the LOS and MP parameter vectors, conditionally upon the $k-1$ first measurements $\boldsymbol{z}_{1:k-1}$. According to Section 3.2.2 and 3.2.3, the prior pdf associated with the LOS parameter vector $\boldsymbol{x}_{0,k}$ can be obtained by using the time propagation model defined in (3.7), whereas the prior pdf associated with the MP parameter vectors is assumed to be constant (uninformative prior). As a consequence, (3.15) can be rewritten as

$$p(\boldsymbol{x}_k|\boldsymbol{z}_{1:k}) \propto p\left(\boldsymbol{z}_k|\boldsymbol{x}_{0,k},\boldsymbol{x}_{1,k},\ldots,\boldsymbol{x}_{M,k},\boldsymbol{z}_{1:k-1}\right)\, p\left(\boldsymbol{x}_{0,k}|\boldsymbol{z}_{1:k-1}\right). \tag{3.16}$$

It is difficult to compute the posterior pdf (3.16) in closed-form, and thus the estimation of the received signal parameter vector $\boldsymbol{x}_k$ from (3.16) cannot be obtained straightforwardly. As an alter-

native, this work proposes an iterative approaches to compute the Bayesian estimators of the signal parameter vector $\boldsymbol{x}_k$, as explained below.

Step 1. Posterior pdf of $\boldsymbol{x}_k$ for a given LOS parameter vector $\boldsymbol{x}_{0,k}$ Assume that the LOS parameter vector $\boldsymbol{x}_{0,k}$ is known at time k, (3.14) can be rewritten as follows

$$\begin{aligned} p(\boldsymbol{x}_k|\boldsymbol{z}_{1:k}) &= p\left(\boldsymbol{x}_{0,k},\boldsymbol{x}_{1,k},\ldots,\boldsymbol{x}_{M,k}|\boldsymbol{z}_{1:k}\right) \\ &= p\left(\boldsymbol{x}_{1,k},\ldots,\boldsymbol{x}_{M,k}|\boldsymbol{x}_{0,k},\boldsymbol{z}_{1:k}\right)\ p\left(\boldsymbol{x}_{0,k}|\boldsymbol{z}_{1:k}\right) \\ &\propto p\left(\boldsymbol{x}_{1,k},\ldots,\boldsymbol{x}_{M,k}|\boldsymbol{z}_{1:k}\right) \end{aligned} \tag{3.17}$$

where $p\left(\boldsymbol{x}_{1,k},\ldots,\boldsymbol{x}_{M,k}|\boldsymbol{z}_{1:k}\right)$ is the posterior pdf of the MP parameter vectors $(\boldsymbol{x}_{1,k},\ldots,\boldsymbol{x}_{M,k})$. Since the prior pdf associated with the MP parameter vectors is assumed to be constant, the posterior pdf of $(\boldsymbol{x}_{1,k},\ldots,\boldsymbol{x}_{M,k})$ is defined as

$$p\left(\boldsymbol{x}_{1,k},\ldots,\boldsymbol{x}_{M,k}|\boldsymbol{z}_{1:k}\right) \propto p\left(\boldsymbol{z}_{1:k}|\boldsymbol{x}_{1,k},\ldots,\boldsymbol{x}_{M,k}\right) \tag{3.18}$$

where $p\left(\boldsymbol{z}_{1:k}|\boldsymbol{x}_{1,k},\ldots,\boldsymbol{x}_{M,k}\right)$ is the likelihood function of the observations $\boldsymbol{z}_{1:k}$ at time k. Thus the estimation of $\boldsymbol{x}_k$ from the observations $\boldsymbol{z}_{1:k}$ and for a given LOS parameter vector can be converted into a maximum likelihood estimator.

Step 2. Posterior pdf of $\boldsymbol{x}_k$ for given MP parameter vectors $(\boldsymbol{x}_{1,k},\ldots,\boldsymbol{x}_{M,k})$ Assume now that the MP parameter vectors $(\boldsymbol{x}_{1,k},\ldots,\boldsymbol{x}_{M,k})$ are known at time k, (3.14) can be rewritten as follows

$$\begin{aligned} p(\boldsymbol{x}_k|\boldsymbol{z}_{1:k}) &= p\left(\boldsymbol{x}_{0,k},\boldsymbol{x}_{1,k},\ldots,\boldsymbol{x}_{M,k}|\boldsymbol{z}_{1:k}\right) \\ &= p\left(\boldsymbol{x}_{0,k}|\boldsymbol{x}_{1,k},\ldots,\boldsymbol{x}_{M,k},\boldsymbol{z}_{1:k}\right) p\left(\boldsymbol{x}_{1,k},\ldots,\boldsymbol{x}_{M,k}|\boldsymbol{z}_{1:k}\right) \\ &\propto p\left(\boldsymbol{x}_{0,k}|\boldsymbol{z}_{1:k}\right) \\ &\propto p\left(\boldsymbol{z}_k|\boldsymbol{x}_{0,k}\right)\ p\left(\boldsymbol{x}_{0,k}|\boldsymbol{z}_{1:k-1}\right) \end{aligned} \tag{3.19}$$

where $p\left(\boldsymbol{z}_k|\boldsymbol{x}_{0,k}\right)$ and $p\left(\boldsymbol{x}_{0,k}|\boldsymbol{z}_{1:k-1}\right)$ are the likelihood function of the kth observation and the conditional pdf of the LOS parameter vector $\boldsymbol{x}_{0,k}$, conditionally upon the $k-1$ first measurements $\boldsymbol{z}_{1:k-1}$. Thus the posterior pdf $p(\boldsymbol{x}_k|\boldsymbol{z}_{1:k})$ for given MP parameter vectors is converted to a posterior pdf of the LOS parameter vector $\boldsymbol{x}_{0,k}$.

We propose to estimate $\boldsymbol{x}_k$ by using steps 1 and 2 iteratively as explained in the next sections.

3.3.2 MP Parameter Estimation Based on the Maximum Likelihood Principle

An estimator of the MP parameters can be obtained by maximizing the likelihood function defined in (3.18) with respect to the MP parameter vectors $(\boldsymbol{x}_{1,k},\ldots,\boldsymbol{x}_{M,k})$. However, it requires the value of

the LOS parameter vector $\boldsymbol{x}_{0,k}$ which is not straightforward to obtain at time k. However, assuming that the posterior pdf $p\left(\boldsymbol{x}_{0,k-1}|\boldsymbol{z}_{1:k-1}\right)$ at time $k-1$ is available, the pdf $p\left(\boldsymbol{x}_{0,k}|\boldsymbol{z}_{1:k-1}\right)$ at time k can be obtained by using the time propagation model of the LOS signal parameters as presented in (3.7). In the frame of the Kalman filter, the pdf $p\left(\boldsymbol{x}_{0,k}|\boldsymbol{z}_{1:k-1}\right)$ can be obtained by the following recursive relationship [82]

$$\begin{aligned} p\left(\boldsymbol{x}_{0,k-1}|\boldsymbol{z}_{1:k-1}\right) &= \mathcal{N}\left(\boldsymbol{x}_{0,k-1};\, \hat{\boldsymbol{x}}_{0,k-1|k-1},\, \boldsymbol{P}_{k-1|k-1}\right) \\ p\left(\boldsymbol{x}_{0,k}|\boldsymbol{z}_{1:k-1}\right) &= \mathcal{N}\left(\boldsymbol{x}_{0,k};\, \hat{\boldsymbol{x}}_{0,k|k-1},\, \boldsymbol{P}_{k|k-1}\right) \end{aligned} \tag{3.20}$$

where

$$\begin{aligned} \hat{\boldsymbol{x}}_{0,k|k-1} &= \boldsymbol{F}_{k|k-1}\hat{\boldsymbol{x}}_{0,k-1|k-1} \\ \boldsymbol{P}_{k|k-1} &= \boldsymbol{F}_{k|k-1}\boldsymbol{P}_{k-1|k-1}\boldsymbol{F}_{k|k-1}^{\mathrm{T}} + \boldsymbol{Q}_{k-1} \end{aligned} \tag{3.21}$$

and where $\mathcal{N}(\cdot)$ is a Gaussian pdf with an argument vector $\boldsymbol{x}$, a mean value vector $\hat{\boldsymbol{x}}$ and the corresponding covariance matrix $\boldsymbol{P}$. Thus the conditional pdf of the LOS parameter vector $\boldsymbol{x}_{0,k}$, conditionally upon the $k-1$ first measurements $\boldsymbol{z}_{1:k-1}$, can be obtained

$$\boldsymbol{x}_{0,k} \sim \mathcal{N}\left(\hat{\boldsymbol{x}}_{0,k|k-1},\, \boldsymbol{P}_{k|k-1}\right). \tag{3.22}$$

Accordingly, a set of sampling values of the LOS parameter vector $\boldsymbol{x}_{0,k}$, denoted as $\left\{\hat{\boldsymbol{x}}_{0,k|k-1}^{i},\, \omega_k^i\right\}_{i=1}^{N}$, can be used to characterize this conditional pdf $p\left(\boldsymbol{x}_{0,k}|\boldsymbol{z}_{1:k-1}\right)$ at time k, i.e.,

$$p\left(\boldsymbol{x}_{0,k}|\boldsymbol{z}_{1:k-1}\right) \approx \sum_{i=1}^{N} \omega_k^i\, \delta\left(\boldsymbol{x}_{0,k} - \hat{\boldsymbol{x}}_{0,k|k-1}^{i}\right) \tag{3.23}$$

and

$$\sum_{i=1}^{N} \omega_k^i = 1$$

where $\delta(\cdot)$ denotes the Dirac's delta function, $\omega_k^i = 1/N$ is the weight of the ith generated sample and N is the number of generated LOS parameter vector samples. This approximation converges almost surely to the true conditional pdf as $N \to \infty$ according to the strong law of numbers. In this work, the required vector $\boldsymbol{x}_{0,k}$ in **Step 1** can be approximated by using the sampling values of the LOS parameter vector associated with the conditional pdf $p\left(\boldsymbol{x}_{0,k}|\boldsymbol{z}_{1:k-1}\right)$ at time k. Using (3.18) and (3.23) in (3.17) leads to

$$p\left(\boldsymbol{z}_{1:k}|\boldsymbol{x}_{1,k},\ldots,\boldsymbol{x}_{M,k}\right) \approx \sum_{i=1}^{N} \omega_k^i\, p\left(\boldsymbol{z}_{1:k}|\hat{\boldsymbol{x}}_{0,k|k-1}^{i},\boldsymbol{x}_{1,k},\ldots,\boldsymbol{x}_{M,k}\right)\, \delta\left(\boldsymbol{x}_{0,k} - \hat{\boldsymbol{x}}_{0,k|k-1}^{i}\right) \tag{3.24}$$

where $i = 1,\ldots,N$ and $\hat{\boldsymbol{x}}_{0,k|k-1}^{i}$ is the ith LOS parameter vector sample associated with the conditional pdf $p\left(\boldsymbol{x}_{0,k}|\boldsymbol{z}_{1:k-1}\right)$. Replacing (3.13) in (3.24), the likelihood functions of the MP parameter

vectors for the ith LOS parameter vector sample $\hat{\boldsymbol{x}}^i_{0,k|k-1}$ at time k can be written as

$$p\left(\hat{\boldsymbol{z}}'_{i,1:k}|\boldsymbol{x}_{1,k},\ldots,\boldsymbol{x}_{M,k}\right)=\frac{1}{\pi^{2J+1}|\boldsymbol{R}_k|}\exp\left(-\frac{1}{2}\left(\hat{\boldsymbol{z}}'_{i,k}-\boldsymbol{\Phi}_k\boldsymbol{\Lambda}_k\right)^{\mathrm{T}}\boldsymbol{R}_k^{-1}\left(\hat{\boldsymbol{z}}'_{i,k}-\boldsymbol{\Phi}_k\boldsymbol{\Lambda}_k\right)\right) \tag{3.25}$$

with

$$\hat{\boldsymbol{z}}'_{i,k}=\boldsymbol{z}_k-\mathbf{h}_0\left(\hat{\boldsymbol{x}}^i_{0,k|k-1}\right)$$

where $i=1,\ldots,N$. Accordingly, the estimation of the MP parameter vectors for the ith LOS parameter vector sample $\hat{\boldsymbol{x}}^i_{0,k|k-1}$ can be performed by maximizing the likelihood function in (3.25). However, this maximization is generally difficult to compute since the matrices $\boldsymbol{\Phi}_k$ and $\boldsymbol{\Lambda}_k$ are both related to the unknown MP signal parameters. When the code delay of the MP signal relative to the LOS signal is equal or larger than 2 chips, it will not impact the correlation function of the LOS signal in the GNSS receiver. Thus we propose an interval grid search based on the maximum likelihood principle to perform the estimation of MP parameters. It is assumed that the MP signals arrive at the receiver later than the LOS signal, i.e., $(\tau_m-\tau_0)\in(0,\,2)$ where $m=1,\ldots,M$, and the code delays of MP signals satisfy $\tau_1<\cdots<\tau_M$. Here, the search grid coincides with the correlator delay θ_j where $j=1,\ldots,J$. Figure 3.2 shows an example of search grid when two MP signals, for the ith LOS parameter vector sample, are considered, i.e., $M=2$. Thus a set $\boldsymbol{\Theta}_i$, including all possible combinations of MP signal code delays for the ith LOS parameter vector sample $\hat{\boldsymbol{x}}^i_{0,k|k-1}$ at time k, is defined as

$$\boldsymbol{\Theta}_i=\left\{\tilde{\boldsymbol{\tau}}^i_{1,k},\,\ldots,\,\tilde{\boldsymbol{\tau}}^i_{S,k}\right\},\ i=1,\ldots,N \tag{3.26}$$

where

$$\tilde{\boldsymbol{\tau}}^i_{s,k}=\left(\tilde{\tau}^i_{s,1,k},\,\ldots,\,\tilde{\tau}^i_{s,M,k}\right)^{\mathrm{T}},\ s=1,\ldots,S$$

and

$$\tilde{\tau}^i_{s,m,k}=\hat{\tau}^i_{0,k|k-1}+\theta_j,\ m=1,\ldots,\ M \text{ and } j=1,\ldots,J$$

and S is the number of possible values of the MP signal code delays. Note that $\tilde{\tau}^i_{s,1,k}<\cdots<\tilde{\tau}^i_{s,M,k}$ and $\hat{\tau}^i_{0,k|k-1}$ is the code delay of the LOS signal which is an element of the ith LOS parameter vector sample $\hat{\boldsymbol{x}}^i_{0,k|k-1}$.

Replacing the sth possible MP signal code delay vector $\tilde{\boldsymbol{\tau}}^i_{s,k}$ and the local generated code delay replica $\tilde{\tau}_k$ into (3.11) leads to the matrix $\boldsymbol{\Phi}^i_{s,k}$ associated with the ith LOS parameter vector sample at time k. As a consequence, the MLE for the sth possible MP parameter vector $\boldsymbol{\Lambda}^i_{s,k}$ at time k can be implemented as follow

$$\frac{\partial\ln p\left(\hat{\boldsymbol{z}}'_{i,1:k}|\boldsymbol{x}_{1,k},\ldots,\boldsymbol{x}_{M,k}\right)}{\partial\boldsymbol{\Lambda}_k}=\frac{\partial\left(\left(\hat{\boldsymbol{z}}'_{i,k}-\boldsymbol{\Phi}^i_{s,k}\boldsymbol{\Lambda}_k\right)^{\mathrm{T}}\boldsymbol{R}_k^{-1}\left(\hat{\boldsymbol{z}}'_{i,k}-\boldsymbol{\Phi}^i_{s,k}\boldsymbol{\Lambda}_k\right)\right)}{\partial\boldsymbol{\Lambda}_k}=0. \tag{3.27}$$

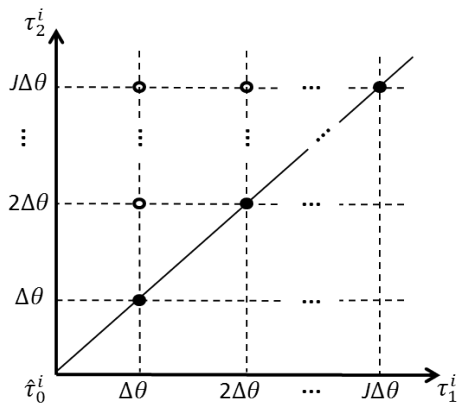

Figure 3.2 – The search grid of code delay when $M = 2$ for the ith LOS parameter vector sample. The approximation values of τ_1: filled cycles; The corresponding possible values of τ_2: empty cycles.

After solving (3.27), the MLE for the vector $\hat{\boldsymbol{\Lambda}}_{s,k}^i$ associated with the sth possible MP signal code delay vector $\tilde{\boldsymbol{\tau}}_{s,k}^i$ for the ith LOS parameter vector sample $\hat{\boldsymbol{x}}_{0,k|k-1}^i$ at time k can be obtained [83]

$$\hat{\boldsymbol{\Lambda}}_{s,k}^i = \left((\boldsymbol{\Phi}_{s,k}^i)^{\mathrm{T}} \boldsymbol{R}_k^{-1} \boldsymbol{\Phi}_{s,k}^i\right)^{-1} (\boldsymbol{\Phi}_{s,k}^i)^{\mathrm{T}} \boldsymbol{R}_k^{-1} \hat{\boldsymbol{z}}_{i,k}' \tag{3.28}$$

where $s = 1, \ldots, S$. When the ith LOS parameter vector sample $\hat{\boldsymbol{x}}_{0,k|k-1}^i$ is given, the MP signal parameter estimation based on the maximum likelihood principle is summarized in Algorithm 1.

Algorithm 1: MP signal parameter estimation based on the maximum likelihood principle.

1: Consider the sth possible MP signal code delay vector $\tilde{\boldsymbol{\tau}}_{s,k}^i \in \boldsymbol{\Theta}_i$ and compute the corresponding matrix $\boldsymbol{\Phi}_{s,k}^i$ at time k, where $s = 1, \ldots, S$

2: Compute the MLE of $\hat{\boldsymbol{\Lambda}}_{s,k}^i$ according to (3.28)

3: Compute each possible MP signal likelihood function $l_{i,s}$ by replacing $\boldsymbol{\Phi}_{s,k}^i$ and $\hat{\boldsymbol{\Lambda}}_{s,k}^i$ into (3.25)
$l_{i,s} = \frac{1}{\pi^{2J+1}|\boldsymbol{R}_k|} \exp\left(-\frac{1}{2}\left(\hat{\boldsymbol{z}}_{i,k}' - \boldsymbol{\Phi}_{s,k}^i \hat{\boldsymbol{\Lambda}}_{s,k}^i\right)^{\mathrm{T}} \boldsymbol{R}_k^{-1} \left(\hat{\boldsymbol{z}}_{i,k}' - \boldsymbol{\Phi}_{s,k}^i \hat{\boldsymbol{\Lambda}}_{s,k}^i\right)\right), \quad s = 1, \ldots, S$

4: Determine the estimator of the MP signal parameters by using the maximum likelihood principle
$\left(\hat{\boldsymbol{\tau}}_k^i, \hat{\boldsymbol{\Lambda}}_k^i\right) = \arg\max_{\left(\boldsymbol{\Phi}_{s,k}^i, \hat{\boldsymbol{\Lambda}}_{s,k}^i\right)} l_{i,s}$

According to (3.24), the final MLE of the MP parameter vectors can be approximated by the mixture of the estimators of the MP signal parameter vectors associated with the LOS parameter vector samples in Algorithm 1, i.e.,

$$\begin{aligned} \hat{\boldsymbol{\tau}}_k &= \sum_{i=1}^{N} \omega_k^i \hat{\boldsymbol{\tau}}_k^i \\ \hat{\boldsymbol{\Lambda}}_k &= \sum_{i=1}^{N} \omega_k^i \hat{\boldsymbol{\Lambda}}_k^i. \end{aligned} \tag{3.29}$$

Finally, the corresponding amplitude and carrier phase of MP signals are extracted by using the estimated parameter vector $\hat{\mathbf{\Lambda}}_k$ in (3.29), i.e.,

$$\begin{aligned} \hat{a}_{m,k} &= \sqrt{\left(\hat{\mathbf{\Lambda}}_k[m]\right)^2 + \left(\hat{\mathbf{\Lambda}}_k[m+M]\right)^2} \\ \hat{\varphi}_{m,k} &= \arctan\left(\frac{\hat{\mathbf{\Lambda}}_k[m+M]}{\hat{\mathbf{\Lambda}}_k[m]}\right) + \tilde{\varphi}_k \end{aligned} \tag{3.30}$$

where $m = 1, \ldots, M$ and $\hat{\mathbf{\Lambda}}_k[m]$ denotes the mth element in the vector $\hat{\mathbf{\Lambda}}_k$, $\tilde{\varphi}_k$ is the local generated replica of carrier phase. With regard to the carrier Doppler frequency, the effect of a frequency error only results in an attenuation of the carrier amplitude in (3.12) which is difficult to separate them form the correlation function measurements. Thus the Doppler frequencies of MP signals are extracted from two successive carrier phase estimations as follows

$$\hat{f}^d_{m,k} = \frac{\hat{\varphi}_{m,k} - \hat{\varphi}_{m,k-1}}{T_a} \tag{3.31}$$

where $\hat{f}^d_{m,k}$ is the carrier Doppler frequency estimation of the mth MP signal and $m = 1, \ldots, M$.

On the one hand, the computational load of Algorithm 1, depending on the number of considered MP M and on the number of multi-correlator delays J, can be effectively constricted by assuming a moderate value of M and by selecting an appropriate value for J; on the other hand, the approximation error associated with the code delay estimation of MP signals can be reduced by decreasing the size of adjacent correlator spacings, leading to increasing the number of correlator delays. As a consequence, there is a trade-off between the computational load and estimation accuracy in Algorithm 1.

3.3.3 LOS Parameter Estimation Based on the Unscented Kalman Filter

According to (3.19), the posterior pdf of the LOS parameter vector $\boldsymbol{x}_{0,k}$ can be obtained as a function of the MP parameter vectors $(\boldsymbol{x}_{1,k}, \ldots, \boldsymbol{x}_{M,k})$. Considering that the MLE of the MP parameter vectors have been obtained in (3.29), the vectors $(\boldsymbol{x}_{1,k}, \ldots, \boldsymbol{x}_{M,k})$ required in **Step 2** can be approximated by the MLE of the MP parameter vectors $(\hat{\boldsymbol{x}}_{1,k}, \ldots, \hat{\boldsymbol{x}}_{M,k})$ at time k. In addition, the measurement equations (3.4) being highly non-linear, a non-linear estimation method can be exploited for implementing the posterior estimation of the LOS parameter vector as a function of the MP parameter vectors. The extended Kalman filter (EKF) is an interesting solution. However, it might diverge due to large linearization errors. The particle filter (PF) [84, 85] might be investigated to perform advantageously this estimation. However, the corresponding computational cost can be prohibitive for practical applications. Thus we consider an unscented Kalman filter (UKF) based on an unscented transformation (UT) that provides an efficient and low-cost solution for highly non-linear equations [86, 87].

The UT technique is a method for calculating the Gaussian distribution of a random variable which undergoes a non-linear transformation. In the UT technique, a set of sigma-points are deterministically calculated by using the mean and covariance of the random variable and are propagated through the true non-linear function. Then the posterior Gaussian distribution can be approximated from the propagated sigma-points and the corresponding weights. Since the mean value vector $\hat{\boldsymbol{x}}_{0,k|k-1}$ and the corresponding covariance matrix $\boldsymbol{P}_{k|k-1}$ of the pdf $p\left(\boldsymbol{x}_{0,k}|\boldsymbol{z}_{1:k-1}\right)$ have been obtained thanks to (3.21), the sigma points are generated in order to propagate the predicted LOS parameter vector $\hat{\boldsymbol{x}}_{0,k|k-1}$ through the non-linear measurement equations [88],

$$\begin{aligned}
\boldsymbol{\chi}_{0,0} &= \hat{\boldsymbol{x}}_{0,k|k-1} \\
\boldsymbol{\chi}_{i,0} &= \hat{\boldsymbol{x}}_{0,k|k-1} + \left(\sqrt{(L+\lambda)\,\boldsymbol{P}_{k|k-1}}\right)_i \\
\boldsymbol{\chi}_{i+L,0} &= \hat{\boldsymbol{x}}_{0,k|k-1} - \left(\sqrt{(L+\lambda)\,\boldsymbol{P}_{k|k-1}}\right)_i, \quad i = 1,\ldots,L
\end{aligned} \tag{3.32}$$

where L is the dimension of the state vector $\hat{\boldsymbol{x}}_{0,k|k-1}$ and $\lambda = \alpha^2(L+\kappa) - L$ is a scaling parameter, α is a constant scaling parameter that determines the spread of the sigma points around $\hat{\boldsymbol{x}}_{0,k|k-1}$ and is set to a small positive value (i.e., $10^{-4} \leq \alpha \leq 1$), κ is a secondary scaling parameter (usually set to $3-L$), $\left(\sqrt{(L+\lambda)\,\boldsymbol{P}_{k|k-1}}\right)_i$ is the ith column of the square root of the matrix $(L+\lambda)\,\boldsymbol{P}_{k|k-1}$, i.e., the lower-triangular matrix constructed using a Cholesky factorization. Accordingly, the weight W_i, corresponding to the sigma point $\boldsymbol{\chi}_i$ and its covariance matrix, can be calculated as follows

$$\begin{aligned}
W_0^m &= \frac{\lambda}{L+\lambda} \\
W_0^c &= \frac{\lambda}{L+\lambda} + \left(1-\alpha^2+\beta\right) \\
W_i^m &= W_i^c = \frac{1}{2(L+\lambda)}, \quad i = 1,\ldots,2L\,.
\end{aligned} \tag{3.33}$$

Then the generated sigma points $\boldsymbol{\chi}_{i,0}$ are transformed to obtain the ith predicted observation when the MLE of the MP parameter vectors $(\hat{\boldsymbol{x}}_{1,k},\ldots,\hat{\boldsymbol{x}}_{M,k})$ is given

$$\hat{\boldsymbol{z}}_{i,k|k-1} = \mathbf{h}(\boldsymbol{\chi}_{i,0}, \hat{\boldsymbol{x}}_{1,k},\ldots,\hat{\boldsymbol{x}}_{M,k}) \tag{3.34}$$

where $i = 1,\ldots,2L+1$ and the function $\mathbf{h}(\cdot)$ is the measurement equation as presented in (3.4). Accordingly, the mean and covariance of the predicted observation $\hat{\boldsymbol{z}}_{k|k-1}$ can be obtained as

$$\begin{aligned}
\hat{\boldsymbol{z}}_{k|k-1} &= \sum_{i=0}^{2L} W_i^m \hat{\boldsymbol{z}}_{i,k|k-1} \\
\boldsymbol{P}_{k|k-1}^{\hat{\boldsymbol{z}}_{k|k-1}\hat{\boldsymbol{z}}_{k|k-1}} &= \sum_{i=0}^{2L} W_i^c \left(\hat{\boldsymbol{z}}_{i,k|k-1} - \hat{\boldsymbol{z}}_{k|k-1}\right)\left(\hat{\boldsymbol{z}}_{i,k|k-1} - \hat{\boldsymbol{z}}_{k|k-1}\right)^{\mathrm{T}} + \boldsymbol{R}_k
\end{aligned} \tag{3.35}$$

and the cross covariance between the predicted LOS parameter vector $\hat{\boldsymbol{x}}_{0,k|k-1}$ and the predicted measurement $\hat{\boldsymbol{z}}_{k|k-1}$ is

$$\boldsymbol{P}_{k|k-1}^{\hat{\boldsymbol{x}}_{0,k|k-1}\hat{\boldsymbol{z}}_{k|k-1}} = \sum_{i=0}^{2L} W_i^c \left(\boldsymbol{\chi}_{0,i} - \hat{\boldsymbol{x}}_{0,k|k-1}\right)\left(\hat{\boldsymbol{z}}_{i,k|k-1} - \hat{\boldsymbol{z}}_{k|k-1}\right)^{\mathrm{T}}. \tag{3.36}$$

The mean vector and covariance matrix of the posterior pdf $p\left(\boldsymbol{x}_{0,k}|\boldsymbol{z}_{1:k}\right)$ computed from the estimated MP parameter vectors can be obtained in the frame of the Kalman filter. Thus the conventional Kalman filter gain is calculated as follows

$$\boldsymbol{K}_k = \boldsymbol{P}_{k|k-1}^{\hat{\boldsymbol{x}}_{0,k|k-1}\hat{\boldsymbol{z}}_{k|k-1}} \left(\boldsymbol{P}_{k|k-1}^{\hat{\boldsymbol{z}}_{k|k-1}\hat{\boldsymbol{z}}_{k|k-1}}\right)^{-1}. \tag{3.37}$$

As a consequence, the maximum a posteriori estimator of the LOS parameter vector and its covariance matrix are defined as

$$\begin{aligned} \hat{\boldsymbol{x}}_{0,k|k} &= \hat{\boldsymbol{x}}_{0,k|k-1} + \boldsymbol{K}_k\left(\boldsymbol{z}_k - \hat{\boldsymbol{z}}_{k|k-1}\right) \\ \boldsymbol{P}_{k|k} &= \boldsymbol{P}_{k|k-1} - \boldsymbol{K}_k \boldsymbol{P}_{k|k-1}^{\hat{\boldsymbol{z}}_{k|k-1}\hat{\boldsymbol{z}}_{k|k-1}} \boldsymbol{K}_k^{\mathrm{T}}. \end{aligned} \tag{3.38}$$

Finally, the maximum likelihood-based UKF for MP mitigation is summarized in Algorithm 2.

Algorithm 2: The maximum likelihood-based UKF for MP mitigation.

	% Initialization
1:	$\hat{\boldsymbol{x}}_{0,0} \sim p\left(\boldsymbol{x}_{0,0}\right)$
	%Time propagation
2:	**for** $k = 1, \ldots, K$ **do**
	%Predict LOS parameter vector
3:	Compute $\hat{\boldsymbol{x}}_{0,k|k-1}$ and $\boldsymbol{P}_{k|k-1}$ according to (3.21)
	%Generate the sampling values associated with the conditional pdf $p\left(\boldsymbol{x}_{0,k}|\boldsymbol{z}_{1:k-1}\right)$
4:	Generate $\hat{\boldsymbol{x}}_{0,k|k-1}^i \sim p\left(\boldsymbol{x}_{0,k}|\boldsymbol{z}_{1:k-1}\right)$, where $i = 1, \ldots, N$
	%Step 1
5:	**for** $i = 1, \ldots, N$ **do**
6:	Compute $\left(\hat{\boldsymbol{\tau}}_k^i, \hat{\boldsymbol{\Lambda}}_k^i\right)$ associated with $\hat{\boldsymbol{x}}_{0,k|k-1}^i$ by using Algorithm 1
7:	**end for**
8:	Determine the estimator of $(\hat{\boldsymbol{x}}_{1,k}, \ldots, \hat{\boldsymbol{x}}_{M,k})$ by using (3.29) $\sim$ (3.31)
	%Generate sigma points
9:	Generate $\boldsymbol{\chi}_{i,0}$ and W_i according to(3.32) and (3.33)
	%Step 2
10:	Propagate $\boldsymbol{\chi}_{i,0}$ using $(\hat{\boldsymbol{x}}_{1,k}, \ldots, \hat{\boldsymbol{x}}_{M,k})$ determined in line 8 and compute $\hat{\boldsymbol{z}}_{k|k-1}$ according to (3.34) and (3.35)
11:	Compute $\hat{\boldsymbol{x}}_{0,k|k}$ and $\boldsymbol{P}_{k|k}$ by using (3.36)$\sim$(3.38)
12:	**end for**

3.4 Posterior Cramér-Rao Bound

In the frame of time-varying estimation, a posterior Cramér–Rao bound (PCRB), which provides the minimum theoretical achievable error variance, is widely used to evaluate the performance of an estimator [89]. In this section, the PCRB of the LOS signal parameter estimation in the absence of MP interferences, i.e., $M = 0$, is derived and used as the reference for evaluating the performance of the maximum likelihood-based UKF. Let $\boldsymbol{x}_{0,1:k} = \{\boldsymbol{x}_{0,1}, \ldots, \boldsymbol{x}_{0,k}\}$ be the true LOS parameter vector and $\boldsymbol{z}_{1:k} = \{\boldsymbol{z}_1, \ldots, \boldsymbol{z}_k\}$ be the multi-correlator measurements from time instants 1 to k. As usual, $p\left(\boldsymbol{x}_{0,1:k}, \boldsymbol{z}_{1:k}\right)$ denotes the joint pdf of the pair $(\boldsymbol{x}_{0,1:k}, \boldsymbol{z}_{1:k})$. According to (3.38), $\hat{\boldsymbol{x}}_{0,k}$ is an estimator of $\boldsymbol{x}_{0,k}$ in the absence of MP interferences, and $\boldsymbol{P}_k$ is the covariance matrix of its estimation error at time k. Using these notations, the PCRB for the estimation error of any unbiased estimator of $\boldsymbol{x}_{0,1:k}$ is lower bounded by the following inequality [90]

$$\boldsymbol{P}_k \triangleq \mathrm{E}\left[\left(\hat{\boldsymbol{x}}_{0,k} - \boldsymbol{x}_{0,k}\right)\left(\hat{\boldsymbol{x}}_{0,k} - \boldsymbol{x}_{0,k}\right)^{\mathrm{T}}\right] \geq \boldsymbol{J}_k^{-1} \tag{3.39}$$

where $\boldsymbol{J}_k$ is the Fisher information matrix that is defined as

$$\boldsymbol{J}_k = \mathrm{E}\left[-\Delta_{\boldsymbol{x}_{0,1:k}}^{\boldsymbol{x}_{0,1:k}} \ln p\left(\boldsymbol{x}_{0,1:k}, \boldsymbol{z}_{1:k}\right)\right] \tag{3.40}$$

where $\mathrm{E}[\cdot]$ denotes the expectation function, $A \geq B$ means that the matrix $A - B$ is positive semi-definite, Δ_a^b denotes the second-order partial derivative of $p\left(\boldsymbol{x}_{0,1:k}, \boldsymbol{z}_{1:k}\right)$ with respect to $\boldsymbol{x}_{0,1:k}$, i.e.,

$$\Delta_a^b = \nabla_a \left(\nabla_b f\right)^{\mathrm{T}}$$

where ∇_a denotes the first-order partial derivative of a function f. As a consequence, $\boldsymbol{J}_k$ can be obtained using the following recursion [91]

$$\boldsymbol{J}_k = \boldsymbol{D}_k^{22} - \boldsymbol{D}_k^{21}\left(\boldsymbol{J}_{k-1} + \boldsymbol{D}_k^{11}\right)^{-1} \boldsymbol{D}_k^{12} \tag{3.41}$$

where

$$\begin{aligned}
\boldsymbol{D}_k^{11} &= \mathrm{E}\left[-\Delta_{\boldsymbol{x}_{0,k-1}}^{\boldsymbol{x}_{0,k-1}} \ln p\left(\boldsymbol{x}_{0,k} | \boldsymbol{x}_{0,k-1}\right)\right] \\
\boldsymbol{D}_k^{12} &= \mathrm{E}\left[-\Delta_{\boldsymbol{x}_{0,k-1}}^{\boldsymbol{x}_{0,k}} \ln p\left(\boldsymbol{x}_{0,k} | \boldsymbol{x}_{0,k-1}\right)\right] \\
\boldsymbol{D}_k^{21} &= \mathrm{E}\left[-\Delta_{\boldsymbol{x}_{0,k}}^{\boldsymbol{x}_{0,k-1}} \ln p\left(\boldsymbol{x}_{0,k} | \boldsymbol{x}_{0,k-1}\right)\right] = \left(\boldsymbol{D}_k^{12}\right)^{\mathrm{T}} \\
\boldsymbol{D}_k^{22} &= \mathrm{E}\left[-\Delta_{\boldsymbol{x}_{0,k}}^{\boldsymbol{x}_{0,k}} \ln p\left(\boldsymbol{x}_{0,k} | \boldsymbol{x}_{0,k-1}\right)\right] + \mathrm{E}\left[-\Delta_{\boldsymbol{x}_{0,k}}^{\boldsymbol{x}_{0,k}} \ln p\left(\boldsymbol{z}_k | \boldsymbol{x}_{0,k}\right)\right]
\end{aligned} \tag{3.42}$$

and the initial information matrix can be calculated using the prior pdf of $\boldsymbol{x}_{0,k}$, i.e.,

$$\boldsymbol{J}_0 = \mathrm{E}\left[-\Delta_{\boldsymbol{x}_{0,0}}^{\boldsymbol{x}_{0,0}} \ln p\left(\boldsymbol{x}_{0,0}\right)\right].$$

As mentioned above, the process noise vector $\boldsymbol{\omega}_{k-1}$ and the measurement noise vector $\boldsymbol{n}_k$ are both additive zero mean Gaussian white noise vectors. Consequently, the ln-pdfs $p\left(\boldsymbol{x}_{0,k}|\boldsymbol{x}_{0,k-1}\right)$ and $p\left(\boldsymbol{z}_k|\boldsymbol{x}_{0,k}\right)$ in the absence of MP interferences at time k in (3.42) can be defined as

$$\begin{aligned}
-\ln p\left(\boldsymbol{x}_{0,k}|\boldsymbol{x}_{0,k-1}\right) &= c_1 + \frac{1}{2}\left(\boldsymbol{x}_{0,k} - \boldsymbol{F}_{k|k-1}\boldsymbol{x}_{0,k-1}\right)^{\mathrm{T}} \boldsymbol{Q}_{k-1}^{-1}\left(\boldsymbol{x}_{0,k} - \boldsymbol{F}_{k|k-1}\boldsymbol{x}_{0,k-1}\right) \\
-\ln p\left(\boldsymbol{z}_k|\boldsymbol{x}_{0,k}\right) &= c_2 + \frac{1}{2}\left(\boldsymbol{z}_k - \mathbf{h}\left(\boldsymbol{x}_{0,k}\right)\right)^{\mathrm{T}} \boldsymbol{R}_k^{-1}\left(\boldsymbol{z}_k - \mathbf{h}\left(\boldsymbol{x}_{0,k}\right)\right)
\end{aligned} \tag{3.43}$$

where c_1 and c_2 are constants. After replacing (3.43) in (3.42), the matrices in (3.42) can be simplified as

$$\begin{aligned}
\boldsymbol{D}_k^{11} &= \boldsymbol{F}_{k|k-1}^{\mathrm{T}} \boldsymbol{Q}_{k-1}^{-1} \boldsymbol{F}_{k|k-1} \\
\boldsymbol{D}_k^{12} &= -\boldsymbol{F}_{k|k-1}^{\mathrm{T}} \boldsymbol{Q}_{k-1}^{-1} = \left(\boldsymbol{D}_k^{21}\right)^{\mathrm{T}} \\
\boldsymbol{D}_k^{22} &= \boldsymbol{Q}_{k-1}^{-1} + \mathrm{E}\left[\left(\nabla_{\boldsymbol{x}_{0,k}} \mathbf{h}^{\mathrm{T}}\left(\boldsymbol{x}_{0,k}\right)\right) \boldsymbol{R}_k^{-1} \left(\nabla_{\boldsymbol{x}_{0,k}} \mathbf{h}^{\mathrm{T}}\left(\boldsymbol{x}_{0,k}\right)\right)^{\mathrm{T}}\right]
\end{aligned} \tag{3.44}$$

with

$$\nabla_{\boldsymbol{x}_{0,k}} \mathbf{h}^{\mathrm{T}}\left(\boldsymbol{x}_{0,k}\right) = \frac{\partial \mathbf{h}^{\mathrm{T}}\left(\boldsymbol{x}_{0,k}\right)}{\partial \boldsymbol{x}_{0,k}}.$$

It is clear that the matrices $\boldsymbol{D}_k^{11}$, $\boldsymbol{D}_k^{12}$ and $\boldsymbol{D}_k^{21}$ are deterministic and can be easily obtained. However, an explicit expression of the expectation appearing in the matrix $\boldsymbol{D}_k^{22}$ cannot be obtained easily as the measurement equations are non-linear. As a consequence, we propose to perform Monte Carlo (MC) simulations to obtain an approximate theoretical PCRB in the absence of MP interferences for evaluating the maximum likelihood-based UKF approach [92].

3.5 Algorithm Assessment

3.5.1 Test Scenarios

In order to validate the proposed MP mitigation approach, we have first simulated a GPS L1 C/A signal assuming a scenario composed of a LOS signal and one reflected MP signal, i.e., $M = 1$. This assumption is realistic in many practical scenarios due to the fact that two reflected signals very close in time can be considered as only one perturbation [38,93]. The GPS L1 C/A signal is based on a pseudo random sequence that is used to spread the data signal around the carrier frequency $f_{\mathrm{ca}} =$ 1575.42 MHz. The PRN code rate is $f_{\mathrm{co}} = 1/T_{\mathrm{co}} = 1.023$ MHz and the length of the PRN code is $N =$ 1023, resulting in a code period of 1 ms. In the following simulation, the carrier-to-noise density ratio of the LOS signal is 42 dB-Hz and a power signal-to-multipath ratio of 6 dB is considered. The sampling frequency of the baseband signal entering the digital receiver is set to $f_s = 10.23$ MHz, providing 10230 data samples during the code period. For the considered application for which vehicles move slowly in an urban environment, we can assume a constant velocity model to describe the dynamic of the vehicle. More precisely, the vehicle velocity is set to $v = 20$ m/s and the

noise standard deviation is $\sigma_v = 0.5$ m/s^2. In addition, the noises associated with the amplitude, code delay, and carrier phase of the LOS signal are $\omega_a = 0.00001$ volt, $\omega_\tau = 0.1$ chip and $\omega_\varphi = 0.1$ rad respectively. The run time for all simulations is 2 s and the MLE-based UKF is synchronised with the correlator measurements. Thus the filter rate is equal to the correlator integration time, i.e., $T_a = 20$ ms. The number of generated LOS parameter vector samples used in Algorithm 1 is $N = 20$. Several scenarios has been generated according to the GNSS signal model (3.2) as follows:

- **Scenario 1** Only a LOS signal, i.e., $M = 0$, is processed inside the receiver.
- **Scenario 2** An MP signal appears during the simulation time interval (0.8s, 1.6s). The MP relative code delay with the LOS signal is $\tau_1 - \tau_0 = 0.32$ chips; moreover, the LOS and MP signals are in-phase, i.e., $\varphi_1 = \varphi_0$ (the constructive MP interference) and their carrier Doppler frequencies are equal, i.e., $f_1^d = f_0^d$.
- **Scenario 3** On the basis of Scenario 2, the MP relative code delay with the LOS signal is set to a random value uniformly distributed over the interval (0, 0.2), i.e., $(\tau_1 - \tau_0) \sim \mathrm{U}(0, 0.2)$ during the simulation time interval (0.8s, 1.6s).

We propose to compare the LOS parameter estimation performance of the proposed approach with that obtained using the standard UKF and the derived PCRB. Since the number of correlators in the receiver impacts the estimation accuracy of MP parameters, the proposed approach has been tested with 11 ($J = 5$ and $\Delta\theta = 0.2$) and 21 ($J = 10$ and $\Delta\theta = 0.1$) correlators, denoted as ML-based UKF(11) and ML-based UKF(21) respectively, whereas the standard UKF been tested with 11 correlators. $N_m = 50$ MC simulations have been run for any scenario. The root mean square errors (RMSE) of the estimates is defined as

$$\mathrm{RMSE} = \sqrt{\frac{1}{N_m}\sum_{i=1}^{N_m}\left(\hat{\boldsymbol{x}}_{0,k}^{(i)} - \boldsymbol{x}_{0,k}\right)^2}$$

where $\hat{\boldsymbol{x}}_{0,k}^{(i)}$ is the ith run result, and $k = 1, \ldots, K$ denotes the kth time instant of the correlator integration output.

3.5.2 Simulation Results

Figure 3.3 shows the RMSEs of the estimated code delay, carrier phase and Doppler frequency of the LOS signal with the different approaches associated with Scenario 1. Since there is not MP signal, the RMSEs of all approaches become close to the PCRB quickly and yield similar performances. Thus the proposed maximum likelihood-based UKF is able to effectively track the LOS signal parameters and provides the same performance as a standard UKF in the absence of MP interferences.

Scenario 2 investigates the effect of different estimation approaches when MP interferences appear or disappear randomly. Since the carrier phases and Doppler frequencies of the LOS and MP signals are equal in this scenario, the RMSEs of the estimated carrier phase and Doppler frequency of the LOS signal, for all approaches, are not impacted by the MP interference, as shown in Figure 3.4 (a) and (b). However, since the correlation function that is sampled at the multi-correlator outputs is distorted in the presence of the constructive MP signal, the estimation of the LOS signal code delay is degraded in this scenario. As shown in Figure 3.4 (c), the standard UKF is strongly impacted and the error of the estimated LOS signal code delay becomes large in the presence of the MP interference, which has not been mitigated by the receiver. On the contrary, since the impact of MP interference on the correlation function has been mitigated by the proposed ML estimator (which estimates the MP signal parameters), the proposed ML-based UKF improves the accuracy

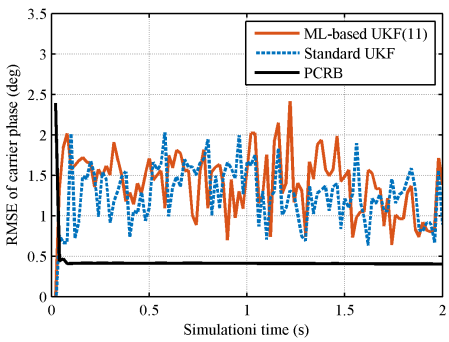

(a) RMSE of carrier phase

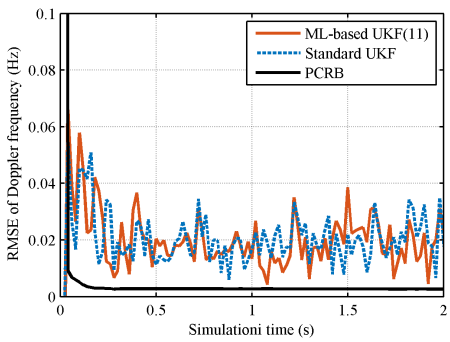

(b) RMSE of Doppler frequency

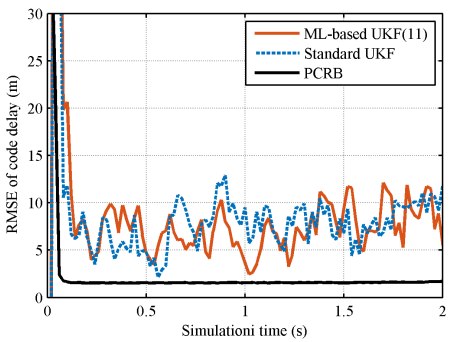

(c) RMSE of code delay

Figure 3.3 – RMSEs of LOS parameter estimation in Scenario 1.

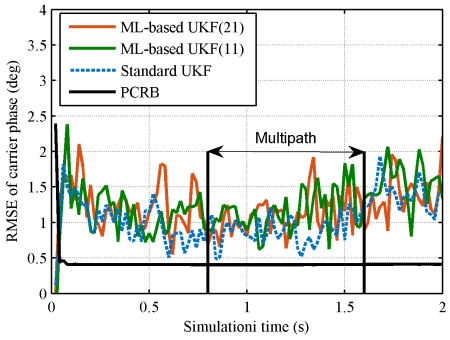

(a) RMSE of carrier phase

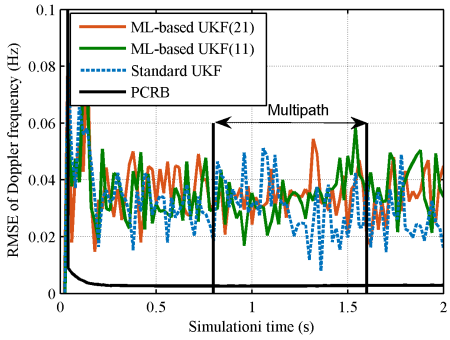

(b) RMSE of Doppler frequency

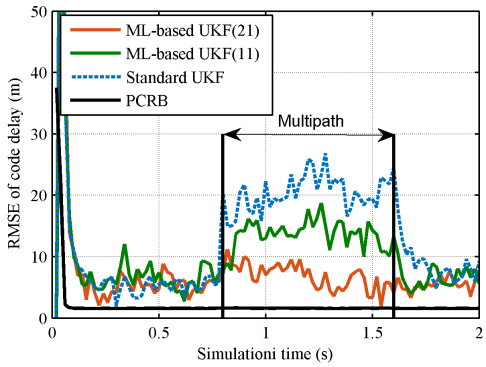

(c) RMSE of code delay

Figure 3.4 – RMSEs of LOS parameter estimation in Scenario 2.

of the code delay estimator. Note that the ML-based UKF(21) estimator shows better results than the ML-based UKF(11), as its RMSE is closer to the PCRB. This conclusion makes sense since the approximation error of the code delay is reduced when the MLE of the MP signal parameters is performed with a smaller adjacent correlator spacing.

Scenario 3 compares the performance of different estimation approaches when the code delay

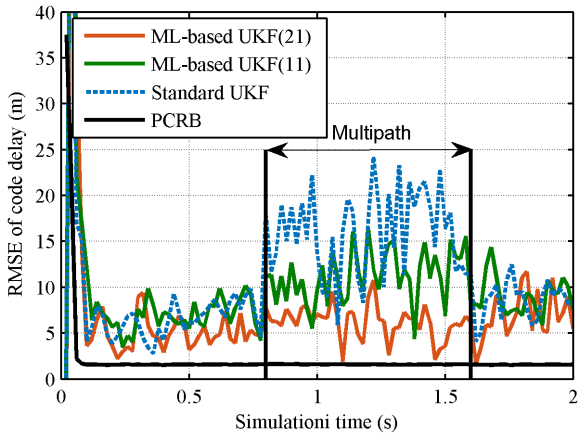

Figure 3.5 – RMSEs of LOS signal code delay in Scenario 3.

of MP interference changes quickly with time. This situation often happens when the receiver is located in intensive obstruction scenarios. As shown in Figure 3.5, the RMSEs of the LOS code delay fluctuate strongly since the MP relative code delay takes a random value in this scenario. Moreover, the performance of each approach is similar to that obtained in Scenario 2, the ML-based UKF(21) reaching the best performance. Our results prove that the proposed approach is more robust than the standard UKF due to the fact that it corrects the presence of abrupt changes corrupting the LOS signal acquired by the receiver in the presence of MP interferences.

3.6 Conclusion

This chapter studied a maximum likelihood-based UKF to estimate the LOS signal parameters in the presence of MP interferences. In order to fully characterize the impact of MP signals on the correlation function, a multi-correlator based receiver, constructing samples of the whole correlation function, was considered. A dynamic model associated with the time propagation of LOS signal parameters and a likelihood model associated with the MP signal parameters were used. Then the signal parameters were estimated iteratively by the proposed approach, i.e., an interval grid search based on the maximum likelihood principle was implemented to estimate the MP signal parameters by using the estimators of the LOS signal parameters, and an UKF method was developed to estimate the LOS signal parameters from estimators of the MP signal parameters. A simulation study was conducted in order to compare the performance of the proposed approach with the standard UKF. In the absence of MP interferences, the performance of the proposed approach is equivalent to that of the standard UKF. On the contrary, in the presence of MP interferences, the estimation accuracy for the LOS signal parameters, especially for the code delay, can be improved by the proposed approach. Moreover, the proposed approach was shown to be more robust than the standard UKF being less sensitive to the abrupt change affecting the received measurements in the presence of MP interferences.

CHAPTER

FOUR

A MARGINALIZED LIKELIHOOD RATIO APPROACH FOR DETECTING AND ESTIMATING MULTIPATH BIASES ON GNSS MEASUREMENTS

In the previous chapter, we proposed a multipath (MP) mitigation technique which operates inside the tracking loop stage of the GNSS receiver. However, this approach cannot be implemented in a commercial off-the-shelf receiver. Generally, such a receiver provides the position, velocity and time solution. Some receivers also deliver pseudo-range (PR) and Doppler measurements, as well as the satellite ephemeris. In this chapter, we attempt to detect and estimate MP biases by dealing with GNSS PR measurements.

In urban canyons, non-line-of-sight (NLOS) MP interferences affect position estimation based on GNSS. This chapter proposes to model the effects of NLOS MP interferences as mean value jumps contaminating the GNSS PR measurements. The marginalized likelihood ratio test (MLRT) is then investigated to detect, identify and estimate the corresponding NLOS MP biases. However, the MLRT test statistics is difficult to compute. Thus we consider a Monte Carlo (MC) integration technique based on bias magnitude sampling. Jensen's inequality allows this MC integration to be simplified. The multiple model algorithm is also used to update the prior information for each bias magnitude sample. Some strategies are designed for estimating and correcting the NLOS MP biases. In order to demonstrate the performance of the MLRT, simulations allowing several localization methods to be compared are performed. Finally, results from a measurement campaign conducted in an urban canyon are presented in order to evaluate the performance of the proposed algorithm in a representative environment.

4.1 Introduction

Generally, NLOS MP interferences frequently occur in urban canyons, where the direct path of a satellite signal is vulnerable to masking or blocking whereas reflected signals can be tracked within the receiver. In the NLOS MP interference situation, the reflected signal due to an MP interference can be converted to a bias appearing on the GNSS PR measurement [94, 95]. Thus this bias resulting from NLOS MP interferences can be detected and mitigated by GNSS measurement processing techniques as mentioned in Section 2.3.2. In this chapter, we propose an approximate marginalized likelihood ratio test based on Jensen's inequality to detect, identify and estimate the NLOS multipath biases affecting GNSS PR measurements. The test statistic resulting from the MLRT is approximated by an MC integration technique based on bias magnitude sampling. Jensen's inequality allows this MC integration to be simplified, and the multiple model algorithm is used to update the prior information for each bias magnitude sample. Some strategies are also designed for estimating and correcting the NLOS MP biases. The empirical cumulative distribution function of the approximate test statistic is analyzed and the corresponding detection threshold is determined via MC simulations. In addition, a comprehensive simulation study is implemented to compare the performance of the proposed approach with other state-of-the-art detection methods. Finally, the proposed approach is evaluated based on data obtained from a measurement campaign conducted in a street urban canyon.

4.2 System Description

4.2.1 State Model

In the framework of the application which considers vehicles moving slowing in an urban environment, we investigate a second-order model (i.e., a constant velocity model) to describe the dynamic of the vehicle in the earth-centered earth-fixed (ECEF) frame. Moreover, the GNSS receiver clock offset and its drift are taken into account. Therefore, the state model can be divided into two parts containing the position and velocity of the vehicle in the ECEF frame, and the receiver clock offset and drift, respectively. More precisely, the state vector considered in this paper is defined as follows [9]

$$\boldsymbol{X}_t = \left(x_t,\ \dot{x}_t,\ y_t,\ \dot{y}_t,\ z_t,\ \dot{z}_t,\ b_t,\ d_t\right)^{\mathrm{T}} \tag{4.1}$$

where $(x_t,\ y_t,\ z_t)$ and $(\dot{x}_t,\ \dot{y}_t,\ \dot{z}_t)$ are the vehicle position and velocity in the ECEF frame (Cartesian coordinate) respectively, b_t and d_t are the GNSS receiver clock offset and drift, $(\cdot)^{\mathrm{T}}$ is the transpose of a vector.

The velocity can be reasonably modelled as a random walk, e.g., $\ddot{x} = e_x$ where e_x is a zero mean Gaussian noise of variance σ_a^2. For short-term applications in which the periodical clock resets of

the GNSS receiver are not taken into account, the GNSS receiver clock offset b_t and its drift d_t can also be modelled as random walks, i.e., $\dot{b}_t = d_t + e_b$ and $\dot{d}_t = e_d$ where e_b and e_d are zero-mean Gaussian white noises of variance σ_b^2 and σ_d^2. Based on the above assumptions, the discrete-time state model which describes the propagation of the vehicle state $\boldsymbol{X}_t$ can be formulated as

$$\boldsymbol{X}_{k+1} = \boldsymbol{\Phi}_{k+1|k}\boldsymbol{X}_k + \boldsymbol{e}_k \tag{4.2}$$

where $k = 1, \ldots, K$ denotes the kth sampling time instant, $\boldsymbol{e}_k = \left(e_x,\ e_y,\ e_z,\ e_b,\ e_d\right)^{\mathrm{T}}$ is the zero mean Gaussian white noise vector of covariance matrix $\boldsymbol{Q}_k$. Considering a relative independence between the kinematic parameters and the GNSS clock parameters, the state matrix $\boldsymbol{\Phi}_{k+1|k}$ is a block-diagonal matrix. More precisely, the matrices $\boldsymbol{\Phi}_{k+1|k}$ and $\boldsymbol{Q}_k$ can be defined as follows

$$\boldsymbol{\Phi}_{k+1|k} = \begin{pmatrix} \boldsymbol{A}_k & \boldsymbol{0} \\ \boldsymbol{0} & \boldsymbol{C}_k \end{pmatrix} \text{ and } \boldsymbol{Q}_k = \begin{pmatrix} \boldsymbol{\Sigma}_k^a & \boldsymbol{0} \\ \boldsymbol{0} & \boldsymbol{\Sigma}_k^c \end{pmatrix} \tag{4.3}$$

where the block matrices $\boldsymbol{A}_k$, $\boldsymbol{C}_k$, $\boldsymbol{\Sigma}_k^a$ and $\boldsymbol{\Sigma}_k^c$ are

$$\boldsymbol{A}_k = \begin{pmatrix} \boldsymbol{C}_k & \boldsymbol{0} & \boldsymbol{0} \\ \boldsymbol{0} & \boldsymbol{C}_k & \boldsymbol{0} \\ \boldsymbol{0} & \boldsymbol{0} & \boldsymbol{C}_k \end{pmatrix},\ \boldsymbol{C}_k = \begin{pmatrix} 1 & \Delta t \\ 0 & 1 \end{pmatrix} \tag{4.4}$$

$$\boldsymbol{\Sigma}_k^a = \begin{pmatrix} \boldsymbol{Q}_k^a & \boldsymbol{0} & \boldsymbol{0} \\ \boldsymbol{0} & \boldsymbol{Q}_k^a & \boldsymbol{0} \\ \boldsymbol{0} & \boldsymbol{0} & \boldsymbol{Q}_k^a \end{pmatrix},\ \boldsymbol{Q}_k^a = \sigma_a^2 \begin{pmatrix} \frac{\Delta t^4}{4} & \frac{\Delta t^3}{2} \\ \frac{\Delta t^3}{2} & \Delta t^2 \end{pmatrix} \tag{4.5}$$

$$\boldsymbol{\Sigma}_k^c = \begin{pmatrix} \sigma_b^2 \Delta t^2 + \sigma_d^2 \frac{\Delta t^4}{4} & \sigma_d^2 \frac{\Delta t^3}{2} \\ \sigma_d^2 \frac{\Delta t^3}{2} & \sigma_d^2 \Delta t^2 \end{pmatrix} \tag{4.6}$$

and where Δt represents the time interval between two successive sampling instants.

4.2.2 Measurement Model in the Presence of MP

We assume that the GNSS system model errors, such as the ephemeris prediction, the ionospheric delay and the tropospheric delay error, have been corrected or compensated using model correction parameters which are contained in the received GNSS navigation data. As the GNSS receiver tracking loops filter MP interferences whose relative delays vary with time, only the MP interferences resulting in a constant bias affecting the pseudo-range measurements (during the observation period) are considered in this work. Thus we introduce a mean value jump affecting the GNSS PR measurements in the presence of NLOS MP interferences. Consequently, the mth in-view satel-

lite PR measurement model including an NLOS MP bias can be defined as [9, 74]

$$Z_k^m = \sqrt{\left(x_k^m - x_k\right)^2 + \left(y_k^m - y_k\right)^2 + \left(z_k^m - z_k\right)^2} + b_k + v_{k,\theta}^m + e_k^m \tag{4.7}$$

where Z_k^m $(m = 1, \ldots, N_s)$ is the PR measurement associated with the mth in-view satellite, N_s is the number of in-view satellites, $(x_k^m,\ y_k^m,\ z_k^m)$ and $(x_k,\ y_k,\ z_k)$ are the mth satellite position and the vehicle position in the ECEF frame, b_k is the GNSS receiver clock offset, $v_{k,\theta}^m$ is the magnitude of the NLOS MP bias associated with the mth PR measurement, characterized by the parameter θ which represents the possible occurrence time of the NLOS MP bias ($\theta = k$ for $v = 0$), and e_k^m is the mth satellite PR measurement noise with a normal distribution $e_k^m \sim \mathcal{N}\left(0, \sigma_r^2\right)$ where $\mathcal{N}(\cdot)$ is a univariate Gaussian distribution with mean value 0 and variance σ_r^2.

In (4.7), the PR measurement related to the vehicle position is defined by a non-linear equation of the vehicle position. An unscented Kalman filter (UKF) and a particle filter (PF) could be investigated with the advantage to estimate the state of this non-linear estimation problem. However, the corresponding computational costs of these filters can be prohibitive for practical applications. Thus, we consider in this chapter an extended Kalman filter (EKF) which leads to apply a conventional Kalman filter (KF) by linearizing the non-linear equations (4.7) and is known to provide an efficient and low-cost solution for weakly non-linear systems.

4.3 NLOS Bias Detection Based on MLRT

4.3.1 Problem Formulation

In the NLOS situation, we propose to model the MP interference as a mean value jump affecting the GNSS PR measurements. We assume that NLOS MP biases do not appear simultaneously on different PR measurements and that the PR measurement which is affected by NLOS MP bias is known. The case of multiple NLOS MP interferences appearing simultaneously on different PR measurements will be discussed in the next section. Assuming that only the mth satellite measurement is contaminated, the NLOS MP bias vector for the PR measurements is denoted as $\boldsymbol{v} = (0, \ldots, v, \ldots, 0) \in \mathbb{R}^{N_s}$ where the only non-zero element of v is located at the known position m.

According to the hypothesis testing theory, the likelihood ratio test (LRT) for detecting the presence or absence of a mean value jump is a binary hypothesis test which compares two likelihoods functions associated with the absence (H_0) and presence (H_1) of a mean value jump in the measurements. The two hypotheses considered in this paper are defined as follows

H_0 : no mean value jump up to present time k,

H_1 : a mean value jump (of amplitude $v \neq 0$) has occurred at time $\theta < k$.

The log-likelihood ratio (LLR) for these two hypotheses is

$$l_k(\theta, \upsilon) = \ln \frac{p(\boldsymbol{Z}_{1:k}|\mathrm{H}_1(\theta, \upsilon))}{p(\boldsymbol{Z}_{1:k}|\mathrm{H}_0)} \tag{4.8}$$

where $\boldsymbol{Z}_{1:k} = \{\boldsymbol{Z}_i\}_{i=1}^k$ is the PR measurement vector sequence up to time k with $\boldsymbol{Z}_i = \left(Z_i^1, \ldots, Z_i^{N_s}\right)$, and N_s is the number of in-view satellites. Note that we have denoted as $p(\boldsymbol{Z}_{1:k}|\mathrm{H}_1(\theta, \upsilon))$ and $p(\boldsymbol{Z}_{1:k}|\mathrm{H}_0)$ the probability density functions (pdf) of the measurement vector associated with the hypotheses H_1 and H_0 respectively.

In the likelihood ratio test, the occurrence time and the magnitude of the mean value jump denoted as θ and υ are assumed to be known. However, in practice the jump magnitude υ is unknown and can be regarded as a nuisance parameter for the LRT. According to the literature, there are two classes of methods for eliminating the nuisance parameter υ. The first method consists of replacing the nuisance parameter by its maximum likelihood estimator (MLE) (maximizing the likelihood function) in the pdf $p(\boldsymbol{Z}_{1:k}|\mathrm{H}_1(\theta, \upsilon))$ leading to the generalized likelihood ratio test (GLRT) [96]. The second method marginalizes the LLR with respect to the nuisance parameter yielding the marginalized likelihood ratio test (MLRT) [97]. The key point of the GLRT based on a state space model is that the MLE of parameter υ can be obtained by the innovation of an appropriate Kalman filter [98]. Contrary to the GLRT, the nuisance parameter υ is eliminated by marginalization of the likelihood function under the hypothesis H_1 in the MLRT. In [99], Gustafsson proposed an MLRT approach based on a state space model as a more robust method for bias detection. Accordingly, different bias detection approaches have been developed based on the MLRT. For instance, Dos Santos proposed in [100] the maximum a posteriori (MAP) criterion based on the marginalization of the likelihood function with a gamma prior distribution. Kiasi proposed in [101] a modified MLRT with a uniform distribution to estimate the occurrence time of fault. Unfortunately, the marginal likelihood function under hypothesis H_1 is generally difficult to compute in the MLRT. An alternative was proposed by Giremus in [102] where a numerical solution of the MLRT based on the unscented transform was used for bias detection in space state models. The method studied in [102] introduced a prior distribution for the nuisance parameter υ which can be obtained from our experience about MP or from previous experiments. This work studies a similar approach which differs from [102] by the use of an approximation based on Jensen's inequality, as explained below. According to the error envelope of MP interferences (which is a function of the MP relative delay interfering the direct signal for a given GNSS receiver configuration [1, 94]), a possible prior distribution for the MP bias with magnitude υ is a uniform distribution defined by $p(\upsilon) \sim \mathrm{U}(\upsilon_{\min}, \upsilon_{\max})$ where $\mathrm{U}(\cdot)$ denotes the uniform distribution, $\upsilon_{\min}$ and $\upsilon_{\max}$ are the minimum and maximum magnitudes of the MP bias, respectively. This distribution reflects the fact that the only knowledge about MP biases is their minimum and maximum values that have to be specified by the user, depending on the environment. Using this prior distribution for the nuisance parameter, we propose an approximate MLRT

based on Jensen's inequality to detect the occurrence time of NLOS MP biases.

The marginalization of (4.8) with respect to v leads to

$$l_k(\theta) = \ln \frac{p(\boldsymbol{Z}_{1:k}|\mathrm{H}_1(\theta))}{p(\boldsymbol{Z}_{1:k}|\mathrm{H}_0)} \tag{4.9}$$

where

$$p(\boldsymbol{Z}_{1:k}|\mathrm{H}_1(\theta)) = \int p(\boldsymbol{Z}_{1:k}|\mathrm{H}_1(\theta, v))\, p(v)\, \mathrm{d}v \tag{4.10}$$

and where $p(v)$ is the prior distribution of v. Considering that the integral in (4.10) is difficult to compute in closed-form, an MC integration method can be used to evaluate (4.10). According to the MC integration, (4.10) is approximated as

$$p(\boldsymbol{Z}_{1:k}|\mathrm{H}_1(\theta)) \approx \sum_{i=1}^{n} \omega^i p(\boldsymbol{Z}_{1:k}|\mathrm{H}_1(\theta, v_i)) \tag{4.11}$$

where v_i $(i = 1, \ldots, n)$ is the ith sampling value of the MP bias magnitude belonging to the interval $(v_{\min}, v_{\max})$, and n is the number of magnitude samples. Accordingly, a group of NLOS MP bias vectors (denoted as $(\boldsymbol{v}_i = (0, \ldots, v_i, \ldots, 0)$ for $i = 1, \ldots, n)$ are generated with weights $\omega^i = 1/n$ such that $\sum_{i=1}^{n} \omega^i = 1$. As a consequence, the test statistic $l_k(\theta)$ in the MLRT can be approximated as

$$l_k(\theta) = \ln \frac{p(\boldsymbol{Z}_{1:k}|\mathrm{H}_1(\theta))}{p(\boldsymbol{Z}_{1:k}|\mathrm{H}_0)} \approx \ln \frac{\sum_{i=1}^{n} \omega^i p(\boldsymbol{Z}_{1:k}|\mathrm{H}_1(\theta, v_i))}{p(\boldsymbol{Z}_{1:k}|\mathrm{H}_0)}. \tag{4.12}$$

By decomposing the PR measurement vector sequence as $\boldsymbol{Z}_{1:k} = \{\boldsymbol{Z}_{1:\theta-1}, \boldsymbol{Z}_{\theta:k}\}$, the probability density functions of the measurement vector associated with the hypotheses H_1 and H_0 can be rewritten as

$$\begin{aligned} p(\boldsymbol{Z}_{1:k}|\mathrm{H}_1(\theta, v)) &= p(\boldsymbol{Z}_{\theta:k}|\boldsymbol{Z}_{1:\theta-1}, \mathrm{H}_1(\theta, v))\, p(\boldsymbol{Z}_{1:\theta-1}|\mathrm{H}_1(\theta, v)) \\ p(\boldsymbol{Z}_{1:k}|\mathrm{H}_0) &= p(\boldsymbol{Z}_{\theta:k}|\boldsymbol{Z}_{1:\theta-1}, \mathrm{H}_0)\, p(\boldsymbol{Z}_{1:\theta-1}|\mathrm{H}_0). \end{aligned} \tag{4.13}$$

Since $v = 0$ for $k < \theta$, using (4.13) in (4.12) leads to

$$l_k(\theta) = \ln \frac{\sum_{i=1}^{n} \omega^i p(\boldsymbol{Z}_{\theta:k}|\boldsymbol{Z}_{1:\theta-1}, \mathrm{H}_1(\theta, v_i))}{p(\boldsymbol{Z}_{\theta:k}|\boldsymbol{Z}_{1:\theta-1}, \mathrm{H}_0)}. \tag{4.14}$$

The MLE of the occurrence time θ is

$$\hat{\theta} = \arg\max_{\theta} l_k(\theta). \tag{4.15}$$

The presence of a mean value jump is decided using the following MLRT rule

$$l_k(\hat{\theta}) \underset{\mathrm{H}_0}{\overset{\mathrm{H}_1}{\gtrless}} \varepsilon \tag{4.16}$$

where ε is a threshold related to the probability of false alarm of the test. In order to reduce the computational complexity, the optimization of θ is constrained to the last L_w units of time, i.e., $k-L_w<\theta\leq k$ at any time k, where L_w is the window length.

4.3.2 An Approximate MLRT Based on Jensen's Inequality

According to the Kalman filter theory, the denominator of (4.14) which is the likelihood function associated with the hypothesis H_0 can be defined as

$$p(\boldsymbol{Z}_{\theta:k}|\boldsymbol{Z}_{1:\theta-1},\mathrm{H}_0)=\prod_{j=\theta}^{k}p\left(\boldsymbol{Z}_j|\boldsymbol{Z}_{1:j-1},\mathrm{H}_0\right) \tag{4.17}$$

with

$$p\left(\boldsymbol{Z}_j|\boldsymbol{Z}_{1:j-1},\mathrm{H}_0\right)=\mathcal{N}\left(\boldsymbol{Z}_j;\hat{\boldsymbol{Z}}^0_{j|j-1},\boldsymbol{S}^0_j\right)=p\left(\boldsymbol{\gamma}^0_j|\mathrm{H}_0\right)$$

where $\mathcal{N}\left(\boldsymbol{Z}_j;\hat{\boldsymbol{Z}}^0_{j|j-1},\boldsymbol{S}^0_j\right)$ is the normal distribution with mean $\hat{\boldsymbol{Z}}^0_{j|j-1}$ and covariance matrix $\boldsymbol{S}^0_j$, $\boldsymbol{\gamma}^0_j=\boldsymbol{Z}_j-\hat{\boldsymbol{Z}}^0_{j|j-1}$ and $\boldsymbol{S}^0_j$ are the filter innovation vector and covariance matrix under the hypothesis H_0 at time j, $\boldsymbol{Z}_j$ and $\hat{\boldsymbol{Z}}^0_{j|j-1}$ are the PR measurement and predicted measurement vectors under the hypothesis H_0 at time j, respectively. Thus, the numerator of (4.14) is a weighted sum of likelihood functions associated with different mean value jump hypotheses with magnitudes v_i $(i=1,\ldots,n)$. Indeed the likelihood function under the hypothesis of a mean value jump with magnitude v_i is

$$p(\boldsymbol{Z}_{\theta:k}|\boldsymbol{Z}_{1:\theta-1},\mathrm{H}_1(\theta,v_i))=\prod_{j=\theta}^{k}p\left(\boldsymbol{Z}_j|\boldsymbol{Z}_{1:j-1},\mathrm{H}_1(\theta,v_i)\right) \tag{4.18}$$

with

$$p\left(\boldsymbol{Z}_j|\boldsymbol{Z}_{1:j-1},\mathrm{H}_1(\theta,v_i)\right)=\mathcal{N}\left(\boldsymbol{Z}_j;\hat{\boldsymbol{Z}}^i_{j|j-1},\boldsymbol{S}^i_j\right)=p\left(\tilde{\boldsymbol{\gamma}}^i_j|\mathrm{H}_1(\theta,v_i)\right)$$

where $\tilde{\boldsymbol{\gamma}}^i_j=\boldsymbol{\gamma}^0_j-\boldsymbol{v}_i$ and $\boldsymbol{S}^i_j$ are the filter innovation vector and its associated covariance matrix under the hypothesis H_1 with a bias magnitude v_i at time j. Note that $\hat{\boldsymbol{Z}}^i_{j|j-1}$ is the predicted measurement vector under the hypothesis H_1 with a bias magnitude v_i at time j.

After replacing (4.17) and (4.18) in (4.14), the MLRT test statistic based on the MC integration can be expressed as follows

$$\begin{aligned} l_k(\theta)&=\ln\frac{\sum_{i=1}^{n}\omega^i\prod_{j=\theta}^{k}\mathcal{N}\left(\boldsymbol{Z}_j;\hat{\boldsymbol{Z}}^i_{j|j-1},\boldsymbol{S}^i_j\right)}{\prod_{j=\theta}^{k}\mathcal{N}\left(\boldsymbol{Z}_j;\hat{\boldsymbol{Z}}^0_{j|j-1},\boldsymbol{S}^0_j\right)}\\ &=\ln\frac{\sum_{i=1}^{n}\omega^i\prod_{j=\theta}^{k}p\left(\tilde{\boldsymbol{\gamma}}^i_j|\mathrm{H}_1(\theta,v_i)\right)}{\prod_{j=\theta}^{k}p\left(\boldsymbol{\gamma}^0_j|\mathrm{H}_0\right)}. \end{aligned} \tag{4.19}$$

According to (4.19), it is clear that the multiplication of several normal pdfs in the denominator

can be easily handled by the logarithm function. Conversely, the numerator of (4.19) is a weighted sum of normal pdfs and thus is not easily tractable after the logarithm operation. Since the natural logarithm is a concave function over its range, Jensen's inequality [103] can be advocated leading to

$$\ln\left[\sum_{i=1}^{n}\lambda_i \mathrm{g}(x_i)\right] \geq \sum_{i=1}^{n}\lambda_i \ln \mathrm{g}(x_i) \tag{4.20}$$

where $\mathrm{g}(\cdot)$ is any functional, $\lambda_i > 0$ and $\sum_{i=1}^{n}\lambda_i = 1$. Expanding the numerator of (4.19), (4.20) leads to

$$\ln\sum_{i=1}^{n}\omega^i \prod_{j=\theta}^{k} p\left(\tilde{\boldsymbol{r}}_j^i|\mathrm{H}_1(\theta, v_i)\right) \geq \sum_{i=1}^{n}\omega^i \ln\prod_{j=\theta}^{k} p\left(\tilde{\boldsymbol{r}}_j^i|\mathrm{H}_1(\theta, v_i)\right). \tag{4.21}$$

After replacing (4.21) in (4.19), the test statistic $l_k(\theta)$ can be rewritten as follows

$$l_k(\theta) = \ln\frac{\sum_{i=1}^{n}\omega^i \prod_{j=\theta}^{k} p\left(\tilde{\boldsymbol{r}}_j^i|\mathrm{H}_1(\theta, v_i)\right)}{\prod_{j=\theta}^{k} p\left(\boldsymbol{r}_j^0|\mathrm{H}_0\right)} \geq \sum_{i=1}^{n}\omega^i \ln\prod_{j=\theta}^{k} p\left(\tilde{\boldsymbol{r}}_j^i|\mathrm{H}_1(\theta, v_i)\right) - \ln\prod_{j=\theta}^{k} p\left(\boldsymbol{r}_j^0|\mathrm{H}_0\right) \triangleq \frac{1}{2}\tilde{l}_k'(\theta), \tag{4.22}$$

i.e.,

$$\tilde{l}_k'(\theta) = \left[\sum_{j=\theta}^{k}\left(\boldsymbol{r}_j^0\right)^{\mathrm{T}}\left(\boldsymbol{S}_j^0\right)^{-1}\left(\boldsymbol{r}_j^0\right) - \sum_{i=1}^{n}\omega^i\sum_{j=\theta}^{k}\left(\tilde{\boldsymbol{r}}_j^i\right)^{\mathrm{T}}\left(\boldsymbol{S}_j^i\right)^{-1}\left(\tilde{\boldsymbol{r}}_j^i\right)\right] + K' \tag{4.23}$$

where

$$K' = \sum_{j=\theta}^{k}\ln\left|\boldsymbol{S}_j^0\right| - \sum_{i=1}^{n}\omega^i\sum_{j=\theta}^{k}\ln\left|\boldsymbol{S}_j^i\right|$$

is independent of the measurements. According to (4.23), in order to obtain filter innovations based on n measurement equations, several measurement equations (as many measurement equations as the number of bias magnitude samples) have to be processed in parallel and the contributions of all these measurement equations are weighted by ω^i. In such case, each sample v_i corresponds to one measurement equation, and the weight of each measurement equation actually depends on how close the magnitude sample v_i is to the exact magnitude v. Thus, the weight associated with each measurement equation is time-varying (hidden Markov chain) and will be denoted as $\tilde{\omega}_j^i$ (weight of the ith measurement equation at time j). After replacing ω^i by $\tilde{\omega}_j^i$ in (4.23), the following result can be obtained

$$\tilde{l}_k(\theta) = \sum_{j=\theta}^{k}\left[\left(\boldsymbol{r}_j^0\right)^{\mathrm{T}}\left(\boldsymbol{S}_j^0\right)^{-1}\left(\boldsymbol{r}_j^0\right) - \sum_{i=1}^{n}\tilde{\omega}_j^i\left(\tilde{\boldsymbol{r}}_j^i\right)^{\mathrm{T}}\left(\boldsymbol{S}_j^i\right)^{-1}\left(\tilde{\boldsymbol{r}}_j^i\right)\right] + K \tag{4.24}$$

where

$$K = \sum_{j=\theta}^{k}\left[\ln\left|\boldsymbol{S}_j^0\right| - \sum_{i=1}^{n}\tilde{\omega}_j^i \ln\left|\boldsymbol{S}_j^i\right|\right].$$

Finally, using the previous derivations, the presence of a mean value jump is accepted or rejected using the following rule

$$\tilde{l}_k(\theta) \underset{\mathrm{H}_0}{\overset{\mathrm{H}_1}{\gtrless}} \varepsilon' \tag{4.25}$$

where ε' is a threshold related to the probability of false alarm of the test. The parameter θ is then replaced by its MLE $\hat{\theta}$ defined as

$$\hat{\theta} = \arg\max_{\theta} \tilde{l}_k(\theta). \tag{4.26}$$

The rest of this section discusses how to adjust the weights $\tilde{\omega}_j^i$ defining $\tilde{l}_k(\theta)$. Considering that several measurement equations need to be processed in parallel, $\tilde{\omega}_j^i$ can be computed based on the multiple model (MM) algorithm which is defined in [90]. A set of measurement models associated with the jump magnitude samples v_i $(i = 1, \ldots, n)$ is denoted as

$$\boldsymbol{M} \triangleq \left\{M^i\right\}_{i=1}^n \tag{4.27}$$

where $M^i = (0, \ldots, v_i, \ldots, 0)$ and the corresponding model probability $\tilde{\omega}_j^i$ can be obtained based on the current measurement $\boldsymbol{Z}_j$ and the predicted model probability, leading to

$$\begin{aligned} \tilde{\omega}_j^i &= p\left(M_j^i | \boldsymbol{Z}_j\right) \\ &= \frac{1}{c} p\left(\tilde{\boldsymbol{r}}_j^i | \mathrm{H}_1(\theta, v_i)\right) p\left(M_j^i | \boldsymbol{Z}_{j-1}\right) \end{aligned} \tag{4.28}$$

where $j = \theta, \ldots, k$ and c is the normalization constant.

4.4 Identification/Estimation/Correction of NLOS MP Biases

According to the test statistic $\tilde{l}_k(\theta)$ resulting from the approximate MLRT derived in Section 4.3, the occurrence time of the NLOS MP bias can be estimated. In order to determine which PR measurements are affected by NLOS MP biases, we study in this section a simultaneous detection and identification procedure which allows NLOS MP biases appearing simultaneously on different PR measurements to be handled. Note that the PR measurements associated with a mean value jump can be isolated after the presence of an MP interference has been confirmed by the bias detection methods, such as the receiver autonomous integrity monitoring (RAIM) method [9] and the method of [102]. However, considering that the number of in-view satellites is limited in urban scenarios, the exclusion of PR measurements may weaken the observability and impair the accuracy of positioning solution based on GNSS. In order to implement the positioning solution with a maximum of PR measurements, we propose in this paper to estimate the NLOS MP biases for correcting measurement errors related to these biases. All these operations referred to as identification, estimation and correction are detailed below.

4.4.1 Identification of NLOS MP Biases

In order to make identification possible, a possible method is to compute one MLRT test statistic for each in-view satellite PR measurement. In this case, two hypotheses for detecting the presence of an NLOS MP bias on the mth ($m = 1, \ldots, N_s$) in-view satellite PR measurement can be defined as follows

H_0^m : no mean value jump for the mth measurement up to present time k,
H_1^m : a mean value jump (of amplitude $v^m \neq 0$) has occurred for the mth measurement at time $\theta < k$.

The detection and identification of NLOS MP biases can be converted into a group of hypothesis tests for all PR measurements. The corresponding test statistic $\tilde{l}_k^m(\theta)$ ($m = 1, \ldots, N_s$) associated with the hypothesis of an NLOS MP bias affecting the mth in-view satellite PR measurement from time θ to k, can be obtained based on the approximate MLRT theory presented in Section 4.3. The MLE of the occurrence time θ associated with the mth measurement is finally defined as

$$\hat{\theta}^m = \arg\max_{\theta} \tilde{l}_k^m(\theta). \tag{4.29}$$

For detecting the presence of an NLOS MP bias at a possible occurrence time $\hat{\theta}^m$, the decision rule can be defined as

$$\tilde{l}_k^m\left(\hat{\theta}^m\right) \underset{\mathrm{H}_0^m}{\overset{\mathrm{H}_1^m}{\gtrless}} \varepsilon' \tag{4.30}$$

where ε' is the mth hypothesis threshold related to a given probability of false alarm. In order to simplify the computation, a set of possible amplitudes (for the NLOS MP biases) v_i ($i = 1, \ldots, n$) can be uniformly sampled in the interval ($v_{\min}$, $v_{\max}$), and used for each calculation of the test statistic $\tilde{l}_k^m(\theta)$. Finally, it is important for the simultaneous detection and identification to ensure that the proposed approximate MLRT can handle several NLOS MP biases occurring at the same time instant.

4.4.2 Estimation and Correction of NLOS MP Biases

The optimization of $\hat{\theta}$ is constrained to the data belonging to a finite window ($k - L_w < \hat{\theta} \leq k$). Since the bias detection has to be performed in real time, the value of L_w is set to a relatively small value, i.e., $L_w = 11$ in [98] or $L_w = 5$ in [99]. Note that a larger threshold could be chosen to control the probability of false alarm.

After it has been detected that the mth satellite PR measurement is affected by an NLOS MP interference, we propose to estimate the magnitude of the NLOS MP bias. The MM algorithm is used to update the measurement model probabilities associated with the magnitude samples defining

the proposed approximate MLRT. Thus the model probability $\tilde{\omega}_j^i$ depends on how close the magnitude sample v_i is to the exact magnitude v and can adaptively adjust for each magnitude sample v_i $(i = 1, \ldots, n)$. The bias magnitude estimation $\hat{v}^m\left(\hat{\theta}_k^m\right)$ for the mth in-view satellite PR measurement at time k can be defined as

$$\hat{v}^m\left(\hat{\theta}_k^m\right) = v_{\hat{\imath}_k} + \hat{r}_{\hat{\imath}_k}^m\left(\hat{\theta}_k^m\right) \tag{4.31}$$

with

$$\hat{\imath}_k = \arg\max_i \tilde{\omega}_k^i \tag{4.32}$$

and

$$\hat{r}_{\hat{\imath}_k}^m\left(\hat{\theta}_k^m\right) = \frac{1}{k - \hat{\theta}_k^m + 1} \sum_{j=\hat{\theta}_k^m}^{k} \tilde{\gamma}_{\hat{\imath}_k, j}^m \tag{4.33}$$

where n is the number of bias magnitude samples, $\hat{\theta}_k^m$ is the MLE of the occurrence time θ associated with the mth measurement at time k, $v_{\hat{\imath}_k}$ is the $\hat{\imath}_k$th sampling value of the NLOS MP bias magnitude, $\tilde{\gamma}_{\hat{\imath}_k, j}^m = Z_j^m - \hat{Z}_{\hat{\imath}_k, j|j-1}^m$ is the filter innovation under the hypothesis H_1^m with a bias sampling magnitude $v_{\hat{\imath}_k}$, Z_j^m and $\hat{Z}_{\hat{\imath}_k, j|j-1}^m$ are the mth in-view satellite PR and predicted PR measurements under the hypothesis H_1^m with a bias sampling magnitude $v_{\hat{\imath}_k}$ at time j, respectively.

Once the NLOS MP bias and its magnitude have been detected and estimated, we propose to correct the corresponding filter innovation and to use it for the positioning solution based on the standard EKF algorithm. For the mth PR measurement which is affected by the NLOS MP bias, the corresponding filter innovation can be corrected as follows

$$\bar{\gamma}_k^m = \gamma_k^m - \hat{v}^m\left(\hat{\theta}_k^m\right) \tag{4.34}$$

where $\bar{\gamma}_k^m$ is the corrected filter innovation which will be used in the EKF algorithm at time k, $\gamma_k^m = Z_k^m - \hat{Z}_{k|k-1}^m$ is the filter innovation under the hypothesis H_0^m at time k, $\hat{Z}_{k|k-1}^m$ is the predicted PR measurement of the mth in-view satellite under the hypothesis H_0^m at time k.

Note that the objective of correcting the filter innovation rather than the PR measurement itself is to enable the detection of an NLOS MP bias during its whole duration. Finally, an approximate MLRT to detect, estimate and correct the NLOS MP biases is summarized in Algorithm 1.

Algorithm 1: The approximate MLRT to detect, estimate and correct NLOS MP biases in GNSS signals.

%Initialization

$\hat{\boldsymbol{X}}_0 \sim p(\boldsymbol{X}_0)$

$v_i \sim \mathrm{U}(v_{\min}, v_{\max})$ | $i = 1, \ldots, n$

$\tilde{\boldsymbol{\omega}}_{m,0} = \left(\tilde{\omega}^1_{m,0}, \ldots, \tilde{\omega}^n_{m,0}\right)$ and $\tilde{\omega}^i_{m,0} = 1/n$ | $m = 1, \ldots, N_s$

%Time propagation

for $k = 1, \ldots, K$ **do**

%State and measurement prediction in the EKF

Compute $\hat{\boldsymbol{X}}_{k|k-1}$ and $\boldsymbol{P}_{k|k-1}$ according to (4.2)

Compute $\hat{\boldsymbol{Z}}^0_{k|k-1} = \left(\hat{Z}^0_{1,k|k-1}, \ldots, \hat{Z}^0_{N_s,k|k-1}\right)^{\mathrm{T}}$ according to (4.7)

%Innovation update under different hypotheses

$\gamma^0_{m,k} = Z_{m,k} - \hat{Z}^0_{m,k|k-1}$ | **for** $m = 1, \ldots, N_s$

$\tilde{\gamma}^i_{m,k} = \gamma^0_{m,k} - v_i$ | **for** $i = 1, \ldots, n$

%Weight prediction and update for bias magnitude samples

$\tilde{\omega}^i_{m,k|k-1} \propto \sum_{i=1}^n \Lambda_i \tilde{\boldsymbol{\omega}}_{m,k-1|k-1}$ | **for** $m = 1, \ldots, N_s$

$\tilde{\omega}^i_{m,k|k} \propto p\left(\tilde{\gamma}^i_{m,k} | \mathrm{H}_1(\theta, v_i)\right) \tilde{\omega}^i_{m,k|k-1}$ | **for** $i = 1, \ldots, n$

%Λ_i is the ith column of the Markov chain transition matrix used in the MM

%$\tilde{\gamma}^i_{m,k} = Z_{m,k} - \hat{Z}^i_{m,k|k-1}$ where $Z_{m,k}$ and $\hat{Z}^i_{m,k|k-1}$ are the mth in-view satellite PR and predicted PR

%measurements under the hypothesis H^m_1 with a bias sampling magnitude v_i at time k

%MP bias detection, estimation and correction

for $m = 1, \ldots, N_s$ **do**

Compute $\tilde{l}^m_k(\theta)$ and ε' according to (4.24) and (4.36)

Set $\hat{\theta}^m_k = \arg\max_\theta \tilde{l}^m_k(\theta)$ $(k - L_w < \hat{\theta}^m_k \leq k)$

if $\tilde{l}^m_k > \varepsilon'$ a bias is detected

Compute $\hat{v}^m\left(\hat{\theta}^m_k\right)$ according to (4.31)

Correct the mth filter innovation according to (4.34)

end if

end for

%State estimation in the EKF

Compute $\hat{\boldsymbol{X}}_{k|k}$ and $\boldsymbol{P}_{k|k}$

end for

4.5 Test Threshold Analysis

According to the hypothesis testing theory, the MLRT threshold can be determined from the cumulative distribution function (cdf) of the test statistic under hypothesis H_0 and the significance level α (false alarm rate). Based on the aforementioned derivations, the test statistic $\tilde{l}(\theta)$ of the proposed approximate MLRT in (4.24) was derived from the test statistic $l(\theta)$ of the MLRT in (4.19). However, the cdfs of the test statistics $l^m(\theta)$ and $\tilde{l}^m(\theta)$ under hypothesis H_0^m have not a closed-form expression when the NLOS MP bias has a uniform distribution. Therefore, the empirical cdfs of the test statistics $l^m(\theta)$ and $\tilde{l}^m(\theta)$ under hypothesis H_0^m have been computed by MC simulations performed using the parameters provided in Table 4.1. In addition, the state space model defined in Section 4.2 has been simulated with the parameters reported in Table 4.1 and the fault-free GNSS PR measurements have been computed based on an almanac file including all useful satellite orbit data in the simulations.

Table 4.1 – Simulation parameters.

Process noise (velocity)	$\sigma_a = 1$ m/s^2
Clock offset noise	$\sigma_b = 3c \times 10^{-10}$ m
Clock drift noise	$\sigma_d = 2\pi c \times 10^{-10}$ m/s
GNSS measurement noise	$\sigma_r = 10$ m

$c = 3 \times 10^8$ m/s denotes the velocity of light.

The empirical cdfs of the test statistics $l^m(\theta)$ and $\tilde{l}^m(\theta)$ under hypothesis H_0^m can be defined as follows

$$\hat{F}_{l,n_s}(l) = \frac{1}{n_s}\sum_{i=1}^{n_s} I\left(l_i^m \le l|\mathrm{H}_0^m\right) \tag{4.35}$$

and

$$\hat{F}_{\tilde{l},n_s}(l) = \frac{1}{n_s}\sum_{i=1}^{n_s} I\left(\tilde{l}_i^m \le l|\mathrm{H}_0^m\right) \tag{4.36}$$

where I is the indicator function, $(l_1^m, \ldots, l_{n_s}^m)$ and $(\tilde{l}_1^m, \ldots, \tilde{l}_{n_s}^m)$ are n_s samples of the test statistics $l^m(\theta)$ and $\tilde{l}^m(\theta)$ under hypothesis H_0^m computed by MC simulations with a finite window length.

As depicted in Figure 4.1, the two empirical cdfs (computed with $L_w = 5$) satisfy the relation $\hat{F}_{l,n_s}(l) > \hat{F}_{\tilde{l},n_s}(l)$. Accordingly, the false alarm rates for the two empirical cdfs satisfy $\alpha' \ge \alpha$ when the test threshold is set as the same value for two empirical cdfs, where $\alpha = \hat{F}_{l,n_s}\left(l \ge \varepsilon|\mathrm{H}_0^m\right)$ and $\alpha' = \hat{F}_{\tilde{l},n_s}\left(l \ge \varepsilon|\mathrm{H}_0^m\right)$. Thus the false alarm rate α' can be considered as an upper bound for α when the test threshold is given.

The test threshold for the approximate MLRT can be determined by the empirical cdf $\hat{F}_{\tilde{l},n_s}(l)$ (which depends on the window length L_w) and the false alarm rate α'. The empirical cdfs of the test statistic $\tilde{l}^m(\theta)$ for different window lengths L_w are displayed in Figure 4.2. The corresponding

thresholds associated with different false alarm rates are given in Table 4.2. It is clear that the empirical cdf decreases as the window length increases. Accordingly, the test threshold is an increasing function of the window length L_w when the false alarm rate α' is given.

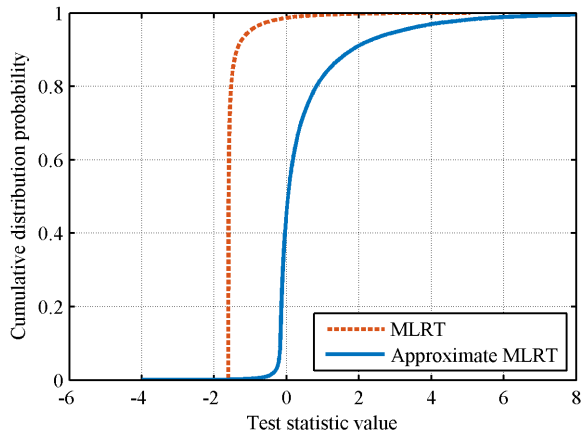

Figure 4.1 – Empirical cdfs of $\hat{F}_{l,n_s}(l)$ (dotted line) and $\hat{F}_{\tilde{l},n_s}(l)$ (solid line) for a data window length $L_w = 5$.

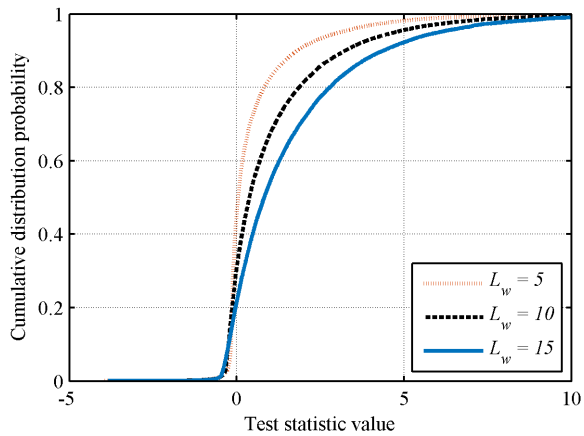

Figure 4.2 – Empirical cdfs associated with different data window lengths.

Table 4.2 – Threshold for different false alarm ratios.

Data window length L_w	False alarm rate		
	0.025	0.05	0.1
5	4.01	2.78	1.62
10	5.83	4.39	2.94
15	7.28	5.62	4.06

4.6 Algorithm Assessment

4.6.1 Simulation Results

Performance Measures and Test Scenarios

In order to evaluate the detection and identification performance of the proposed approximate MLRT approach, and to compare it with the approach studied in [102], the following performance measures have been used in this paper:

- **Average probability of correct detection** (denoted as P_{CD}): a correct detection is obtained when an NLOS MP bias has been detected and a bias is effectively present.
- **Average probability of correct detection and identification** (denoted as P_{CDI}): a correct detection and identification is obtained when an NLOS MP bias has been detected and when the bias sample associated with the largest model probability is the closest to the exact bias magnitude (at a given time).
- **Average probability of correct detection and incorrect identification** (denoted as P_{CDII}): a correct detection and incorrect identification is obtained when an NLOS MP bias has been detected and the bias sample associated with the largest model probability is not the closest to the exact bias magnitude (at a given time).
- **Mean detection delay and standard deviation of correct detection** (denoted as $\bar{\tau}$ (s) and σ (s) respectively): a mean detection delay time (s) is obtained by averaging 100 differences between the time instant of the first bias appearance and the time instant of the first bias detection

In order to evaluate the impact of different numbers of biases on the performance of the approximate MLRT, the MM algorithm has been tested with 3, 5 and 7 biases denoted as MLRT(3), MLRT(5) and MLRT(7), for all simulation scenarios. In theory, the PR MP error can reach magnitudes close to 0.5 of a code chip, i.e., 150 m in the C/A case, depending on the receiver correlation technology [1, 2]. We have assumed in this study that the prior distribution of the MP bias magnitude v is a uniform distribution in the interval (−75m, 75m), i.e., $p(v) \sim \mathrm{U}(-75, 75)$. The values of the MP bias magnitudes used in our simulations are summarized in Table 4.3.

Table 4.3 – Bias magnitude samples used for the MM.

	Bias sampling magnitudes (m)						
	1	2	3	4	5	6	7
MLRT(3)	-20	0	20				
MLRT(5)	-30	-20	0	20	30		
MLRT(7)	-35	-25	-15	0	15	25	35

Finally, it is assumed that there are 4 in-view satellite PR measurements during the simulation. In order to reduce the influence of false alarms, the threshold has been set to ensure a false alarm rate of 0.1. The length of the data window is $L_w = 5$ and the filter period equals 1 Hz in all simulations. All algorithms have been coded using MATLAB and run on a laptop with Intel i-7 4710MQ and 8GB RAM.

Results for Single MP Detection

Scenarios with different bias magnitudes have been generated according to the measurement model (4.7) and 100 MC runs. In each scenario, an NLOS MP bias with a deterministic magnitude appears on the first PR measurement (satellite #1) at the 100th second and the bias duration is 20s.

First, in order to evaluate the influence of Jensen's inequality used in (4.22) on the detection performances and on the computation load required to compute the test statistic $l(\theta)$ and $\tilde{l}(\theta)$, Table 4.4 shows the detection results and the execution times for 100 MC runs by using the different test statistics with 3 different bias samples. It is clear that the values of P_{CD} for the test statistic $l(\theta)$ and $\tilde{l}(\theta)$ are similar in each scenario. However, the execution time for $\tilde{l}(\theta)$ is much less than that for $l(\theta)$. Thus, without impacting the detection performance, Jensen's inequality can reduce the computation load of the MLRT.

Tables 4.5 and 4.6 show the detection performance and the delay measures for the GLRT and the approximate MLRT approaches with different bias samples. The results reported in Table 4.5 indicate that more than 70% of NLOS MP biases cannot be correctly detected for all approaches when the NLOS MP bias magnitude is less than or close to the measurement noise. The value of P_{CD} gradually increases with the NLOS MP bias magnitude for any detector, as expected. In addition, the value of P_{CD} is larger for the proposed approach than for the GLRT when the bias magnitude is small. This difference between the two detectors gradually disappears as the bias magnitude increases. Due to the excessive competition between too many models in the MM, P_{CDII} significantly increases with the number of models considered in the MM for the proposed approximate MLRT.

Table 4.4 – Detection performance using the different test statistics.

NLOS MP bias	$l(\theta)$		$\tilde{l}(\theta)$	
magnitude (m)	P_{CD}	Time (s)	P_{CD}	Time (s)
7	0.06	12.0477	0.05	10.9283
12	0.29	12.0416	0.26	10.9405
18	0.55	12.0378	0.62	10.9456
24	0.94	12.0125	0.98	10.9218
28	0.97	12.0239	0.95	11.0296
32	0.97	12.0198	0.97	10.8992

Table 4.5 – Detection performance for different scenarios.

NLOS MP bias magnitude (m)	MLRT(3)			MLRT(5)			MLRT(7)			GLRT
	P_{CD}	P_{CDI}	P_{CDII}	P_{CD}	P_{CDI}	P_{CDII}	P_{CD}	P_{CDI}	P_{CDII}	P_{CD}
7	0.05	-	-	0.07	-	-	0.10	-	-	0
12	0.26	0.20	0.06	0.30	0.27	0.03	0.24	0.18	0.06	0.14
18	0.62	0.57	0.05	0.59	0.34	0.25	0.74	0.32	0.42	0.40
24	0.98	0.97	0.01	0.90	0.59	0.31	0.94	0.45	0.49	0.61
28	0.95	0.95	0	0.97	0.61	0.36	0.96	0.47	0.49	0.93
32	0.97	0.97	0	0.96	0.50	0.46	0.98	0.47	0.51	0.98

Table 4.6 – Detection delay for different scenarios.

NLOS MP bias magnitude (m)	MLRT(3)		MLRT(5)		MLRT(7)		GLRT	
	$\bar{\tau}$	σ	$\bar{\tau}$	σ	$\bar{\tau}$	σ	$\bar{\tau}$	σ
7	6.54	-	6.34	-	7.86	-	8.67	-
12	4.23	3.17	4.63	3.04	4.58	3.21	4.75	4.56
18	1.14	2.39	1.27	1.55	1.38	1.79	1.78	3.59
24	-0.66	1.51	-0.94	1.53	-0.86	1.24	1.19	1.79
28	-0.56	1.43	0.76	1.36	-0.80	1.10	0.19	0.87
32	0.52	1.24	-0.71	1.34	-0.78	1.06	0.18	0.71

The results reported in Table 4.6 indicate that the detection delays for all approaches are decreasing functions of the NLOS MP bias magnitude. The decrease of detection delay for the approximate MLRT is smaller than with the GLRT as the bias magnitude increases. Although the mean detection delay and the standard deviation of the proposed approach are slightly inferior to those of the GLRT, the proposed approach significantly improves the probability of correct detection. Thus the proposed approach provides better bias detection performance than the GLRT for a single NLOS MP.

Results for Multiple MP Detection

In order to evaluate the detection performance in the presence of several NLOS MP biases appearing at the same time instant, a second scenario has been generated according to the measurement model (4.7) as follows:

- The first satellite PR measurement (satellite #1) is affected by a mean value jump of 28 m during the time interval (40s, 80s), and an NLOS MP bias of -26 m appears during the time interval (100s, 140s).
- The second satellite PR measurement (satellite #2) is affected by an NLOS MP bias of 32 m occurring during the time interval (70s, 150s).

Since the approach studied in [102] excludes a contaminated measurement after the presence of a mean value jump has been detected, we propose to compare 1) the multiple bias detection per-

formance of the proposed approach with that obtained using the approach of [102] and the GLRT, and 2) the positioning estimation accuracy of the proposed approach with that obtained using the standard EKF, the approach of [102] respectively. 100 MC simulations have been run for any scenario. The accurate detection times for multiple NLOS MP (denoted by M) is used to compute the root mean square errors (RMSE) of the estimates defined by $\sqrt{M^{-1}\sum_{i=1}^{M}\left(\hat{\boldsymbol{X}}_k^{(i)}-\boldsymbol{X}_k\right)^2}$, where $\hat{\boldsymbol{X}}_k^{(i)}$ is the ith run result, and $k=1,\ldots,K$ denotes the kth sampling time instant.

The accurate detection times for multiple NLOS MP are depicted in Figure 4.3. These results show that the detection performances of the proposed approximate MLRT and the approach studied in [102] are more reliable than for the GLRT due to the prior information considered for the bias magnitude. Moreover, the performance of the approach studied in [102] is close to that of the MLRT(3) and more models in the MM can facilitate the bias detection.

In order to evaluate the effect of different NLOS bias detection approaches on the positioning solution, the RMSEs of the estimated positions with different detection approaches in the Y-direction of the ECEF frame are depicted in Figure 4.4. The NLOS MP biases severely impair the positioning solution based on GNSS, as expected. Although the exclusion of contaminated PR measurements can partly improve the position accuracy, the accuracy obtained with the MLRT(7) is much better than that obtained with the approach of [102]. This improvement can be explained by the fact that the corrected PR measurements allow a better system observability.

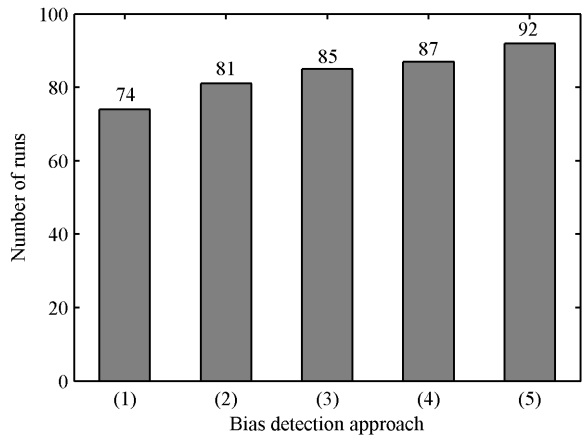

Figure 4.3 – Accurate detection times for multiple NLOS MP. The bias detection approaches corresponding to the sequence number in the figure are: (1)-GLRT; (2)-Approach in [102]; (3)-MLRT(3); (4)-MLRT(5); (5)-MLRT(7).

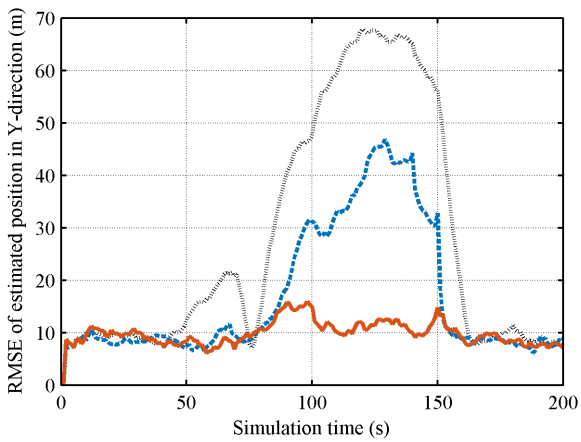

Figure 4.4 – RMSEs of positioning estimations with different detection approaches. The proposed approach: red solid line; The approach in [102]: blue dashed line; Standard EKF: black dotted line.

4.6.2 Experiment Results

Measurement Campaign

In this section, the proposed approach is evaluated based on experimental data collected during a measurement campaign carried out in Toulouse center (France). A synchronized integrated navigation system composed of a Novatel receiver coupled to a tactical grade IMAR IMU has been used to provide a reference trajectory. Taking advantage of a ground reference station, differential corrections have been performed to obtain position accuracy close to 1 m for the reference trajectory, which is considered as the ground truth. For assessing the algorithm performance, the vehicle has been equipped with a UBLOX 6T receiver. This receiver delivers not only the position, velocity and time solution, but also, for each satellite, the raw PR and Doppler frequency measurements, as well as the navigation message. It allows us to compute satellite locations, and to perform timing and propagation correction on the measured PR. As the aim of the algorithm is to detect and mitigate PR biases in presence of MP, Doppler frequencies that are related to the vehicle velocity are not used here. Data are collected in street urban canyons during which the receiver is strongly affected by MP interferences, and post-processed using Matlab.

Figure 4.5 shows the trajectory considered in our measurement campaign (lasting 230 s). Figure 4.6 displays the evolution of the trip distance (considered in our experiment) versus time, where the original point is defined as the initial position on the trajectory and the trip distance represents the horizontal distance travelled from the initial position. It is clear that the trip distance does not change during the time interval (71s, 154s), as the vehicle is stopped in the middle of two buildings during this period. In this case, the receiver is very sensitive to any MP interference. As it appears at the LOS frequency (The Doppler frequency related to the vehicle velocity is zero), PR measurements are severely impacted by MP interference during this period.

Figure 4.5 – Urban canyon trajectory used in the proposed experiments (obtained with Google Earth).

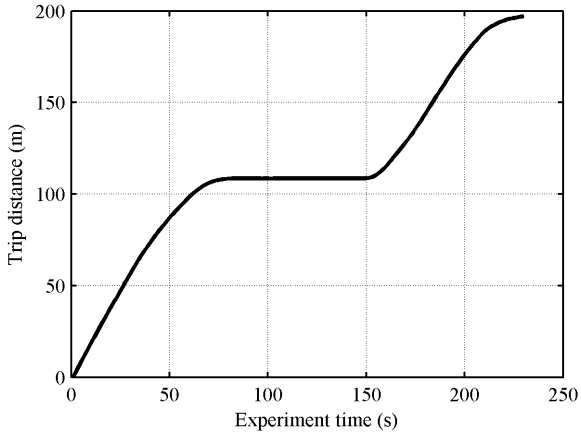

Figure 4.6 – Trip distance versus time.

We propose to compare the positioning estimation accuracy of the MLRT(5) with that obtained using the standard EKF. The in-view satellites observed during the experience are satellites #3, #6, #19, #26, and #27. The standard deviations, which are used to define the process and measurement noises are $\sigma_a = 0.4$ m/s^2 and $\sigma_r = 4$ m respectively. The bias sampling magnitudes considered in the MM for the MLRT(5) are set as (−8m, −4m, 0m, 4m, 8m) in order to make the algorithm sensitive to short-delay MP interferences which characterize urban canyons. Accordingly, we obtain five estimators corresponding to the different bias magnitudes referred to as estimators #1 : −8 m; #2 : −4 m; #3 : 0 m; #4 : 4 m; #5 : 8 m. The length of the data window is set to $L_w = 5$.

Results

The results reported in Table 4.7 indicate the MP appearance time period detected by the MLRT(5). According to the results of the detection algorithm, no MP interference impacting PR measurements has been detected for the satellites #3 and #27. Conversely, the PR measurements of satellites #6, #16 and #19, which are impacted by the MP interference, are detected by the proposed approach during the same period. The elevation angles of the different in-view satellites are also reported in Table 4.7. Note that the elevation angles for satellites #3, #6 and #27 are larger than 75°, whereas the elevation angles for satellites #16 and #19 are less than or equal to 60°. The signals from low-elevation-angle satellites, such as satellites #16 and #19, are usually vulnerable to the MP interferences in urban canyons. Conversely, the signals from satellites with high elevation angles, such as satellites #3 and #27, can hardly be impacted by the MP interferences. Accordingly, the detection results for MP appearance coincide with the in-view satellite elevations as reported in Table 4.7. As mentioned above, five measurement models associated with different bias sampling magnitudes in the MM are considered for MLRT(5). The estimators, which correspond to bias sampling magnitudes with the largest model probability for the detected time intervals, are indicated in Table 4.7. Since the magnitude of the MP interferences changes for different time instants, the magnitude of the bias sample associated with the largest model probability also changes with time.

Table 4.7 – Estimated MP appearance times.

In-view satellite	Satellite elevation (°)	Detected MP appearance time (s)	Bias sample with the largest model probability	
			Experiment time (s)	Sequence index
satellite #3	81.9 − 82.4	-	-	-
satellite #6	77.9 − 77.5	71 − 79	71 − 78	#3
			79 − 92	#2
			93 − 97	#1
satellite #16	56.1 − 55.5	42 − 113 127 − 182	42 − 46	#3
			47 − 49	#4
			50 − 113	#5
			127 − 129	#5
			130 − 131	#4
			132 − 182	#5
satellite #19	60.8 − 60.3	73 − 96 99 − 154	73 − 78	#3
			79 − 81	#4
			82 − 96	#5
			99 − 154	#5
satellite #27	82.95 − 82.92	-	-	-

Figures 4.7 and 4.8 display the positioning results (illustrated with Google Earth) and the corresponding positioning errors (the horizontal and vertical errors versus time) for the different approaches. It is clear that MP interferences severely impair the positioning solution if these interferences are not processed within the receiver. As shown in Figure 4.8, the time instances, from which the horizontal and vertical positioning errors based on standard EKF start to deteriorate, coincide with the MP appearance time determined by the proposed approach. Conversely, the positioning errors obtained with the proposed approach remains lower than 10 m, confirming that the MP interferences appearing on the PR measurements have been detected and mitigated.

Figure 4.9 displays the horizontal and vertical errors versus the trip distance. It is clear that the positioning accuracy, especially in the vertical direction, is sensitive to the MP interferences when the vehicle stops in the middle of two buildings. As a consequence, the impact resulting from the MP interference error is the maximum during this period. However, the proposed approach can effectively mitigate the impact of the MP interference in this case. Increasing the duration of the observation window depending on the vehicle dynamic could also facilitate MP detection when the vehicle remains at the same location.

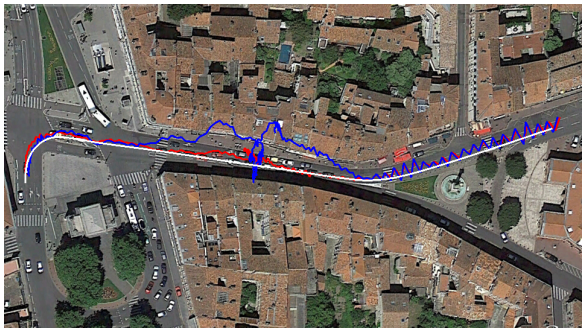

Figure 4.7 – Positioning results for different approaches in a urban canyon (obtained with Google Earth). Reference trajectory: white line; Proposed approach: red line; Standard EKF: blue line.

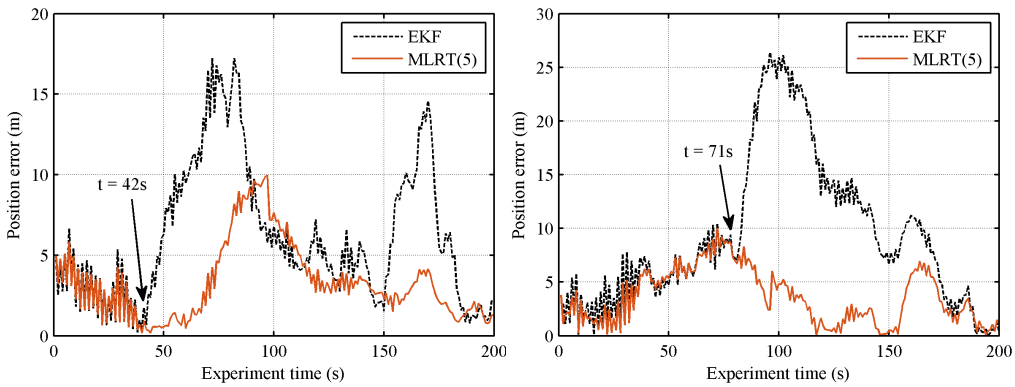

(a) Horizontal error **(b)** Vertical error

Figure 4.8 – Positioning errors versus time.

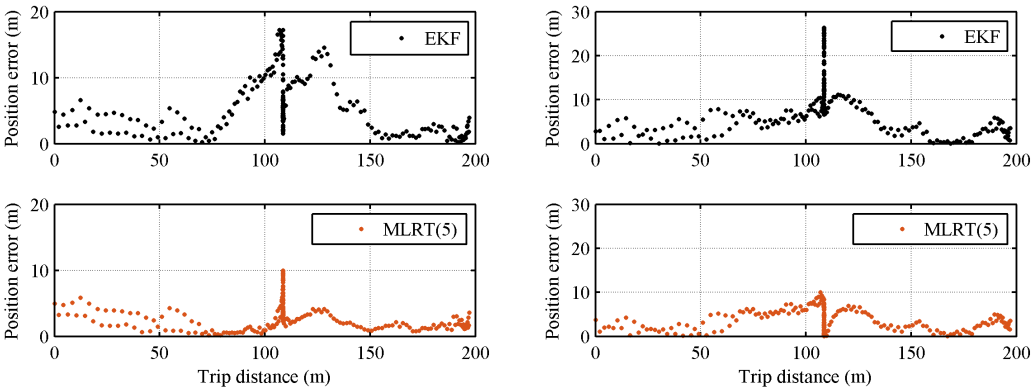

(a) Horizontal error

(b) Vertical error

Figure 4.9 – Positioning errors versus trip distance.

4.7 Conclusion

In this chapter, an approximated MLRT based on Jensen's inequality was proposed to detect, identify and estimate the NLOS multipath biases affecting GNSS PR measurements in urban canyons. The effects of NLOS multipath interferences were modeled as mean value jumps. The proposed approach was based on a marginalized likelihood ratio test approximated using an MC integration and Jensen's inequality. The multiple model algorithm was introduced to update the prior information of each bias magnitude sample in order to improve its detection. A simulation study was implemented in order to compare the performance of the proposed approach with the GLRT and the approach studied in [102]. Although the mean detection delay and the standard deviation of the proposed approach were slightly inferior to those of the GLRT, the probability of correct detection increases significantly (when compared to the GLRT) due to the introduction of a prior information about the bias magnitude. A comparison with the standard EKF and the approach studied in [102] showed that the positioning accuracy was improved by the proposed approach. Finally, the proposed approach was validated by processing data collected from a measurement campaign carried out in an urban environment. The proposed approach proved its efficiency for MP interference detection and mitigation, resulting in improving positioning accuracy.

CHAPTER

FIVE

A VISION AIDED IMU/GNSS INTEGRATION FOR RELIABLE POSITIONING IN MULTIPATH ENVIRONMENTS

It has been mentioned throughout this thesis that GNSS multipath (MP) mitigation in a constricted environment (urban canyons or other intensive obstructions scenarios) is a challenging task. This is, in fact, the main motivation for the thesis itself. In the previous chapters, several approaches for mitigating MP interferences in the GNSS receiver have been proposed and analyzed. Nevertheless, the proposed algorithms have only focused on MP mitigation techniques based on the GNSS signal or on GNSS measurement processing, whereas the complementarity information provided by different sensors has not been taken in account. In this chapter, a multi-sensor integration architecture, consisting of an inertial measurement unit (IMU), a GNSS receiver, a monocular vision sensor and a baro-altimeter is proposed to facilitate the detection and processing of MP interferences with the ultimate goal to improve the reliability of the positioning algorithm in urban environments.

The proposed approach aims at exploiting the reliable GNSS measurements in urban environments to ensure the required navigation accuracy and reliability. To achieve this objective, a multi-sensor integration architecture, i.e., a monocular vision sensor and a baro-altimeter aided IMU/GNSS integration, is investigated in this chapter. In order to improve the detection performance of GNSS pseudo-range (PR) and delta-range (DR) errors resulting from MP interferences, the vision sensor and the baro-altimeter are used to calibrate the IMU solution drift so as to improve the a priori estimate of the vehicle state. As these sensor measurements lead to long-term errors, reliable GNSS measurements are selected and combined with the IMU to provide a bounded-error state estimation of the vehicle. A quaternion-based unscented Kalman filter is designed to perform the integration of the IMU and other sensors, in which the quaternion normalization constraint is taken into account in the unscented transformation. Finally, results from a measurement campaign conducted in urban canyons are presented in order to evaluate the availability of the proposed approach in practice.

5.1 Introduction

In urban canyon scenarios, the MP interferences can result in GNSS measurement errors. As mentioned in Section 2.3.2, these measurement errors can be detected and mitigated by using GNSS measurement processing techniques. However, these techniques usually require an accurate a priori knowledge of the current vehicle state which is a challenge in urban environments. In order to overcome this problem, a multi-sensor integration architecture is proposed in order to facilitate MP detection and provide reliable positioning in a constricted environment.

Nowadays, the integration of an IMU and a GNSS receiver is considered as an efficient combination and is widely applied [2, 9, 104]. Due to biases and noises affecting inertial sensor measurements, the positioning error based on the IMU grows with time. Thus the IMU/GNSS integration is very sensitive to the availability of GNSS measurements. It is known that the GNSS measurement is vulnerable to the influence of MP interferences in constricted environments such as urban canyons. As a consequence, the performance of IMU/GNSS integration is severely degraded where GNSS measurements are subject to MP interferences. Considering that improving a priori knowledge of the vehicle state can facilitate detection of GNSS measurement errors, we propose to use a monocular vision sensor and a baro-altimeter to calibrate the IMU solution drift so as to improve a priori estimate of the vehicle state. A vision sensor, relying on sensing the differential displacement and rotation between two successive sampling images, provides the position and attitude of the vehicle by performing dead reckoning [105, 106]. Similar with other dead reckoning systems, such as inertial navigation systems, the vision-based navigation performance depends on the errors of displacement and rotation measurements. Thus the accuracy of a navigation solution provided by a vision-based odometer degrades with time [106–108]. We propose to use the motion flow measurements between two successive sampling images captured by the monocular vision sensor. This approach allows accumulated errors to be avoided when reliable GNSS measurements are available. In addition, a baro-altimeter, relying on atmospheric pressure readings, provides an indirect measure of altitude above a nominal sea level [109]. On the one hand, the position and velocity errors for IMU navigation solution are unbounded in the vertical direction, i.e., these errors become very large within a relatively short period of time [110]; on the other hand, GNSS measurements, especially in the vertical direction, are sensitive to the MP interferences in constricted environments. Thus the baro-altimeter is used as a supplementary navigation aid for the height direction [111].

The basic idea of the proposed approach is to ensure that GNSS measurements are fully utilized by improving the a priori knowledge of the vehicle state for facilitating detection of GNSS measurement errors. Thus the implementation of the approach mainly consists of three steps: 1) the integration of an IMU, a monocular vision sensor and a baro-altimeter is performed in order to calibrate the IMU solution drift so as to improve the a priori estimate of the vehicle state; 2) GNSS measurements are processed for detecting the measurements contaminated by the MP interfer-

ences and 3) reliable GNSS measurements and IMU data are combined to provide the final vehicle state estimation. A quaternion-based unscented Kalman filter (UKF) with total-state (i.e., the highly non-linear inertial solution equations are embedded in the filter state model) is designed to implement the integration of the IMU and other sensors. The quaternion normalization constraint is also taken into account in the unscented transformation. Finally, the proposed approaches are validated using data obtained from a measurement campaign conducted in a street urban canyon.

5.2 Navigation System Architecture

The architecture considered in this work for IMU/GNSS integration aided by a monocular vision sensor and a baro-altimeter is shown in Figure 5.1. A hierarchical sensor integration approach is proposed for the estimation of vehicle position, velocity and attitude. The vehicle state is estimated by a multiple-step procedure described below,

(1) The vehicle state which includes the position, velocity and attitude is propagated by exploiting IMU measurements through a non-linear model defined by the classical inertial solution equations,

(2) The IMU is integrated with a monocular vision sensor and a baro-altimeter. The purpose of this filter is to reduce the solution drift which is due to noises and biases of IMU measurements and to improve the accuracy of the state estimation,

(3) The improved knowledge of the vehicle state facilitates the detection of contaminated pseudo-range and delta-range measurements and thus improves GNSS reliability,

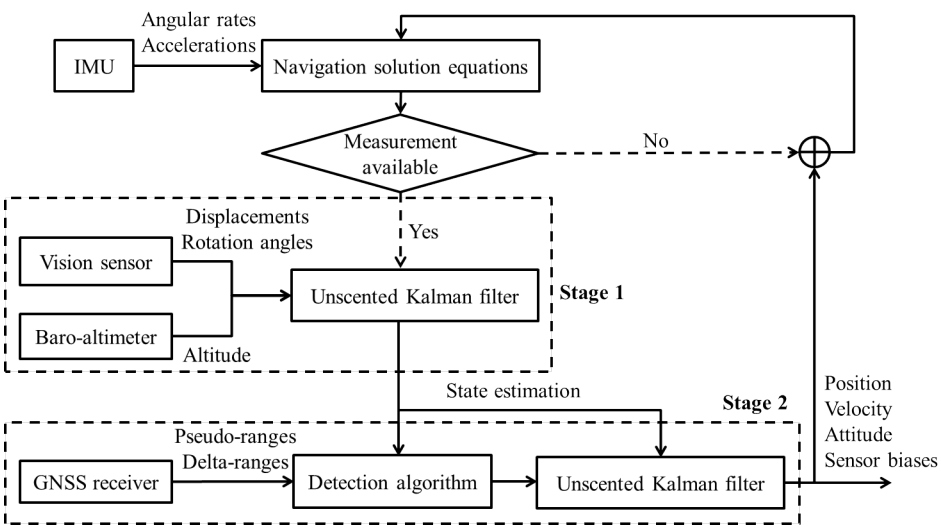

Figure 5.1 – Schematic diagram of a monocular vision sensor and a baro-altimeter aided IMU/GNSS integrated system.

(4) The GNSS integration is performed by considering only reliable measurements. Considering that GNSS measurements are independent of the vision sensor and barometer outputs, the state estimation can be updated by the non-contaminated GNSS measurements.

5.3 Navigation Sensor Models

5.3.1 Inertial Measurement Unit Model

The IMU is composed of accelerometers and gyroscopes which deliver the specific force $\boldsymbol{f}_{ib}^{b}$ and the angular rate $\boldsymbol{\omega}_{ib}^{b}$ measurements of the body frame (forward-right-down) with respect to the inertial frame expressed in body frame axes. These measurements are processed by the navigation solution equations which recursively solve the vehicle position, velocity, and attitude in real time [109]. Thus the inertial state vector $\boldsymbol{X}$, which represents the vehicle position, velocity, and attitude expressed in the local navigation (north-east-down) frame, can be written

$$\boldsymbol{X} = (\boldsymbol{P},\ \boldsymbol{V},\ \boldsymbol{Q})^{\mathrm{T}} \tag{5.1}$$

where $\boldsymbol{P} = (l,\ \lambda,\ h)^{\mathrm{T}}$ is a position vector associated with the vehicle latitude, longitude and altitude respectively, $\boldsymbol{V} = (v_n,\ v_e,\ v_d)^{\mathrm{T}}$ is a velocity vector associated with the vehicle north, east and down velocity in the navigation frame, $\boldsymbol{Q} = \left(q_0,\ q_1,\ q_2,\ q_3\right)^{\mathrm{T}}$ is the quaternion vector associated with the vehicle attitude, i.e., the vehicle body frame orientation (roll, pitch and yaw) with respect to the navigation frame. Accordingly, the simplified inertial solution equations in the local navigation frame can be written as follows

$$\begin{aligned}
\boldsymbol{P}_{k+1} &= \boldsymbol{P}_k + \Delta t\, \boldsymbol{V}_k \\
\boldsymbol{V}_{k+1} &= \boldsymbol{V}_k + \Delta t \left(\boldsymbol{C}_b^n(\boldsymbol{Q}_k)\, \boldsymbol{f}_{ib,k}^{b} - \left(2\boldsymbol{\omega}_{ie,k}^{n} + \boldsymbol{\omega}_{en,k}^{n}\right) \times \boldsymbol{V}_k + \boldsymbol{g}_k^n\right) \\
\boldsymbol{Q}_{k+1} &= \Delta \boldsymbol{q}_k \otimes \boldsymbol{Q}_k
\end{aligned} \tag{5.2}$$

with

$$\Delta \boldsymbol{q}_k = \left(\cos\left(\frac{\|\Delta \boldsymbol{\theta}_k\|}{2}\right),\quad \frac{\Delta \boldsymbol{\theta}_k}{\|\Delta \boldsymbol{\theta}_k\|} \sin\left(\frac{\|\Delta \boldsymbol{\theta}_k\|}{2}\right)\right)^{\mathrm{T}}$$

and

$$\Delta \boldsymbol{\theta}_k = \Delta t \left(\boldsymbol{\omega}_{ib,k}^{b} - \left(\boldsymbol{C}_b^n(\boldsymbol{Q}_k)\right)^{\mathrm{T}} \left(\boldsymbol{\omega}_{ie,k}^{n} + \boldsymbol{\omega}_{en,k}^{n}\right)\right)$$

where $k = 1, \ldots, \infty$ denotes the kth sampling time instant of the inertial sensor, $\boldsymbol{\omega}_{ie,k}^{n}$ is the rotational rate vector of the earth-centred earth-fixed (ECEF) frame relative to the inertial frame expressed in the navigation frame, $\boldsymbol{\omega}_{en,k}^{n}$ is the rotational rate vector of the navigation frame relative to the ECEF frame expressed in the navigation frame at time k, $\Delta \boldsymbol{\theta}_k$ is the integral of the angular rate from the sampling time instant k to $k+1$, Δt represents the time interval between two suc-

cessive sampling time instants, $\boldsymbol{C}_b^n(\boldsymbol{Q}_k)$ is the attitude transition matrix from the body frame to the navigation frame that is a function of the quaternion vector $\boldsymbol{Q}_k$, $\boldsymbol{g}_k^n$ is the gravity expressed in the navigation frame. The notations $\times$ and $\otimes$ represent the cross-product of two vectors and quaternion product between two quaternion vectors, respectively. More details about the inertial solution equations can be found in [104, 109–111].

In practice, the accuracy of the propagated inertial state $\boldsymbol{X}$ obtained by (5.2) depends on the quality of inertial sensors (accelerometers and gyroscopes). Due to biases and noises affecting inertial sensor measurements and initial misalignment errors, inertial state errors are known to grow with time. It is assumed that static errors of inertial sensors, such as the fixed bias or the turn-on bias, have been corrected through the laboratory calibration [112]. Thus only random errors are taken into account by using the following models

$$\begin{aligned} \tilde{\boldsymbol{f}}_{ib}^b &= \boldsymbol{f}_{ib}^b + \boldsymbol{b}_a + \boldsymbol{n}_a \\ \tilde{\boldsymbol{\omega}}_{ib}^b &= \boldsymbol{\omega}_{ib}^b + \boldsymbol{b}_g + \boldsymbol{n}_g \end{aligned} \tag{5.3}$$

where $\boldsymbol{f}_{ib}^b$ and $\boldsymbol{\omega}_{ib}^b$ are the true acceleration and angular rate values, $\boldsymbol{n}_a$ and $\boldsymbol{n}_g$ are the acceleration and gyroscope measurement noise vectors with zero mean Gaussian distributions and covariance matrices $\boldsymbol{Q}_a$ and $\boldsymbol{Q}_g$, $\boldsymbol{b}_a$ and $\boldsymbol{b}_g$ are inertial sensor random biases that are modelled as random walks, i.e.,

$$\begin{aligned} \dot{\boldsymbol{b}}_a &= \boldsymbol{n}_{ba} \\ \dot{\boldsymbol{b}}_g &= \boldsymbol{n}_{bg} \end{aligned} \tag{5.4}$$

where $\boldsymbol{n}_{ba}$ and $\boldsymbol{n}_{bg}$ are zero mean Gaussian white noise vectors of covariance matrices $\boldsymbol{Q}_{ba}$ and $\boldsymbol{Q}_{bg}$. More precisely, the covariance matrices $\boldsymbol{Q}_{ba}$, $\boldsymbol{Q}_{bg}$, $\boldsymbol{Q}_a$ and $\boldsymbol{Q}_g$ are defined as

$$\boldsymbol{Q}_{ba} = \begin{pmatrix} \sigma_{ba}^2 & 0 & 0 \\ 0 & \sigma_{ba}^2 & 0 \\ 0 & 0 & \sigma_{ba}^2 \end{pmatrix}, \boldsymbol{Q}_{bg} = \begin{pmatrix} \sigma_{bg}^2 & 0 & 0 \\ 0 & \sigma_{bg}^2 & 0 \\ 0 & 0 & \sigma_{bg}^2 \end{pmatrix}, \boldsymbol{Q}_a = \begin{pmatrix} \sigma_a^2 & 0 & 0 \\ 0 & \sigma_a^2 & 0 \\ 0 & 0 & \sigma_a^2 \end{pmatrix}, \boldsymbol{Q}_g = \begin{pmatrix} \sigma_g^2 & 0 & 0 \\ 0 & \sigma_g^2 & 0 \\ 0 & 0 & \sigma_g^2 \end{pmatrix}.$$

5.3.2 GNSS Measurement Model

Two kinds of GNSS measurements, including PR and DR measurements are considered in this work. It is assumed that GNSS system errors such as ionospheric and tropospheric errors, as well as satellite clock biases, relativistic effects have been compensated within the receiver. Consequently, the mth in-view satellite PR measurement model without MP interferences can be defined as [1, 4]

$$\rho_{m,t} = \left\| \boldsymbol{P}_{m,t} - \boldsymbol{P}_t^e \right\| + b_t + n_{\rho,t} \tag{5.5}$$

where $t = 1, \ldots, \infty$ denotes the tth sampling time instant of the GNSS measurement, $\rho_{m,t}$ is the PR measurement associated with the mth in-view satellite at time t, $\boldsymbol{P}_{m,t} = (x_{m,t},\ y_{m,t},\ z_{m,t})$ and $\boldsymbol{P}_t^e = (x_t,\ y_t,\ z_t)$ are the mth satellite position and the vehicle position in the ECEF frame, b_t is the GNSS receiver clock offset, $n_{\rho,t}$ is the mth satellite PR measurement noise with a normal distribution $n_{\rho,t} \sim \mathcal{N}\left(0, \sigma_\rho^2\right)$.

Considering that the vehicle state in (5.1) is expressed in the navigation frame, the coordinate transformation from the navigation frame to the ECEF frame at time t can be written as follows

$$\begin{aligned} x_t &= (N + h_t)\cos(l_t)\cos(\lambda_t) \\ y_t &= (N + h_t)\cos(l_t)\sin(\lambda_t) \\ z_t &= (N + h_t)\sin(l_t) \end{aligned}$$

where $N = \frac{a}{\sqrt{1-e^2\sin^2 L_t}}$ and the parameters a and e denotes the semi-major axis and the eccentricity of the Earth's ellipsoid, respectively.

Accordingly, the mth in-view satellite DR measurement model without MP interferences can be defined as [1, 4]

$$\dot{\rho}_{m,t} = \boldsymbol{u}_{m,t} \left\| \boldsymbol{V}_{m,t} - \boldsymbol{V}_t^e \right\| + d_t + n_{\dot{\rho},t} \tag{5.6}$$

with

$$\boldsymbol{u}_{m,t} = \left(\frac{x_{m,t} - x_t}{\left\| \boldsymbol{P}_{m,t} - \boldsymbol{P}_t^e \right\|}, \frac{y_{m,t} - y_t}{\left\| \boldsymbol{P}_{m,t} - \boldsymbol{P}_t^e \right\|}, \frac{z_{m,t} - z_t}{\left\| \boldsymbol{P}_{m,t} - \boldsymbol{P}_t^e \right\|} \right)^{\mathrm{T}}$$

where $t = 1, \ldots, \infty$ denotes the tth sampling time instant, $\boldsymbol{u}_{m,t}$ is the line-of-sight (LOS) vector between the vehicle and the mth in-view satellite at time t, $\dot{\rho}_{m,t}$ is the DR measurement associated with the mth in-view satellite, $\boldsymbol{V}_{m,t} = (v_{m,x,t},\ v_{m,y,t},\ v_{m,z,t})$ and $\boldsymbol{V}_t^e = (v_{x,t},\ v_{y,t},\ v_{z,t})$ are the mth satellite velocity and the vehicle velocity in the ECEF frame, d_t is the GNSS receiver clock drift, $n_{\dot{\rho},t}$ is the mth in-view satellite DR measurement noise with a normal distribution $n_{\dot{\rho},t} \sim \mathcal{N}\left(0, \sigma_{\dot{\rho}}^2\right)$. Similarly, the coordinate transformation from the navigation frame to the ECEF frame needs to be performed as follow

$$\boldsymbol{V}_t^e = \begin{pmatrix} -\sin(l_t)\cos(\lambda_t) & -\sin(\lambda_t) & -\cos(l_t)\cos(\lambda_t) \\ -\sin(l_t)\sin(\lambda_t) & \cos(\lambda_t) & -\cos(l_t)\sin(\lambda_t) \\ -\cos(l_t) & 0 & -\sin(l_t) \end{pmatrix} \boldsymbol{V}_t$$

where $\boldsymbol{V}_t = \left(v_{n,t},\ v_{e,t},\ v_{d,t}\right)^{\mathrm{T}}$ is the velocity vector at time t in the navigation frame. Moreover, the GNSS receiver clock bias b_t and drift d_t can be modelled as the following random walks

$$\begin{aligned} \dot{b}_t &= d_t + n_b \\ \dot{d}_t &= n_d \end{aligned} \tag{5.7}$$

where n_b and n_d are zero-mean Gaussian white noises of variance σ_b^2 and σ_d^2.

It is important to note that the sampling frequency of the inertial sensor is much higher than that of the GNSS measurement, i.e., $t = n_s k$ where n_s denotes the iteration times of (5.2) between two successive sampling time instants of the GNSS measurement.

5.3.3 Monocular Vision Sensor Measurement Model

In this work, it is assumed that the monocular vision frame coincides with the vehicle's body frame and the alignment error between these two frames has been compensated. A probabilistic block-matching technique based on the monocular vision sensor is used to extract a motion flow measurement of the vehicle between two successive sampling images and provide the corresponding statistical properties of motion measurement errors. A more detailed description on this approach can be found in [113]. On the basis of this approach, two kinds of measurements based on the monocular vision sensor, including the direction vector and rotational vector at time t with respect to the vision frame at time $t-1$, can be obtained.

The direction vector denotes the motion direction of the vehicle displacement between two successive sampling images and can be defined as

$$\frac{\boldsymbol{T}_t}{\|\boldsymbol{T}_t\|} = \frac{\boldsymbol{D}_t}{\|\boldsymbol{D}_t\|} + \frac{\boldsymbol{n}_{T,t}}{\|\boldsymbol{T}_t\|} \tag{5.8}$$

with

$$\boldsymbol{D}_t = \sum_{k=1}^{n_s} \boldsymbol{C}_{n,t-1+k/n_s}^{b} \boldsymbol{V}_{t-1+k/n_s} \Delta t$$

where $t = 1, \ldots, \infty$ denotes the tth sampling time instant of the vision sensor, $\boldsymbol{T}_t$ is the differential displacement obtained at the time t which is expressed with respect to the vision frame defined at time $t-1$ and $\boldsymbol{D}_t$ is the displacement computed by integration of the vehicle velocity from $t-1$ to t. Note that the vehicle velocity $\boldsymbol{V}$ defined in the navigation frame needs to be transformed with the matrix $\boldsymbol{C}_n^b$ from the navigation frame to the vision frame. Considering that the sampling frequency of inertial sensors is higher than that of the monocular vision sensor, n_s is the number of inertial solution equation outputs between two successive sampling image times. $\boldsymbol{n}_{T,t}$ is the corresponding measurement noise vector which is a zero mean Gaussian white noise of covariance matrix $\boldsymbol{R}_T$.

Accordingly, the rotational vector denotes the vehicle rotational motion between two successive sampling images and can be defined as

$$\boldsymbol{Q}_t^V = \boldsymbol{Q}_{t-1}^* \otimes \boldsymbol{Q}_t + \boldsymbol{n}_{V,t} \tag{5.9}$$

where $t = 1, \ldots, \infty$ denotes the tth sampling time instant of the vision sensor, $\boldsymbol{Q}_t^V$ is the quaternion vector which describes the vehicle rotational transformation provided by the monocular vision sen-

sor, i.e., the body frame orientation at time t with respect to the body frame at time $t-1$, $\boldsymbol{Q}_t$ is the quaternion vector which describes the vehicle attitude provided by the IMU solution equations at time t and $\boldsymbol{Q}^*_{t-1}$ is the conjugate attitude quaternion vector at time instant $t-1$. Note that $\boldsymbol{n}_{V,t}$ is the corresponding measurement noise vector which is a zero mean Gaussian white noise vector of covariance matrix $\boldsymbol{R}_V$. Note also that the above direction and rotational measurements for the monocular vision sensor and the corresponding statistical properties of measurement noises are obtained from the probabilistic block-matching algorithm as described in [113].

5.3.4 Baro-altimeter Measurement Model

The baro-altimeter measures the altitude h by sensing the atmospheric pressure P when the sea level standard atmospheric pressure P_0 is known. The relation between the atmospheric pressure P and the altitude h for the baro-altimeter is [114]

$$P = P_0\left(1-\frac{L}{T_0}h\right)^{\frac{g\,M}{R\,\tilde{T}}} = P_0\,\mathrm{g}(h) \tag{5.10}$$

where $\tilde{T}$ is the temperature lapse rate, T_0 is the sea level standard temperature, g is the gravity, M is the molar mass of dry air, R is the universal gas constant. Note that the altitude measurement obtained from the baro-altimeter differs from that of GNSS which represents the height relative to the surface of the Earth which is modelled in the WGS-84 (World Geodetic System 1984). It is known that this height difference can be corrected by a geodetic model [115]. We consider that a radio link allows the vehicle to communicate with a base station which transmits the values of P_0. Thus the baro-altimeter measurement equation in this work can be defined as

$$H_{B,t} = h_t + n_{B,t} \tag{5.11}$$

with

$$H_{B,t} = \mathrm{g}^{-1}\left(\frac{P}{P_0}\right) + \Delta H^{\mathrm{GNSS}}_{\mathrm{sea}}$$

where $t = 1,\ldots,\infty$ denotes the tth sampling time instant of the baro-altimeter, $\mathrm{g}(\cdot)$ is the function described in (5.10), ΔH is the altitude correction which denotes the height of the sea level with respect to the WGS-84 ellipsoid and $n_{B,t}$ is the baro-altimeter measurement noise that has a normal distribution $n_{B,t} \sim \mathcal{N}\left(0,\ \sigma^2_B\right)$.

Note that the sampling frequency of the inertial sensor is much higher than those of the observation sensors and we assume that the observation sensors are synchronized in this work. The sampling time instant of the observation sensors is denoted as $t = 1,\ldots,\infty$ and $t = n_s k$ where n_s is the iterations of the inertial solution equations between two successive sampling time instants of the observation sensors.

5.4 Multi-sensor Integration Using Quaternion-based UKF

In this work, the inertial navigation equations in (5.2) are embedded in the Kalman filter system model, which is known as the total-state Kalman filter [9]. In this way, the absolute position, velocity, and attitude of the vehicle are estimated using a Kalman filter. Considering that the inertial navigation equations are highly non-linear equations, the extended Kalman filter (EKF) could diverge due to large linearization errors [88]. Although the particle filter (PF) could be investigated to estimate the state of this non-linear estimation problem [116–118], the corresponding computational cost can be prohibitive for practical applications. Thus we consider an unscented Kalman filter (UKF) based on the unscented transformation and provides an efficient and low-cost solution for highly non-linear systems. In the unscented transformation, a minimal set of deterministic samples is required to approximate a Gaussian probability density function. These samples called sigma points are propagated through non-linear equations, in order to obtain the posterior distribution of the state vector [86, 87]. In addition, the normalization constraint for the quaternion vector in the unscented transformation needs to be taken into account [119]. Thus the implementation of multi-sensor integration using a quaternion-based UKF is given in this section. It is important to note that the quaternion-based UKF is an approach which combines a quaternion vector and a rotational angle vector for performing the vehicle attitude propagation and update in the UKF, i.e., the quaternion vector is propagated and update by using the quaternion product chain rule and the corresponding rotational angle vector performs the covariance matrix calculation in order to fulfil the normalization constraint of the quaternion vector.

5.4.1 State Model

According to the sensor models as described in Section 5.3, the state vector includes the vehicle state represented by the position, velocity and attitude. In addition, the inertial sensor biases, as well as the clock bias and drift of the GNSS receiver are also considered. Thus the state vector $\boldsymbol{x}_k$ at time k can be defined as

$$\boldsymbol{x}_k = \left(\boldsymbol{X}_k,\ \boldsymbol{b}_{a,k},\ \boldsymbol{b}_{g,k},\ b_k,\ d_k\right)^{\mathrm{T}}. \tag{5.12}$$

Accordingly, the corresponding process noise vector is defined as

$$\boldsymbol{v}_k = \left(\boldsymbol{n}_{a,k},\ \boldsymbol{n}_{g,k},\ \boldsymbol{n}_{ba,k},\ \boldsymbol{n}_{bg,k},\ n_{b,k},\ n_{d,k}\right)^{\mathrm{T}} \tag{5.13}$$

and

$$\boldsymbol{v}_k \sim \mathcal{N}\left(\boldsymbol{0},\ \boldsymbol{Q}^{v}\right)$$

where $\boldsymbol{Q}^{v}$ is the covariance matrix of the noise vector $\boldsymbol{v}_k$.

As a consequence, the discrete time state equations for propagating state vector, which is composed of (5.2), (5.4) and (5.7), is denoted as

$$\boldsymbol{x}_k = \mathbf{f}(\boldsymbol{x}_{k-1},\ \boldsymbol{u}_k,\ \boldsymbol{v}_{k-1}) \tag{5.14}$$

where $k = 1, \ldots, \infty$ denotes the kth sampling time instant of the inertial sensor, $\boldsymbol{u}_k = \left(\tilde{\boldsymbol{f}}^b_{ib,k},\ \tilde{\boldsymbol{\omega}}^b_{ib,k}\right)^{\mathrm{T}}$ is a measurement vector which contains the specific force and the angular rate measured by the inertial sensors at time k. Note that the propagation frequency of (5.14) is equal to the sampling frequency of the inertial sensor.

It is clear that the process noises are not additive in (5.14). Thus an augmented state vector needs to be considered in order to propagate the state vector $\boldsymbol{x}_k$ when an UKF is performed. In addition, the degree of freedom for a quaternion vector is three due to the quaternion normalization constraint. As a consequence, there is a dimensional mismatch between the state vector and the state error covariance. In this work, this dimensional mismatch can be solved by transforming the quaternion vector error into its corresponding rotational angle vector. The initial augmented state vector can be represented as

$$\hat{\boldsymbol{x}}^a_0 = \left(\hat{\boldsymbol{x}}^x_0,\ \hat{\boldsymbol{x}}^v_0\right) \tag{5.15}$$

and

$$\boldsymbol{P}^a_0 = \begin{pmatrix} \boldsymbol{P}^x_0 & \mathbf{0} \\ \mathbf{0} & \boldsymbol{Q}^v_0 \end{pmatrix} \tag{5.16}$$

where $\hat{\boldsymbol{x}}^a_0$ and $\boldsymbol{P}^a_0$ are the initial mean and error covariance matrix of the augmented state vector respectively. They include two parts:

- $\hat{\boldsymbol{x}}^x_0$ and $\boldsymbol{P}^x_0$ denote the initial mean and error covariance matrix of the state vector $\boldsymbol{x}_k$,
- $\hat{\boldsymbol{x}}^v_0$ and $\boldsymbol{Q}^v_0$ denote the initial mean and error covariance matrix of the process noise $\boldsymbol{v}_k$.

The detailed state vector $\hat{\boldsymbol{x}}^x_0$ and its error vector (i.e., the estimation minus the real) can be written as follows

$$\hat{\boldsymbol{x}}^x_0 = \begin{pmatrix} \hat{\boldsymbol{P}}_0 \\ \hat{\boldsymbol{V}}_0 \\ \hat{\boldsymbol{Q}}_0 \\ \hat{\boldsymbol{b}}_{a,0} \\ \hat{\boldsymbol{b}}_{g,0} \\ \hat{b}_0 \\ \hat{d}_0 \end{pmatrix}_{18\times 1} \quad \text{and} \quad \delta\hat{\boldsymbol{x}}^x_0 = \begin{pmatrix} \hat{\boldsymbol{P}}_0 - \boldsymbol{P}_0 \\ \hat{\boldsymbol{V}}_0 - \boldsymbol{V}_0 \\ \boldsymbol{\psi}\left(\hat{\boldsymbol{Q}}_0 \otimes \boldsymbol{Q}_0^{-1}\right) \\ \hat{\boldsymbol{b}}_{a,0} - \boldsymbol{b}_{a,0} \\ \hat{\boldsymbol{b}}_{g,0} - \boldsymbol{b}_{g,0} \\ \hat{b}_0 - b_0 \\ \hat{d}_0 - d_0 \end{pmatrix} = \begin{pmatrix} \delta\hat{\boldsymbol{P}}_0 \\ \delta\hat{\boldsymbol{V}}_0 \\ \delta\hat{\boldsymbol{\varphi}}_0 \\ \delta\hat{\boldsymbol{b}}_{a,0} \\ \delta\hat{\boldsymbol{b}}_{g,0} \\ \delta\hat{b}_0 \\ \delta\hat{d}_0 \end{pmatrix}_{17\times 1}$$

with

$$\delta\hat{\boldsymbol{\varphi}}_0 = \boldsymbol{\psi}\left(\hat{\boldsymbol{Q}}_0 \otimes \boldsymbol{Q}_0^{-1}\right)$$

where $\boldsymbol{\psi}(\cdot)$ is the operator which transforms the quaternion vector into its corresponding rotational angle vector. Accordingly, $\boldsymbol{\psi}^{-1}(\cdot)$ is defined as the inverse operator of $\boldsymbol{\psi}(\cdot)$ which transforms the rotational angle vector into its corresponding quaternion vector [104]. The dimension of the rotational vector $\delta\hat{\boldsymbol{\varphi}}_0$ is 3×1. Thus the dimension of the error covariance matrix $\boldsymbol{P}_0^x = \mathrm{E}\left[\left(\delta\hat{\boldsymbol{x}}_0^x\right)\left(\delta\hat{\boldsymbol{x}}_0^x\right)^{\mathrm{T}}\right]$ is 17×17 where $\mathrm{E}[\cdot]$ denotes the expectation function. It is clear that the dimension of the state vector $\hat{\boldsymbol{x}}_0^x$ is one more than that of its error vector $\delta\hat{\boldsymbol{x}}_0^x$.

In the total-state UKF, the augmented state vector needs to be iterated by using (5.14) at the same rate as the inertial navigation equations. However, the propagation of the error covariance matrix can be made at a lower rate, which is the same as the observation sensors, e.g., the frequency of GNSS measurements.

5.4.2 State Propagation and Update

1. State Propagation In the UKF frame, a set of sigma points is generated for capturing the mean and covariance matrix of the Gaussian random vector $\boldsymbol{x}^a$ and propagated by the non-linear equations. Then the posterior mean and covariance of the random vector which undergoes a non-linear transformation can be calculated by the unscented transformation. At the beginning of the propagation step, the sigma point $\boldsymbol{\chi}_i^a$ can be calculated from $\hat{\boldsymbol{x}}_0^a$ and $\boldsymbol{P}_0^a$ [120]

$$\begin{aligned}
\boldsymbol{\chi}_{0,0}^a &= \hat{\boldsymbol{x}}_0^a \\
\boldsymbol{\chi}_{i,0}^a &= \hat{\boldsymbol{x}}_0^a + \left(\sqrt{(L+\lambda)\boldsymbol{P}_0^a}\right)_i \\
\boldsymbol{\chi}_{i+L,0}^a &= \hat{\boldsymbol{x}}_0^a - \left(\sqrt{(L+\lambda)\boldsymbol{P}_0^a}\right)_i, \quad i = 1,\ldots,L
\end{aligned} \tag{5.17}$$

with

$$\boldsymbol{\chi}_{i,0}^a = \left(\boldsymbol{\chi}_{i,0}^x,\ \boldsymbol{\chi}_{i,0}^v\right) \tag{5.18}$$

where L is the dimension of the augmented state vector $\hat{\boldsymbol{x}}_0^a$ and $\lambda = \alpha^2(L+\kappa) - L$ is a scaling parameter, α is a constant scaling parameter that determines the spread of the sigma points around $\hat{\boldsymbol{x}}_0^a$ and is set to a small positive value (i.e., $10^{-4} \le \alpha \le 1$), κ is a secondary scaling parameter (usually set to $3-L$), $\left(\sqrt{(L+\lambda)\boldsymbol{P}_0^a}\right)_i$ is the ith column of the square root of the matrix $(L+\lambda)\boldsymbol{P}_0^a$, i.e., the lower-triangular matrix constructed using a Cholesky factorization. Accordingly, the weight W_i, corresponding to the sigma point $\boldsymbol{\chi}_i^a$, can be calculated as follows

$$\begin{aligned}
W_0^m &= \frac{\lambda}{L+\lambda} \\
W_0^c &= \frac{\lambda}{L+\lambda} + \left(1-\alpha^2+\beta\right) \\
W_i^m &= W_i^c = \frac{1}{2(L+\lambda)}, \quad i = 1,\ldots,2L
\end{aligned} \tag{5.19}$$

where W_i^m and W_i^c are weight factors associated with the mean and covariance matrix of the ith sigma point, β is used to incorporate prior knowledge of the distribution of $\hat{\boldsymbol{x}}_0^a$. As mentioned in Section 5.4.1, there is a dimensional mismatch between the state vector $\hat{\boldsymbol{x}}_0^x$ and the state error covariance matrix $\boldsymbol{P}_0^x$, thus the sigma point $\boldsymbol{\chi}_{i,0}^x$ is given as follows

$$\boldsymbol{\chi}_{i,0}^x = \begin{pmatrix} \hat{\boldsymbol{P}}_0 + \Delta\hat{\boldsymbol{P}}_{i,0} \\ \hat{\boldsymbol{V}}_0 + \Delta\hat{\boldsymbol{V}}_{i,0} \\ \boldsymbol{\psi}^{-1}\left(\Delta\hat{\boldsymbol{\varphi}}_{i,0}\right) \otimes \hat{\boldsymbol{Q}}_0 \\ \hat{\boldsymbol{b}}_{a,0} + \Delta\hat{\boldsymbol{b}}_{a,i,0} \\ \hat{\boldsymbol{b}}_{g,0} + \Delta\hat{\boldsymbol{b}}_{g,i,0} \\ \hat{b}_0 + \Delta\hat{b}_{i,0} \\ \hat{d}_0 + \Delta\hat{d}_{i,0} \end{pmatrix}, \boldsymbol{\chi}_{i+L,0}^x = \begin{pmatrix} \hat{\boldsymbol{P}}_0 - \Delta\hat{\boldsymbol{P}}_{i,0} \\ \hat{\boldsymbol{V}}_0 - \Delta\hat{\boldsymbol{V}}_{i,0} \\ \boldsymbol{\psi}^{-1}\left(-\Delta\hat{\boldsymbol{\varphi}}_{i,0}\right) \otimes \hat{\boldsymbol{Q}}_0 \\ \hat{\boldsymbol{b}}_{a,0} - \Delta\hat{\boldsymbol{b}}_{a,i,0} \\ \hat{\boldsymbol{b}}_{g,0} - \Delta\hat{\boldsymbol{b}}_{g,i,0} \\ \hat{b}_0 - \Delta\hat{b}_{i,0} \\ \hat{d}_0 - \Delta\hat{d}_{i,0} \end{pmatrix} \text{ where } \left(\sqrt{(L+\lambda)\boldsymbol{P}_0^x}\right)_i = \begin{pmatrix} \Delta\hat{\boldsymbol{P}}_{i,0} \\ \Delta\hat{\boldsymbol{V}}_{i,0} \\ \Delta\hat{\boldsymbol{\varphi}}_{i,0} \\ \Delta\hat{\boldsymbol{b}}_{a,i,0} \\ \Delta\hat{\boldsymbol{b}}_{g,i,0} \\ \Delta\hat{b}_{i,0} \\ \Delta\hat{d}_{i,0} \end{pmatrix}$$

and $i = 1, \ldots, L$.

In order to obtain the a set of sigma points $\boldsymbol{\chi}_{i,t}^x$ $(i = 1, \ldots, 2L)$ that capture the prior distribution propagation of the state vector $\boldsymbol{x}_{t|t-1}^x$ from time instant $t-1$ to t, the generated sigma points $\boldsymbol{\chi}_{i,k}^x$ associated with the state vector are propagated by using the sigma points $\boldsymbol{\chi}_{i,k}^v$ associated with the process noise until the observation is received. Thus the propagation of sigma point $\boldsymbol{\chi}_{i,k}^x$ is conducted with (5.14) at the rate of the inertial navigation equations

$$\boldsymbol{\chi}_{i,k}^x = \mathbf{f}\left(\boldsymbol{\chi}_{i,k-1}^x, \boldsymbol{u}_k, \boldsymbol{\chi}_{i,k-1}^v\right) \tag{5.20}$$

where $i = 0, \ldots, 2L$. At time instant $t = n_s k$ (corresponding to the time instant when the observation is available) and n_s is the iteration times of (5.20) between two successive observation sampling times. The predicted state vector $\hat{\boldsymbol{x}}_{t|t-1}^x$ can be computed by using the set of sigma points

$$\hat{\boldsymbol{x}}_{t|t-1}^x = \sum_{i=0}^{2L} W_i^m \boldsymbol{\chi}_{i,t}^x \tag{5.21}$$

where $\boldsymbol{\chi}_{i,t}^x$ is the ith sigma point obtained at the end of the propagation step $(t = n_s k)$. Due to the fact that the unit quaternion is not mathematically closed for addition and scalar multiplications [121], the re-normalization for the quaternion vector is implemented

$$\hat{\boldsymbol{Q}}_{t|t-1} = \frac{\hat{\boldsymbol{Q}}_{t|t-1}}{\left\|\hat{\boldsymbol{Q}}_{t|t-1}\right\|}. \tag{5.22}$$

Taking advantage of this normalization, the corresponding error covariance matrix $\boldsymbol{P}_{t|t-1}^x$ can be

obtained, by using a rotational angle representation, as follows

$$\boldsymbol{P}^{x}_{t|t-1} = \sum_{i=0}^{2L} W_i^c \left(\delta\hat{\boldsymbol{x}}^{x}_{t|t-1}\right)\left(\delta\hat{\boldsymbol{x}}^{x}_{t|t-1}\right)^{\mathrm{T}} \tag{5.23}$$

where

$$\delta\hat{\boldsymbol{x}}^{x}_{t|t-1} = \boldsymbol{\chi}^{x}_{i,t} - \hat{\boldsymbol{x}}^{x}_{t|t-1} = \begin{pmatrix} \hat{\boldsymbol{P}}_{i,t} - \hat{\boldsymbol{P}}_{t|t-1} \\ \hat{\boldsymbol{V}}_{i,t} - \hat{\boldsymbol{V}}_{t|t-1} \\ \boldsymbol{\psi}\left(\hat{\boldsymbol{Q}}_{i,t} \otimes \hat{\boldsymbol{Q}}^{-1}_{t|t-1}\right) \\ \hat{\boldsymbol{b}}_{a,i,t} - \hat{\boldsymbol{b}}_{a,t|t-1} \\ \hat{\boldsymbol{b}}_{g,i,t} - \hat{\boldsymbol{b}}_{g,t|t-1} \\ \hat{b}_{i,t} - \hat{b}_{t|t-1} \\ \hat{d}_{i,t} - \hat{d}_{t|t-1} \end{pmatrix}.$$

Note that the dimension of the predicted state error vector $\delta\hat{\boldsymbol{x}}^{x}_{t|t-1}$ is still one less than that of the predicted state vector $\hat{\boldsymbol{x}}^{x}_{t|t-1}$.

2. State Update According to Section 5.3, the measurement noises of observation sensors, such as the GNSS, the monocular vision sensor and the baro-altimeter, are purely additive. In this case, the state vector doesn't need to be augmented for modelling the measurement noises. Thus the covariances of the measurement noises can be incorporated into the state covariance using a simple additive procedure [88]. Based on the predicted state vector $\hat{\boldsymbol{x}}^{x}_{t|t-1}$ and its error covariance matrix $\boldsymbol{P}^{x}_{t|t-1}$, the new sigma points are generated for measurement update

$$\begin{aligned} \boldsymbol{\chi}'_{0,t|t-1} &= \hat{\boldsymbol{x}}^{x}_{t|t-1} \\ \boldsymbol{\chi}'_{i,t|t-1} &= \hat{\boldsymbol{x}}^{x}_{t|t-1} + \left(\sqrt{(L'+\lambda')\boldsymbol{P}^{x}_{t|t-1}}\right)_i \\ \boldsymbol{\chi}'_{i+L',t|t-1} &= \hat{\boldsymbol{x}}^{x}_{t|t-1} - \left(\sqrt{(L'+\lambda')\boldsymbol{P}^{x}_{t|t-1}}\right)_i, \quad i = 1,\ldots,L' \end{aligned} \tag{5.24}$$

where L' is the dimension of the state vector $\hat{\boldsymbol{x}}^{x}_{t|t-1}$, $\lambda' = \alpha^2(L'+\kappa') - L'$ is a scaling parameter, $\kappa' = 3 - L'$, $\left(\sqrt{(L'+\lambda')\boldsymbol{P}^{x}_{t|t-1}}\right)_i$ is the ith column of the square root of the matrix $(L'+\lambda')\boldsymbol{P}^{x}_{t|t-1}$. Accordingly, the new weight W_i', corresponding to the new sigma point $\boldsymbol{\chi}'_{i,t|t-1}$, needs to be recalculated as follows

$$\begin{aligned} W_0^{m\prime} &= \frac{\lambda'}{L'+\lambda'} \\ W_0^{c\prime} &= \frac{\lambda}{L'+\lambda'} + \left(1-\alpha^2+\beta\right) \\ W_i^{m\prime} = W_i^{c\prime} &= \frac{1}{2(L'+\lambda')}, \quad i = 1,\ldots,2L'. \end{aligned} \tag{5.25}$$

Similarly, the new sigma point $\boldsymbol{\chi}'_{i,t|t-1}$ is generated as follows

$$\boldsymbol{\chi}'_{i,t|t-1} = \begin{pmatrix} \hat{\boldsymbol{P}}_{t|t-1} + \Delta\hat{\boldsymbol{P}}_{i,t|t-1} \\ \hat{\boldsymbol{V}}_{t|t-1} + \Delta\hat{\boldsymbol{V}}_{i,t|t-1} \\ \boldsymbol{\psi}^{-1}\left(\Delta\hat{\boldsymbol{\varphi}}_{i,t|t-1}\right) \otimes \hat{\boldsymbol{Q}}_{t|t-1} \\ \hat{\boldsymbol{b}}_{a,t|t-1} + \Delta\hat{\boldsymbol{b}}_{a,i,t|t-1} \\ \hat{\boldsymbol{b}}_{g,t|t-1} + \Delta\hat{\boldsymbol{b}}_{g,i,t|t-1} \\ \hat{b}_{t|t-1} + \Delta\hat{b}_{i,t|t-1} \\ \hat{d}_{t|t-1} + \Delta\hat{d}_{i,t|t-1} \end{pmatrix}, \boldsymbol{\chi}'_{i+L',t|t-1} = \begin{pmatrix} \hat{\boldsymbol{P}}_{t|t-1} - \Delta\hat{\boldsymbol{P}}_{i,t|t-1} \\ \hat{\boldsymbol{V}}_{t|t-1} - \Delta\hat{\boldsymbol{V}}_{i,t|t-1} \\ \boldsymbol{\psi}^{-1}\left(-\Delta\hat{\boldsymbol{\varphi}}_{i,t|t-1}\right) \otimes \hat{\boldsymbol{Q}}_{t|t-1} \\ \hat{\boldsymbol{b}}_{a,t|t-1} - \Delta\hat{\boldsymbol{b}}_{a,i,t|t-1} \\ \hat{\boldsymbol{b}}_{g,t|t-1} - \Delta\hat{\boldsymbol{b}}_{g,i,t|t-1} \\ \hat{b}_{t|t-1} - \Delta\hat{b}_{i,t|t-1} \\ \hat{d}_{t|t-1} - \Delta\hat{d}_{i,t|t-1} \end{pmatrix}$$

where

$$\left(\sqrt{(L'+\lambda')\boldsymbol{P}^{x}_{t|t-1}}\right)_i = \begin{pmatrix} \Delta\hat{\boldsymbol{P}}_{i,t|t-1} \\ \Delta\hat{\boldsymbol{V}}_{i,t|t-1} \\ \Delta\hat{\boldsymbol{\varphi}}_{i,t|t-1} \\ \Delta\hat{\boldsymbol{b}}_{a,i,t|t-1} \\ \Delta\hat{\boldsymbol{b}}_{g,i,t|t-1} \\ \Delta\hat{b}_{i,t|t-1} \\ \Delta\hat{d}_{i,t|t-1} \end{pmatrix}$$

and $i = 1, \ldots, L'$.

According to the unscented transformation, the generated sigma points $\boldsymbol{\chi}'_{i,t|t-1}$ are transformed to obtain the predicted observation

$$\hat{\boldsymbol{z}}_{i,t|t-1} = \mathbf{h}\left(\boldsymbol{\chi}'_{i,t|t-1}\right) \tag{5.26}$$

where the function $\mathbf{h}(\cdot)$ depends on the sensor observation model used in different integration stages. As shown in Figure 5.1, the monocular vision sensor and the baro-altimeter are used for updating the estimate of the vehicle state in order to improve its accuracy in stage 1. This processing allows us to reduce the inertial solution drift before processing GNSS measurements. Thus the function $\mathbf{h}(\cdot)$ in stage 1 is composed of (5.8), (5.9) and (5.11). After applying the update step in stage 1, the state estimation provides an improved knowledge of the vehicle state and thus can be used to process and merge GNSS measurements. Reliable GNSS measurements are considered to update the vehicle state in stage 2. Thus the function $\mathbf{h}(\cdot)$ in stage 2 is composed of (5.5) and (5.6). Thus the predicted measurement and its covariance matrix can be obtained

$$\begin{aligned} \hat{\boldsymbol{z}}_t &= \sum_{i=0}^{2L'} W_i^{m\prime} \hat{\boldsymbol{z}}_{i,t|t-1} \\ \boldsymbol{P}_t^{\hat{\boldsymbol{z}}_t\hat{\boldsymbol{z}}_t} &= \sum_{i=0}^{2L'} W_i^{c\prime} \left(\hat{\boldsymbol{z}}_{i,t|t-1} - \hat{\boldsymbol{z}}_t\right)\left(\hat{\boldsymbol{z}}_{i,t|t-1} - \hat{\boldsymbol{z}}_t\right)^{\mathrm{T}} + \boldsymbol{R}_t \end{aligned} \tag{5.27}$$

where $\boldsymbol{R}_t$ is the measurement noise covariance matrix depending on the sensor observation model used in different integration stages. Accordingly, the cross covariance between the predicted state vector $\hat{\boldsymbol{x}}^x_{t|t-1}$ and the predicted measurement $\hat{\boldsymbol{z}}_t$ is given by

$$\boldsymbol{P}_t^{\hat{\boldsymbol{x}}^x_{t|t-1}\hat{\boldsymbol{z}}_t} = \sum_{i=0}^{2L'} W_i^{c\prime}\left(\boldsymbol{\chi}'_{i,t|t-1} - \hat{\boldsymbol{x}}^x_{t|t-1}\right)\left(\hat{\boldsymbol{z}}_{i,t|t-1} - \hat{\boldsymbol{z}}_t\right)^{\mathrm{T}}. \tag{5.28}$$

Note that the calculation for the term $(\boldsymbol{\chi}'_{i,t|t-1} - \hat{\boldsymbol{x}}^x_{t|t-1})$ is the same as (5.23). The conventional Kalman filter gain $\boldsymbol{K}_t$ and the state correction term $\Delta\hat{\boldsymbol{x}}_t$ can then be obtained

$$\boldsymbol{K}_t = \boldsymbol{P}_t^{\hat{\boldsymbol{x}}^x_{t|t-1}\hat{\boldsymbol{z}}_t}\left(\boldsymbol{P}_t^{\hat{\boldsymbol{z}}_t\hat{\boldsymbol{z}}_t}\right)^{-1}, \Delta\hat{\boldsymbol{x}}_t = \boldsymbol{K}_t(\boldsymbol{z}_t - \hat{\boldsymbol{z}}_t) = \begin{pmatrix} \Delta\hat{\boldsymbol{P}}_t \\ \Delta\hat{\boldsymbol{V}}_t \\ \Delta\hat{\boldsymbol{\varphi}}_t \\ \Delta\hat{\boldsymbol{b}}_{a,t} \\ \Delta\hat{\boldsymbol{b}}_{g,t} \\ \Delta\hat{b}_t \\ \Delta\hat{d}_t \end{pmatrix}. \tag{5.29}$$

Finally, the state vector estimation $\hat{\boldsymbol{x}}^x_{t/t}$ is obtained by correcting the predicted state vector $\hat{\boldsymbol{x}}^x_{t|t-1}$ with the correction term $\Delta\hat{\boldsymbol{x}}_t$ leading to

$$\hat{\boldsymbol{x}}^x_{t|t} = \begin{pmatrix} \hat{\boldsymbol{P}}_{t|t-1} + \Delta\hat{\boldsymbol{P}}_t \\ \hat{\boldsymbol{V}}_{t|t-1} + \Delta\hat{\boldsymbol{V}}_t \\ \boldsymbol{\psi}^{-1}\left(\Delta\hat{\boldsymbol{\varphi}}_t\right) \otimes \hat{\boldsymbol{Q}}_{t|t-1} \\ \hat{\boldsymbol{b}}_{a,t|t-1} + \Delta\hat{\boldsymbol{b}}_{a,t} \\ \hat{\boldsymbol{b}}_{g,t|t-1} + \Delta\hat{\boldsymbol{b}}_{g,t} \\ \hat{b}_{t|t-1} + \Delta\hat{b}_t \\ \hat{d}_{t|t-1} + \Delta\hat{d}_t \end{pmatrix} \tag{5.30}$$

and its error covariance matrix is

$$\boldsymbol{P}^x_{t|t} = \boldsymbol{P}^x_{t|t-1} - \boldsymbol{K}_t \boldsymbol{P}_t^{\hat{\boldsymbol{z}}_t\hat{\boldsymbol{z}}_t} \boldsymbol{K}_t^{\mathrm{T}}. \tag{5.31}$$

It is important to note in this quaternion-based UKF that the quaternion vector is propagated and updated using the quaternion product chain rule [122] which leads to a natural way of maintaining the normalization constraint.

5.4.3 Simulation Validation

In order to evaluate the performance of the quaternion-based UKF, especially for the normalization constraint for the quaternion vector when the unscented transformation is performed, a simple scenario is defined considering an IMU/GNSS integration which uses a quaternion-based UKF. The performance of this approach is first assessed using synthetic data. A vehicle dynamic trajectory corresponding to a constant velocity motion with an acceleration noise has been simulated using the parameters reported in Table 5.1. Figure 5.2 shows the simulation trajectory in 3D view and 2D view, respectively.

Accordingly, the IMU outputs, including specific forces and angular rates corresponding to the vehicle motion, have been computed using the power spectral density (PSD) of IMU sensor noises reported in Table 5.2. The initial alignment error for the IMU solution is not taken into account and the IMU data frequency is set to 100 Hz in the simulation. Moreover, the corresponding GNSS PR measurements have been also simulated based on an almanac file including all useful satellite orbit data. The noise parameters used for simulating GNSS PR measurements are reported in Table 5.3. It is assumed that there are 4 in-view satellites PR measurements (satellite #11, #7, #4, #12 and the corresponding elevation angles are 60° - 80°) during the simulation. The frequency of GNSS data is set at 2 Hz.

In the frame of UKF for this scenario, the state vector in (5.12), the state equations in (5.14) and the GNSS PR measurement equation in (5.5) are applied for validating the quaternion-based UKF.

Table 5.1 – Dynamic motion parameters in the simulation.

Simulation time	1200 s
Velocity	10 m/s
Acceleration variance	0.2 m/s^2

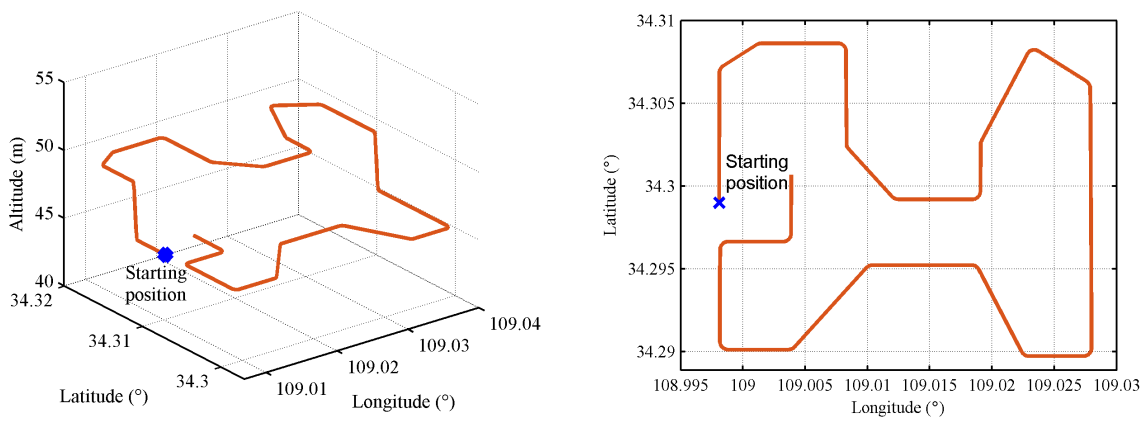

(a) Simulation trajectory in 3D view

(b) Simulation trajectory in 2D view

Figure 5.2 – Simulation trajectory.

Table 5.2 – PSD of IMU sensor noises in the simulation.

	Gyroscope	Accelerometer
White noise	5×10^{-4} (rad/s/$\sqrt{\text{Hz}}$)	5×10^{-4} (m/s^2/$\sqrt{\text{Hz}}$)
Random walk driving noise	2.0×10^{-5} (rad/s/s/$\sqrt{\text{Hz}}$)	1.5×10^{-4} (m/s^2/s/$\sqrt{\text{Hz}}$)

Table 5.3 – GNSS measurement parameters in the simulation.

Clock offset noise	$\sigma_b = 4c \times 10^{-10}$ m
Clock drift noise	$\sigma_d = 2\pi c \times 10^{-10}$ m/s
GNSS measurement noise	$\sigma_r = 10$ m

$c = 3 \times 10^8$ m/s denotes the velocity of light.

The filter period is equal to the frequency of GNSS PR measurement. Finally, $M = 100$ Monte Carlo simulations have been run for this simulation. The root mean square errors (RMSE) of the state vector estimations, defined by $\sqrt{M^{-1}\sum_{i=1}^{M}\left(\hat{\boldsymbol{x}}_t^{(i)} - \boldsymbol{x}_t\right)^2}$ where $\hat{\boldsymbol{x}}_t^{(i)}$ is the ith state vector estimation result, are computed in order to evaluate the estimation accuracy of the quaternion-based UKF.

Figure 5.3 displays the quaternion values versus the simulation time used to evaluate the quaternion-based UKF. Since the change of yaw in the simulated vehicle trajectory is much more important than those of roll and pitch, the elements q_0 and q_3 in the quaternion vector, which contain the yaw information, obviously change with the yaw of the vehicle, whereas the changes in q_1 and q_2, which contain the roll and pitch information, are lower. Note that the quaternion normalization is obtained during the whole simulation by using this quaternion-based approach. Thus the quaternion-based UKF can maintain the normalization constraint for the quaternion vector in the unscented transformation.

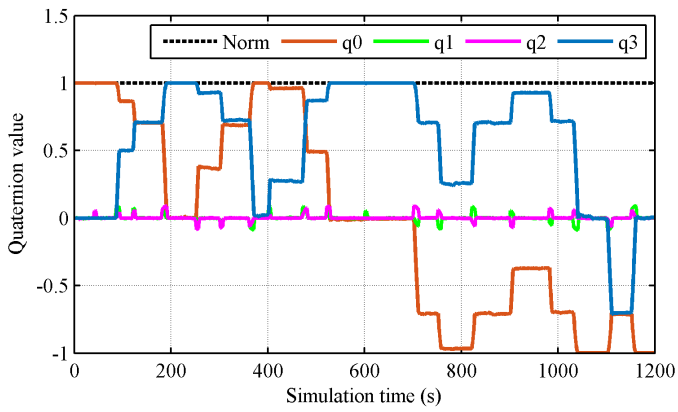

Figure 5.3 – Quaternion values versus time.

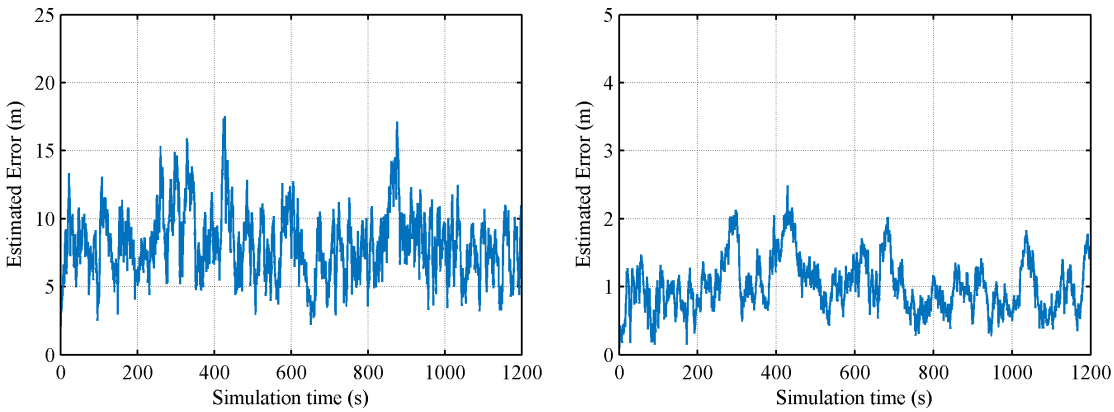

(a) RMSE in horizontal direction **(b)** RMSE in vertical direction

Figure 5.4 – RMSEs of position estimation.

Figure 5.4 displays the RMSEs of the position estimation in horizontal and vertical directions. The RMSE in the horizontal direction fluctuates from 5 m to 15 m which coincides with the GNSS PR measurement noise. Moreover, the RMSE in the vertical direction remains around 1 m during the simulation due to the high elevation angles of the in-view satellites. Thus the quaternion-based UKF can be used to achieve the multi-sensor integration and guarantee the normalization requirement for the quaternion vector.

5.5 Processing GNSS Measurements

As shown in Figure 5.1, an improved knowledge of the vehicle state can be obtained by integrating the IMU with the monocular vision sensor and the baro-altimeter, facilitating the processing of GNSS measurements. In order to detect and eliminate GNSS measurements which are affected by MP interferences, a statistical hypothesis testing can be carried out for detecting contaminated measurements. In this work, MP interferences will be considered as abrupt mean value jumps affecting both PR and DR measurements [76, 123]. We consider the two following hypotheses

$$\mathrm{H}_0 : \text{MP absence}$$
$$\mathrm{H}_1 : \text{MP presence}$$

and the following test statistic for the mth satellite measurements

$$l_{m,t} = \sum_{j=t-N+1}^{t} \frac{I_{m,j}^2}{\boldsymbol{P}_{m,j}^{\hat{\boldsymbol{z}}_j \hat{\boldsymbol{z}}_j}} \tag{5.32}$$

where $I^2_{m,j} = \boldsymbol{z}_{m,j} - \hat{\boldsymbol{z}}_{m,j}$ is the measurement innovation for the mth satellite and $\boldsymbol{z}_{m,j}$ is the mth in-view satellite measurement at time j (i.e., the PR or the DR related to the mth satellite). In (5.32), $\boldsymbol{P}^{\hat{\boldsymbol{z}}_j \hat{\boldsymbol{z}}_j}_{m,j}$ is the innovation covariance matrix associated with the mth considered PR or DR measurement. Here $m = 1, \ldots, m_s$ where m_s is the number of in-view satellites, N is the number of measurements chosen in order to ensure a bias-variance trade-off. Accordingly, the decision rule is given by

$$l_{m,t} \underset{\mathrm{H}_0}{\overset{\mathrm{H}_1}{\gtrless}} \varepsilon \tag{5.33}$$

where ε is a detection threshold which depends on the desired probability of false alarm (PFA). Under the hypothesis H_0, the distribution of the test statistic $l_{m,t}$ is a central χ^2 distribution with N degrees of freedom (denoted as χ^2_N) which allows to compute ε as a function of the PFA [124].

It is important to clearly point out that the detection performance depends on the covariance of the estimated state vector. Improving the vehicle state estimation by exploiting data of the vision sensor and the baro-altimeter is therefore of high relevance. Moreover, in case of slow fading channel, coherent MP interferences can be observed depending on the direction of the vehicle motion. Such MP interferences degrade the PR measurement without affecting the DR measurement. As a consequence, we propose a two-step detection procedure (as illustrated in Figure 5.5) for each in-view GNSS satellite measurements.

- **The first step** (PR bias detection): Contaminated PR measurements are discarded if the test statistic $l^{\mathrm{PR}}_{m,t}$ exceeds the threshold. DR measurements associated with the discarded PR measurements are then considered in the second step.

- **The second step** (DR bias detection): This step is applied to satellites associated with contaminated PRs. DR measurements are discarded if the test statistic $l^{\mathrm{DR}}_{m,t}$ exceeds the threshold.

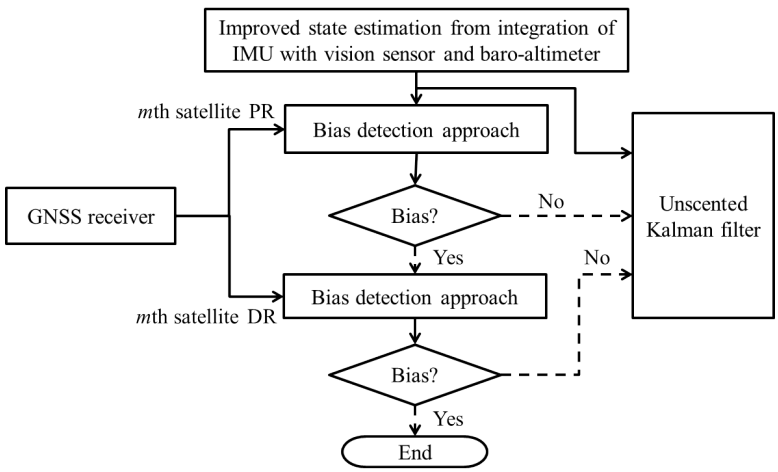

Figure 5.5 – MP bias detection procedure.

This procedure allows reliable GNSS measurements to be selected. As PR and DR associated with a given satellite are strongly correlated, only one of these measurements will be used for navigation, with a preference for PR measurements.

5.6 Algorithm Assessment

5.6.1 Measurement Campaign

In this section, the proposed algorithm is validated on the basis of experimental data. Data have been obtained from a measurement campaign carried out in Toulouse center (France). The measurement campaign lasted 2000 s. A synchronized integrated navigation system composed of a Novatel receiver combined with a tactical grade IMAR IMU has been used to provide a reference trajectory. Taking advantage of a ground based station, differential corrections have been performed to obtain a position accuracy close to 1 m. The trajectory followed by the vehicle is shown in Figure 5.6. The receiver is strongly affected by MP interferences in urban canyons.

For the proposed approach assessment, the vehicle has been equipped with a UBLOX 4T receiver with sampling frequency set to 1 Hz. In this kind of environment, we can consider that the standard deviation of PR measurements is 10 m whereas that of DR measurement is 1 m/s. IMU measurements were obtained by degrading the tactical grade IMAR IMU. The value of the noise PSD for the gyroscope and the accelerometer are given in Table 5.4. The monocular vision sensor and baro-altimeter measurements and their related measurement noises are generated according to [113] and [114]. Moreover, it is assumed that all sensor observations are synchronized and that the data frequency is 1 Hz. In order to facilitate the detection of MP interferences, the size of the sliding window is $N = 3$ for computing the test statistic in (5.32) and the corresponding value of PFA is fixed to 0.05.

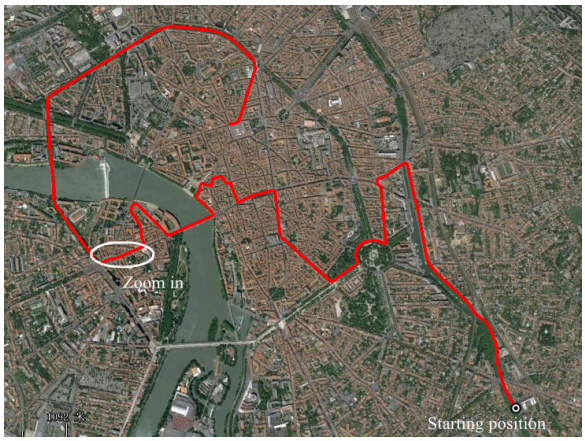

Figure 5.6 – Measurement campaign used for validating the proposed approach (obtained with Google Earth).

Table 5.4 – PSD of IMU sensor noises in measurement campaign.

	Gyroscope	Accelerometer
White noise	9×10^{-4} (rad/s/$\sqrt{\text{Hz}}$)	9×10^{-4} (m/s^2/$\sqrt{\text{Hz}}$)
Random walk driving noise	2.2×10^{-5} (rad/s/s/$\sqrt{\text{Hz}}$)	1.6×10^{-4} (m/s^2/s/$\sqrt{\text{Hz}}$)

5.6.2 Results

Three different approaches are compared in this study:

- **Approach 1**: Only PR measurements are considered as observations and GNSS measurement processing is not performed. Update is carried out using all available incoming GNSS measurement data.
- **Approach 2**: PR and DR measurements are considered as observations. The GNSS measurement processing consists of detecting contaminated measurements.
- **Approach 3**: IMU/GNSS integration is aided by the vision sensor and the baro-altimeter. The full processing described in Figure 5.1 is implemented in this approach.

Figure 5.7 shows the horizontal position errors of the different approaches versus the experiment time. Although the horizontal error of the approach 2 is smaller than that of the approach 1, the position accuracy of the approach 3 is the highest among these three approaches. This result can be explained by the fact that contaminated GNSS measurements are more easily detected and mitigated due to the improved vehicle state estimation obtained by using the vision sensor and the baro-altimeter measurements in the approach 3.

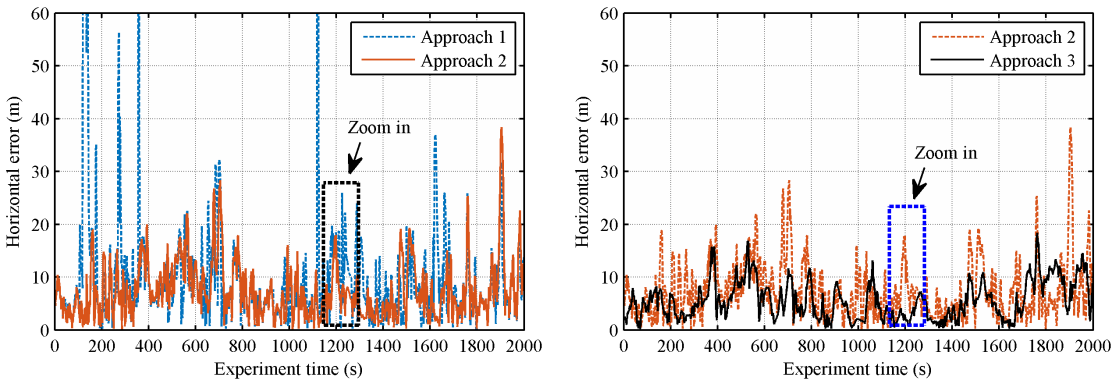

(a) Horizontal errors of the approach 1 and 2

(b) Horizontal errors of the approach 2 and 3

Figure 5.7 – Horizontal errors of different approaches.

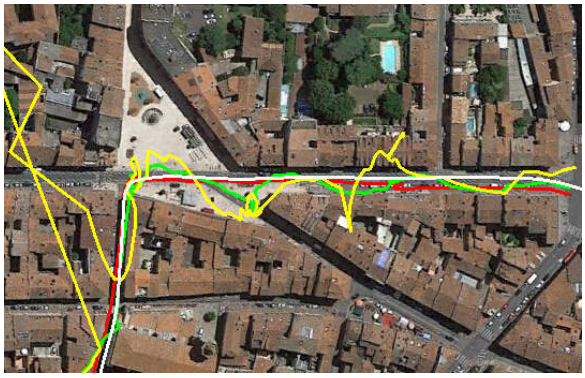

Figure 5.8 – Positioning results for different approaches in a urban canyon (obtained with Google Earth). Reference trajectory: white line; The approach 1: yellow line; The approach 2: green line; The approach 3: red line.

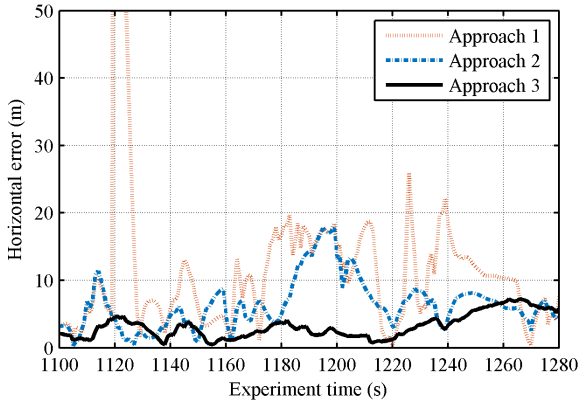

Figure 5.9 – Horizontal errors in a urban canyon.

Figures 5.8 and 5.9 display the positioning results (illustrated in Google Earth) and the corresponding positioning errors for the different approaches when the vehicle moves in a severe environment (corresponding to the zoom highlighted in Figures 5.6 and 5.7). It is clear that the approach 3 provides the best results since the use of complementary measurements facilitates MP mitigation and improves the positioning accuracy.

Figure 5.10 shows that the improvement for positioning accuracy is related to the quality of the test processing applied to GNSS measurements. Indeed, in Figure 5.10 (a), the number of discarded PR measurements is larger when the approach 3 is considered. Moreover, Figure 5.10 (b) shows that, in that case, DR measurements can be preferred to PR measurements. This situation occurs in case of coherent MP inteferences that do not affect the estimation of the Doppler frequency computed by the receiver, whereas the delay lock loop provides a biased estimation of the propagation delay. Figure 5.11 displays the performance of the test statistic when the satellite #5 is considered. It can be observed that the use of complementary sensors to improve the initial information of the vehicle state facilitates the detection of contaminated measurements.

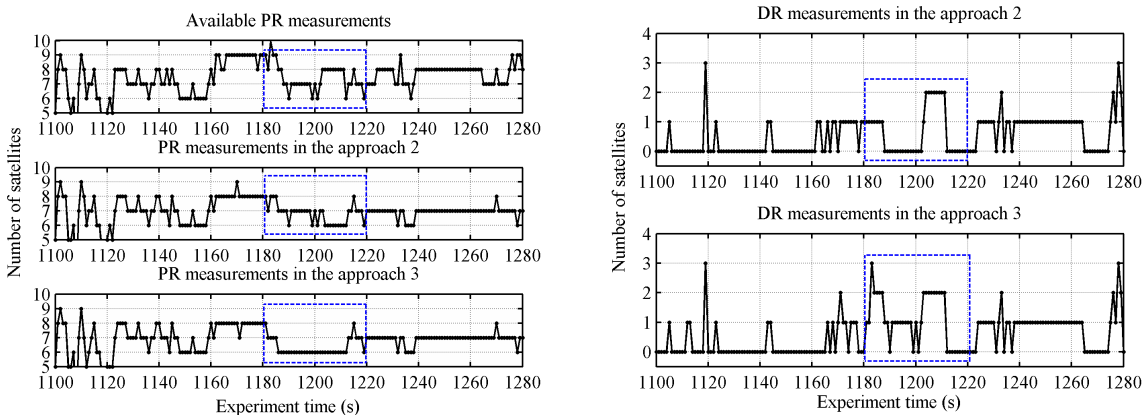

(a) Number of PR measurements

(b) Number of DR measurements

Figure 5.10 – Number of GNSS measuements for the three approaches.

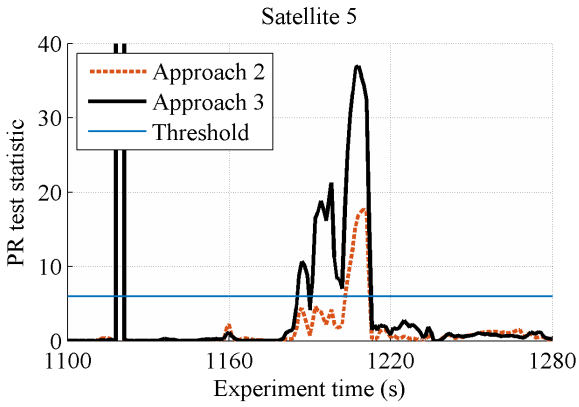

Figure 5.11 – PR test value for satellite #5.

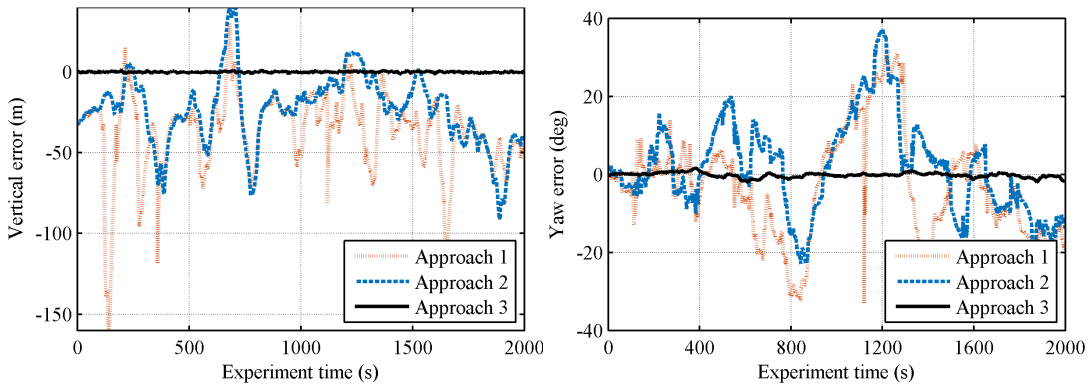

(a) Vertical error

(b) Yaw error

Figure 5.12 – Vertical and yaw errors for the three approaches.

Finally, the baro-altimeter provides a measurement of the vehicle altitude while the GNSS measurements, especially in the vertical direction, is sensitive to the MP interferences in the constricted

environment. Meanwhile, the vision sensor provides an observation of the vehicle attitude which is exploited advantageously by the approach proposed in this work. Figure 5.12 displays the vertical position and attitude errors of the estimated vehicle state for the different approaches. It can be observed that the vertical position and yaw errors are significantly reduced with the approach 3, which takes advantage of baro-altimeter and vision sensor measurements.

5.7 Conclusion

In this chapter, a tightly-coupled IMU/GNSS integration aided by a monocular vision sensor and a baro-altimeter was proposed for improving the positioning reliability in MP environments. The proposed approach aimed at handling efficiently GNSS measurements by using improved a priori knowledge about the vehicle state obtained from the integration of an IMU with a monocular vision sensor and a baro-altimeter. A hierarchical sensor integration approach was proposed for state estimation: 1) IMU was integrated with a vision sensor and a baro-altimeter in order to improve the accuracy of the vehicle state, 2) GNSS measurement(PR and DR) errors were detected and contaminated data were eliminated, 3) only reliable GNSS measurements were used for updating the vehicle state. Considering that MP errors associated with GNSS measurements are small in urban environments, a statistical test was implemented to detect GNSS measurements using a two-step detection procedure applied to the PR and DR of each in-view satellite. Because the sensor models used in this work were both described by non-linear equations, a quaternion-based unscented Kalman filter was implemented in order to maintain the normalization constraint for the quaternion vector in the unscented transformation. Experimental IMU and GNSS data were used to validate the proposed approach. Due to the additional sensor information, the proposed approach was able to detect and mitigate MP errors associated with GNSS measurements. The positioning accuracy was obviously improved in MP environments.

CHAPTER

SIX

CONCLUSIONS AND FUTURE WORK

Satellite navigation is playing a role more and more important in the modern society. Nevertheless, with the new applications new challenges are emerging as well. In this thesis, one of the largest challenge, i.e., the multipath (MP) interference mitigation within the GNSS receiver, has been studied. After an introduction to the subject of MP mitigation inside the GNSS receiver in Chapter 2, the three following chapters presented the main contributions of this research. These contributions are summarized in this chapter, and some recommendations for future work follow.

6.1 Thesis Research Conclusions

An ML-based UKF for MP Mitigation in a Multi-correlator based GNSS Receiver (Chapter 3) In this chapter, a maximum likelihood-based UKF was proposed to estimate the LOS signal parameters in the presence of MP interferences. In order to fully characterize the impact of MP signals on the correlation function, a multi-correlator based receiver, constructing samples of the whole correlation function, was considered. A dynamic and a likelihood models were exploited to describe the LOS signal and the MP signal parameters respectively. Then the signal parameters were estimated iteratively by the proposed approach, i.e., an interval grid search based on the maximum likelihood principle was implemented to estimate the MP signal parameters by using the estimators of the LOS signal parameters, and an UKF method was developed to estimate the LOS signal parameters from estimators of the MP signal parameters. A simulation study was conducted in order to compare the performance of the proposed approach with the standard UKF. In the absence of MP interferences, the performance of the proposed approach is equivalent to that of the standard UKF. On the contrary, in the presence of MP interferences, the estimation accuracy for the LOS signal parameters, especially for the code delay, can be improved by the proposed approach. Moreover, the proposed approach was shown to be more robust than the standard UKF being less sensitive to the abrupt change affecting the received measurements in the presence of MP interferences.

An MLRT for Detecting and Estimating NLOS MP Biases on GNSS PR measurements (Chapter 4)
In this chapter, an approximated MLRT based on Jensen's inequality was proposed to detect, identify and estimate the NLOS multipath biases affecting GNSS PR measurements in urban canyons. The effects of NLOS multipath interferences were modeled as mean value jumps. The proposed approach was based on a marginalized likelihood ratio test approximated using an MC integration and Jensen's inequality. The multiple model algorithm was introduced to update the prior information of each bias magnitude sample in order to improve its detection. A simulation study was implemented in order to compare the performance of the proposed approach with the GLRT and the approach studied in [102]. Although the mean detection delay and the standard deviation of the proposed approach were slightly inferior to those of the GLRT, the probability of correct detection increased significantly (when compared to the GLRT) due to the introduction of a prior information about the bias magnitude. A comparison with the standard EKF and the approach studied in [102] showed that the positioning accuracy was improved by the proposed approach. Finally, the proposed approach was validated by processing data collected from a measurement campaign carried out in an urban environment. The proposed approach proved its efficiency for MP interference detection and mitigation, resulting in improving positioning accuracy.

A Vision aided IMU/GNSS Integration for Reliable Positioning in MP Environments (Chapter 5)
In this Chapter, a tightly-coupled IMU/GNSS integration aided by a monocular vision sensor and a baro-altimeter was proposed for improving the positioning reliability in MP environments. The proposed approach aimed at handling efficiently GNSS measurements by using improved a priori knowledge about the vehicle state obtained from the integration of an IMU with a monocular vision sensor and a baro-altimeter. A hierarchical sensor integration approach was proposed for state estimation: 1) IMU was integrated with a vision sensor and a baro-altimeter in order to improve the accuracy of the vehicle state, 2) GNSS measurement(PR and DR) errors were detected and contaminated data were eliminated and 3) only reliable GNSS measurements were used for updating the vehicle state. Considering that MP errors associated with GNSS measurements are small in urban environments, a statistical test was implemented to detect GNSS measurements using a two-step detection procedure applied to the PR and DR of each in-view satellite. Because the sensor models used in this work were both described by non-linear equations, a quaternion-based unscented Kalman filter was implemented in order to maintain the normalization constraint for the quaternion vector in the unscented transformation. Experimental IMU and GNSS data were used to validate the proposed approach. Due to the additional sensor information, the proposed approach was able to detect and mitigate MP errors associated with GNSS measurements. The positioning accuracy was obviously improved in MP environments.

6.2 Future Work

In line with the research results here presented, several questions are also raised for future work:

- In Chapter 3, an interval grid search was proposed to determine the possible code delays of MP signals, but high computation load is required by this approach. Moreover the estimation results of the proposed approach based on a bank of correlators were not optimal due to the fact that the estimation of the MP code delay is approximated to the nearest correlator delay, resulting in the approximation error inevitably. Thus a more reliable approach based on optimization methods, such as the Newton iteration or the expectation-maximization algorithm, could be investigated to determine the code delays of MP signals.

- In Chapter 4, one of the fundamental assumptions was that the magnitude of MP biases appearing on the pseudo-range measurement followed a uniform distribution in a specific interval. According to measurement campaign data, the MP bias magnitude could follow a Rayleigh distribution in a very constricted environment. Thus the Rayleigh distribution assumption about the MP bias magnitude could be envisaged to be applied in the approximate marginalized likelihood ratio test, rendering it more reliable in practice.

- In Chapter 5, the proposed integration architecture was validated by using post-processed measurement campaign data. However, the real-time implementation with the vision sensor could allow us to validate the performance of the proposed method. It is important to note that the vision is used here as a simple optic flow sensor requiring no landmark storage. With regard to this approach, the detection method could take advantage of an accurate classification of MP errors in different urban environments. This classification could be investigated on the basis of data obtained from measurement campaigns.

BIBLIOGRAPHY

[1] P. Misra and P. Enge, *Global Positioning System: Signals, Measurements and Performance.* Ganga-Jamuna Press, 2001.

[2] E. Kaplan and C. Hegarty, *Understanding GPS: Principles and Application.* Artech House, 2nd ed., 2006.

[3] P. Esteves, *High-sensitivity Adaptive GNSS Acquisition Schemes.* PhD thesis, Universite de Toulouse, 2014.

[4] B. Parkinson, J. Spilker Jr, P. Axelrad, and P. Enge, *Global Positioning System: Theory and Application, Volume 1.* American Institute of Astronautics and Aeronautics, 1996.

[5] J. Tsui, *Fundamentals of Global Positioning System Receivers: A Software Approach.* John Wiley & Sons, 2nd ed., 2005.

[6] K. Borre, D. Akos, N. Bertelsen, and P. Rinder, *A Software-Defined GPS and Galileo Receiver - A Single-Frequency Approach.* Birkhäuser, 2007.

[7] M. Simon, *Spread Spectrum Communications Handbook.* McGraw-Hill, 1994.

[8] J. Proakis, *Digital Communications.* McGraw Hill, 4th ed., 2005.

[9] P. D. Groves, *Principles of GNSS, Inertial and Multisensor Integrated Navigation Systems.* Artech House, 2008.

[10] B. Parkinson, J. Spilker Jr, P. Axelrad, and P. Enge, *Global Positioning System: Theory and Application, Volume 2.* American Institute of Astronautics and Aeronautics, 1996.

[11] *Navstar GPS Space Segment/Navigation User Interfaces (IS-GPS-200G).* United States Government, 2013.

[12] United States Government, "Official U.S. Government Information about the Global Positioning System (GPS) and related topics." `www.gps.gov`. Accessed: 15/04/2015.

[13] *Navstar GPS Space Segment/User Segment L5 Interfaces (IS-GPS-705C).* United States Government, 2013.

[14] *Navstar GPS Space Segment/User Segment L1C Interface (IS-GPS-800C).* United States Government, 2013.

[15] C. Hegarty and E. Chatre, "Evolution of the Global Navigation Satellite System (GNSS)," *Proceedings of the IEEE*, vol. 96, no. 12, pp. 1902–1917, 2008.

[16] Russian Institute of Space Device Engineering, *GLONASS Interface Control Document - Navigational Radiosignal in Bands L1, L2 (Edition 5.1).* Russian Government, 2013.

[17] Y. Urlichich, V. Subbotion, G. Stupak, and V. Dvorkin, "GLONASS Modernization," *GPS World*, pp. 34–39, 2011.

[18] European Space Agency, "Navipedia - The Reference for Satellite Navigation Know-How." `www.navipedia.net`. Accessed: 15/04/2015.

[19] European Space Agency, *Galileo Open Service Signal in Space Interface Control Document (OS SIS ICD) Issue 1.* European Union, 2010.

[20] China Satellite Navigation Office, *BeiDou Navigation Satellite System Open Service Performance Standard (Version 1.0).* China Government, 2013.

[21] China Satellite Navigation Office, *BeiDou Navigation Satellite System Signal In Space Interface Control Document - Open Service Signal (Version 2.0).* China Government, 2013.

[22] China Satellite Navigation Office, "China Successfully Launched the First New-Generation Beidou Navigation Satellite." `www.beidou.gov.cn`. Accessed: 15/04/2015.

[23] Indian Space Research Organization, "Satellites Navigation." `http://www.isro.org/spacecraft/satellite-navigation`. Accessed: 08/04/2015.

[24] Indian Space Research Organization, "Indian Regional Navigation Satellite System." `www.isro.gov.in/irnss-programme`. Accessed: 08/04/2015.

[25] Quasi-Zenith Satellite System Service. `qzss.go.jp/en/`. Accessed: 08/04/2015.

[26] Electronic Navigation Research Institute (Japan), "Development of QZSS." `www.enri.go.jp/~sakai/qzss_e.htm`. Accessed: 08/04/2015.

[27] S. Daneshmand, A. Broumandan, N. Sokhandan, and G. Lachapelle, "GNSS multipath mitigation with a moving antenna array," *IEEE Transactions on Aerospace and Electronic Systems*, vol. 49, no. 1, pp. 693–698, 2013.

[28] Z. Y. Jiang and P. D. Groves, "NLOS GPS signal detection using a dual-polarisation antenna," *GPS Solutions*, vol. 18, no. 1, pp. 15–26, 2014.

[29] P. D. Groves, "Shadow matching: A new GNSS positioning technique for urban canyons," *Journal of Navigation*, vol. 64, no. 3, pp. 417–430, 2011.

[30] A. Bourdeau, M. Sahmoudi, and J.-Y. Tourneret, "Constructive use of GNSS NLOS-multipath: Augmenting the navigation Kalman filter with a 3D model of the environment," in *Proceedings of the* 15th *International Conference on Information Fusion (FUSION 2012)*, (Singapore), 2012.

[31] M. Spangenberg, *Safe Navigation for Vehicles.* PhD thesis, Universite de Toulouse, 2009.

[32] L. Y. Liu and M. G. Amin, "Tracking performance and average error analysis of GPS discriminators in multipath," *Signal Processing*, vol. 89, no. 6, pp. 1224–1239, 2009.

[33] B. Townsend and P. Fenton, "A practical approach to the reduction of pseudorange multipath errors in a L1 GPS receiver," in *Proceedings of the* 7th *International Technical Meeting of the Satellite Division of the Institute of Navigation (ION GNSS 1994)*, (Lake City, UT, USA), 1994.

[34] R. D. J. van Nee, B. Townsend, P. Fenton, and A. J. van Dierendonck, "L1 carrier phase multipath error reduction using MEDLL technology," in *Proceedings of the* 8th *International Technical Meeting of the Satellite Division of the Institute of Navigation (ION GPS 1995)*, (Palm Springs, CA, USA), 1995.

[35] M. Irsigler and B. Eissfeller, "Comparison of multipath mitigation techniques with consideration of future signal structures," in *Proceedings of the* 16th *International Technical Meeting of the Satellite Division of the Institute of Navigation (ION GNSS 2003)*, (Portland, OR, USA), 2003.

[36] S. F. S. Dardin, V. Calmettes, B. Priot, and J.-Y. Tourneret, "Design of an adaptive vector-tracking loop for reliable positioning in harsh environment," in *Proceedings of the* 26th *International Technical Meeting of the Satellite Division of the Institute of Navigation (ION GNSS 2013)*, (Nashville, TN, USA), 2013.

[37] X. Chen, F. Dovis, S. L. Peng, and Y. Morton, "Comparative studies of GPS multipath mitigation methods performance," *IEEE Transactions on Aerospace and Electronic Systems*, vol. 49, no. 3, pp. 1555–1568, 2013.

[38] M. Spangenberg, A. Giremus, P. Poire, and J.-Y. Tourneret, "Multipath estimation in the global positioning system for multicorrelator receivers," in *Proceedings of the* 32th *IEEE International Conference on Acoustics, Speech and Signal Processing (ICASSP 2007)*, (Honolulu, HI , USA), 2007.

[39] M. S. Braasch, "Performance comparison of multipath mitigating receiver architectures," in *2001 IEEE Proceedings-Aerospace Conference*, (Big Sky, MT, USA), 2001.

[40] A. J. van Dierendonck, P. Fenton, and T. Ford, "Theory and performance of narrow correlator spacing in a GPS receiver," *Journal of Navigation*, vol. 39, no. 3, pp. 265–283, 1992.

[41] L. Garin, F. van Diggelen, and J. M. Rousseau, "Strobe & Edge correlator multipath mitigation for code," in *Proceedings of the* 9th *International Technical Meeting of the Satellite Division of the Institute of Navigation (ION GPS 1996)*, (Kansas City, MO, USA), 1996.

[42] S. M. Kanekal and M. S. Braasch, "Multipath mitigation with gated signal technique," in *Proceedings of the* 54th *Annual Meeting of the Institute of Navigation*, (Denver, CO, USA), 1998.

[43] G. A. McGraw and M. S. Braasch, "GNSS multipath mitigation using gated and high resolution correlator concepts," in *Proceedings of the National Technical Meeting of the Institute of Navigation (ION NTM 1999)*, (San Diego, CA, USA), 1999.

[44] J. Jone, P. Fenton, and B. Simth, "Theory and performance of the pulse apeture correlator," tech. rep., NovAtel, 2004.

[45] A. J. van Dierendonck and M. S. Braasch, "Evaluation of GNSS receiver correlation processing techniques for multipath and noise mitigation," in *Proceedings of the National Technical Meeting of the Institute of Navigation (ION NTM 1997)*, (Santa Monica, CA, USA), 1997.

[46] N. Jardak and N. Samama, "Short multipath insensitive code loop discriminator," *IEEE Transactions on Aerospace and Electronic Systems*, vol. 46, no. 1, pp. 278–295, 2010.

[47] N. Jardak, A. Vervisch-Picois, and N. Samama, "Multipath insensitive delay lock loop in GNSS receivers," *IEEE Transactions on Aerospace and Electronic Systems*, vol. 47, no. 4, pp. 2590–2609, 2011.

[48] M. Sahmoudi and R. Landry Jr., "multipath mitigation techniques using maximum-likelihood principle," *Inside GNSS*, vol. 3, no. 8, pp. 24–29, 2008.

[49] R. D. J. van Nee and J. Siereveld, "The multipath estimating delay lock loop - approaching theoretical accuracy limits," in *Proceedings of the* 6th *International Technical Meeting of the Satellite Division of the Institute of Navigation (ION GPS 1993)*, (Salt Lake, UT, USA), 1993.

[50] B. R. Townsend, P. Fenton, K. J. van Dierendonck, and R. D. J. van Nee, "Performance evaluation of the multipath estimating delay lock loop," *Journal of Navigation*, vol. 42, no. 3, pp. 502–514, 1995.

[51] L. R. Weill, "Multipath mitigation using modernized Gps signals: How good can it get?," in *Proceedings of the* 15th *International Technical Meeting of the Satellite Division of the Institute of Navigation (ION GNSS 2002)*, (Portland, OR, USA), 2002.

[52] J. Jones, P. Fenton, and A. J. van Dierendonck, "The theory and performance of NovAtel Inc.'s Vision correlator," in *Proceedings of the* 18th *International Technical Meeting of the Satellite Division of the Institute of Navigation (ION GNSS 2005)*, (Long Beach, CA, USA), 2005.

[53] J. Selva, "An efficient newton-type method for the computation of ML estimators in a uniform linear array," *IEEE Transactions on Signal Processing*, vol. 53, no. 6, pp. 2036–2045, 2005.

[54] J. Selva, *Efficient Multipath Mitigation in Navigation Systems*. PhD thesis, Universitat Politecnica de Catalunya, 2004.

[55] J. Selva, "Complexity reduction in the parametric estimation of superimposed signal replicas," *Signal Processing*, vol. 84, no. 12, pp. 2325–2343, 2004.

[56] M. Sahmoudi and M. G. Amin, "Robust tracking of weak GPS signals in multipath and jamming environments," *Signal Processing*, vol. 89, no. 7, pp. 1320–1333, 2009.

[57] J. Selva, "Interpolation of bounded bandlimited signals and applications," *IEEE Transactions on Signal Processing*, vol. 54, no. 11, pp. 4244–4260, 2006.

[58] M. Sahmoudi and M. G. Amin, "Fast iterative maximum-likelihood algorithm (fimla) for multipath mitigation in the next generation of GNSS receivers," *IEEE Transactions on Wireless Communications*, vol. 7, no. 11, pp. 4362–4374, 2008.

[59] N. Blanco-Delgado and F. D. Nunes, "Multipath estimation in multicorrelator GNSS receivers using the maximum likelihood principle," *IEEE Transactions on Aerospace and Electronic Systems*, vol. 48, no. 4, pp. 3222–3233, 2012.

[60] M. Lentmaier and B. Krach, "Maximum likelihood multipath estimation in comparison with conventional delay lock loops," in *Proceedings of the* 19th *International Technical Meeting of the Satellite Division of the Institute of Navigation (ION GNSS 2006)*, (Forth Worth, TA, USA), 2006.

[61] F. D. Nunes, F. M. G. Sousa, and J. M. N. Leitao, "Nonlinear least-squares algorithm for close-in multipath mitigation in GNSS receivers," in *Proceedings of the* 20th *International Technical Meeting of the Satellite Division of the Institute of Navigation (ION GNSS 2007)*, (Fort Borth, TA, USA), 2007.

[62] F. Antreich, O. Esbri-Rodriguez, J. A. Nossek, and W. Utschick, "Estimation of synchronization parameters using SAGE in a GNSS receiver," in *Proceedings of the* 18th *International Technical*

Meeting of the Satellite Division of the Institute of Navigation (ION GNSS 2005), (Long Beach, CA , USA), 2005.

[63] P. Closas, C. Fernandez-Prades, and J. A. Fernandez-Rubio, "ML estimation of position in a GNSS receiver using the SAGE algorithm," in *Proceedings of the* 32th *IEEE International Conference on Acoustics, Speech and Signal Processing (ICASSP 2007)*, (Honolulu, HI , USA), 2007.

[64] A. Lehner and A. Steingass, "A novel channel model for land mobile satellite navigation," in *Proceedings of the* 18th *International Technical Meeting of the Satellite Division of the Institute of Navigation (ION GNSS 2005)*, (Long Beach, CA , USA), 2005.

[65] A. Steingass and A. Lehner, "Measuring the navigation multipath channel - a statistical analysis," in *Proceedings of the* 18th *International Technical Meeting of the Satellite Division of the Institute of Navigation (ION GNSS 2004)*, (Long Beach, CA , USA), 2004.

[66] P. Closas, C. Fernandez-Prades, J. Diez, and D. de Castro, "Nonlinear bayesian tracking loops for multipath mitigation," *International Journal of Navigation and Observation*, 2012.

[67] P. Closas, C. Fernandez-Prades, and J. A. Fernandez-Rubio, "Bayesian Dll for multipath mitigation in navigation systems using particle filters," in *Proceedings of the* 31th *IEEE International Conference on Acoustics, Speech and Signal Processing (ICASSP 2006)*, (Toulouse, France), 2006.

[68] B. Krach, M. Lentmaier, and P. Robertson, "Joint Bayesian positioning and multipath mitigation in gnss," in *Proceedings of the* 33th *IEEE International Conference on Acoustics, Speech and Signal Processing (ICASSP 2008)*, (Las Vegas, NV, USA), 2008.

[69] P. Closas, C. Fernandez-Prades, and J. A. Fernandez-Rubio, "A bayesian approach to multipath mitigation in GNSS receivers," *IEEE Journal of Selected Topics in Signal Processing*, vol. 3, no. 4, pp. 695–706, 2009.

[70] M. Lentmaier, B. Krach, P. Robertson, and T. Thiasiriphet, "Dynamic multipath estimation by sequential monte carlo methods," in *Proceedings of the* 20th *International Technical Meeting of the Satellite Division of the Institute of Navigation (ION GNSS 2007)*, (Forth Worth, TA, USA), 2007.

[71] M. Lentmaier, B. Krach, and P. Robertson, "Bayesian time delay estimation of GNSS signals in dynamic multipath environments," *International Journal of Navigation and Observation*, 2008.

[72] B. Krach, P. Robertson, and R. Weigel, "An efficient two-fold marginalized bayesian filter for multipath estimation in satellite navigation receivers," *EURASIP Journal on Advances in Signal Processing*, pp. 1–12, 2010.

[73] J. M. Huerta, J. Vidal, A. Giremus, and J.-Y. Tourneret, "Joint particle filter and ukf position tracking in severe non-line-of-sight situations," *IEEE Journal of Selected Topics in Signal Processing*, vol. 3, no. 5, pp. 874–888, 2009.

[74] A. Giremus, J.-Y. Tourneret, and V. Calmettes, "A particle filtering approach for joint detection/estimation of multipath effects on GPS measurements," *IEEE Transactions on Signal Processing*, vol. 55, no. 4, pp. 1275–1285, 2007.

[75] C. Cheng, J.-Y. Tourneret, Q. Pan, and V. Calmettes, "A marginalized likelihood ratio approach for detecting and estimating multipath biases on GNSS measurements," in *Proceedings of the* 17th *International Conference on Information Fusion (FUSION 2014)*, (Salamanca, Spain), 2014.

[76] M. Spangenberg, V. Calmettes, O. Julien, J.-Y. Tourneret, and G. Duchateau, "Detection of variance changes and mean value jumps in measurement noise for multipath mitigation in urban navigation," *Journal of Navigation*, vol. 57, no. 1, pp. 35–52, 2010.

[77] V. Pereira, A. Giremus, and E. Grivel, "A Boltzmann machine to model the multipath environment for particle filtering based GPS navigation," in *Proceedings of the* 20th *European Signal Processing Conference (EUSIPCO 2012)*, (Bucharest, Romania), 2012.

[78] V. Pereira, A. Giremus, and E. Grivel, "Modeling of multipath environment using copulas for particle filtering based GPS navigation," *IEEE Signal Processing Letters*, vol. 19, no. 6, pp. 360–363, 2012.

[79] N. Viandier, J. Marais, A. Rabaoui, and E. Duflos, "GNSS pseudorange error density tracking using Dirichlet process mixture," in *Proceedings of the* 13th *International Conference on Information Fusion (FUSION 2010)*, (Edinburgh, UK), 2010.

[80] A. Rabaoui, N. Viandier, E. Duflos, J. Marais, and P. Vanheeghe, "Dirichlet process mixtures for density estimation in dynamic nonlinear modeling: Application to gps positioning in urban canyons," *IEEE Transactions on Signal Processing*, vol. 60, no. 4, pp. 1638–1655, 2012.

[81] J.-H. Won, D. Dotterbock, and B. Eissfeller, "Performance comparison of different forms of Kalman filter approaches for a vector-based GNSS signal tracking loop," *Journal of Navigation*, vol. 57, no. 3, pp. 185–199, 2010.

[82] M. S. Arulampalam, S. Maskell, N. Gordon, and T. Clapp, "A tutorial on particle filters for online nonlinear/non-gaussian Bayesian tracking," *IEEE Transactions on Signal Processing*, vol. 50, no. 2, pp. 174–188, 2002.

[83] S. M. Kay, *Fundamentals of Statistical Signal Processing, Volume I Estimation Theory*. Prentice Hall, 2001.

[84] A. Doucet, S. Godsill, and C. Andrieu, "On sequential Monte Carlo sampling methods for Bayesian filtering," *Statistics and Computing*, vol. 10, no. 3, pp. 197–208, 2000.

[85] A. Doucet, N. de Freitas, and N. Gordon, *Sequential Monte Carlo Methods in Practice*. Springer, 2001.

[86] E. A. Wan and R. van Der Merwe, "The unscented Kalman filter for nonlinear estimation," in *Proceedings of 2000 IEEE Adaptive Systems for Signal Processing, Communications, and Control Symposium (AS-SPCC 2000)*, (Alberta, Canada), 2000.

[87] S. J. Julier and J. K. Uhlmann, "Unscented filtering and nonlinear estimation," *Proceedings of the IEEE*, vol. 92, no. 3, pp. 401–422, 2004.

[88] S. Haykin, *Kalman Filtering and Neural Networks*. John Wiley & Sons, 2001.

[89] A. Farina, B. Ristic, and L. Timmoneri, "Cramér-Rao bound for nonlinear filtering with $P_d < 1$ and its application to target tracking," *IEEE Transactions on Signal Processing*, vol. 50, no. 8, pp. 1916–1924, 2002.

[90] Y. Bar Shalom, X.-R. Li, and T. Kirubarajan, *Estimation with Applications to Tracking and Navigation: Theory Algorithms and Software*. John Wiley & Sons, 2004.

[91] P. Tichavsky, C. H. Muravchik, and A. Nehorai, "Posterior Cramér-Rao bounds for discrete-time nonlinear filtering," *IEEE Transactions on Signal Processing*, vol. 46, no. 5, pp. 1386–1396, 1998.

[92] K. Xiong, H. Y. Zhang, and C. W. Chan, "Performance evaluation of UKF-based nonlinear filtering," *Automatica*, vol. 42, no. 2, pp. 261–270, 2006.

[93] J. Soubielle, I. Fijalkow, P. Duvaut, and A. Bibaut, "GPS positioning in a multipath environment," *IEEE Transactions on Signal Processing*, vol. 50, no. 1, pp. 141–150, 2002.

[94] R. Ercek, P. de Doncker, and F. Grenez, "Statistical determination of the PR error due to NLOS-multipath in Urban Canyons," in *Proceedings of the* 19th *International Technical Meeting of the Satellite Division of the Institute of Navigation (ION GNSS 2006)*, (Forth Worth, TA, USA), 2006.

[95] R. Ercek, P. de Doncker, and F. Grenez, "NLOS-multipath effects on pseudo-range estimation in urban canyons for gnss applications," in *Proceedings of 2006 European Conference on Antennas and Propagation (EuCAP 2006)*, (Nice, France), 2006.

[96] S. M. Kay, *Fundamentals of Statistical Signal Processing, Volume II Detection Theory.* Prentice Hall, 2001.

[97] F. Gustafsson, *Adaptive Filtering and Change Detection.* John Wiley & Sons, 2000.

[98] A. S. Willsky and H. L. Jones, "A generalized likelihood ratio approach to the detection and estimation of jumps in linear systems," *IEEE Transactions on Automatic Control*, vol. 21, no. 1, pp. 108–112, 1976.

[99] F. Gustafsson, "The marginalized likelihood ratio test for detecting abrupt changes," *IEEE Transactions on Automatic Control*, vol. 41, no. 1, pp. 66–78, 1996.

[100] D. A. dos Santos and T. Yoneyama, "A Bayesian solution to the multiple composite hypothesis testing for fault diagnosis in dynamic systems," *Automatica*, vol. 47, no. 1, pp. 158–163, 2011.

[101] F. Kiasi, J. Prakash, S. Patwardhan, and S. L. Shah, "A unified framework for fault detection and isolation of sensor and actuator biases in linear time invariant systems using marginalized likelihood ratio test with uniform priors," *Journal of Process Control*, vol. 23, no. 9, pp. 1350–1361, 2013.

[102] A. Giremus and J. Grolleau, "An unscented Kalman filter based maximum likelihood ratio for NLOS bias detection in UMTS localization," in *Proceedings of the* 16th *European Signal Processing Conference (EUSIPCO 2008)*, (Lausanne, Switzerland), 2008.

[103] D. J. C. MacKay, *Information Theory, Inference and Learning Algorithms.* Cambridge University Press, 2003.

[104] J. Farrell and M. Barth, *The Global Positioning Systems and Inertial Navegation.* McGraw-Hill, 1999.

[105] E. Royer, M. Lhuillier, M. Dhome, and J.-M. Lavest, "Monocular vision for mobile robot localization and autonomous navigation," *International Journal of Computer Vision*, vol. 74, no. 3, pp. 237–260, 2007.

[106] M. Achtelik, S. Weiss, and R. Siegwart, "Onboard IMU and monocular vision based control for MAVs in unknown in-and outdoor environments," in *Proceedings of 2011 IEEE International Conference on Robotics and Automation (ICRA)*, (Shanghai, China), 2011.

[107] D. Nister, O. Naroditsky, and J. Bergen, "Visual odometry," in *Proceedings of 2004 IEEE Computer Society Conference on Computer Vision and Pattern Recognition (CVPR 2004)*, (Washington D.C., USA), 2004.

[108] D. Scaramuzza and F. Fraundorfer, "Visual odometry [tutorial]," *IEEE Robotics & Automation Magazine*, vol. 18, no. 4, pp. 80–92, 2011.

[109] D. Titterton and J. L. Weston, *Strapdown Inertial Navigation Technology*. The Institution of Engineering and Technology, 2004.

[110] P. G. Savage, *Strapdown Analytics*. Strapdown Associates, 2000.

[111] M. S. Grewal, L. R. Weill, and A. P. Andrews, *Global Positioning Systems, Inertial Navigation, and Integration*. John Wiley & Sons, 2007.

[112] N. El-Sheimy, H. Y. Hou, and X. J. Niu, "Analysis and modeling of inertial sensors using allan variance," *IEEE Transactions on Instrumentation and Measurement*, vol. 57, no. 1, pp. 140–149, 2008.

[113] D. Vivet, C. Deymier, B. Priot, and V. Calmettes, "Probabilistic block-matching based 6D camera localization," in *Proceedings of 2012 IEEE International Conference on Robotics and Biomimetics (ROBIO)*, (GuangZhou, China), 2012.

[114] S.-S. Jan, D. Gebre-Egziabher, T. Walter, and P. Enge, "Improving GPS-based landing system performance using an empirical barometric altimeter confidence bound," *IEEE Transactions on Aerospace and Electronic Systems*, vol. 44, no. 1, pp. 127–146, 2008.

[115] National Imagery and Mapping Agency, *Earth Geopotential Model (EGM) 1996 Geoid Calculation*. United States Government, 1996.

[116] F. Gustafsson, F. Gunnarsson, N. Bergman, U. Forssell, J. Jansson, R. Karlsson, and P.-J. Nordlund, "Particle filters for positioning, navigation and tracking," *IEEE Transactions on Signal Processing*, vol. 50, no. 2, pp. 425–437, 2002.

[117] A. Giremus, A. Doucet, V. Calmettes, and J.-Y. Tourneret, "A Rao-blackwellized particle filter for INS/GPS integration," in *Proceedings of the* 29th *IEEE International Conference on Acoustics, Speech and Signal Processing (ICASSP 2004)*, (Montreal, Canada), 2004.

[118] A. Giremus, A. Doucet, A.-C. Escher, and J.-Y. Tourneret, "Non-linear filtering approaches for INS/GPS integration," in *Proceedings of the* 12th *European Signal Processing Conference (EUSIPCO 2004)*, (Vienna, Austria), 2004.

[119] Y. h. Yang, J. C. Zhou, H. Nies, O. Loffeld, and S. Knedlik, "Development of a deeply-coupled GPS/INS integration algorithm using quaternions," in *Proceedings of the* 16th *International Conference on Information Fusion (FUSION 2013)*, (Istanbul, Turkey), 2013.

[120] S. J. Julier, "The scaled unscented transformation," in *Proceedings of 2002 American Control Conference*, (Anchorage, AK, USA), 2002.

[121] Y. h. Yang, J. C. Zhou, and O. Loffeld, "Quaternion-based Kalman filtering on INS/GPS," in *Proceedings of the* 15th *International Conference on Information Fusion (FUSION 2012)*, (Singapore), 2012.

[122] F. Z. Zhang, "Quaternions and matrices of quaternions," *Linear Algebra and its Applications*, vol. 251, pp. 21–57, 1997.

[123] N. Viandier, D. F. Nahimana, J. Marais, and E. Duflos, "GNSS performance enhancement in urban environment based on pseudo-range error model," in *Proceedings of 2008 IEEE/ION Position, Location and Navigation Symposium (PLAN 2008)*, (Monterey, CA, USA), 2008.

[124] R. V. Hogg, J. McKean, and A. T. Craig, *Introduction to Mathematical Statistics.* Pearson Education, 2005.